

UNIVERSITY OF TRENTO

DOCTORAL THESIS

**Linear and non linear coupling effects in
sequence of microresonators**



Author: Mattia Mancinelli

Supervisor: Lorenzo Pavesi

September 2013

Contents

Abbreviations	v
1 Introduction	1
1.1 Optical network on chip: state-of-the-art	8
1.1.1 Waveguides	8
1.1.2 Sources	11
1.1.3 Routing blocks: optical microresonators	11
1.1.3.1 Optical router	14
1.1.3.2 Coherent control of the routing	15
1.1.4 Active modulators	17
1.1.5 Delay lines	18
1.1.6 Detectors	18
1.1.7 External interface: grating coupler	19
1.2 Non linear optics on chip	20
2 Optical network on chip components and its applications	22
2.1 Introduction	22
2.2 SOI based Optical waveguides	23
2.2.1 Waveguides theory	24
2.2.2 Simulations of waveguides	27
2.3 Directional coupler	30
2.4 Bends	34
2.5 Straight-bend directional coupler	37
2.6 Surface roughness	38
2.7 Chip to fiber interface	42
2.7.0.1 In plane coupling	43
2.7.0.2 Out of plane coupling: gratings	44
2.8 Optical microresonators	45
2.9 Microresonator theory	46
2.9.1 Spectral response	48
2.9.2 Phase shift and group delay	52
2.10 Optical microresonator experimental investigation	54
2.10.1 Effective index and group index	54
2.10.2 Bend effective index	57
2.11 Surface roughness effect on microresonators	58

3	Introduction to fabrication Process: main techniques and fabrication errors	60
3.1	Introduction	60
3.2	Three layer (Si- SiO_2 -Si) structure fabrication	61
3.2.1	SIMOX-SOI (Separation by IMplanted OXYgen)	61
3.2.2	Bond and Etch-back SOI (BESOI)	62
3.2.3	Smartcut Process (Unibond)	63
3.3	Deep UltraViolet photolithography	63
3.3.1	Metal wires as thermal heaters	68
3.4	Fabricated wafer	69
3.5	Global and local disorder on a SOI wafer	69
4	Side-coupled integrated spaced sequence of resonators (SCISSOR)	71
4.1	Some hints on the SCISSOR theory	72
4.2	SCISSOR experimental characterization	75
4.2.1	Racetracks based SCISSOR	75
4.2.2	Rings based SCISSOR	77
4.3	Introduction to the <i>coupled resonators induced transparency</i> effect	79
4.3.1	Theoretical description	80
4.3.2	Experimental investigation	84
4.4	Localized states in a SCISSOR structure	87
4.4.1	Localized states in a SCISSOR structure	87
4.4.1.1	Local optical tuning of a localized state	89
4.5	Fabrication defects and localized states	91
4.5.1	Statistical investigation of the localized states	92
4.5.2	Test device for fabrication process errors estimate	95
5	Coupled resonator induced transparency for routing application	99
5.1	Introduction	99
5.2	Exploiting CRIT in a tapered SCISSOR	101
5.2.1	Working principle	101
5.2.2	Two different ways to control the coherence condition	104
5.2.2.1	Local method	104
5.2.2.2	Bragg method	106
5.3	Performances of the CRITAD: spectral investigation	107
5.4	Performances of the CRITAD: Switching capability	110
5.4.1	Switching through an R variation	111
5.4.2	Switching through an L_c variation	112
5.5	Performances of the CRITAD: delay investigation	114
5.6	Performances of the CRITAD: errors robustness	114
5.7	CRITAD based multiplexer/demultiplexer	116
5.8	CRITAD based 2x2 router	118
5.9	CRITAD vs ADF	119
5.10	Experimental investigation	121
5.10.1	Bragg based CRITAD: Transmission spectrum	122
5.10.2	Switching capability: ΔR method	124
5.10.3	Switching capability: ΔL_c method	126

5.10.4	Robustness to fabrication defects	129
5.10.5	Proof of concepts of the 1x4 CRITAD based multiplexer	130
5.11	Dynamic switching capability of the CRITAD	132
5.11.1	Experimental setup	133
5.11.2	Experimental results	134
5.11.3	CRIT channel eye diagram	139
5.12	Conclusions	140
6	Interferometric switching in reconfigurable optical device	144
6.1	Introduction	144
6.2	Some hints on CROW theory	145
6.2.1	Interferometric ADF	147
6.3	The proposed interferometric band interleaver (BIL)	151
6.3.1	Experimental test	152
6.3.2	Influence of the resonators number	155
6.3.3	Influence of the fabrication defects	156
6.4	Conclusions	158
7	Non linear effects in single and coupled microresonators	160
7.1	Introduction	160
7.2	Nonlinear optical medium: General theoretical introduction	162
7.2.1	TPA induced nonlinearities in silicon	163
7.3	Thermal bistability: theory and experiment	166
7.3.1	Experimental verification: TOE induced optical bistability	168
7.3.2	Nonlinear spectrum deformation	169
7.3.3	Non linear resonance broadening	171
7.4	A more in depth view of optical bistability	172
7.4.1	Optical bistability with one nonlinearity	172
7.4.2	Optical bistability with two nonlinearities: self pulsing phenomena	175
7.5	Self pulsing in single microresonator: experiment and simulation results	177
7.5.1	Experiment	177
7.5.2	Simulations	180
7.6	Non linear effects in a SCISSOR device	184
7.6.1	Studied device: self-pulsation induced by localized states	185
7.6.2	Non linear regime: fixed power at different λ	186
7.6.3	Non linear regime: fixed λ at different powers	189
7.6.4	Non linear regime: characteristics time distribution and auto-correlation	190
7.6.5	A possible approach to prove the presence of chaos	192
7.7	Conclusions	193
8	Conclusions	195
9	List of publications	197
A	Time domain analysis of the cavity dynamics	198

A.1	Resonance frequency shift induced by small refractive index perturbations	198
A.1.0.1	Resonance frequency shift induced by thermo optic effect	199
A.1.0.2	Resonance frequency shift induced by free carrier dispersion	200
A.1.0.3	Resonance frequency shift induced by Kerr effect	200
A.1.1	Cavity energy dynamics	201
A.1.2	Temperature dynamics	203
A.1.3	Free carrier dynamics	204
A.1.4	Final set of coupled equations	204
B	Experimental Set-Up	207
B.0.5	Transmission spectrum setup	207
B.0.6	Optical pump setup	209
B.0.7	Electrical setup	210
B.0.8	Non-linear setup	211
C	A simplified model to describe the Ti:Sa external pump effect in a CRITAD	212
	Bibliography	215
	Acknowledgements	215

Abbreviations

WG	Wave Guide
OC	Optical Circuit
CF	Confinement Factor
CMOS	Complementary Mmetal Oxide Semiconductor
RMS	Root Mean Square
CMT	Coupled Mode Theory
CG	Coupling Gap
LER	Line Edge surface Roughness
FEM	Finite Element Domain
PML	Perfect Matched Layer
CC	power Coupling Coefficient
ONC	Optical Network on Chip
MMI	Multi Mode Interference
RTR	Race Track Rresonator
RR	Ring Rresonator
TMM	Tranfer Matrix Method
FWHM	Full Width at Half Maximum
ER	Extionction Ratio
FSR	Free Spectral Mrange
EF	Enhancement Factor
DBR	Distributed Bragg Reflector
DUV	Deep Ultra Violet
PVD	Physical Vapour Deposition
WDM	Wavelength Division Multiplexing
AWG	Aarray Waveguide Grating

SCISSOR	S ide C oupled I ntegrated S paced S equence O f R esonators
CROW	C oupled R esonator O ptical W aveguide
CRIT	C oupled R esonator I duced T ransparency
CRITAD	C oupled R esonator I duced T ransparency A dd D rop filter
BIL	B and I nterleaver
SMF	S ingle M ode F iber
ASE	A mplified S pontaneous E mission
OSA	O ptical S pectrum A nalyzer
TOE	T ermo O ptic E ffect
FCD	F ree C arrier D ispersion
FCA	F ree C arrier A bsorption
OB	O ptical B istability
ChC	C oherence C ondition
SB	S ub B and
MZI	M ach Z hender I nterferometer
SP	S elf P ulsing
GDS	G raphic D atabase S ystem
IC	I ntegrated C ircuit

Ad Alessandra che mi é sempre vicina ...

*Alla mia famiglia che, nonostante la distanza, sento sempre al mio
fianco ...*

Chapter 1

Introduction

Integrated photonics is a quite old research field since the first ideas of integrated devices were born at the end of 1970 [1, 2, 3]. The early work was associated with ferroelectric materials such as Lithium Niobate (LiNbO₃), and III-V semiconductors such as Gallium Arsenide (GaAs) and Indium Phosphide (InP) based systems. LiNbO₃ was interesting almost solely due to the fact that it possesses a large electro optic coefficient enabling optical modulation via the Pockels effect [4]. Alternatively, III-V compounds were interesting because of the relative ease of laser fabrication, and the prospect of optical amplification and electronic integration.

However, no great advancements in integration density followed those first years. The reasons can be looked for a poor market demand, in the use of an exotic compound semiconductor and in the high costs needed to process and fabricates devices.

The stalemate was unlocked when the development of silicon-based microelectronics makes available to photonics a mature production process, and urged an alternative solution for the power dissipation problem and for the bottleneck in high bandwidth requirement in VLSI industry.

For this reason, starting with this century there has been an explosion of research and achievements in Group IV photonics [5, 6]. Group IV photonics is a technology which is based on standard CMOS processing, i.e. to fabricate photonic devices.

Many basic components, which enable an optical network-on-chip (ONC), were designed and fabricated [2, 3, 7]. Nowadays, thanks to the enabling CMOS fabrication technologies, essential silicon photonic passive and active components have been demonstrated, including low-loss sub-micrometer-sized waveguides [8], micrometer-scale optical filters [8, 9], gigabit/second-speed low-power-consumption (pJ/bit) modulators [10, 11], hybrid-integrated evanescent lasers [12], and gigahertz-bandwidth SiGe photodetectors

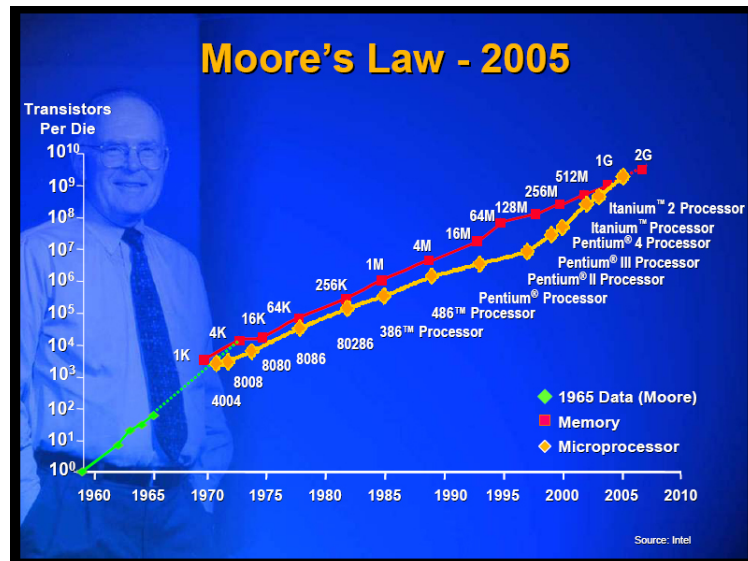


FIGURE 1.1: Moore's law. Source Intel.

[13, 14]. These silicon photonic devices make on-chip optical interconnection a real possibility. The small footprint and the CMOS compatibility makes a silicon photonic chip a perfect candidate to be integrated in a microelectronic chip. This is one of the big goals of silicon photonics since this integration appears to be the only possible solution to widen the future super-computers performances preserving the continuity of Moore's law [15].

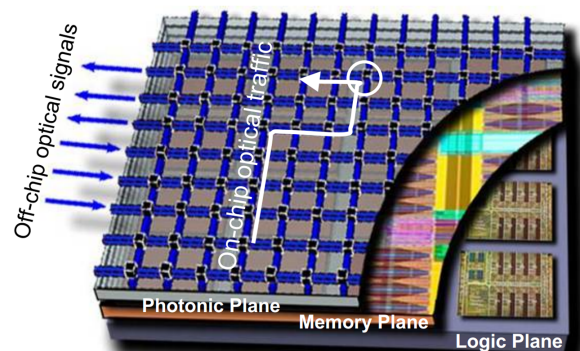


FIGURE 1.2: 3D integration of electronics and photonics on a single CMOS chip. Image taken from [16].

In particular, multi-core microprocessors are based on the integration of sixteen or more cores in a single processor chip. The number of cores per chip is expected to double every 18 months [17]. Therefore, it is fundamental to replace the conventional metallic interconnection by its photonic counterpart. As pointed out in the International Technology Roadmap for Semiconductors (ITRS), optical communication on a chip is one alternative interconnection technology that promises high-data-rate signal transmission and low power consumption. On-chip optical interconnection thus promises a new

paradigm in computer system design. At the same time, it also opens an entirely new set of associated fundamental problems and engineering challenges spanning from materials science, to nanoelectronics and to nanophotonics, and to on-chip network [18, 19].

The components needed to build a ONC can be summarized as follows:

- Waveguides
- Sources
- Active modulators
- Detectors
- Delay lines
- Routing blocks

All these components should have the highest performance in terms of bandwidth (capacity), power consumption, footprint and scalability. A sketch illustrating an application of these building blocks in an ONC is shown in figure 1.3. Hybrid laser sources provide the signals which is pulsed through optical modulators which encode on the optical signal the datastream generated by the electronic signals. The data are then processed by routing blocks composed by active and passive microresonators and crossings [20] arranged in a specific topology (matrix switch in figure 1.3) [21]. Through this stage, the data can be either redirected to other networks, N-E-S, or be delayed, W, or be extracted to another electronic level by means of detectors.

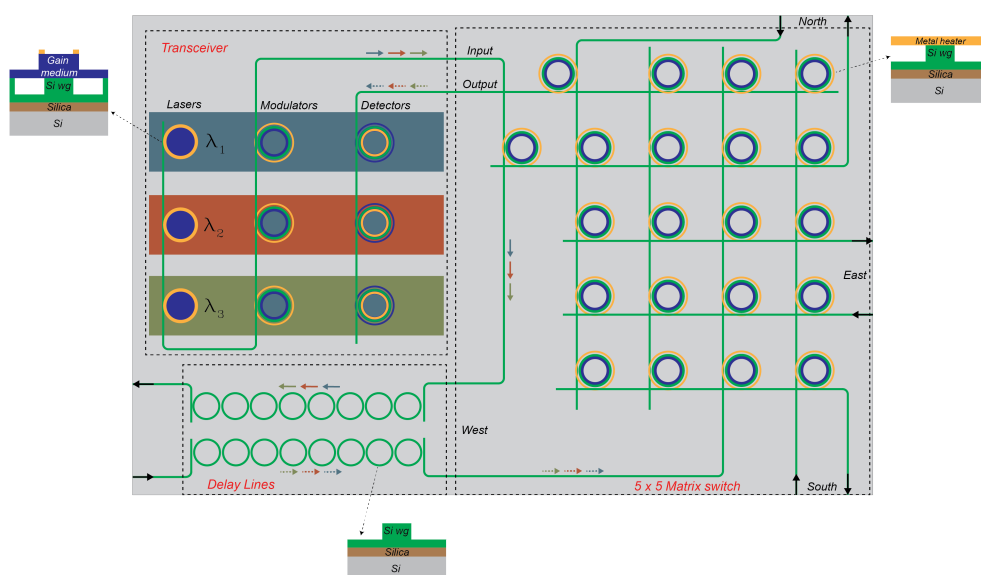


FIGURE 1.3: Optical network on chip sketch.

Wavelength division multiplexing (WDM) is another way to increase the communication bandwidth between cores. It is extensively used in telecommunication networks to increase the maximum bandwidth without the need of installing additional optical fibers. WDM is a technology which multiplexes a number of optical carrier signals onto a single optical fiber by using different wavelengths (i.e. colours) of laser light (see Fig. 1.4). This technique enables bidirectional communications over one strand of fiber, as well as multiplication of capacity. A WDM system uses a multiplexer at the transmitter to join together the signals, and a demultiplexer at the receiver to split them apart [23]. The optical filtering devices which were used in the past, were etalons: stable solid-state single-frequency FabryPérot interferometers in the form of thin-film-coated optical glasses. These were large and expensive devices. So large that a WDM node occupied an entire room. The same operations can be nowadays performed by using integrated photonics and benefiting of its low footprint and low cost. Several configurations have been demonstrated as, for example, the arrayed waveguide grating (AWG)[24] or the microresonator based multiplexer/demultiplexer matrix [25].

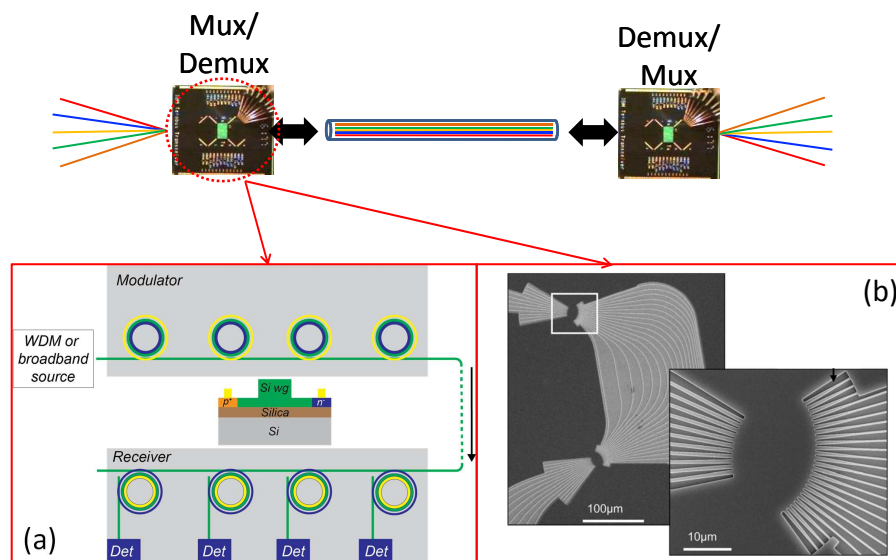


FIGURE 1.4: Sketch of the WDM principle with zooms on the basic block: (a) Microresonator based mux/demux, (b) AWG based mux/demux [24].

Optical microresonators are important for ONC as well. They form the basic node of the network. In this thesis we deal specifically with single optical microresonators and with sequences of microresonator systems, like SCISSORs (side-coupled integrated spaced-sequences of resonators) and CROWs (coupled resonator optical waveguides) (see figure 1.5) [26, 27, 28, 29, 30].

We carried out this study within the european project WADIMOS [31]. WADIMOS aims to build a complex photonic interconnect layer incorporating multi-channel microsources, microdetectors and different advanced wavelength routing functions directly integrated

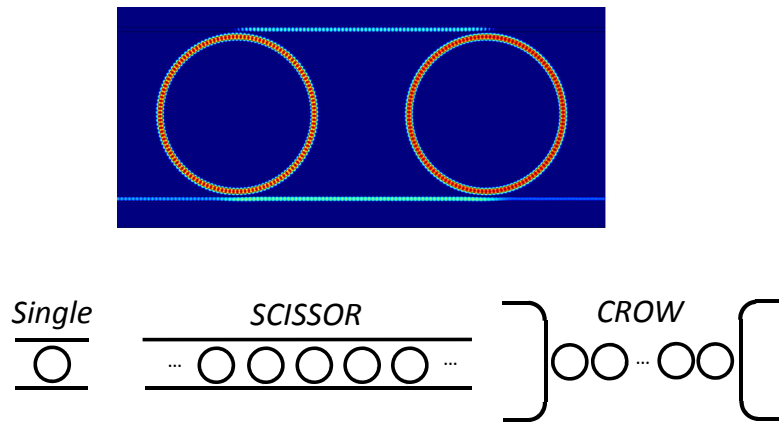


FIGURE 1.5: Example of resonance in 1x2 SCISSOR and the 3 main microresonator configurations: Single resonator, SCISSOR, CROW.

with electronic driver circuits. In WADIMOS such electro-photonic ICs will be used in two representative applications:

- Optical Network on Chip for ST Microelectronics multi-processor chips.
- Terabit optical datalink for MAPPER [32]

The first studies were performed on a 8 ring SCISSOR [33]. We observed multiple anomalous resonances in the device response. These resonances were induced by nanometer scale fabrication disorders and were the results of multiple coupled resonator induced transparency (CRIT resonances)[11]. Since this discovery, we searched for ways to reduce the effect of defects in the optical response of a device and, at the same time, exploit the narrow line width of CRIT. A modified SCISSOR with tapered radii was proposed [34]. The control of the radii in the resonator chain allowed to tuning the CRIT at the desired resonant wavelength. This component can be used as an hitless switching element of an ONC [35]. As a result, we experimentally demonstrated a 1×4 mux/demux based on this design [36].

Exploiting the link between random fabrication defects and CRIT resonances, we developed an all-optical on-chip test device to quantify the errors in any fabrication process of integrated optical components.

In parallel we developed several devices based on the interference of two input signals, with a controlled phase relation, that co-propagates within a microresonator sequence (SCISSOR version [37], CROW version [38]). These devices exploit the characteristics of a classic Mach Zehnder interferometer [39] and of SCISSOR or CROW. In fact, they show the spectral response of the latter and the phase reconfigurability of the former.

The characteristic transmission lineshape of these devices is of the Fano type because it derives from the interference between the discrete resonator state and the waveguide continuum of propagation modes. Optical interleaving [40] and coarse WDM are possible applications of our proposed devices, thanks to their characteristic periodic and wide band response.

The last part of this work focuses on the behaviour of sequence of resonators in the non-linear regime. We focused, in particular, on the dispersive effects that arises in silicon-based single and multiple cavities such as the *free carrier dispersion* (FCD) and the *thermo-optic effect* (TOE) generated by *two photon absorption* (TPA)[41, 42]. Firstly, we verified the main phenomena that occur in an integrated resonator subjected to a high incident power in continuous regime, such as optical bistability (OB) [43] and self-pulsing (SP) [44, 45]. Subsequently, the effect of these non-linearities has been studied in a SCISSOR system. We found the presence of oscillations of complex shape and also of chaotic oscillations with a strong dependence on the number of cavities involved [46]. From the chaotic sequence we were able to extract random sequences. To our knowledge, this is a new result that could pave the way for the creation of a device able to generates random sequences to be used in ONC and for all-optical signal cryptography.

My work was carried out with the aim of devising and characterize new devices for signal routing in optical networks on chip. Particular attention has been paid in the study of structures robust with respect to manufacturing defects. In fact, these structures do not need to be readjusted after production which turns out into a saving of energy. Energy efficiency is one of the points needed to be considered for the development of future computing and communication networks. All devices were fabricated through a standard CMOS facility by using deep UV lithography in order to verify the reliability of resolution and throughput similar to those required for commercial applications. In fact, for research purposes, nanophotonic components are traditionally fabricated by using e-beam lithography, which is slow and unsuitable for mass-fabrication. Deep UV lithography at 248nm or 193nm, the technology used for advanced CMOS fabrication, offers both the resolution and throughput needed for commercial applications.

In my PhD work I have covered the various steps necessary for the fabrication of a device for integrated optics, a part device processing. These steps are:

- Device conception
- Preliminary device simulations for the performance estimation
- GDS mask design
- Construction of the experimental setup

- Samples characterizations
- Confirmation of the obtained results through both analytical and numerical simulations

The fundamental step of sample fabrication were carried out externally by LETI [47] and IMEC [48] by using process technologies on 200mm SOI wafers. These, in general, were fabricated with a 220nm thickness of the Si core layer on 2 μ m buried oxide substrate and a SiO₂ top cladding 0.75 μ m thick. It was used a DUV 193nm lithography.

In the first part of chapter 2, will be presented a brief introduction on the theory of waveguides and their applications. With the help of a finite element method software (COMSOL [49]) the parameters of the SOI WGs, that will be used during the rest of the work, will be estimated. I will also calculate the coupling coefficients for a directional coupler composed by a straight-straight WG section and straight-curved WG section and the effect of the surface roughness in a straight WG. The second part introduces the optical microresonator which is the basic component of all the studied devices. A transfer matrix code will be used to describe the operation of micro resonators. From the measurements of some microresonator test devices, the values of losses, effective index, group index, effective curved index are estimated. These values are used by the transfer matrix code to design new devices and to understand the experimental results.

Chapter 3 introduces the various steps of the optical lithography process and the common techniques used to fabricate the SOI wafers. The main causes of fabrication errors and their effects on the final device are explained.

Chapter 4 describes the theory and the experimental characterization of the SCISSOR device and of its main spectral characteristics. The difference between *localized states* and *CRIT* state will be explained and demonstrated. Then, I will show that the origin of these phenomena can be attributed to manufacturing errors. This effect is then exploited to propose a test device able to quantify the defects in a wafer with just a white source and a photodiode.

In chapter 5 the acquired knowledge of the defects in a SCISSOR is used to design a new type of device that exploits the CRIT phenomenon to perform signal routing. This device, which uses a *tapered SCISSOR* is called *CRITAD*. At first, the theoretical investigation of the device is carried out, that includes the characterization of the losses and crosstalk, the switching capability, and the robustness to defects. Some optical networks topologies, suitable for this device, are proposed. In the second part, the CRITAD performances, both stationary and dynamic, will be experimentally investigated .

Chapter 6 introduces the *CROW interferometric device*. After a brief theoretical introductions, the experimental characterization of this device is shown.

In the first part of chapter 7, the theory of nonlinear optics in silicon, with attention to the phenomenon of two photon absorption, is described. Subsequently, the *optical bistability* and *self-pulsation* regime is experimentally demonstrated in a single microring device together with the theoretical simulations. In the second part, it is shown, through experiments on a SCISSOR structure, the existence of *chaotic* regimes from which aperiodic sequence of optical pulses can be extracted.

1.1 Optical network on chip: state-of-the-art

This section reports an overview of the major advances in the design and characterization of integrated optical components for ONC. I will focus, in particular, on microresonators and on routing devices. For an in depth description of these arguments, refer to already existing review articles [22, 50, 51, 52].

The components for an ONC can be summarized as follows:

- Waveguides(crossing, splitting)
- Sources
- Active modulators
- Delay lines
- Routing blocks
- Detectors
- External interface: grating coupler

Other key passive components such as distributed Brag reflectors (DBRs) [53], arrayed waveguide gratings (AWGs) [54] have all been demonstrated, in each case with very low losses.

1.1.1 Waveguides

There is a wide variety of waveguide geometries that have been developed in silicon-compatible systems; nearly any transparent material with a refractive index higher than

glass can be deposited on top of an oxidized silicon substrate and turned into a waveguide. For purposes of CMOS process compatibility, however, the community has converged on a few fairly standard geometries. The most common is the high-confinement waveguides made by a thin active device layer, either etched fully to the bottom oxide layer or partially etched [55, 56]. It took several years to reduce the losses of these sub-micron waveguides to acceptable levels, since the strong interaction of the optical fields with the sidewalls lead to substantial losses, driven by roughness [57]. Propagation losses can be reduced either by process optimization to smooth the sidewall [58] or by waveguide geometry optimization to reduce modal field intensity at the sidewall [59]. One can either make the core very thin [59], so that most of the optical mode field spreads into the waveguide cladding, or make the core very thick combined with a shallow ridge [60, 61], so that most of the field is confined within the Si core. Both approaches aim to minimize the optical overlap with the interfaces.

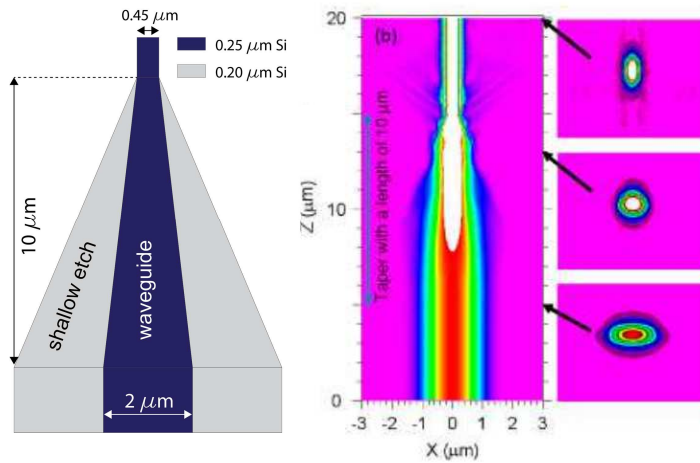


FIGURE 1.6: Schematic top view of a double-level taper which couples light from shallow-ridge waveguides to narrow strip waveguides [61].

Typical losses for high-confinement guides are in the $2\text{dB}/\text{cm}$ range for commercial processes, today [62]. Low-loss multimode straight waveguides in combination with tight single-mode waveguide bends turn out to be an optimal choice for routing, achieving $0.026\text{ dB}/\text{cm}$ [63]. More recently, CMOS compatible waveguides that can be formed in a dielectric, e.g. made out of silicon nitride, have become available. With dedicated processing, the losses of these waveguides, called *nano-core* waveguides, are extraordinarily low ($0.4 - 0.8\text{dB}/\text{m}$), though the compatibility of such processes with front-end active devices is an open issue, given the requirement for an high-temperature growth [64].

Another desirable feature for efficient routing is to yield a high-density of components, including tightly spaced parallel waveguides and tight bends. In addition, if the waveguide routing is implemented on a single photonic layer [65], waveguide crossings will become an essential element. Although waveguide crossings can potentially be made

very low loss ($\sim 0.1dB$) and low crosstalk ($40dB$) through the shallow etch techniques [66], they present severe constraints to network scaling as a massive number of crossings may be needed for single-layer routing. One way to avoid this problem is to use multi-layer routing [67], which avoids waveguide crossings but needs interlayer optical couplers [68]. The actual choice is also linked to the choice of the interfacing techniques with the electronic level that can be realized either on the same layer as the photonic circuitry or on different levels exploiting, for example, the flip-chip technique [69].

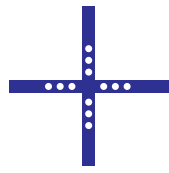
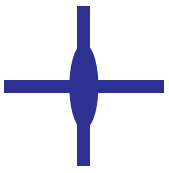
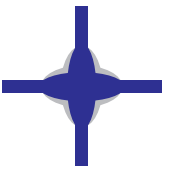
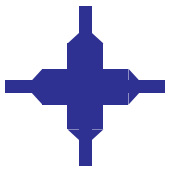
Working Principle	Resonant tunnelling (1998)	Mode field expander (2005)	Mode field expander (2007)	Multimode interference (2006)
Device type	Holes in waveguide 	Elliptical tapering 	Double-etching elliptical 	Tapered multimode waveguides 
Footprint	---	$1.6 \times 10.4 \mu m^2$	$6 \times 6 \mu m^2$	$11 \times 11 \mu m^2$
Platform	Proposal	SOI	SOI	SOI
Performance	0.45 dB insertion loss < -30 dB crosstalk Narrowband	0.65 dB insertion loss < -30 dB crosstalk Broadband	0.16 dB insertion loss < -40 dB crosstalk Broadband	0.4 dB insertion loss < -30 dB crosstalk Broadband

FIGURE 1.7: Some examples of low-Loss High-Index-Contrast Wire Waveguide Crossings [50].

Together with the crossings, there might be also the need to have a broadband component that splits or combines the signal. Multi-mode interferometers (MMI) are the evolution of the more simple Y-junction, where the excess splitter loss was of the order of $1.5dB$. These can be used to redistribute light in different waveguides. The simplest example is a 1×2 symmetric splitter, which can be used for signal distribution, or to split light in a symmetric MZI. A state-of-art MMI shows excess loss of the order of $0.2dB$ or less, with

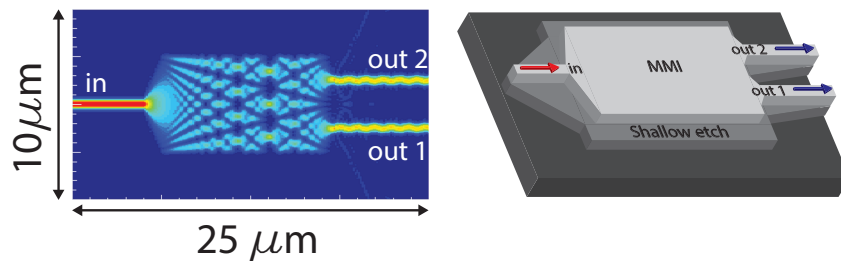


FIGURE 1.8: MMI 1x2 splitter example

an imbalance lower than $0.02dB$. Such kind of structures is quite tolerant to fabrication errors up of $100nm$ for a maximum allowed splitter loss of only $0.20dB$ [70]. With the

same technique it is possible to obtain a $1 \times N$ divider as shown in ref. [71], where an 1×12 divider is demonstrated.

1.1.2 Sources

One of the main challenges of the silicon photonics platform is the lack of an on-chip light source. The current generation of silicon chips uses light from an external laser. While edge and grating couplers have both seen improvements in coupling efficiency (see next sections), the lack of an on-chip laser source limits the potential applications of these chips.

A number of techniques has been proposed to address the light source issue. Hybrid silicon lasers have been demonstrated using both bonding [72] and epitaxial growth [73] to transfer III-V materials to the silicon wafer. These techniques, however, are hindered by the incompatibility of III-V materials with the standard CMOS process along with the high cost and low yield of bonding and the small size of the available III-V wafers. Germanium has been proposed as a CMOS compatible gain medium, though its photo emission efficiency is hindered by its indirect band gap. The small difference (134 meV) between the indirect and direct band gaps can be overcome by a combination of strain and heavy n-type doping. Recently the first electrically driven laser using a germanium gain medium on silicon was demonstrated [74].

1.1.3 Routing blocks: optical microresonators

Passive silicon waveguide structures have shown an unprecedented reduction in footprint of waveguides, and especially wavelength selective devices [24, 70]. Ring resonators are a first example of this. Ring resonators silicon photonics have reached very small size. In fact, thanks to the high index contrast between silicon and silica, radii of the order of some wavelength without a significant loss increase can be used [70]. A $1.5 \mu m$ bend still shows only $0.05 dB/90^\circ$. Using such a small radius, a ring microresonator with a Q of 10000 was demonstrated [75].

A generic ring resonator consists of an optical waveguide which is looped back on itself, such that a resonance occurs when the optical path length of the resonator is exactly a whole number of wavelengths. Ring resonators therefore support multiple resonances, and the spacing between these resonances, the free spectral range (FSR), depends on the resonator optical length.

For routing applications, it is preferred to have a relatively large FSR (several nm). A large FSR means small bends that in turn force to have high optical confinement

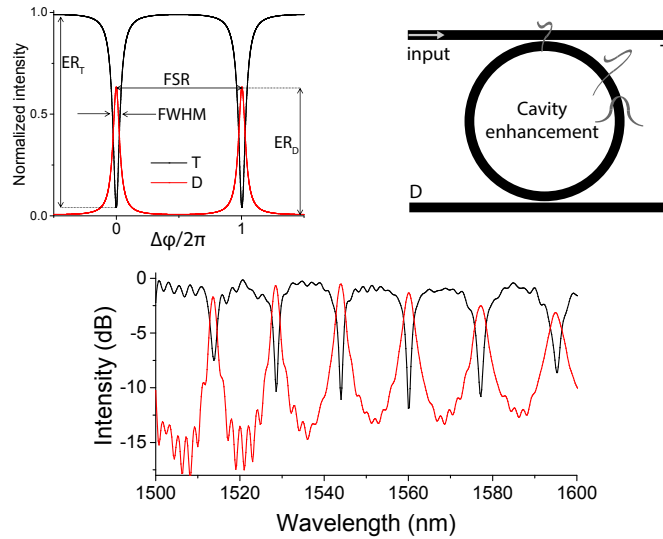


FIGURE 1.9: Ring resonator example and spectral response.

to reduce the mode losses. The SOI platform with its tight waveguide geometries, ensures such high confinement. Usually, ring resonators are coupled with a bus by the co-directional evanescent coupling method. The transmission spectrum of the bus waveguide with a single ring resonator will show dips around the ring resonances. This way, the ring resonator behaves as a spectral filter, which can be used for applications in optical communication, especially wavelength division multiplexing (WDM). There are several types of resonators as, microdisks, polygonal microdisk, microspiral and double notch-shaped microdisk [76], but we are going to focus on the most used types in the ONC, i.e. ring and racetrack resonators. Ring resonator is the most widespread single mode cavity. The racetrack resonator is the answer to the needs of high coupling to the bus waveguide in the case of a high confined mode. A microresonator coupled to 2

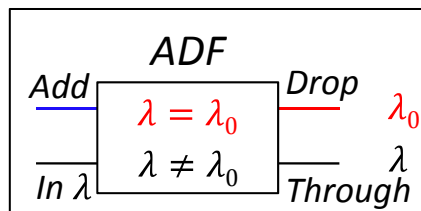


FIGURE 1.10: Schematic view of an add drop filter

bus waveguides is called add-drop filter (ADF). The wavelength selectivity of this device makes it suitable to route a single wavelength to the through or drop port. While the add port is used to add a new wavelength into the network. These features have brought the ADF to be the main component of an ONC. To obtain higher performance or to

shape the system optical response for the final application, multiple resonators are used both in coupled and in uncoupled configurations.

Applications include band filters [9], multi-bit delay lines [8, 77], slow-wave devices [78] and high-sensitivity sensor functionality [79]. The parameters of the individual ring resonators and the coupling between ring resonators and input/output waveguides give the degrees of freedom to be used in the design to tailor the device characteristics to the required specification. The Vernier effect is often exploited to create filters with an extended FSR [80]. The design of multi-ring resonator circuits in silicon requires knowledge of effects with a particular influence in silicon: ring resonance matching, process biases and coupling induced frequency shifting (CIFS) [81].

The resonance matching of ring resonators in a multi-ring device plays a critical role. Even in tailored process technology, the uniformity of ring resonators closely packed (i.e. placed in nearby position on the chip) is of the order of $0.5nm$. This is of the same order as the typical channel spacing used in a WDM system or of the resolution required for sensor devices. In cascaded ring devices, this will lead to faulty devices if the rings are not tuned or trimmed. However, trimming process requires extra power which decreases the power efficiency of the network.

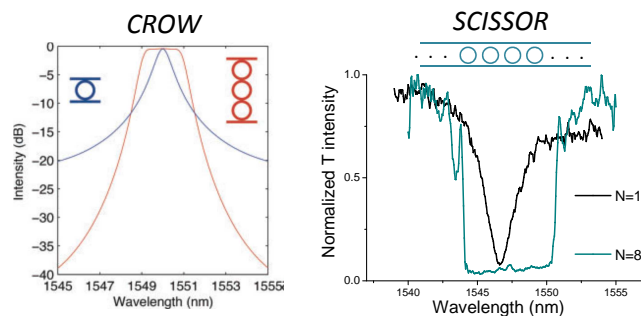


FIGURE 1.11: Spectral response examples of CROW (image taken from [22]) and SCISSOR.

The two common configurations of sequence of ring resonators are the Coupled Resonator Optical Waveguide (CROW) and the Side-Coupled Integrated Spaced Sequence Of Resonators (SCISSOR). The CROW configuration is being used to make the optical analogue of electronic high order filtering and for optical delay line. The SCISSOR can generate large flat stop band [82] and is being used to control the device dispersion and to slow down the light [83]. SCISSOR are also used for other applications, such as: all optical analogues of the electromagnetic induced transparency [11], slow light [78], tunable delay line [84, 85] and XOR/XNOR logic [86].

As mentioned above, variation in device dimensions due to fabrication process variations is inevitable. A solution to overcome these variations is either trimming or active tuning

of devices. Since the process of tuning do not require a fast time response, thermal tuning is the most widely used technique because of the large thermo-optic response of silicon [4]. This is achieved by using micro-heaters. The most common heater conguration is placing the heater on top of the device after a layer of silica to avoid the optical mode coupling to the metal. The silica, being an insulator, has the advantage to limit the thermal crosstalk to the nearby cavities but limits also the tuning efficiency. The

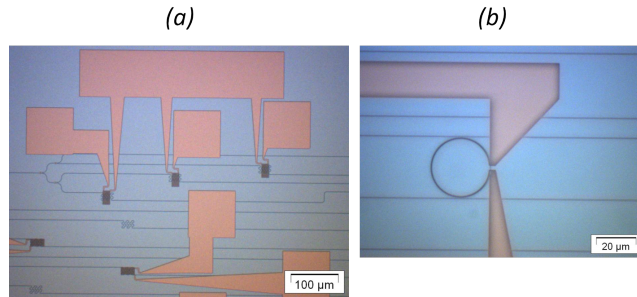


FIGURE 1.12: Heater example.

thermal efficiency can be improved by reducing the heat loss and confining the heat flow to the device, which resulted in an efficiency of $4.8nm/mW$ but with a slow tuning speed of $170\mu s$ [87]. A similar approach was followed in [88], where the silicon substrate was removed to improve conduction loss.

Another method corrects the resonance position after the device production by a modification of the cladding refractive index either by using photo-oxidation of polymer cladding [89] or by inducing stress to BOX layer [90]. This trimming method is permanent and cannot be reversed.

1.1.3.1 Optical router

The thermo-optic switches integrated in a network topology constitute an on-chip optical router. Here we give an example of a representative microresonator-based optical router. Sherwood-Droz et al [91] demonstrated a 4×4 nonblocking silicon optical router using thermo-optic switching. The device uses eight microring resonators and ten waveguide crossings, with a footprint of $0.07mm^2$ [91]. The insertion loss of each crossing was shown to be $0.51dB$. Their design enabled bidirectional communications among the four input ports and the four output ports. Each communication path demonstrated a maximum extinction rate of $20.79dB$ and a bandwidth of $38.5GHz$. The shortcomings of such optical routers are relatively slow switch on/off times, of the order of μs linked to the used switching method, and a relatively high power consumption for the resonance wavelength tuning ($0.25nm/mW$) [91].

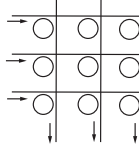
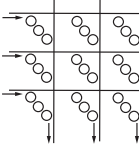
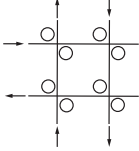
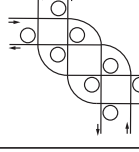
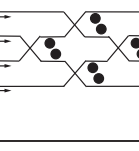
Cross grid	Microring resonator cross-grid array (2000)		<ul style="list-style-type: none"> • Non-blocking
	Third-order coupled microring resonator cross-grid array (2008)		<ul style="list-style-type: none"> • Non-blocking • Third order coupled mirroring for each cross-grid
	Two microring resonator coupled cross-grid array (2007)		<ul style="list-style-type: none"> • 4x4 switch • Each crossing routes two links simultaneously • Blocking
	4x4 optical hittless router (2008)		<ul style="list-style-type: none"> • 4x4 switch • Non-blocking
Banyan network	Second order coupled microdisk resonator based add-drop filters array		<ul style="list-style-type: none"> • 4x4 switch • Multiple wavelength channel for routing • Non-blocking

FIGURE 1.13: Some examples of router matrix topologies. [21]

1.1.3.2 Coherent control of the routing

Resonance lineshape tuning by means of coherent interference provides additional functionalities. This means that the routing protocol is not only the wavelength, as for a resonant system, but also the signal phase, as commonly used by Mach-Zehnder interferometers. There are three common schemes proposed and demonstrated in silicon microresonators:

1. coherent interference between a microresonator resonance and a detuned microresonator resonance, as in electromagnetically induced transparency (EIT) [11].
2. coherent interference between a microresonator resonance and a nonresonant background, as in Fano resonances [92]
3. coherent interference between a microresonator resonance and a coherent feedback [93]

Let us explain these three methods in detail:

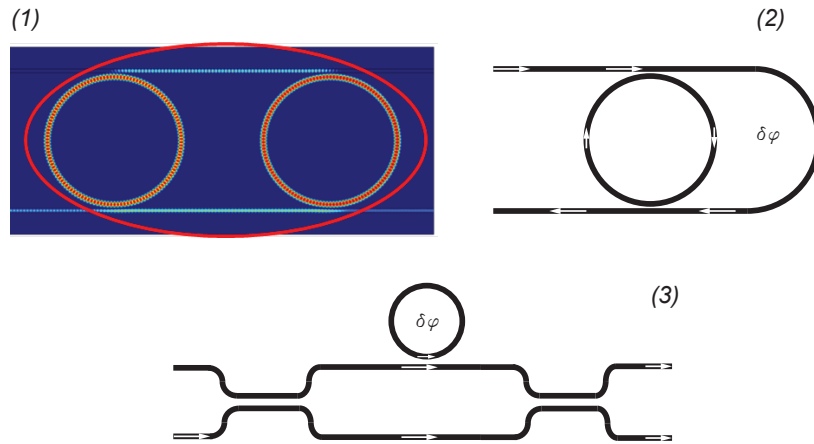


FIGURE 1.14: Phase based routing devices: (1) CRIT , (2) Micro resonator with feedback, (3) Mach-Zehnder assisted by a micro resonator. [22]

1. SCISSOR structure that exhibits the coupled resonator induced transparency (CRIT) [33]. EIT-like phenomenon can occur in a microresonator system in which two coupled microresonators coherently interfere [11]. The coherent signal from two slightly detuned microresonators destructively interfere at the throughput port. Such silicon coupled microresonator structures with EIT-like lineshapes have found applications in tunable optical delay lines [84, 85] or DWDM [34].
2. Resonance interference with a coherent feedback The resonance lineshape can also be enhanced or suppressed by means of interference with a coherent feedback [93]. By tuning the feedback phase and amplitude it is possible to enhance or suppress the resonance. Such coherent feedback control highly depends on the resonance wavelength thus, the resonance lineshape modulation varies among resonances. The feedback-microresonator, that enables controlled resonance lineshape tuning with a large dynamic on-off ratio, offers more functionalities than simple waveguide-coupled microresonator resonators. The fact that the phase and the microresonator resonance can be tuned separately it has been used for reconfigurable filters [93, 94], switches and modulators [76, 95].
3. Resonance interference with a coherent background. The first proposed configuration was a MZI assisted by a microresonator [92]. The resonance pathway corresponds to the lightwave propagating in the microresonator-coupled MZI arm, and the coherent background pathway corresponds to the amplitude-split lightwave propagating in the MZI reference arm. The two lightwaves recombine at the MZI output ports. The system transfer function is characterized by an asymmetrical Fano resonance lineshapes. The lineshapes can be controlled by modulating the

phase in the MZI reference arm. The sharp asymmetrical lineshapes find applications in biosensing [96]. The MZI-coupled Micro resonator have also been proposed for tailoring the filter lineshape with a flat-top and box-like spectral response [97].

1.1.4 Active modulators

Apart from the already discussed thermo-optic modulation, that is mainly used for trimming, modulation in silicon is most commonly achieved by means of free carrier dispersion effect [4]. Free-carrier density changes induce changes in the refractive index which modulates the light. Several different mechanisms for manipulating free-carrier densities have been implemented in monolithic devices [98]. Among them, carrier-depletion mode devices, usually based on a reverse-biased pn junction, are widely used to achieve high speed. Since the first GHz silicon modulator was demonstrated by Intel [99], modulator performance metrics have been significantly improved. Mach-Zehnder interferometer (MZI) structures [100] are typically used for amplitude modulation. With traveling-wave designs, data rates of up to 50 Gb/s have been experimentally demonstrated [101, 102]. At 20 Gb/s, a record low power consumption of 200 fJ/b has recently been reported [103]. Resonant structures can be used to dramatically reduce device footprints and further reduce power consumptions, although at the cost of a significantly narrower operating wavelength window and high thermal sensitivity. First introduced by Xu et al. [10] in 2005, high-speed ring modulators have been demonstrated to operate at up to 40 Gb/s [104] and, recently, were reported to achieve 7 fJ/b at 25 Gb/s and with thermal tuning capabilities [105]. Recent development includes breaking the cavity photon lifetime limit by means of coupling modulation [106].

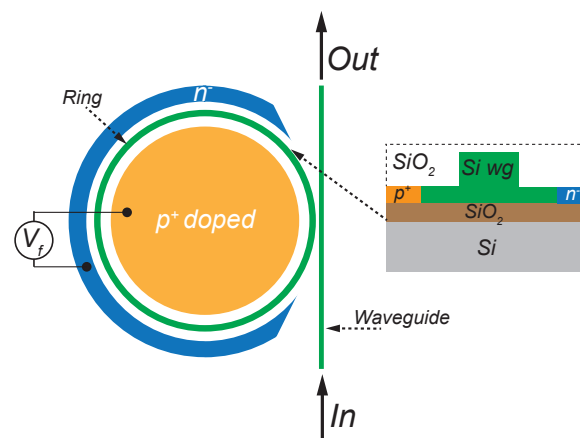


FIGURE 1.15: First high speed silicon based ring modulator demonstration [10].

1.1.5 Delay lines

Optical delay lines are another key component for on-chip optical interconnects. The traditional way to obtain optical delay is by passing the light through a dispersive medium. Other than relying on a strongly dispersive medium, the strong dispersion can be obtained from microresonator based structures. Figure 1.16 summarizes the state-of-the-art of microresonator-based optical delay lines on silicon chips found literature. The key performance metrics for the optical delay lines are time delay, bandwidth, insertion loss and delay tunability. The figure-of-merit is the delay-bandwidth product (DBP).

Structure	Material	N	Delay (ps)	Bandwidth (GHz)	DBP	Insertion loss (dB)
Single element	SOI	1	95	3.5	0.3	40
	SOI	1	80	5	0.4	28
	SOI	1	84	1.5	0.132	38
EIT	SOI	2	25	–	–	–
	SOI	2	29	–	–	30
SCISSOR	SOI	56	510	54	27	25
	Hydex	8	2,483	2.5	6	6
		32	357	40	14	10
CROW	SOI	100	220	–	–	26
	SOI	235	145	625	90	19
	SiON	8	800	6.25	5	8
	SiN	101	110	18.75	2	50

N : number of cascaded microresonators. DBP: delay–bandwidth product.

FIGURE 1.16: Comparison between several delay line structures. [22]

1.1.6 Detectors

At the operating wavelengths of a silicon photonic chip, materials with a narrower bandgap than silicon need to be integrated to function as the detection (absorption) medium. Germanium or SiGe can be grown and can absorb light at the telecommunication wavelengths [107], which is necessary for compatibility with standard CMOS infrastructure. Bonded III-V materials are also used for photodetection [108], based on bonding technologies. These materials are integrated close to or directly connected to a silicon waveguide, so that the guided light can be evanescently coupled or butt coupled into the photodetector and the photodetector can have a small cross section to reduce device capacitance and improve speed [109]. The state of the art of germanium photodetectors, in a photodiode configuration, is a 120GHz bandwidth with responsivity of 0.8 A/W [109]. A responsivity of 1.05 A/W was demonstrated at 20GHz for a

wavelength of 1.550nm [110], which amounts to 84% quantum efficiency. Very low photodetector capacitance of 2.4fF has been achieved in a photoconductive device [111] with an estimated quantum efficiency of 90% operating with a bandwidth of 40GHz . Low bias avalanche detection with 10dB gain and improved noise performance was achieved by IBM, with a speed exceeding 30GHz [112].

1.1.7 External interface: grating coupler

One of the drawbacks of the high refractive index contrast is the large mismatch in mode size and mode shape between the fundamental mode of the SOI waveguide and the mode of the optical fiber, making efficient coupling of light from waveguide to fiber an important issue.

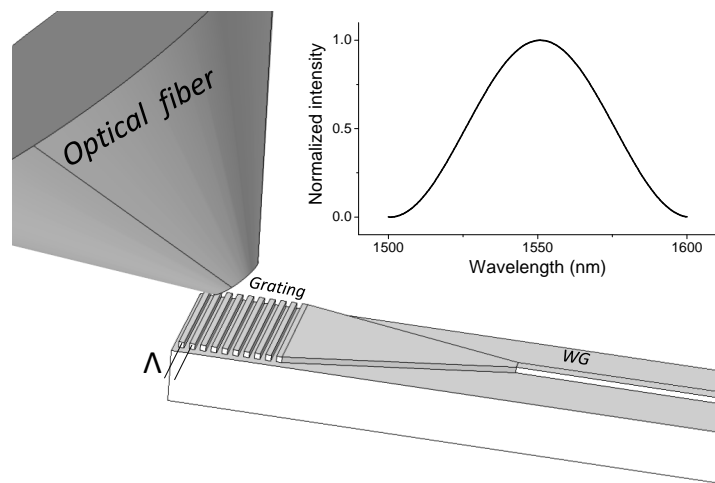


FIGURE 1.17: A grating coupler sketch together its spectral response.

In the literature, one-dimensional [113] and two-dimensional [114] grating structures were proposed to tackle this problem. These grating couplers have the advantage to enable wafer-scale testing of the integrated circuits and holds the promise of low-cost packaging. Furthermore, they are very compact and have a large optical bandwidth. Although one-dimensional structures are polarization dependent, a polarization diversity scheme based on a two-dimensional grating coupler can be used in practical applications [114]. To obtain a high coupling efficiency, different strategies can be followed. By including a bottom mirror to redirect the downward diffracted light, a high coupling efficiency can be obtained. This can be a metallic mirror [115] or a distributed Bragg reflector-type mirror [116]. Another way to improve the coupling efficiency is to optimize the design parameters of the grating unit cell while tailoring the pitch and duty cycle of the individual grating periods [117]. The use of a slanted grating coupler was proposed to obtain high coupling efficiency to a vertically positioned optical fiber [118, 119]. The

efficiency of these devices, which settles around 20% with relative ease, and the complete compatibility with the CMOS process makes them the best candidates for interfacing to the outside world an integrated photonics chip.

1.2 Non linear optics on chip

The high index contrast provided by SOI platform allows to have a tight light confinement in a sub-micrometer waveguide. Such a small confinement enhances the material nonlinearities as a consequence of a higher power density. Moreover, the silicon third-order nonlinearity exceeds that of silica exhibiting a Kerr coefficient 100 times larger [120] and a Raman gain coefficient 1000 times larger [121] in the telecom window. Silicon is also optically transparent above $1.1\mu m$ allowing to realize low loss photonics device [122]. Therefore, a great effort has been used to study nonlinear effects in silicon as self-phase modulation (SPM) [123, 124, 125, 126], cross-phase modulation (XPM) [127, 128], stimulated Raman scattering (SRS) [78, 129], and four-wave mixing (FWM) [130, 131]. Furthermore, the semiconductor propriety of silicon together with the imaginary part of the third-order nonlinearity give rise to several peculiar effects as two photon absorption (TPA) [120, 123], free-carrier dispersion [4], and anisotropic and dispersive third-order nonlinearity [132]. The passive and active linear and nonlinear proprieties of SOI based photonic devices allow many degrees of freedom to create integrated optical devices for practically whichever applications [133, 134, 135, 136].

Naturally, in a microresonator these effects become more pronounced, since close to a resonance there is a strong increase in power density. In magnitude, the thermal effects are actually dominant, but they are slow. Bistable behavior has been demonstrated in silicon microring resonators [43, 44]: the increased optical power will result in a skewing of the resonance peak. This is illustrated qualitatively in Fig. 20 for the drop port transmission of an ADF filter. At a certain power level, the resonance peak will fold back, resulting in three possible transmission levels, of which only two are stable solutions.

The thermal nonlinearities translate the optical power into a phase shift. A similar effect occurs with the free carriers generated through TPA. The resulting free carriers can be used in a ring resonator to induce a non-linear change in the real part of the refractive index [42, 137]. These carrier effects are much faster than thermal effects. When combining both effects with a different time scale, this can result in self-pulsing behavior [44, 138, 139, 140].

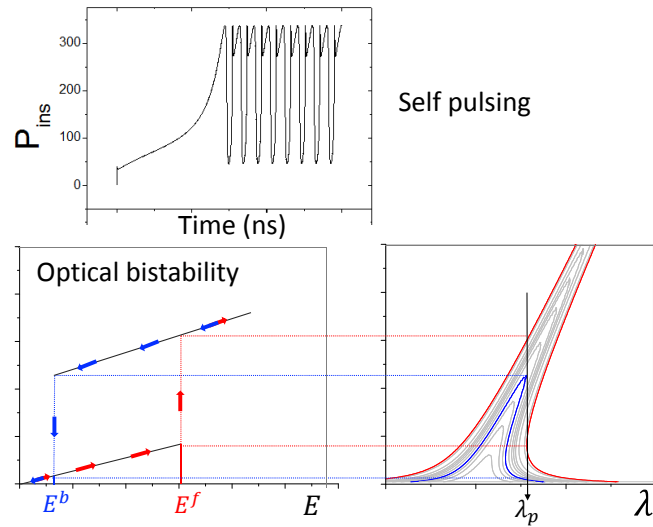


FIGURE 1.18: Optical bistability and self pulsing phenomena.

Together to the self pulsing effect, theoretically it was predicted the existence of chaotic states in coupled cavity systems with a kerr nonlinearity [46, 141, 142]. This effect has not yet been demonstrated experimentally. Chaotic system in integrated device could be very useful to generate all-optical random bit sequences for signal processing.

Chapter 2

Optical network on chip components and its applications

2.1 Introduction

In the first part of this chapter, will be presented a brief introduction on the theory of WGs and their applications. With the help of the COMSOL software the parameters of the SOI WGs, that will be used during the rest of the work, will be estimated. In particular, the coupling coefficients for a directional coupler (straight-straight and straight-curve) and the effect of the surface roughness in a straight WG will be calculated. The effect of a WG bend on the guided mode inside a WG will be also described by simulations [143].

The second part of this chapter will introduce the optical microresonator component with information about the main sources of linear losses, e.g. line edge roughness (LER) induced losses. Theory will be developed by means of simulations performed using a transfer matrix code. Examples will be given only for a racetrack resonator since it is almost equivalent to a ring resonator with an elongated coupling section. The theoretical transmission spectrum and the group delay are presented. Then, several test samples are experimentally investigated in order to estimate the values of losses, of the effective index, of the group index and of the effective curved index. The extracted parameters are introduced in the transfer matrix code which is then used to design new devices and to understand the experimental results.

We design the width of our waveguide for both TE and TM polarization while still preserving the single mode condition. The racetrack resonator (RTR) and the ring resonator (RR) are the resonators types treated. The former is used in the case of TE

polarization, where the high mode confinement does not ensure enough coupling to the bus WG, while the latter is used in TM polarization since, the small effective coupling section limits the coupling to the bus WG in the case of TE polarization. One of the advantage of the use of silicon as guiding material is to allows using small bending radius while maintaining low losses. Therefore, in our work we use bending radii of maximum $7\mu\text{m}$ in order to minimize the footprint of the final device.

2.2 SOI based Optical waveguides

All the waveguides (WG) used through this work are SOI based and are covered by a SiO_2 layer. That means that the index contrast between the core and the cladding is symmetric in the xy plane (See Fig 2.1). This has important consequences, as this type of geometry allows always the propagation of the fundamental mode. Thus it is possible to shrink the WG size maintaining the condition of guiding light.

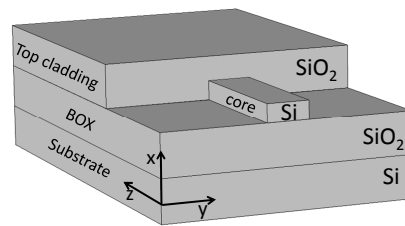


FIGURE 2.1: Example of SOI based optical WG. For clarity part of the top cladding has been removed to better show the core.

A sketch of a SOI WG is shown in figure 2.1. The guiding material is provided by the silicon core with a refractive index of 3.4. The core hosts the most of the optical mode power. The index contrast is provided by the silica box and top cladding that have a refractive index of 1.4. In this configuration the index contrast is 2.4, 2 orders of magnitude greater than that of an optical fiber. In fact, the SOI material provide the basis for the *high index contrast photonics*. A high contrast allows to fabricate devices with a very small footprint. For example, a bend can be reduced up to the wavelength of the traveling light while maintaining low losses.

Generally TE or TM linearly polarized light will be used. The definition of TE is shown in Figure 2.2, where it is seen that the electric field exists only along the yz plane. The TM is characterized by the electrical field in the xz plane since \mathbf{E} and \mathbf{H} are orthogonal. The z axis indicates the propagation directions.

These support materials allow to build sub-nanometer guides maintaining low losses. A guide with characteristic dimensions smaller than the wavelength of the guided light exhibits a non-negligible part of the field which propagates outside of it. This peculiarity

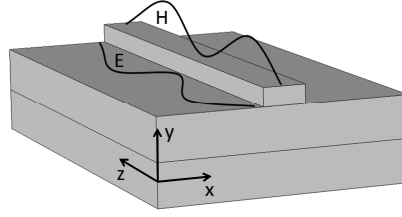
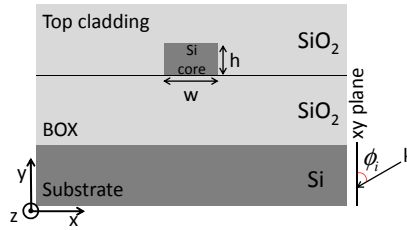


FIGURE 2.2: TE polarized light. Z is the propagation direction.

is the heart of integrated photonics and is one of the foundations for the construction of complex integrated photonic networks.

2.2.1 Waveguides theory

Figure 2.3 represents the cross section of a SOI based WG. A wave propagating through the z direction in the core is guided or not depending on the value of the angle ϕ_i created by the wavevector k and xy plane. ϕ_i must be greater than the *critical angle* defined as $\sin(\phi_c) = n_{cl}/n_{co}$ where n_{cl} and n_{co} are the refractive index of the cladding and the core respectively.

FIGURE 2.3: Left: Cross section of a WG and its characteristics dimensions: the height h and the width w . The z axis indicates the propagation direction and the xy plane contains the oscillating fields. Right: lateral view of the WG with the definition of ϕ_i .

The electric(magnetic) field of an electromagnetic wave propagating through the z direction in the core can be written as:

$$\vec{E} = E_0 e^{\vec{k}z \pm \omega t} \vec{H} = H_0 e^{\vec{k}z \pm \omega t} \quad (2.1)$$

The term $\phi = \vec{k}z \pm \omega t$ is called *phase* of the field. The time variations of phase gives

$$\frac{\partial \phi}{\partial t} = \omega \quad (2.2)$$

omega the angular frequency of the wave, also expressed as $2\pi f$ where f is the frequency.

The spatial variations of phase gives

$$\frac{\partial \phi}{\partial z} = k \quad (2.3)$$

where k is the *wavevector* of the wave. The propagation in the core material is described by the refractive index:

$$k = k_0 n_{co} \quad (2.4)$$

where k_0 is the *free space wavevector* and is related to the wavelength by

$$k_0 = \frac{2\pi}{\lambda} \quad (2.5)$$

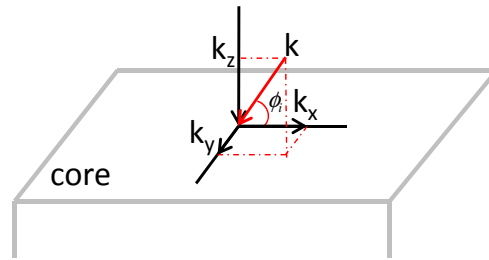


FIGURE 2.4: Wavevector decomposition inside the core.

The wavevector k can be decomposed into its components xyz ,

$$\vec{k} = k_x \hat{x} + k_y \hat{y} + k_z \hat{z} \quad k_z = k_0 n_{co} \sin(\phi_i) \quad (2.6)$$

valid for a k lying in the xz plane. The z component is imaginary and is also called $k_z = \beta$, the *propagation constant* of the wave. The z wavevector component depends on the medium refractive index and on the incident angle. In the core of the WG, the components k_x and k_y are imaginary while in the cladding these are real. This means that the field will be attenuated exponentially to a degree determined by the *decay constant* following this law:

$$E_{x(y)}^{cl} = E_0^{cl} e^{-k_{x(y)} x(y)} \quad (2.7)$$

$E_{x(y)}^{cl}$ represents the field amplitude in the cladding. The fact that the field outside the core is non-zero is represented by the *evanescent field* concept. It is worth to say that, even β in a real case has a real part, called α , which is related to the losses of the material in which the wave propagates.

For the x axis, for example, we can write the phase shift (neglecting the delay at the boundaries) as:

$$\phi_w = 2k_x w = 2\pi m \quad (2.8)$$

where m is the mode number that comes from the discretization of the eigensolutions, called *modes*, along this axis imposed by w , the width of the WG (see fig. 2.3). Such a treatment may also be made for the k_y , considering h the height of the core. The confinement along y adds another mode number, n . The mode identified by $m = 0$ and $n = 0$ is called the *fundamental mode*. Therefore, the WG dimensions, the index contrast (or the incident angle equivalently), the light wavelength and the polarization set the number of allowed modes in the WG. Depending on these parameters may exist single mode or multi mode WG. Figure 2.5 shows the field distributions of these modes labelled by the term TEM_{mn} .

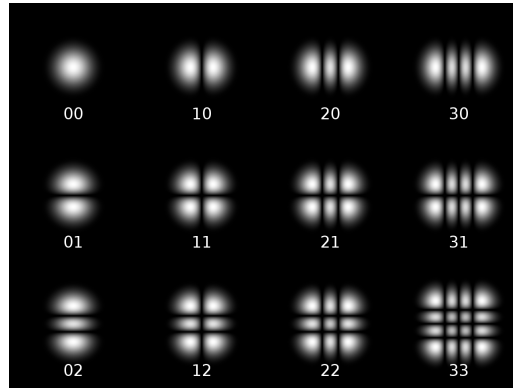


FIGURE 2.5: Rectangular transverse mode patterns TEM_{mn} . Image taken from Wikipedia.

The mode numbers are the evidence of the fact that there are two standing waves that propagate in the x, y direction. These values correspond to the number of minima of the field profile along x , for m , and along y , for n . β is an important parameter because describes the rate at which a wave propagates. To simplify the treatment of the propagation of light, the effects of the incident angle may be incorporated inside the effective index, n_{eff} . For k lying in the xz plane, we define it such that:

$$n_{eff}^{xz} = n_{co} \sin \phi_i$$

Then the equation for β becomes:

$$\beta = n_{eff}^{xz} k_0$$

Note the similarity with the equation $k = k_0 n_{co}$. This is equivalent to think of the mode as propagating straight down the waveguide, without bouncing back and forth, with an effective refractive index n_{eff}^{xz} . The effective index n_{eff} is then calculated making the same considerations but for the yz plane and by using, instead of n_{co} , n_{eff}^{yz} . The effective index always ranges between the core index and the cladding index.

To describe the magnitude of the evanescent field, the field which propagates out from the core, it is usually used the *confinement factor*. This parameter is the ratio between the energy confined in the core and the sum of the energy in the core and in the cladding. It is defined as [144]:

$$\Gamma = \frac{\int \int_{core} E^2(x, y) dx dy}{\int \int_{-\infty}^{\infty} E^2(x, y) dx dy} \quad (2.9)$$

2.2.2 Simulations of waveguides

The WG is the basis of any integrated ONC. In this section we want clarify the order of magnitude of the fundamental parameters that characterize a WG, in order to have the basic guidelines to develop the structures studied throughout this work.

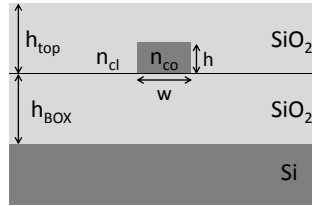


FIGURE 2.6: Cross section of a WG and its characteristic dimensions, the height h , the width w . h_{box} is the height of the buried oxide layer and h_{top} is the height of the top cladding.

Figure 2.6 shows the section of the used waveguides. They are of the strip WG type. The constructive parameters are given in the following table:

TABLE 2.1: WGs parameters

	h	w	h_{BOX}	h_{top}	n_{co}	n_{cl}
TM	220nm	500nm	1.5 – 2 μ m	\geq 0.75 μ m	3.47	1.44
TE	220nm	450nm	1.5 – 2 μ m	\geq 0.75 μ m	3.47	1.44

As can be seen, it was chosen a different width for the two polarizations in order to allow, for both, only the propagation of the fundamental mode at the wavelength of 1550nm and avoid the coupling between the TE and TM mode (i.e. birefringence). The refractive index values for the silicon and the silica are considered at room temperature and as a

function of the wavelength through the Sellmeier equations in order to compensate for the material dispersion. In the table we specified these values for $\lambda = 1.55\mu m$. In what follows, if it is said that a device is designed for the TE(TM) polarization, then the WGs of which it is composed have a width of $450nm(500nm)$.

Here is reported a table with the commonly used values of the BOX and of the WG height found in the literature:

TABLE 2.2: SOI wafer thickness specification for silicon photonics found in literature

	WG height (nm)	BOX (nm)
IBM	220	2000
MIT	220	1000
Uni. Glasgow	260	1000
Cornell Univ	240	3000
Intel	500	1000

From figure 2.7 it is possible to see that the TM mode has substrate losses 1 or 2 order of magnitude higher than the TE mode. This is due to the less vertical confinement of TM mode. In this work we use a BOX of $1.5\mu m$ that gives losses of about $0.1dB/cm$. In any case, in order to estimate the losses of a mode, the scattering losses due to roughness have to be taken into account since they typically dominates(see section 2.6).

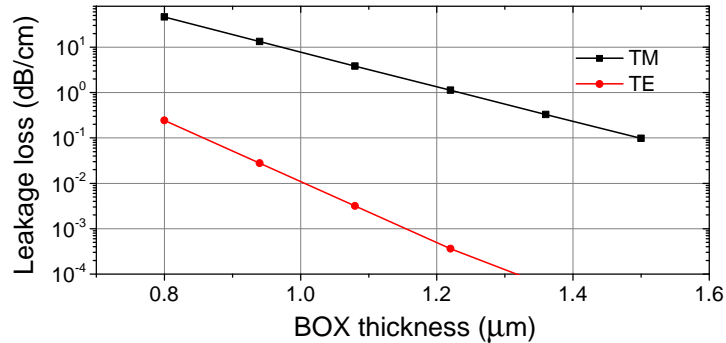


FIGURE 2.7: Substrate leakage loss in dB/cm as a function of BOX thickness (μm) for the TE and TM polarization at $\lambda = 1550nm$

Figure 2.8 reports the simulated values of the effective index and of the confinement factor (Equation 2.9) for a wavelength range of $1500 - 1600nm$ and TE/TM polarization of the fundamental mode TEM_{00} .

We can see that the TM mode has a lower effective index compared to the TE mode. The same applies to the CF. This is due to the fact that $h < w$. It is important to remark that the CF for the TE mode is about 0.5. This means that half of the energy propagates outside of the core. For the TM the CF is even lower, 0.15.

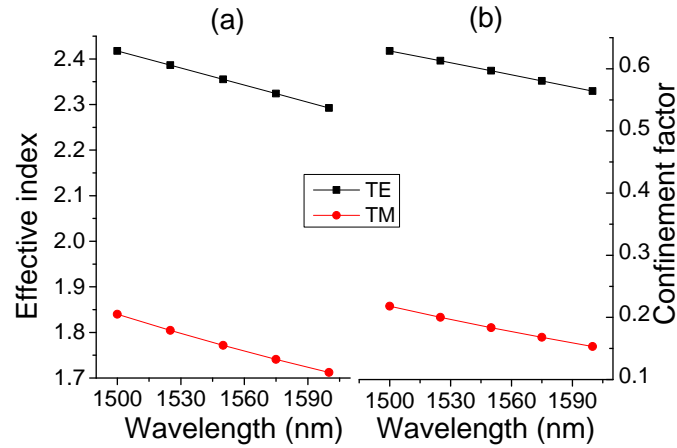


FIGURE 2.8: (a) Simulated effective index for TE and TM polarization. (b) Simulated confinement factor for TE and TM polarization. Fundamental mode TEM_{00} . Simulation parameters reported in the tab 2.1.

For convenience, the values of the n_{eff} and CF are reported in table 2.3

TABLE 2.3: n_{eff} and CF for several values of λ and for TE and TM polarization

$\lambda(nm)$	TE	TM	TE	TM
	n_{eff}	n_{eff}	CF	CF
1500	2.417	1.840	0.62	0.21791
1525	2.386	1.800	0.611	0.20
1550	2.355	1.772	0.59	0.18
1575	2.324	1.741	0.58	0.16
1600	2.293	1.712	0.56	0.15

Observing the field profile of the WG in the picture 2.9 you can realize how much energy travels outside the core. This has a negative impact on mode losses. A low confined mode "feels" more the presence of defects and roughness on the surface of the WG and cladding, increasing its propagation losses.

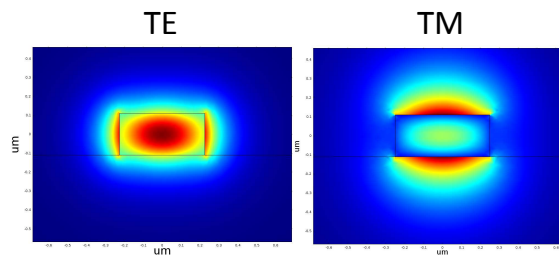


FIGURE 2.9: Simulated fundamental mode profile for TE and TM polarizations. Plot of the Electric field module.

Just to give an idea, the modern CMOS facilities are able to produce sub-nanometer WG with losses of about $3 - 2 dB/cm$ for the TE mode [145][?] without any thermal

treatment to reduce the surface roughness [146, 147]. In fact, achieving low loss without post processing is desirable to avoid fabrication overhead and complexities.

Some values of WG losses, found in the literature, are reported in the following table:

TABLE 2.4: WGs propagation loss comparison. Fabrication technology: 193 and 248nm lithography. TE polarization.

Reference	Cross-section(nm)	TE loss (dB/cm)	
CEA-LETI	512x200	4.18 ± 0.21	[47]
MIT-BAE	420x200	8.2 ± 0.5	[148]
	470x200	5.7 ± 0.5	
	520x200	4.6 ± 0.5	
	570x200	4.3 ± 0.5	
Ghent Univ.-imec	515x220	2.74 ± 0.06	[146]
	500x220	2.73 ± 0.1	
	485x220	2.85 ± 0.07	

2.3 Directional coupler

In the previous section we said that part of the field propagates outside the waveguide. Let's see how this effect is used in the *directional coupler*. These devices serve to exchange energy between two WGs separated in space and are widely used in ONC.

The coupled mode theory (CMT) is the most fundamental theoretical approach to the design and construction of practical integrated photonic devices.

CMT is the theory that describes the interaction between modes and the new modes arising from the modified structure.

The fundamental principle on which it is based is that there is an orthogonal relation between the modes supported by a waveguide structure, which implies that each mode propagates independently along the waveguide without power exchange among the modes itself. The modes become mutually coupled when energy transfer between them takes place if the original waveguide structure is altered.

There are many articles (see for example [149]) that describe in depth the CMT for electromagnetic fields, here an approximate version is presented, anyway useful to understand the physics behind this phenomenon.

Figure 2.10 reports the system under study.

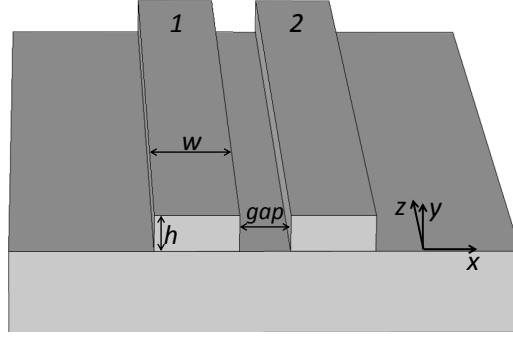


FIGURE 2.10: System under study. w and h are the size of the WG, cg is the separation between WGs (coupling gap). The two WGs are labelled whit 1 and 2 .

Let's start from these equations

$$\frac{da_1(z)}{dz} = i k_c a_2(z) e^{-(\beta_2 - \beta_1)z} \quad (2.10)$$

$$\frac{da_2(z)}{dz} = i k_c a_1(z) e^{(\beta_2 - \beta_1)z} \quad (2.11)$$

derived from Maxwell's equations in perturbation theory [150, 151]. These equations describe the propagation of the fields a_1 and a_2 in the two WGs along the z direction. k_c is a field integral of the field which indicates how much of the two modes overlaps. This parameter is strongly linked to the size of the evanescent field, that is $k_{x,y}$. In the CMT the approximation of k_c small is used , i.e. $k_{x,y}gap > 1$, this means a rapid decay of the field outside the WG.

$$F = \frac{1}{1 - \delta/k_c}; \quad \delta = \beta_2 - \beta_1$$

where F is the power-coupling efficiency, β_1 and β_2 are the propagation constants of the first and second WG and 2δ is the *mismatching*. For two equal WGs $\beta_1 = \beta_2$. This is called *perfect phase matching conditions* for which all the power can be exchanged between the WGs, and F , the efficiency, is 1.

Using these ansatz

$$a_1(z) = x_1 e^{ik_c z} + x_2 e^{-ik_c z} \quad (2.12)$$

$$a_2(z) = y_1 e^{ik_c z} + y_2 e^{-ik_c z} \quad (2.13)$$

and solving for $x_{1,2}$, $y_{1,2}$ we obtain:

$$a_1(z) = a_1(0) \cos(k_c z) - a_2(0) i \sin(k_c z) \quad (2.14)$$

$$a_2(z) = a_1(0) - i \sin(k_c z) + a_2(0) \cos(k_c z) \quad (2.15)$$

By imposing as initial conditions that only the first WG is excited $a_1(0) = a_0, a_2(0) = 0$, we get:

$$a_1(z) = a_0 \cos(k_c z) \quad (2.16)$$

$$a_2(z) = -i a_0 \sin(k_c z) \quad (2.17)$$

To obtain the power exchanged between the WGs, we have to square them:

$$P_1(z) = 1 - \sin^2(k_c z) \quad (2.18)$$

$$P_2(z) = \sin^2(k_c z) \quad (2.19)$$

with $a_0 = 1$. These equations tell us that energy is periodically exchanged between the WGs, with a period of k_c . The maximum power coupled between the two WGs is reached at $z = \frac{\pi}{2k_c}(2m + 1)$, ($m = 0, 1, 2, \dots$) and the length z at $m = 0$ is called *coupling length* (L_{cp}).

$$L_{cp} = \frac{\pi}{2k_c} \quad (2.20)$$

Even if the CMT works in a weak coupling regime, it can nevertheless be used to provide an approximate representation of the light propagation in two strongly coupled photonic WGs (as, for example, working near L_{cp}).

To do that, we have to consider the two interacting WGs as one system where a splitting of the first symmetric and second anti-symmetric order modes occurs. The equation for the electric field can be approximated by a sum of the even and odd modes:

$$E(x, z) = E_e(x)e^{-i\beta_e z} + E_o(x)e^{-i\beta_o z} \quad (2.21)$$

with $E_{e,o}$ and $\beta_{e,o}$ the even and odd mode electric fields and propagation constant respectively. We can extract the coupling coefficient k_c by looking at the eigen modes of the previous equations. For $z = 0$ we find the first eigen mode $E_1(x)$:

$$E(x, z) = |E_e(x) + E_o(x)| = E_1(x) \quad (2.22)$$

For any z :

$$|E(x, z)| = |E_e(x) + E_o(x)e^{i(\beta_e - \beta_o)z}|, \quad (2.23)$$

that at $z = \frac{\pi}{(\beta_e - \beta_o)}$ becomes

$$E(x, z) = |E_e(x) - E_o(x)| = E_2(x) \quad (2.24)$$

where $E_2(x)$ denotes the eigen mode of the second WG. If we compute at which length there is the maximum power transfer we found:

$$L_{cp} = \frac{\pi}{\beta_e - \beta_o} = \frac{\pi}{2k_c}, \quad (2.25)$$

so finally the coupling coefficient is:

$$k_c = \frac{\beta_e - \beta_o}{2} \quad (2.26)$$

Using the relation $\beta = 2\pi/\lambda n_{eff}$ we can write k_c as a function of n_{eff} .

$$k_c = \frac{\lambda}{2(n_{eff}^e - n_{eff}^o)} \quad (2.27)$$

Figure 2.11 is the cross section of the geometry in figure 2.10. It shows the profile of the E_x field within the structure for the TE polarization. The panel (a) shows the profile of the even eigenstate while panel (b) the odd.

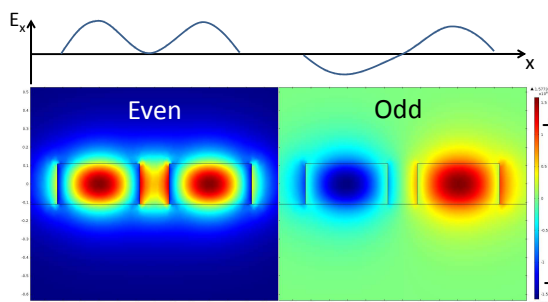


FIGURE 2.11: X component of the electric field for the even (a) and odd (b) modes.

TABLE 2.5: Relative effective index variations for the even and off mode

	Δn_{eff}^e	Δn_{eff}^o	n_{eff}
160 nm	-0.81%	1.1%	2.36
200 nm	-0.62%	0.74%	2.36

The two eigenstates are characterized by an effective index which differs from that of the single isolated WG: greater for the even and lower for the odd. The deviation from n_{eff} is negligible for large separations but, in resonator systems where also a slight variation of the effective index can induce resonance shifts, this effect can become relevant especially

for small gaps. These are called *coupling-induced resonance frequency shifts* (CIFS) and can have deleterious effects on high-order resonant filters [152]. For example, the relative variation for a $\lambda = 1550\mu m$, a gap of $160nm$ and $200nm$ and TE polarization are:

$$\Delta n_{eff}^e = 0.90\%$$

$$\Delta n_{eff}^0 = -0.71\%$$

The gap clearly influences the magnitude of the index mismatch.

The table below reports the values of L_{cp} for several parameters. The simulation refers to the geometries defined in table 2.1.

TABLE 2.6: L_{cp} for several values of gap

$\lambda(nm) \backslash gap(nm)$	TE			TM		
	160	180	200	200	250	300
1500	$21.1\mu m$	$25.4\mu m$	$30.4\mu m$	$7.91\mu m$	$10.40\mu m$	$13.66\mu m$
1550	$17.2\mu m$	$20.4\mu m$	$24.3\mu m$	$6.88\mu m$	$8.76\mu m$	$11.15\mu m$
1600	$14.1\mu m$	$16.6\mu m$	$19.5\mu m$	$6.20\mu m$	$7.68\mu m$	$9.51\mu m$

The values of L_{cp} for the TM polarization is always smaller than the one for TE. This is due to the lower confinement of TM mode. Moreover, the TM mode is so leaky in the y axis that they evanescently couple with the silicon substrate through the $1.5\mu m$ silica BOX. For this reason in an ONC the use of the TE polarization is preferred to maintain low losses.

The TM polarization is used, for example, only in the case in which the coupling is "punctual" or very short and the TE mode does not ensures a sufficient coupling.

Figure 2.12 shows the profile of the electric field as a function of the propagation distance z. As expected from table 2.6 for $\lambda = 1550nm$ and $gap = 160nm$, the maximum energy transfer rates between the WGs take place in correspondence of L_{cp} . After $2L_{cp}$ the energy is completely re-coupled back in the starting guide. Figure 2.12(b) confirms that the trend of energy follows the $\sin(z)^2$ (see eq. 2.18).

2.4 Bends

Bends are present in nearly all ONC. Although it may seem a simple component that has not to be treated individually, we will see that bends involve several important phenomena that, if neglected, can ruin the network performance.

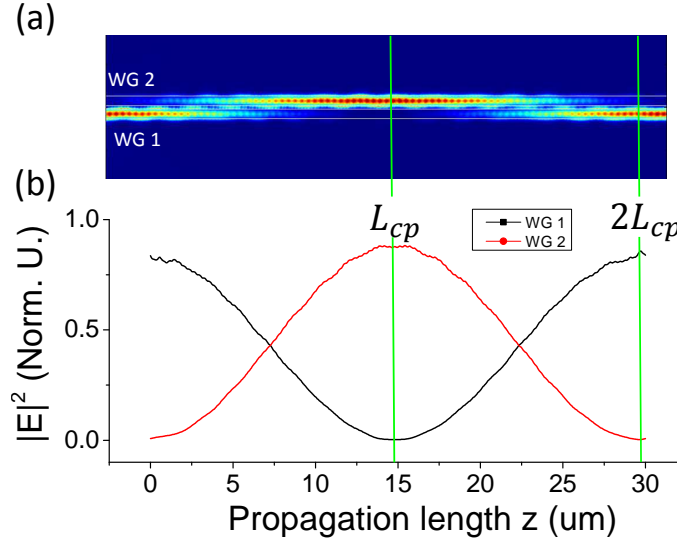


FIGURE 2.12: (a) TE mode top view of 2 coupled WGs system: Modulus square of the electric field is shown. At $z=0$ the WG 1 is being excited. (b) Modulus square of the electric field as a function of z . Simulation parameter: gap=160 nm, $\lambda = 1550\text{nm}$, TE mode.

It is possible to approximate imagine the behaviour of light inside a WG bend like this: since the arc of the bend at the outside is longer than the arc at the inside, light at the outer cladding must propagate more quickly than light at the inner cladding, in order to maintain the phase relationship across the mode.

Two effects are then generated:

1. The light propagates with a refractive index (n_{eff}^b) that differs from the straight one n_{eff} .
2. The optical mode feels more the outer surface defects leading to higher losses.
3. There is an increase of radiation losses due to the outer portion of the mode.

In low contrast optical media such as optical fiber, any bend is an important source of losses because, as the evanescent tail extends into the outer cladding, a distance is eventually reached where light in the outer cladding has to exceed the velocity of unguided light in the same material, in order to maintain the guided mode. This is a paradox, so light is radiated and lost from the mode. So, in low index contrast material, the curvature radius has to be made as large as possible. On the contrary, high contrast waveguide great confinement factor reduces the problem of radiation losses. Thus, it is possible to shrink the radius of a bend down to the wavelength of the light ($1.5\mu\text{m}$) and still have a well guided mode[75]. However, that the losses induced by the surface roughness, also called LER [153, 154], are enhanced by the bends. Since this is the main

source of losses in SOI WG it is important to carefully chose the bend radius depending on the final application.

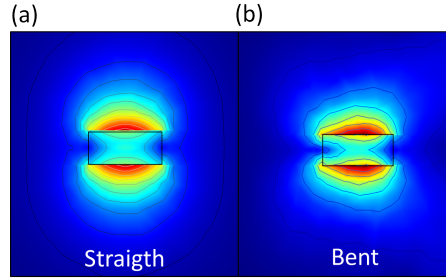


FIGURE 2.13: Profile of the electric field for the fundamental TM mode in a straight WG (a) and bent WG (b).

Figure 2.13 shows the profile of the electric field of the fundamental TM mode in a straight WG (a) and in a bend with a radius of curvature of $3\mu m$ (b) (the curvature is to the right). The bend presents an asymmetrical mode profile which shows a shift of the mode towards the outer interface.

A way to explain this observation is by the Fermat's principle. Fermat's principle states that the path of a light ray between two points follows a stationary optical path (minimal in refractive media) with respect to variations of the path. The fact that the optical mode propagates toward the outer part of the WG means that this one is the shortest optical path, even if the effective radius is greater. The only way to satisfy this condition is that the effective index of the mode in the bend is lower than the straight one. So, for a half of bend we can write:

$$n_{eff}^s \pi R \geq n_{eff}^b (R + \delta R)$$

where n_{eff}^s and n_{eff}^b are the effective index of the straight and bent WG. Therefore

$$n_{eff}^b \leq n_{eff}^s \frac{R}{R + \delta R}$$

with R the mean radius of bent and δR the deviation from the mean radius. From the former equation we can state that n_{eff}^b is always smaller than n_{eff}^s . A way to get δR in order to calculate n_{eff}^b is to solve the field equation for E and H in cylindrical coordinates [150]. The values for δn_{eff} , defined as $n_{eff}^b - n_{eff}^s$, as a function of bent radius are reported in figure 2.14 for TE polarization and WG width of $450nm$. For radii up to $4 - 5\mu m$ the value of δn_{eff} is lower than 0.1% but below this threshold quickly increases. These numbers may seem small but, for example, 1% change in the effective index in an optical resonator with a radius of $7\mu m$ leads to a shift of the resonance comparable to its free spectral range.

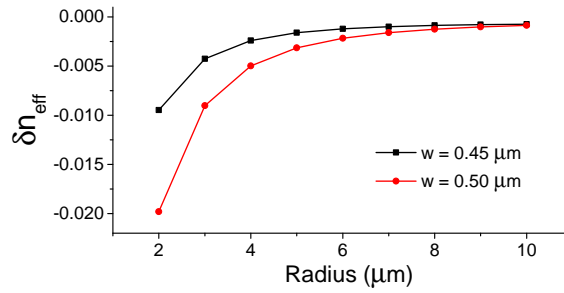


FIGURE 2.14: Simulated percentage change δn_{eff} as a function of the bent radius. TE polarization, $w = 450nm$. Data taken from [150].

2.5 Straight-bend directional coupler

The CMT can be also applied, at least for the TE polarization, to find the power coupling coefficient (CC) of a straight and a curved WG. Since CMT is based on the approximation of small coupling and large curves (with respect to λ) this theory can be applied up to radii of about $30\mu m$ [155]. For TM polarization, the most convenient approach remains the use of a finite element method (FEM) simulator. Figure 2.15 reports the studied system. The light is injected from the port In and collected from the Out. A perfectly matched layer (PML) layer is applied on the other ports to avoid reflections. The used polarization is TM and the gap, radius and wavelength were varied in order to verify the effects on the CC.

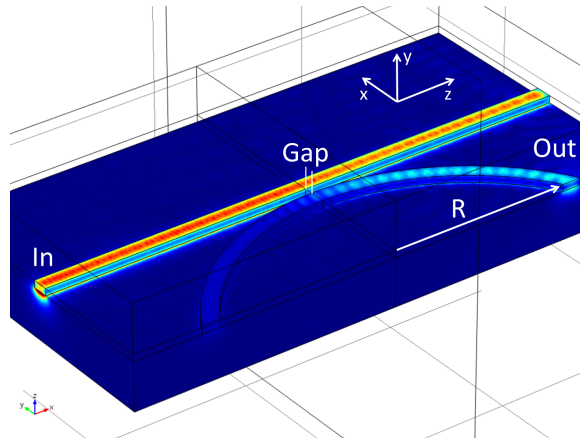


FIGURE 2.15: System under study. Simulation parameters: gap=200-300 nm, $\lambda = 1500 - 1600nm$, $R = 3 - 8\mu m$ TM mode. The image shows the case of $R = 7$ and $gap = 250nm$.

Figure 2.16 shows the value of CC obtained using a 3D FEM simulator. For a fixed gap, bigger bends give higher CC. This can be explained by thinking that:

- as R tends to infinity the effective coupling region grows and the system becomes similar to the directional coupler explained in the section 2.3.

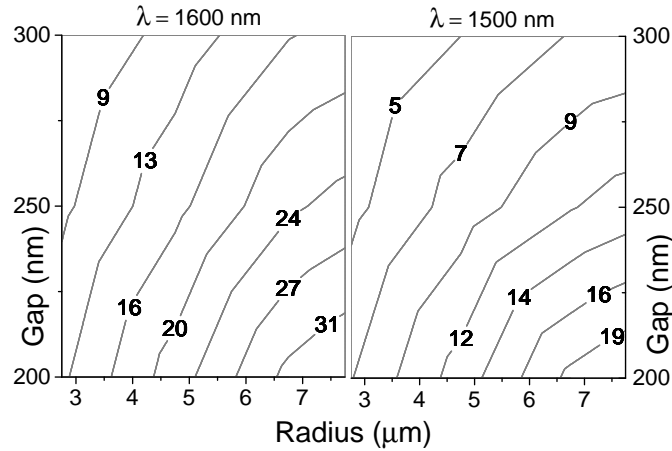


FIGURE 2.16: Simulated CC in percentage as a function of several simulation parameters: gap=200-300 nm, $\lambda = 1500 - 1600\text{nm}$, $R = 3 - 8\mu\text{m}$ TM mode.

- as R tends to infinity the bend-straight effective index mismatch decreases and the system approach to the perfect phase matching conditions

It is important to note that as the radius and the gap decreases (i.e. for large perturbations), the reflection to the In port increases (Fig. 2.17).

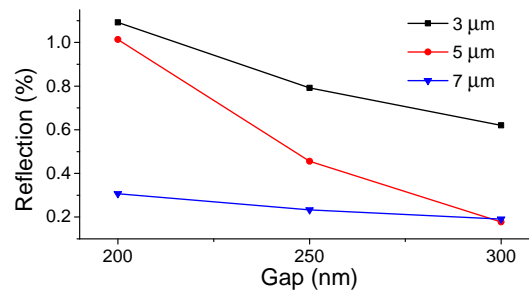


FIGURE 2.17: Reflected percentage to the In port as a function of gap for several ring radii: $R = 3, 5, 7\mu\text{m}$.

2.6 Surface roughness

Although this topic is more related to the fabrication process, it is important to introduce now this phenomenon since it is the main source of losses in the structures treated until now. The Line-edge roughness (LER) is a kind of defect introduced by the fabrication process during the etch procedure and affects sidewall of the WG that, instead of being ideally smooth, presents small roughnesses (see Fig. 2.18).

LER causes scattering loss. The origin of sidewall roughness can be found in both lithography [153], resist chemistry [154], and etching. The exact causes are still under

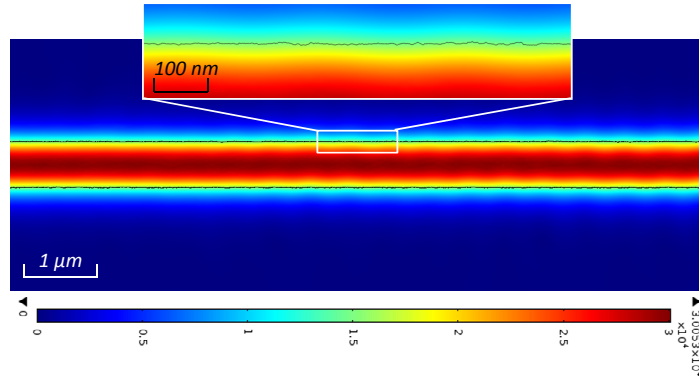


FIGURE 2.18: Simulation: top view of the propagating TE mode inside a WG. The inset shows a detail of the effect of the WG edge roughness on the optical mode.

debate, however. The etching transfers the LER already present in the resist pattern to the etched material while adding new roughness.

The LER can be represented by sidewall roughness by adding to the WG a random variation of the width, with a specific correlation length Λ_c . Such a variation leads to local variations of the effective index corresponding to the formation of a pseudograting along the sidewall. Thus, the sidewall roughness acts as a dipole which can be excited by the incident WG mode. As a fraction of the dipole cannot be recovered, scattering loss effects take place.

Therefore, a real WG shows actual losses far greater than the ideal one. These losses, in *linear* regime, are mainly caused by the roughness. There are several models to explain the dependence of the losses on the roughness [145, 156, 157]. The common denominator in these studies is that the losses depend on the square of the surface roughness, as showed in the following equation below[144]:

$$\alpha_s = \Phi^2(w/2)(n_{co}^2 - n_{cl}^2)^2 \left(\frac{k_0^2}{8n_{co}}\right) \left(\frac{1}{n_{eff} - n_{cl}}\right) \rho^2 \quad (2.28)$$

where ρ^2 is the root mean square(RMS) of the surface roughness, Δn^2 is the index contrast, $\Phi^2(w/2)$ is the intensity of the field at the core/cladding interface using this power normalization: $\int \Phi^2(x, y) dx dy = 1$. However this equation assumes that $\delta n/n_{eff}$ (see section 2.4) is small and that the bending is a small perturbation on the modal intensity profile of the straight guiding mode.

The Marcuse, Payne and Lacey model [156], shows that for accurate loss calculations it is necessary to take into account not only the roughness standard deviation ρ , but also the autocorrelation length Λ_c .

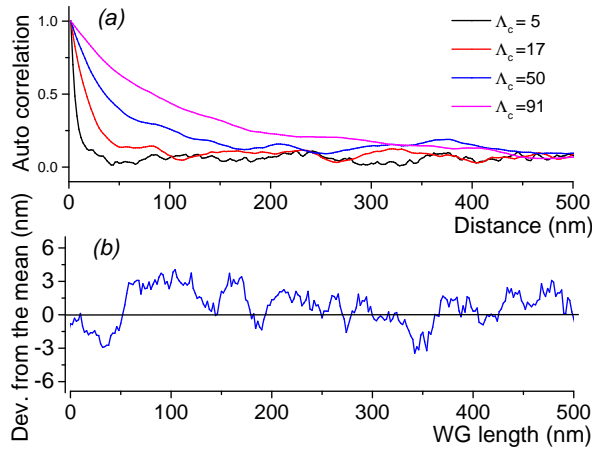


FIGURE 2.19: (a) Auto-correlation of 4 sequences used to simulate the roughness: the blue curve is relative to the sequence in (b). (b) A particular of a roughness sequence.

In order to investigate this phenomenon we set up a simulation, carried out with COMSOL, that measures the transmission of a WG with rough edges. The used geometry is reported in figure 2.18. We limit the simulation to the TE polarization and to 2D geometry in order to save machine time. The LER is modelled through a code that generates sequences of normal random numbers with a specific exponential correlation. The model is quite simple and is based on a recurrence equation:

$$s[n - 1] = a s[n] + b R_n[n] \quad (2.29)$$

where n is an index linked to the spatial coordinate, R_n are normal distributed random number and a and b are coefficients through which is possible to change the correlation distance. An example of the result is shown in figure 2.19(b). From the auto-correlation of the sequence is possible to determine its correlation length. The figure 2.19(a) reports some correlation curves for different Λ_c .

Varying the parameters σ_r and Λ_c , the changes of the WG optical response are investigated with an eye on the values of $\sigma \sim 2nm$ and $\lambda_c \sim 50nm$, since these were reported as typical for the WGs used in this work [145, 147].

The results are reported in figure 2.20. Firstly roughness standard deviation is fixed to $2nm$ and λ_c is varied.

The results are divided into three panels which report: 2.20(a) the losses at the end of the WG, 2.20(b) the reflections to the input and 2.20(c) the scattering outside it. In general, the losses (a) increase with an increasing of Λ_c and the trend is related to that of the scattering (c) to confirm what has been said previously. A complete randomness of the roughness would give rise to a flat transmission spectrum. Instead, the presence

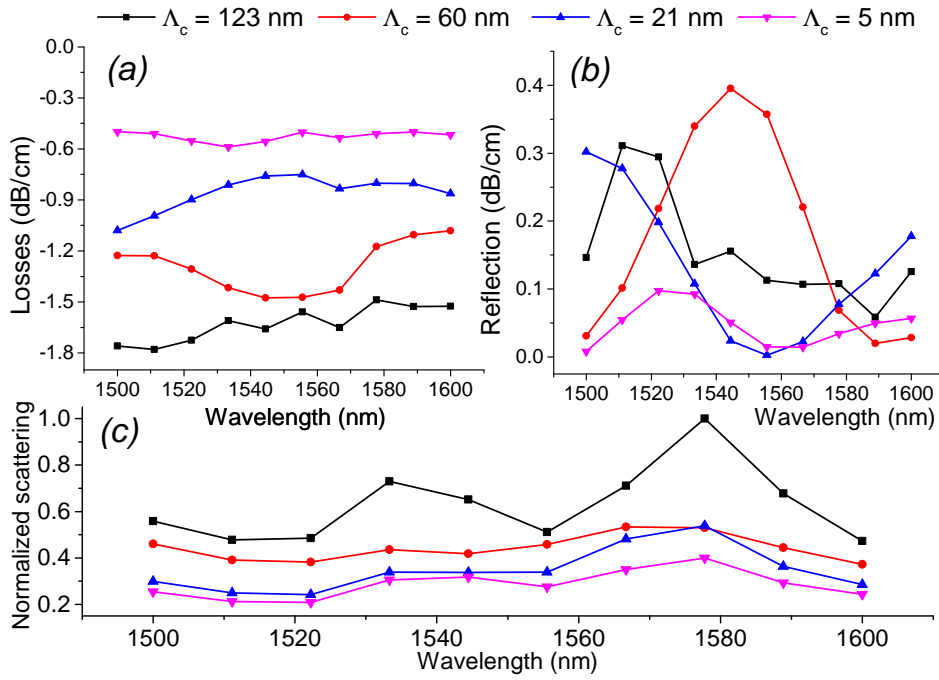


FIGURE 2.20: WG Transmission spectrum (a), reflection spectrum (b), scattering spectrum (c) for several Λ_c : 5, 21, 60, 123 nm. Simulation parameters: $w = 450$ nm, $\sigma = 2$ nm.

of a Λ_c generates some bands in which the losses and reflection (b) increases. It can be assumed that the system behaves as a *Distributed Bragg Reflector* (DBR). Since the reflection never exceeds the 10%, the missing energy is lost through scattering as reported in figure 2.21.

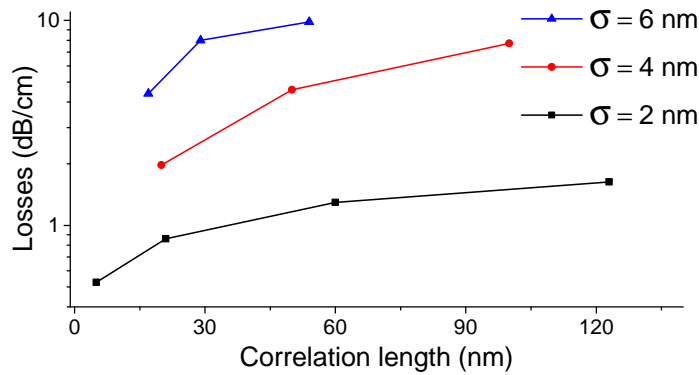


FIGURE 2.21: Average losses between 1500 – 1600 nm as a function of Λ_c for several values of σ_r : 2, 4, 6 nm.

In the figure 2.21 the average losses between $1.5\mu\text{m}$ and $1.6\mu\text{m}$ are plotted as a function of Λ_c for different σ : 2, 4, 6 nm. It is interesting to note that the results found for a $\sigma_r = 2$ and Λ_c of 60-120 nm, are consistent with those found in [147], which confirms what was found experimentally.

From this model the propagation losses can be expected to be of the order or below $1 - 5 \text{ dB/cm}$. This estimate is an upper limit even for the TM mode, since the electric field maxima are located along the vertical interfaces where the surface is smooth to the atomic level.

2.7 Chip to fiber interface

Efficient coupling between standard single mode fibres (SMF) and single mode WG is a key challenge in silicon photonics. Integrated circuits need an interface to the outside world, and that is what the coupling devices attempt to provide. Since energy efficiency is one key points of silicon photonics, it is fundamental to keep as small as possible any source of losses. Unfortunately the small size of single mode silicon on insulator WG compared with the diameter of a single mode fibre makes coupling inefficient. A common silicon waveguide with size of $0.5\mu\text{m} \times 0.220\mu\text{m}$, as used in this work, has a core cross sectional area of approximately $0.1\mu\text{m}^2$. By comparison an optical fiber has a core cross sectional area of around $250\mu\text{m}^2$ (for a diameter of $9\mu\text{m}$), three orders of magnitude larger (see figure 2.22).

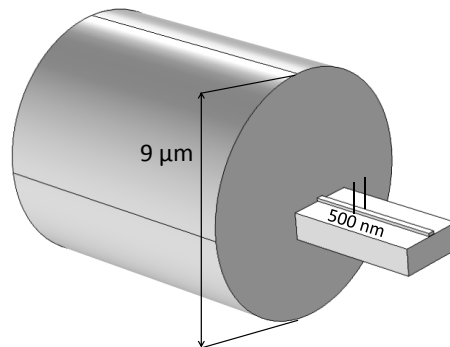


FIGURE 2.22: Simple butt coupling scheme example.

This mode volume mismatch leads to high losses since most of the light will propagate unguided outside the WG core. Another issue comes from the high index contrast between the WG silicon core and the air that generates reflection on the WG facet. An estimate of this quantity through Fresnel equations give a reflectivity of about 30% that corresponds to about -1.5 dB of losses. Even if the latter effect can be fixed using an index matching material, the volume mismatch remains a big issue that, for the simple butt coupling, leads to prohibitive coupling losses. Several solutions exist to face this problem that can be divided into 2 classes:

- In plane coupling
 - WG tapering
 - Tapered lensed fiber
 - Inverse WG tapering
- Out of plane coupling
 - Grating coupler

2.7.0.1 In plane coupling

The straightforward solution is to enlarge the mode of the WG and reduce the one of the fiber by performing a tapering. The WG taper is composed of a WG that increases or decreases its width along the propagation direction of light in order to change the mode volume (or the mode effective index) into one as similar as possible to the fiber mode. Tapered optical fibers are commercially available with a minimum tapering point of $2\mu\text{m}$. Therefore, it is possible to tapering up at least to $2\mu\text{m}$ the WG. Even if the WG width equals the fiber tip, this is not true for the height. However, to avoid excessive coupling to radiation modes in the taper, the required typical taper length must be of the order of millimeters. The WG height is fixed by the used SOI wafer to 220nm , thus the mode mismatch issue is still present. This coupling technique introduces about 10 dB of insertion losses for each facet.

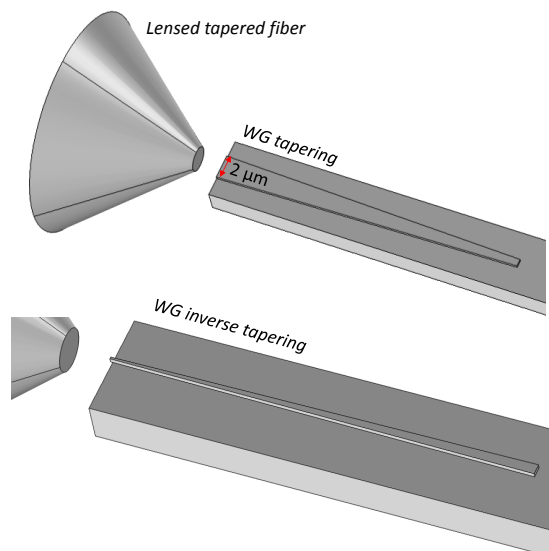


FIGURE 2.23: Tapered lensed fiber butt coupled to a tapered and inverse tapered WG.

A different approach is the inverse tapering technique. The WG mode is forced to expand outside the core by shrinking the WG dimensions. The evanescent field of the WG can reach even the fiber size allowing to reach insertion losses of about $0.6dB$ [158]. In addition, thanks to the small input cross section, the facet reflections are reduced. A drawback is the needs of a coupling region of several tens of microns to achieve good coupling.

2.7.0.2 Out of plane coupling: gratings

A completely different strategy is used in the *grating coupler* concept. These devices take advantage of the Bragg diffraction phenomenon to couple the light coming from a fiber. Figure 2.24 shows the grating-fiber coupling scheme. This method allows to couple a standard optical fiber (also without tapering) but with the disadvantage of a limited working band. The product working band-insertion loss is constant, then in general it optimizes the operation of the device by fixing the working band and minimizing losses. The grating solves the problem of the limited height of the WG which is present in the in-plane coupling method.

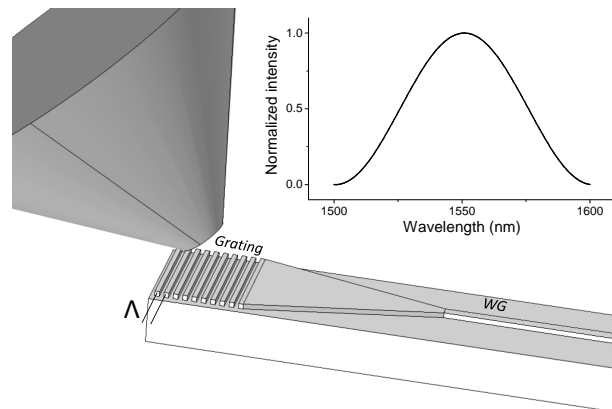


FIGURE 2.24: Grating-fiber coupling scheme. Λ is the grating periodicity. The inset shows a measured spectral response of a grating optimized to work in the 3 telecom window.

When the incident light comes to the surface of a periodic structure, it will be diffracted. The Bragg condition describes the relation between the wave-vectors of the incident and diffracted waves. When there is no grating at the interface between the two materials, the Bragg condition is the same as Snells Law, which describes refraction at the interface between two materials.

The first order Bragg diffraction is governed by the periodicity of the grating Λ as follows:

$$k_{in} \sin(\theta) + \frac{2\pi}{\Lambda} = \beta \quad (2.30)$$

with $\beta = \frac{2\pi}{\lambda} n_{eff}$. The Bragg condition is only exact for infinite structures. In finite structures there is a finite range of k vectors around the predicted one in which diffraction occurs.

Improvements from this simple relation can be obtained realizing a tapered periodicity or using a focusing geometry[159].

2.8 Optical microresonators

A racetrack resonator is composed of 2 bent waveguides and two straight waveguides connected to form a closed loop as shown in figure 2.25 . The resonator "talks" to the external world through an external waveguide (WG1 green rectangle) that exchange power by means of a directional coupler (red rectangle). If only one direction coupler is present, the configuration is called an all pass filter (APF), while with two bus waveguides is called add drop filter (ADF). The former is commonly used as a delay line or phase shifter while the latter is able to route a signal to one of the two bus WGs depending on its wavelength. For this reason the ADF is the fundamental component of an ONC network.

There are several main effects that contributes to the linear absorption in a silicon microring resonator coupled to a WG: Radiation losses, surface-roughness-induced light scattering in the microresonator sidewalls, optical leakage in the coupling gap between the side-coupled waveguide and the microresonator, optical leakage from the undercladding layer to the silicon substrate and through the device slab layer and material absorption losses. There exist also sources of non-linear absorption but will be treated in the chapter 7.

1. Surface-roughness-induced scattering loss from the microresonator or waveguide sidewalls is largely due to the dry-etching process. In the case of a microring resonator with both inner and outer sidewalls, the scattering loss can be particularly severe compared with a microdisk resonator with only the outer sidewall. In order to mitigate the sidewall surface roughness, fabrication of silicon microresonator-based devices typically employs the forming and removal of an oxidation layer [160]. The oxidation process of silicon is usually homogeneous, resulting in tens of nanometers of oxide that upon removal can effectively mitigate the surface roughness formed after the dry etching.

2. Scattering loss in the coupling gap spacing. The bus waveguide and the microresonator sidewalls in the coupling region inevitably scatter light. Besides, when the submicrometer-sized coupling gap spacing is not fully filled by the silica cladding layer, light is strongly scattered by the air voids. The latter can be mitigated by filling the gap spacing instead with boron phosphorus silicon glass followed by thermal reflow to eliminate air voids [161].
3. Optical leakage from the undercladding layer and the device slab layer. Due to the submicrometer dimensions of silicon waveguides, the optical mode is largely exposed outside the waveguide core and significantly overlaps with the undercladding layer. In the case of silicon rib waveguides with a thin slab layer, optical leakage also occurs via the device layer. In order to reduce such optical leakage, the undercladding silica layer can be undercut by wet etching in buffered hydrofluoric acid. Such undercut microdisk resonators have been demonstrated with a Q value as high as 5×10^6 [162].

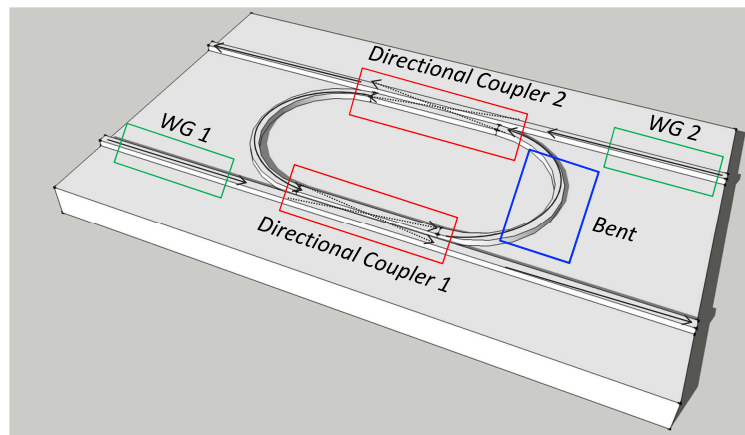


FIGURE 2.25: Main building blocks of a racetrack resonator: (red) directional couplers, (blue) bent, (green) WGs.

2.9 Microresonator theory

In the following section we will examine the theoretical optical behavior of a racetrack resonator (RTR). After a brief description of its main parameters, the basic formalism of the transfer matrix method (TMM) will be introduced. All the results are valid also for a ring resonator (RR) by imposing the condition of $c_s = 0$ (see Fig. 2.26).

The APF and the ADF are the common configurations for a single microresonator. They are suitable to be used with disk, ring and racetrack resonators.

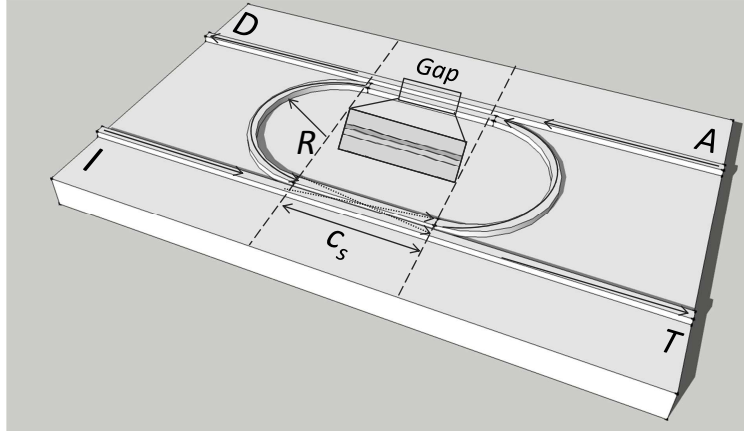


FIGURE 2.26: Schema of a racetrack resonator. The add-drop filter configuration has 4 ports: input (I), through (T), drop (D), add (A). R is the radius, the gap and the coupling sections (c_s).

The resonant frequency is fixed by the effective *optical path* in the RTR. We start from this statement to write:

$$OP(\lambda) = 2n_{neff}^s(\lambda)c_s + 2n_{neff}^b(\lambda)\pi R + (\Delta n_1(\lambda) + \Delta n_2(\lambda))c_s \quad (2.31)$$

with R and c_s the radius and the coupling section of the RTR (Fig. 2.26). The equation takes into account all the phenomena that induce variations on the effective index of the unperturbed mode. These variations are represented using a specific refractive index: n_{neff}^s straight effective index, n_{neff}^b bend effective index and $\Delta n_{1,2}$ for the coupler region (see Fig. 2.25). $\Delta n_{1,2}$ indicates the mismatch between the straight and a directional coupler mode and is defined as $\Delta n = n_{neff}^s - (n_{neff}^e + n_{neff}^o)/2$.

In order to simplify the subsequent calculations we define a mean effective index,

$$OP = \bar{n}_{eff}; p \quad \bar{n}_{eff} = \frac{2n_{neff}^s(\lambda)c_s + 2n_{neff}^b(\lambda)\pi R + (\Delta n_1(\lambda) + \Delta n_2(\lambda))c_s}{2\pi R + 2c_s} \quad (2.32)$$

with $p = 2\pi R + 2c_s$ the physical mean perimeter of the RTR. We define also

$$\bar{n}_g(\lambda) = \bar{n}_{neff}(\lambda) - \lambda \frac{\partial \bar{n}_{neff}(\lambda)}{\partial \lambda} \quad (2.33)$$

$$GVD(\lambda) = -\frac{\lambda}{c} \frac{\partial^2 \bar{n}_{neff}(\lambda)}{\partial \lambda^2} \quad (2.34)$$

where \bar{n}_g is the group index, the GVD is the group velocity dispersion and c is the speed of light.

The resonant condition is satisfied when, after a whole round trip, the light is in phase with himself. Which translates into the following equation:

$$\Delta\phi = \bar{\beta}_m p = 2\pi m; \quad \bar{n}_{eff} p = \lambda_m m \quad (2.35)$$

where $\bar{\beta}_m$ is propagation constant at resonance. The free spectral range (FSR) is defined as $\lambda_m - \lambda_{m-1}$ and can be derived from $\bar{\beta}_{m-1}$ knowing that:

$$\bar{\beta}_{m-1} = \frac{2(m-1)\pi}{p} = \bar{\beta}_m - \frac{2\pi}{p}$$

Making a first order Taylor expansion of the $\bar{\beta}_m |_{\lambda_m}$ around λ_m we obtain the FSR:

$$FSR \approx \frac{\lambda_m^2}{\bar{n}_g(\lambda_m)p} \quad (2.36)$$

The FSR is inversely proportional to the RTR optical path $p = 2\pi R + 2c_s$. The resonant wavelength is directly extracted from eq. 2.35:

$$\lambda_m = \frac{p \bar{n}_{eff}}{m} \quad (2.37)$$

2.9.1 Spectral response

Before starting the discussion, we fix the convention for the sign of the exponent of propagation. For example, a propagation from A to B is related to a phase shift of the optical modes in A and B as $B = e^{-i\phi} A$. This convention fixes also the formalism for the time propagation as $e^{i\omega t}$. From now on this will be the used convention.

The directional coupler presented in the section 2.3 is theoretically described through the transfer matrix of a beam splitter [163]. This matrix, for a lossless splitter, is written as:

$$\begin{pmatrix} c \\ d \end{pmatrix} = \begin{pmatrix} t & i\kappa \\ i\kappa & t \end{pmatrix} \begin{pmatrix} a \\ b \end{pmatrix} \quad (2.38)$$

where i is the imaginary unit, k^2 and t^2 represents amount of power coupled into the resonator and transmitted power respectively. This matrix links the amplitude of the outgoing fields c, d with the incoming fields a, b . The field distribution in the beam splitter are shown in figure 2.27(b).

In a lossless beam splitter the quantity k and t are related by the energy conservation $k^2 + t^2 = 1$ (extracted making the matrix determinant). In a real scenario, a non punctiform coupling section could generates some additional losses. It is possible to modify the matrix 2.38 in order to include this *coupling losses* c . The parameter c is

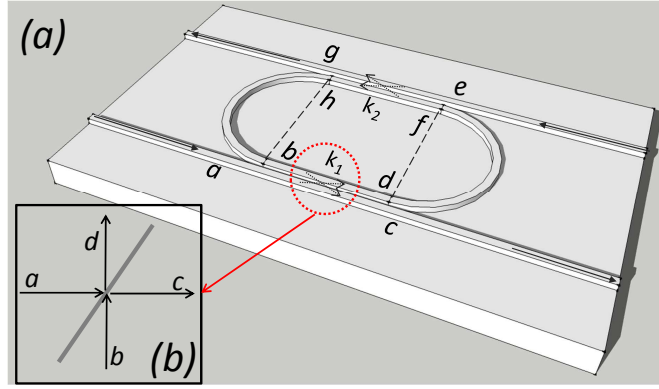


FIGURE 2.27: (a) Labels for the field amplitudes at the main interfaces for the transfer matrix approach. (b) Sketch of the beam splitter generalization for a directional coupler.

defined directly through the energy conservation $k^2 + t^2 = c^2$. Taking into account this relation the matrix 2.38 is modified as follow. Using, for the matrix

$$M = \begin{pmatrix} x_1 & y_1 \\ x_2 & y_2 \end{pmatrix}$$

,a general propriety of matrix formalism:

$$\begin{pmatrix} x' \\ y' \end{pmatrix} = \begin{pmatrix} x_1 & y_1 \\ x_2 & y_2 \end{pmatrix} \begin{pmatrix} x \\ y \end{pmatrix} \rightarrow \begin{pmatrix} y \\ x' \end{pmatrix} = \frac{1}{y_1} \begin{pmatrix} -x_1 & 1 \\ -\det(M) & y_2 \end{pmatrix} \begin{pmatrix} x \\ x' \end{pmatrix} \quad (2.39)$$

instead of the matrix 2.38 we get:

$$\begin{pmatrix} b \\ d \end{pmatrix} = \frac{1}{ik} \begin{pmatrix} -t & 1 \\ -c^2 & t \end{pmatrix} \begin{pmatrix} a \\ c \end{pmatrix} \quad (2.40)$$

It is important to take into account the c term for a precise description of the behavior of a RTR especially for a long c_s . For a RR, instead, c is typically neglected. Since the c term adds a small perturbation to the optical response of a RTR, during the following discussion we are going to use $c = 1$ to preserve a simple treatment. Let us start writing the matrix for the coupling region of a RTR (see Fig. 2.27).

$$\begin{pmatrix} c \\ d \end{pmatrix} = \begin{pmatrix} t & i\kappa \\ i\kappa & t \end{pmatrix} \begin{pmatrix} a \\ b \end{pmatrix} e^{-i\beta_c c_s} \quad (2.41)$$

where $\beta_c = \beta_s - \beta_{\Delta n}$ ($\beta_{\Delta n}$ refers to the index perturbation of the directional coupler). The exponential term corrects the relation for the simple splitter taking into accounts the phase variation going from a to c . We adds another simplification by considering $k_1 = k_2 = k, t_1 = t_2 = t$, this in general is not verified.

By using again the relation 2.39 we obtain:

$$\begin{pmatrix} b \\ d \end{pmatrix} = \frac{i}{k} \begin{pmatrix} t & -e^{i\beta_c c_s} \\ e^{-i\beta_c c_s} & -t \end{pmatrix} \begin{pmatrix} a \\ c \end{pmatrix} \equiv K \begin{pmatrix} a \\ c \end{pmatrix} \quad (2.42)$$

where K is what we called *coupling matrix*. The propagation inside the resonator is described by the *propagation matrix* P defined as:

$$\begin{pmatrix} f \\ h \end{pmatrix} = \begin{pmatrix} 0 & \frac{1}{\gamma} e^{-i\pi R \beta_b} \\ \gamma e^{i\pi R \beta_b} & 0 \end{pmatrix} \begin{pmatrix} b \\ d \end{pmatrix} \equiv P \begin{pmatrix} b \\ d \end{pmatrix} \quad (2.43)$$

where $\gamma = e^{-\alpha\pi R}$ is the loss for an half of a round trip and β_b is the propagation constant for the bent mode. The factor γ represents the losses in a half of a bend and α is the already known attenuation constant. Thus, the propagation inside a RTR is described by the following matrix multiplication $M' = KPK$. The relation between the fields e, c and g, a is described by the matrix M extracted from the M' through the relation 2.39

$$\begin{pmatrix} c \\ e \end{pmatrix} = \frac{1}{m_{22}} \begin{pmatrix} -m_{21} & 1 \\ \text{Det}[M'] & m_{12} \end{pmatrix} \begin{pmatrix} a \\ g \end{pmatrix} \equiv M \begin{pmatrix} a \\ g \end{pmatrix} \quad (2.44)$$

where the terms $m_{x,x}$ are the 4 elements of the matrix M' . To find the spectral response of the T and D ports of a single RTR is sufficient to calculate the following ratios considering $e = 0$.

$$D = \left| \frac{g}{a} \right|^2 = \left| -\frac{m_{21}}{m_{22}} \right|^2; \quad T = \left| \frac{c}{a} \right|^2 = \left| -\frac{\text{Det}(M)}{m_{22}} \right|^2 \quad (2.45)$$

By expanding the previous relations, we obtain an explicit form for the T and D ports transmission.

$$T = \left| \frac{c}{a} \right|^2 = \frac{t^2 + t^2 \gamma^2 - 2t^2 \gamma \cos(\Delta\phi)}{1 + t^4 \gamma^2 - 2t^2 \gamma \cos(\Delta\phi)} \quad (2.46)$$

$$D = \left| \frac{g}{a} \right|^2 = \frac{k^4 \gamma^2}{1 + t^4 \gamma^2 - 2t^2 \gamma \cos(\Delta\phi)} \quad (2.47)$$

In the resonant condition, $\Delta\phi = 2\pi R \beta_b + 2c_s \beta_c = m2\pi$, the T port shows a minimum while the D port shows a maximum. In presence of losses, i.e. $\gamma \neq 1$, the D port cannot reach 1. While, the T port can assumes the value of 0 in the so called *critical coupling* condition. This condition is satisfied only for asymmetric coupling condition,

i.e. $k_1 \neq k_2$, when the parameter t_1 assumes the value of $t_2\gamma$. The *over-coupling* condition is defined for $k_{1,2} \gg \gamma$ while the *under-coupling* condition for $k_{1,2} \ll \gamma$.

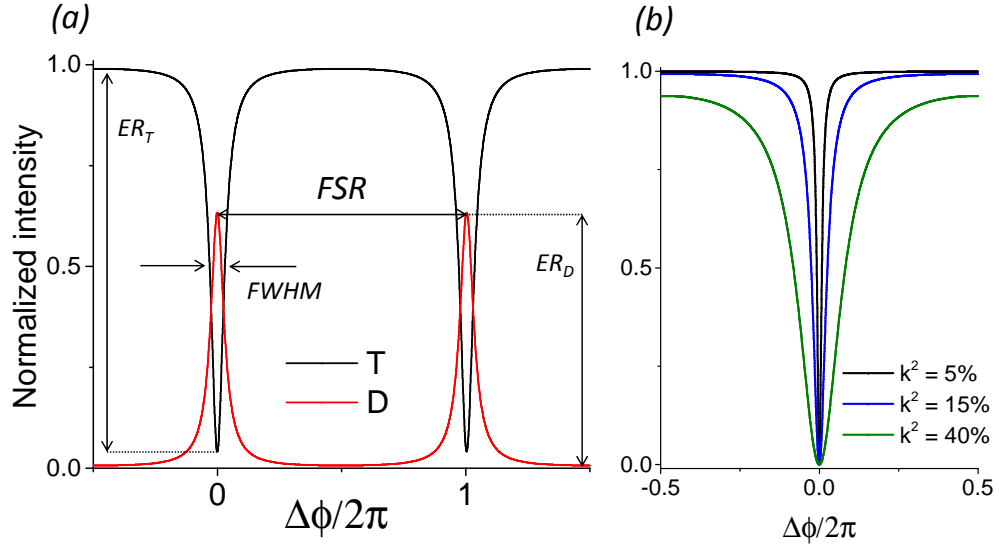


FIGURE 2.28: (a) Simulated T (black) and D (red) ports normalized intensity as function of $\Delta\phi$. Meaning of the labels: $ER_{T(D)}$ extinction ratio of the T(D) and the full width at half maximum (FWHM). (b) Transmission spectra of T port for several k^2 : 5%, 15%, 40%.

The figure 2.46 shows the theoretical T (black) and D (red) ports normalized intensity as function of $\Delta\phi$ and reports the key parameters that define the performance of a microresonator: FSR, the spectral distance between the nearby resonances, the extinction ratio of the T port $ER_T = 10 \log(T_{min}/T_{max})$ and for the D port $ER_D = 10 \log(D_{min}/D_{max})$ and the full width at half maximum of the resonance.

Performing a first order expansion of the equation 2.28 around the resonance, the equation takes the form of a lorentzian. Then by the definition of FWHM, we deduce the FWHM of the ADF.

$$FWHM = \frac{(1 - t^2\gamma)\lambda_m^2}{\pi n_g(\lambda_m) p t \sqrt{\gamma}} \quad (2.48)$$

Then using the definition of the *quality factor* $Q = \frac{\lambda_m}{FWHM}$ and the former equation we get:

$$Q = \frac{\pi n_g(\lambda_m) p t \sqrt{\gamma}}{(1 - t^2\gamma)\lambda_m} \quad (2.49)$$

The parameter Q represents the quality factor of the resonator. This parameter is closely related to the FWHM and is mainly influenced by three parameters:

$$\gamma = 1 \implies Q \propto \frac{p t}{k^2}; \quad \gamma \rightarrow 0 \implies Q \propto p \sqrt{\gamma}$$

- the coupling coefficient k^2 is $1 - t^2$, which is a design parameter.

- the resonator optical path p , which is a design parameter.
- the attenuation constant α , i.e. γ , that is fixed by the material losses and fabrication defects.

The larger is p , the greater is Q . The larger are k and α , the lower is Q . Q is linked to another important parameter that is exploited in *nonlinear optics* (see chapter 7) applications, the enhancements factor (EF) that describes the amount of energy stored inside the cavity:

$$EF = \frac{P_{int}}{P_{inc}} = \frac{\lambda_m k^2 Q^2}{(1 - k^2)(pn_g \pi)^2} \quad (2.50)$$

The previous relation is extracted by solving the equations 2.43 and 2.41 at a m-th resonance for $\left|\frac{f}{a}\right|^2$. The square power of Q leads to a great stored power for high Q resonator, considering that common SOI microresonators can easily reach a Q of the order of $10^3 - 10^4$. The power enhance is not for free. For the energy conservation we have to find some modification in the time response of the resonator.

2.9.2 Phase shift and group delay

An optical microresonator falls in the group of linear time-invariant system. These systems are characterized through the *transfer function*, that is the fourier transform of the time impulse response. From this theory we know that the *phase shift* φ and the group delay (GD) are defined as [164]:

$$\varphi = Arg(H(\omega)); \quad GD = -\frac{d\varphi}{d\omega} \quad (2.51)$$

where $H(\omega)$ is the transfer function, in general a complex quantity. In the case of a microresonator, the transfer function of the T port, H_T , correspond to the complex ratio between the output field c and the incident field a . Respectively for the D port $H_D = \frac{g}{a}$. Once we know the functions $H_{T,D}$, by solving the equations 2.43 and 2.41, it is possible to calculate the phase shift and the GD using the equations 2.51. To compute these quantity as functions of λ we write:

$$\frac{d\varphi}{d\omega} = \frac{d\varphi}{d\lambda} \frac{d\lambda}{d\omega} = -\frac{d\varphi}{d\lambda} \frac{2\pi c}{\lambda^2} \quad (2.52)$$

Figure 2.29(a) reports the induced phase shift, for an optical wave transmitted at the T and D ports. Near the resonance there is a steep change of the phase which is reflected in the growth of GD (Fig. 2.29(a)).

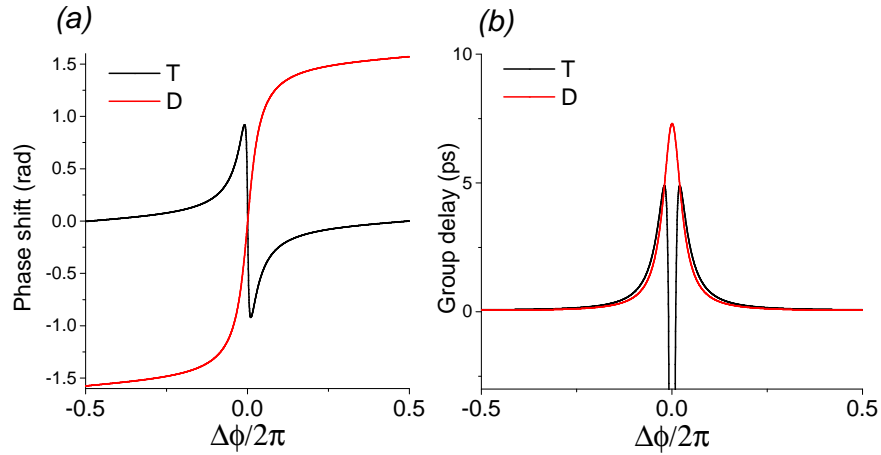


FIGURE 2.29: (a)((b)) Phase shift (group delay) of the T(black) and D(red) port as a function of $\Delta\phi$.

Figure 2.30 shows how the variation of the coupling coefficient is reflected on these physical quantities for the D port. It is seen that as the CC decreases (i.e. the Q

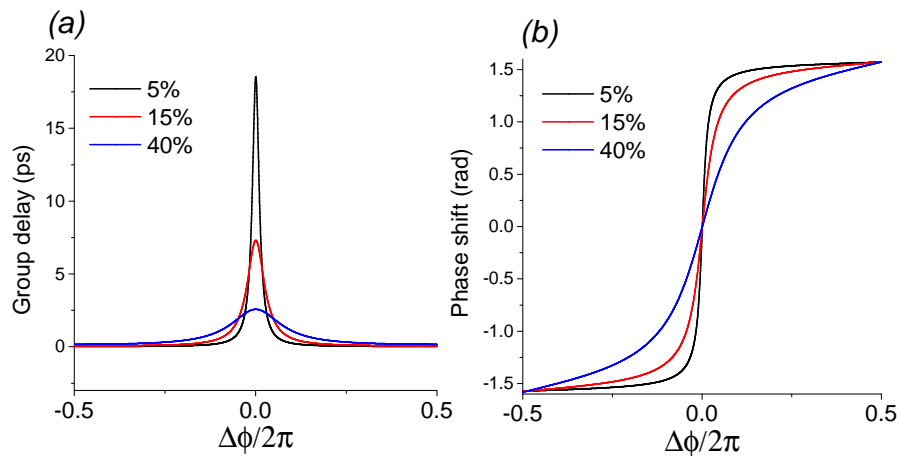


FIGURE 2.30: (a)((b)) Phase shift (group delay) of the D port as a function of the of $\Delta\phi$ for several values of k^2 : 5%, 15%, 40%.

grows) the phase response becomes increasingly steep and then the GD grows. The order of magnitude of the GD is of tens of ps . The GD is a fundamental parameter to control, since it tells how a signal will be delayed (thus also distorted) by passing through the device. For telecom application it is important to have devices that are engineered to have a constant group delay inside its bandwidth in order to preserve the signal information. On the other side, the GD of a device could be engineered to obtain all optical buffer or delay lines [8, 165].

2.10 Optical microresonator experimental investigation

In the following section we are going to investigate the validity of simulations by comparing them with some experimental measures. The aim is to extract the experimental curves for:

- the n_{eff} dispersion for both TE and TM polarization
- the n_g dispersion
- the bend-straight index mismatch δn_{eff} for both TE and TM polarization
- some values of the CC for the straight-bend coupler in TM polarization

In the following calculations we will neglect the coupling losses c and also the even and odd index mismatch Δn corrections since it was found to be smaller than the experimental errors induced by the reference oscillations and the fabry-perot noise.

2.10.1 Effective index and group index

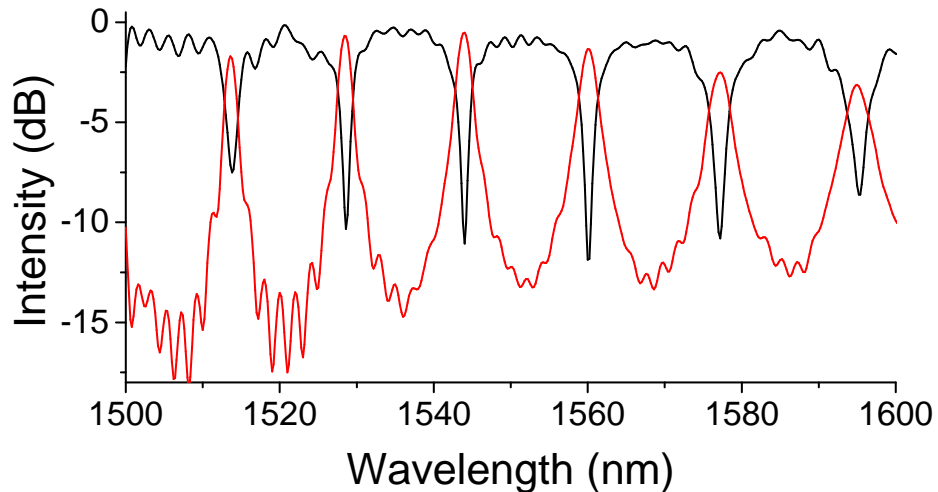


FIGURE 2.31: Experimental transmission spectrum of the T (black) and D (red) ports of a RR based ADF for TM polarization. The geometrical parameters are: $R = 6.75\mu m$, $gap = 220nm$ and $c_s = 0$.

Figure 2.31 shows the experimental transmission spectrum of a $6.75\mu m$ RR based ADF. From now on, the parameter R , relative to a real device, is intended as the mean radius, i.e. $R - w/2$, where w is the WG width.

By performing a series of lorentzian fit (see Fig. 2.32) on each resonance we can extract the following parameters: FSR , λ_m , $FWHM$ and $ER_{T,D}$.

From these experimental values and their theoretical equations can be derived, n_{eff} , (FSR, λ_m) , $n_g(FSR)$, $CC(FWHM, ER_{T,D})$.

While the first and the second quantities are relatively simple to obtain, given that in the linear regime there is no variation between the input and the output λ , CC is the most difficult parameter to estimate using the $ER_{T,D}$ since it depends on how good is the data acquisition. Moreover, Fabry-Perot oscillations due to multiples reflections between the input and the output facets are superimposed on the transmission spectra(as visible in Fig. 2.31). This results in a "quasi-sine wave" amplitude modulation of short period that further complicated the process of data extraction. For this reason, the estimate of the CC will be done using the FWHM and the equation 2.48.

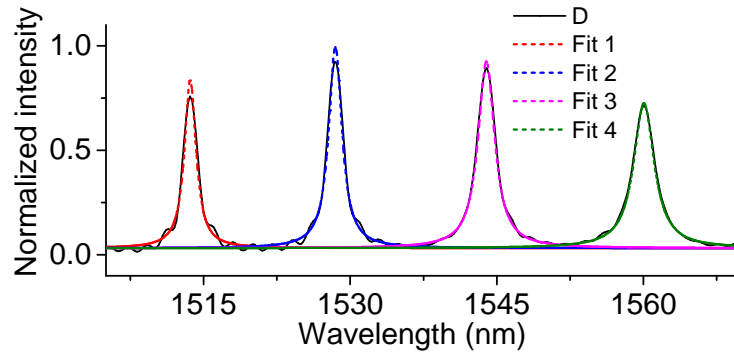


FIGURE 2.32: Series of lorentzian fit applied on the first 4 D port resonances. The resonances are numbered going from left to right.

TABLE 2.7: Extracted values for each resonance number.

	$\lambda_m \pm 0.01$ (nm)	$FSR \pm 0.01$ (nm)	$FWHM \pm 0.01$ (nm)
1	1513.63	14.8	1.4
2	1528.48	15.5	1.6
3	1543.94	16.1	2.0
4	1560.06	17.1	2.5
5	1577.13	17.9	2.9
6	1594.99	—	3.9

The presence of the dispersion is inherent in the increasing of the FSR as the wavelength increases. Let's proceed with the first and second parameters. Assuming that the index dispersion follows a quadratic law, $n_{eff}(\lambda) = a\lambda^2 + b\lambda + c$, we have from eq. 2.33:

$$ng(\lambda) = c - a\lambda^2 \quad (2.53)$$

As a consequence, the group index depends only from two parameters, a and c . Using the FSR equation and the values of table 2.7 we set a system of 2 eq. and 2 unknowns.

Once a and c are known, we can derive the n_g law. For $\lambda = 1550$ nm it is:

$$n_g(1550) = 3.45 \pm 0.02$$

The error is estimated using the remaining parameters. That is, using n parameters there are $n - 2$ equations and only 2 unknowns that are not degenerate because of the error in the experimental data and in the fitting procedure. Since all the coefficients belong to the same population is possible to determine a set of estimates of n_g whose mean is the expected value and the standard deviation is the error associated. The same procedure is applied to estimate the mean and error of the other parameters.

The values of a and c in equation 2.35, that links the center of the resonance and the n_{eff} , are not sufficient to determine the dispersion of n_{eff} because we lack information on the resonance order m . Therefore we claim that the right m , m_c , is the one that gives an effective index dispersion close to the simulated one (Fig. 2.8). This is not trivial since m is an integer and, especially for large FSR resonator, also $m_c \pm 1$ are compatible. The smaller the resonator, the easier the FSR calculus. Then setting $m_1 = 31$ as the order for the first resonance we get:

$$n_{eff}(1550) = 1.77 \pm 0.01$$

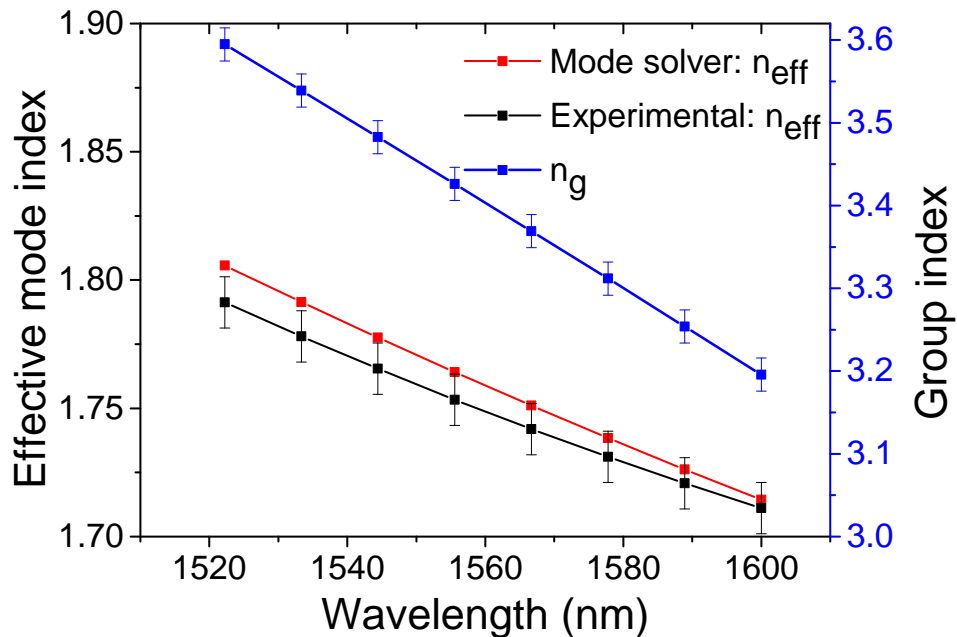


FIGURE 2.33: (Red) Mode solver n_{eff} dispersion law. (Black) Experimental n_{eff} dispersion law. (Blue) Experimental n_g dispersion law. Polarization used, TM.

In order to estimate the CC using the FWHM formula, we fix the value of bending loss to 0.005 dB/cm , as suggested for an $R = 7 \mu\text{m}$ [145], and then we make use of the measured FWHM reported in table 2.7.

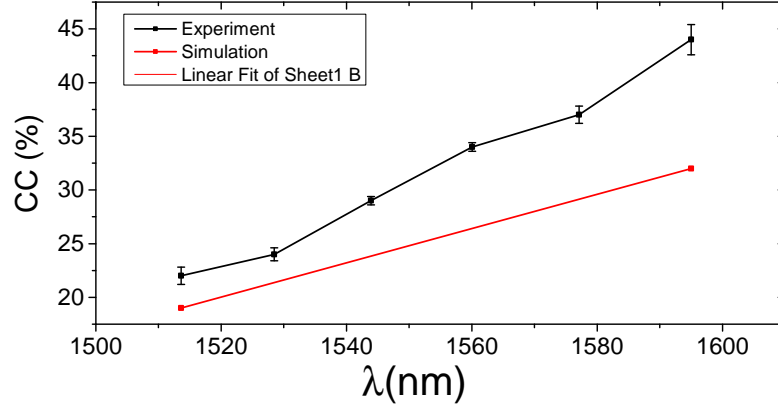


FIGURE 2.34: (Black) Measured CC as a function of wavelength for TM polarization. (Red) Simulated point.

The discrepancy between the two curves is not due to a wrong estimate of dispersion (slope) but rather to an offset attributable or, to a wrong choice of α or, to the proximity effect error of the fabrication [166].

TABLE 2.8: CC , n_{eff} and n_g dispersion laws: $n = a\lambda^2 + b\lambda + c$, $CC[\%] = b\lambda + c$.

	TE		
	$a(1/\text{nm}^2)$	$b(1/\text{nm})$	c
n_{eff}	4.76×10^{-7}	-2.6×10^{-3}	5.42
n_g	—	$(-1 \pm 0.1) \times 10^{-3}$	6.1 ± 0.1
	TM		
	$a(1/\text{nm}^2)$	$b(1/\text{nm})$	c
n_{eff}	2.41×10^{-6}	-8.5×10^{-3}	9.2
n_g	—	$(7 \pm 0.2) \times 10^{-3}$	14 ± 0.3
$CC(\%)$	0.27 ± 0.02	-390 ± 30	

2.10.2 Bend effective index

As mentioned in Section 2.4, a bent WG has a lower effective mode index compared to a straight one. To verify this phenomena, the dispersion was measured for 3 ADF composed of RR and RTR with different radii: $3 \mu\text{m}$, $6.75 \mu\text{m}$ and $3.25 \mu\text{m}$. According to the figure 2.14 the Δn_{eff} induced by the radius of $6.75 \mu\text{m}$ should be negligible, especially for the TE mode that is the farthest from the cut off.

In both RR cases one can see that the larger radius has an n_{eff} very similar to the simulated straight one, while the minor radius returns a minor n_{eff} . The effect is

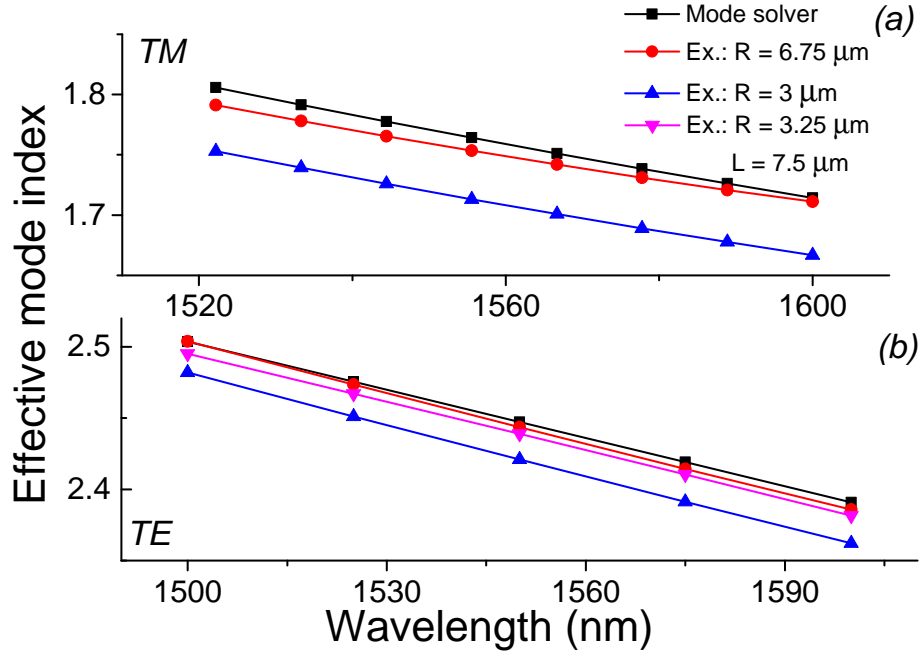


FIGURE 2.35: Effective index dispersion measured on 3 ADF for TM(a) and TE(b) polarizations: (red) RR with $R = 6.75\mu\text{m}$, (blue) RR with $R = 3\mu\text{m}$ and (pink) RTR with $R = 3.25\mu\text{m}$, $c_s = 7.5\mu\text{m}$. (Black) Mode solver calculation. The WG width is $0.5\mu\text{m}$.

greater in the case of TM polarization because the mode is less confined, i.e. close to the cut-off. The found δn values are:

$$TM : \delta n = 0.05 \pm 0.01 \quad TE : \delta n = 0.02 \pm 0.01 \quad (2.54)$$

To comment the curve of the RTR (pink) we have to consider that the reduction of the n_{eff} due to the small bending is compensated by the straight sections (eq. 2.32). Therefore, a RTR will have a larger n_{eff} compared to a RR with equal radius. This statement is confirmed in figure ??(b).

2.11 Surface roughness effect on microresonators

The first theoretical study of this phenomenon goes back to nineties [167]. In this article the roughness is described as correlated random perturbation as previously reported in section 2.6. A micro resonator with LER loses the degeneracy of forward (a_{cw}) and backward (a_{ccw}) propagating waves resulting in a splitting of the original resonance (see Fig. 2.36). The LER, in this case, can be seen as something that induces a coupling K between the fields a_{cw} and a_{ccw} . K^2 is the power coupled between the modes. The equations that describes the dynamic of the cavity fields are written using the time CMT

[162]:

$$\frac{da_{cw}}{dt} = -(\gamma_t/2 + i\Delta\omega)a_{cw} + i\beta a_{ccw} + ks_i \quad (2.55)$$

$$\frac{da_{ccw}}{dt} = -(\gamma_t/2 + i\Delta\omega)a_{ccw} + i\beta a_{cw} \quad (2.56)$$

where γ_t is the total decay rate, $\Delta\omega$ the frequency detuning, β represent the degree of coupling between the modes. The factor K is related to β through $\beta = K\sqrt{p/v_g}$. As it is seen from figure 2.36(a), β fixes also the frequency of the two modes.

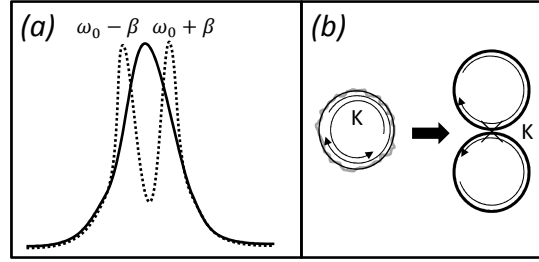


FIGURE 2.36:

It is worth to note that the system is completely analogous to two directly coupled resonators (CROW) as is showed in figure 2.36(b). Again, K^2 dictates the power coupled between the resonators. The critical condition to have the mode splitting is [167]:

$$\frac{K^2}{CC^2} > 1 \quad (2.57)$$

where the CC is the WG resonator coupling coefficient. Such relation suggests that in high Q resonators, ie with low CC, this phenomenon can be present. Resonators with high CC are immune to this effect. The relation between the roughness magnitude and the mode splitting in high Q resonators has been studied in [162] for several radii. They suggest a method to measure K through a measure of the spectral separation between the two modes. Knowing that is possible to calculate the Q factor as follows:

$$Q_\beta = \frac{\omega_0}{2\beta} = \frac{\sqrt{2}}{\pi^{3/4}\delta n V_s \bar{u}_s} \quad (2.58)$$

where \bar{u}_s is the normalized, spatially-averaged polarized electric field energy density at the resonator edge and $\delta_n^2 = n_d^2 - n_0^2$ is the core-cladding index contrast. V_s is the effective mode volume and for a disk resonator, it is expressed as $\sqrt{R\Lambda_c}h\sigma_R$ whit R the radius of the disk, Λ_c the LER correlation length, h the disk height and σ_R the RMS deviation of the LER .

Chapter 3

Introduction to fabrication

Process: main techniques and fabrication errors

3.1 Introduction

One of the strengths of silicon, which is the basis of its success, is the low cost of raw material. It is therefore important to use a manufacturing process that maintains a low final product cost without compromising the choice of a cheap raw material. CMOS microelectronics has evolved in this way: increase the transistor density to share the manufacturing cost on many different devices. A crucial aspect was to upgrade the currently used production technique, e.g. optical lithography, to force the increased miniaturization request. In fact, optical lithography fulfils all the requirements needed to be applied on an industrial scale such as: resolution, reliability, speed, and overlay accuracy. The semiconductor industry is pushing to reduce the transistor gate length down to 18 nm by 2014 [168].

Despite this high resolution, fabrication errors are always present and, especially in interferometric optical structures (RR and RTR for example), can affect significantly the actual optical response compared to the ideal one.

Fabrication techniques with higher spatial resolution are used to limit the fabrication defects such as:

- E-Beam lithography. It uses an electron beam as writing method and, since electrons have wavelengths much smaller than those of photons, it allows a higher

resolution than DUV. Its major drawback is the ability to write only on small areas thus limiting the total throughput. Developments projects aim at using multiple parallel e-beams to increase the throughput [32].

- Nano-imprint [169]. Nanoimprint is an emerging lithographic technology that promises high-throughput patterning of nanostructures. Based on the mechanical embossing principle, nanoimprint technique can achieve pattern resolutions beyond the limitations set by the light diffractions or beam scatterings in other conventional techniques. This is a promising technique but still at the experimental level

In this chapter we are going to introduce how the defects are introduced during the production flow. Furthermore, the standard fabrication steps of a SOI passive photonic device are also explained: firstly the most common techniques for the realization of the basic planar three layer $Si - SiO_2 - Si$ structure are discussed. Then, Deep UltraViolet (DUV) lithography and etching are treated.

3.2 Three layer (Si- SiO_2 -Si) structure fabrication

Many fabrication methods are available to produce SOI wafers, all of them start with a circular silicon wafer of several inches of diameter (8 inches in the present work) grown usually by Czochralski method. Users have to choose the one that best fit their requirements, most wide spreads are SIMOX-SOI, Bond and Etch-back SOI (BESOI) and SmartCut Process.

3.2.1 SIMOX-SOI (Separation by IMplanted OXYgen)

Figure 3.1 summarizes the SIMOX process. Buried Oxide Layer (BOX) is realized by oxygen ion implantation of a crystalline quality silicon overlayer (Fig. 3.1(1)). Main process windows concern the energy and dose ($\frac{ions}{cm^2}$) of implanted species, the first sets the depth of the layer, the second modifies the thickness. Typical values are $200KeV$ for the energy and over $10^{18}cm^{-2}$ for the dose. SIMOX-SOI allows the realization of very thin core heights (i.e $\ll 1\mu m$) but it's rather a destructive technique, thermal annealing at high temperatures ($1300C$) (Fig. 3.1(2)) is always needed to obtain a box like shaped silica layer concentration profile and to restore crystal order(Fig. 3.1(3)).

Workflow of the SIMOX process:

1. Oxygen ion implantation (1)

2. Thermal annealing (2)
3. Final result, uniform BOX layer without lattice defects(3)

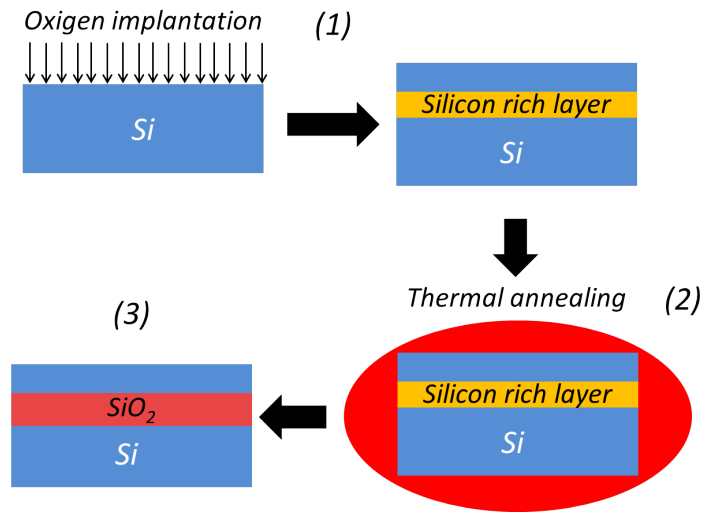


FIGURE 3.1: SIMOX process workflow.

3.2.2 Bond and Etch-back SOI (BESOI)

A thin silica layer is thermally grown on the wafer surface which is then brought to contact with the same layer of a second identical handle wafer . When temperature is raised over 1100 C, they form strong bonds and the basic structure is obtained. Since the two silicon layers are hundreds μm thick, Chemical Mechanical Polishing (CMP) [170] is performed to reduce the device layer height. This is a fast, cheap but quite rough method that does not allow to obtain core thickness below $10\mu m$. A more refined technique is the Etch-Stop BESOI that improves the thickness uniformity of the device layer and reduce the minimum thickness to the nm scale. The etch-stop layer separates the future device layer from the rest of the wafer. During the thinning process, the etch-stop protects the device layer until the sacrificial wafer has been removed. The removal of the etch-stop then leaves a uniform device layer. As a compensation for the limited selectivity of the etch-stops, a double etch-stop has frequently been proposed. Nowadays the BESOI methods are mainly reserved for the fabrication of thick layer SOI substrates for which the simple grind-and-polish approach is sufficient.

Workflow of the BESOI process:

1. Thermal oxidation (1)
2. Wafer bonding (2)

3. Chemical Mechanical Polishing (3)

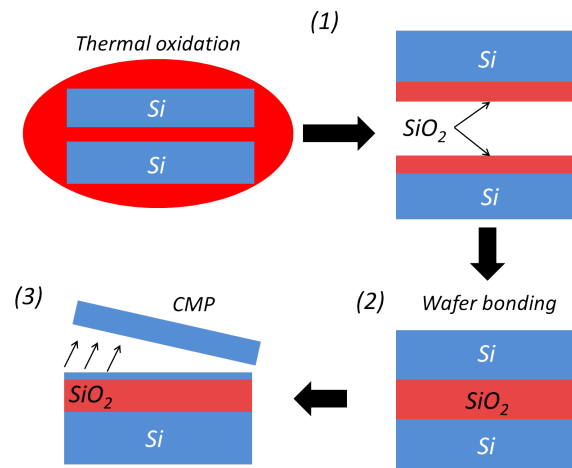


FIGURE 3.2: BESOI process workflow.

3.2.3 Smartcut Process (Unibond)

It's one of the most important and widespread technique because it allows to obtain very small core heights with high precision and small surface roughness. It combines elements of both SIMOX and BESOI processes: first, a thin Hydrogen layer is created by ion implantation slightly below the silicon wafer surface and, then, a silica layer is thermally grown (fig.3.3); a second handle wafer is bonded to the first by BESOI process and a thermal annealing is performed. The thermal process has many effects: it creates a sharp cut along the hydrogen layer, where lattice bonds have been strongly weakened by ion implantation, the remaining hydrogen ions evaporate and lattice defects are removed. The final result is a SOI structure with a very thin core height and small surface roughness, since no coarse polishing methods have been employed.

3.3 Deep UltraViolet photolithography

Once the basic structure has been created, photonic structures have to be printed and successively etched in the core. This fundamental step can be accomplished either by electron beam lithography or by DUV photolithography. We concentrate on the latter because it is the one employed to fabricate all the devices used in this work. The fundamental steps are show in fig.3.4 .

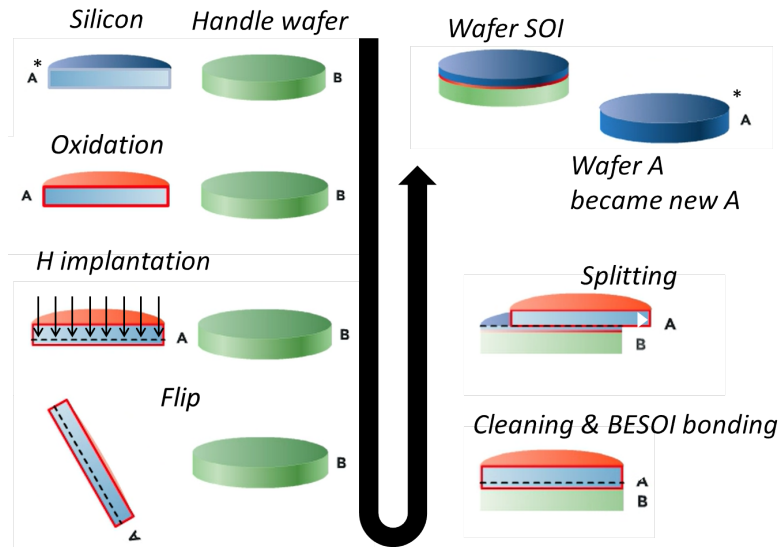


FIGURE 3.3: Smart cut process workflow.

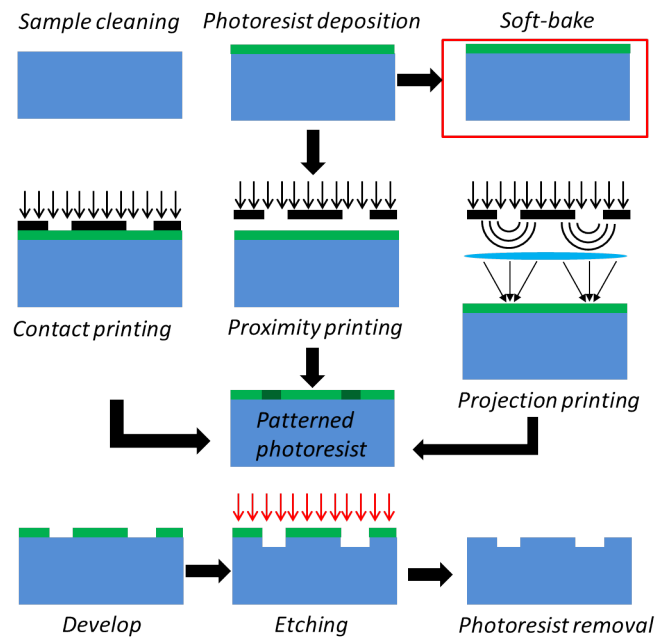


FIGURE 3.4: Lithography workflow.

1. *Sample cleaning:* the sample has to be properly cleaned by hydrogen peroxide solutions in order to ensure a subsequent uniform photoresist deposition (step 2) and to remove scattering centers.
2. *Photoresist deposition:* the photoresist is a special polymer that alters its chemical and physical properties when it is illuminated by light of a well defined spectral window (in case of DUV photolithography, UV light). Positive photoresists become solubles in developing substances when exposed to light, while negative photoresists become insolubles when this happens. The most common kind of photoresist used in DUV photolithography is *Phenol formaldehyde resin (DNQ/Novolac)*. Photoresist is poured on the centre of the wafer surface and spread by rotation of the holder, exactly as it happens in a centrifuge. The spin coating typically runs at 1200 to 4800 rpm for 30 to 60 seconds, and produces a layer between 0.5 and 2.5 micrometres thick. The spin coating process results in an uniform thin layer, usually with uniformity to within 5-10 nanometres.
3. *Soft pre-baking:* a thermal annealing at $90 - 100^{\circ}C$ for 30-60 seconds fixes the photoresist, contributes to get more a uniform surface and evaporates any excess.
4. *Exposition:* photoresist is selectively illuminated by light that passes through an optical mask which contains the photonic circuit pattern. Transparencies are obtained by laser etching of a chrome layer which is sputtered on a molten quartz thin plate. Different printing possibilities exist: contact, proximity and projection. In contact printing, mask is directly placed in contact with the wafer and covers the whole surface, this allows a good resolution and makes the process fast and low cost, but can easily damage the surface and a strong uniform illumination is needed. In proximity printing the mask is placed at a small distance from the wafer, so surface is not damaged but resolution is smaller because of diffraction effects [171]. In projection printing a focusing optical system is placed between the mask and the wafer and only a small portion of the surface is covered, so a smaller mask is needed. The whole wafer is printed by repeatedly mechanically moving in discrete steps the mask and the illumination system, these printers are called steppers and the repetition units are called *dies*. Projection printing offers many advantages with respect to the previous two: illumination must be uniform over a smaller area, focusing lenses allow to reduce the image size and then potential errors in the mask pattern, the latter is not placed in direct contact with the surface. These improvements are at the expense of higher costs and a globally slower process. Resolution limit is dictated essentially by diffraction and the quality of the optical systems, current state of art DUV projection printing uses $193nm$ DUV light produced by Argon Fluoride excimer lasers and water

immersion optical lenses, which enable to obtain resolutions down to $50nm$ [172]. Fig.3.5 shows how the image of a narrow slit changes with the printing method, tails of the intensity distribution are of great importance because combined with different exposure doses allows to continuously change the structure sizes to be subsequently etched, this concept will be further discussed later. The exposure dose is the amount of energy absorbed by the resist per unit area ($\frac{mJ}{cm^2}$) and it's a crucial parameter because it determines the removed thickness in the developing stage (step 5). From now on, we refer only to positive photoresists, because the same concepts are also valid for negative resists, where illuminated portions have to be exchanged with the not illuminated ones. With reference to fig.3.6, we note that below a threshold value E_o (dose D_0 in fig.3.7) no photoresist will be removed, while for doses over E_1 (dose D_{100} in fig.3.7, also called critical dose D_{CR}) the whole thickness is developed.

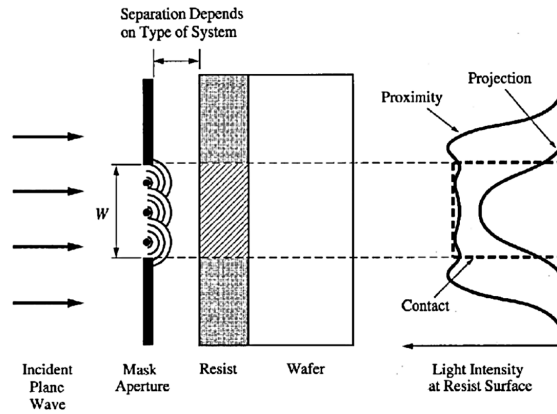


FIGURE 3.5: Different light intensity distribution of a narrow slit in the mask: contact and proximity printing corresponds to Fresnel diffraction patterns while projection printing to Fraunhofer ones [170].

When we shine a slit using two different exposure times t_1 and t_2 with $t_1 < t_2$, the per cent critical dose $D_{CR}^{\%}$ defined as the ratio between the critical and the maximum dose D_{MAX} at the center of the image will be higher in the first case with respect to the second because $D_{MAX1} < D_{MAX2}$:

$$D_{CR1}^{\%} = \frac{D_{CR}}{D_{MAX1}} > D_{CR2}^{\%} = \frac{D_{CR}}{D_{MAX2}}$$

this means that by increasing the exposure time the size of the removed photoresist will also increase because image tails progressively get a sufficient dose to completely remove the resist (see fig. 3.7). If two neighboring slits are used to print a strip waveguide, higher exposure doses will decrease its size. This can be useful to get a continuously range of widths without changing the mask pattern.

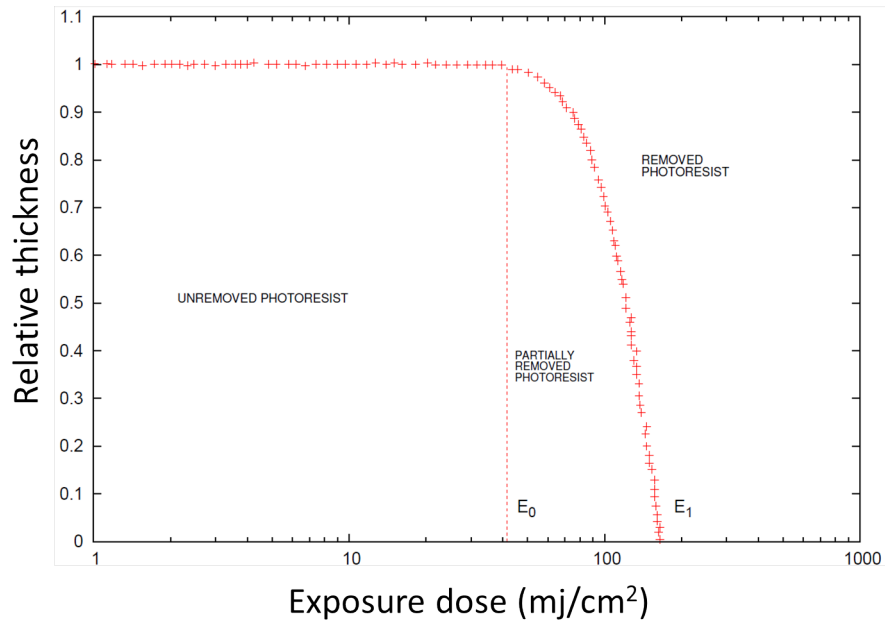


FIGURE 3.6: Example of characteristic curve of relative photoresist thickness removal vs exposure dose, also known as Hurter-Driffield curve [62].

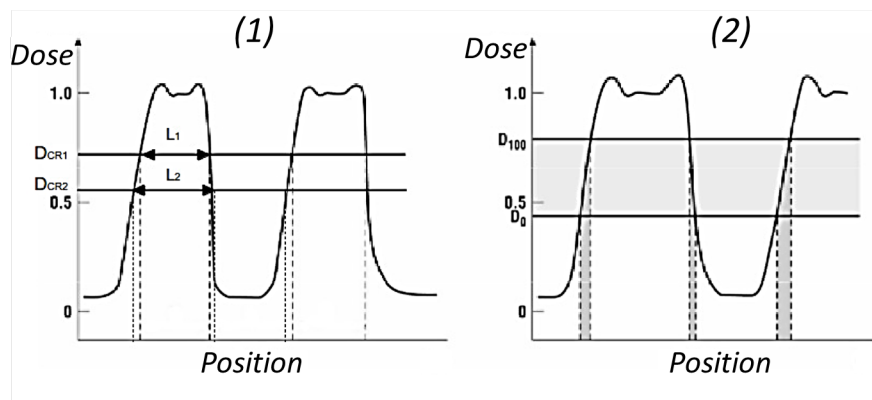


FIGURE 3.7: Percentual exposure doses vs position on the sample of a two slit system, which can be used to realize a strip waveguide. (1) Higher exposure times (corresponding to a lower percentual critical dose $D_{CR2}^{\%}$) allow to completely develop more photoresist with respect to lower ones (corresponding to an higher critical dose $D_{CR1}^{\%}$). (2) Exposure doses between D_{100} and D_0 will only partially develop the photoresist, creating structures with not well defined boundaries. [170].

5. *Developing stage*: Photoresist's portions that have absorbed doses over D_{CR} are completely removed by wafer immersion in a solvent, which in general can be $NaOH$ or *Tetramethylammonium Hydroxide (TMAH)* . Sodium hydroxide has the drawback that residual ionic impurities could persist in the final structure, these may give rise to ionic conduction that can constitute a problem especially in microelectronic .
6. *Hard bake*: a thermal annealing between $120 - 180^{\circ}C$ for 20-30 minutes removes residual traces of solvent and hardens the photoresist.
7. *Etching stage*: this stage removes photoresist's uncoated portions of the silicon overlayer creating the grooves for the photonic structures, usually by dry plasma etching. Dry etching is preferred to wet etching because allows a more anisotropic material removal, which is of fundamental importance in fabricating structures with sharp edges as the silicon photonics ones. Plasma etching details are beyond the scope of this chapter, interested readers can refer to specialized books.
8. *Photoresist's removal*: the remaining resist is removed from the surface by using proper solvents.

3.3.1 Metal wires as thermal heaters

The lithography process allows to deposit metal layer as another lithography step through physical vapour deposition (PVD). Some of the sample tested in this work, were fabricated with a thin metal layer $100nm$ above the top silica cladding. The metal stack is composed of $Ti(30nm) + TiN(60nm) + AlCu(440nm) + Ti(10nm) + TiN(40nm)$. A silica layer is deposited first, then etched in places where contacting is needed. The metal stack is then deposited and etched down to the silica layer. The metal wires are used as local heaters to change the local index through the *thermo-optic-effect*. An example of a built device with above the metal wires is shown in figure 3.8

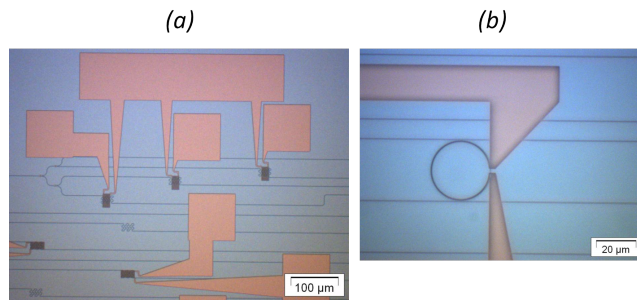


FIGURE 3.8: Example of metal wires (orange stripes) above the optical layer: (a) Square contact pads, (b) "omega" heater above a RR.

3.4 Fabricated wafer

The tested devices were fabricated at CEA-LETI laboratories in France [47], using a 8 inch SOI wafer fabricated by SOITEC through smart-cut process [173]. The fabrication parameters are: SOI wafer of 200 mm diameter, with $1.52 - 2\mu\text{m}$ of BOX thickness, 220 nm of silicon overlayer and 745 nm thick SiO_2 top cladding. Photorepetition units (dies) have sizes $(6 \times 5)\text{mm}^2$ and each contains several structures printed with 193 nm DUV photolithography. Dies cover the whole surface of the wafer forming a matrix. They are realized with different exposures: each column in the matrix receives a different dose of radiation, sweeping from 15 mJ to 28 mJ with 0.3 mJ steps. In this way, we achieve a gradual change in parameters sizes (see sect.3.3). A photograph of one of the fabricated wafers, with dies and devices to scale, is shown in figure 3.9.

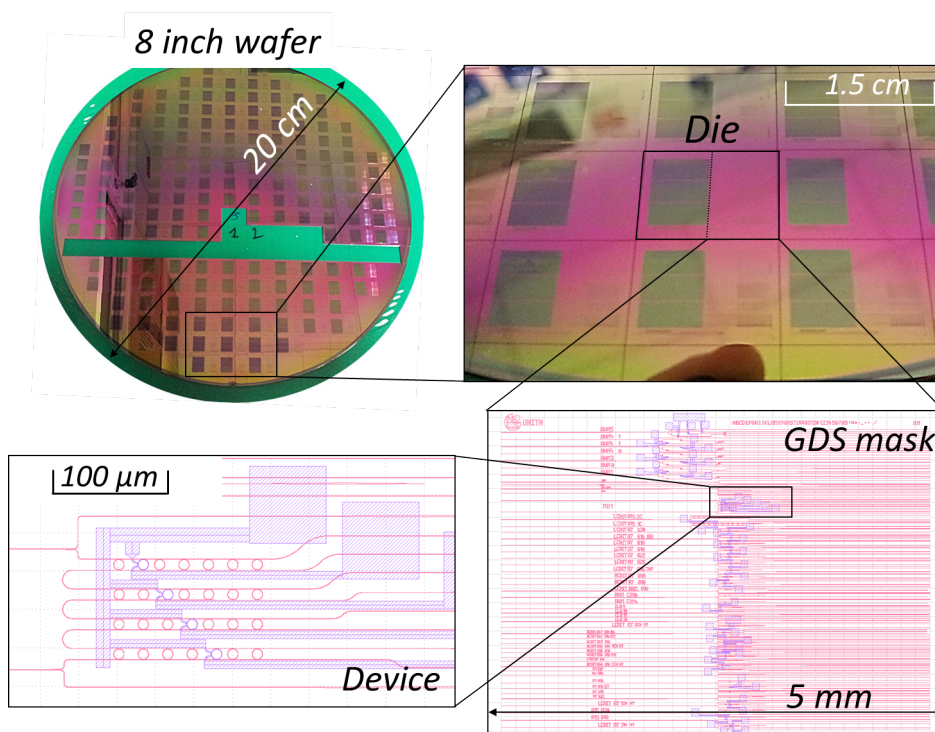


FIGURE 3.9: Photograph of the wafer and of the dies. Image of the GDS mask with a zoom on a device.

3.5 Global and local disorder on a SOI wafer

Traditional sources of geometrical disorder could be the grid resolution and photore-sist/etching imperfections. Lithography limits dictate that masks must be designed on a grid with a minimum pixel size of 5 nm [62], so every parameter will suffer deviations from the nominal values at least at the order of the pixel size. Photoresist's quality and deposition also play an important role. Indeed a non uniform layer deposition or

local imperfections combined with a low contrast material provide common sources of errors during the subsequent etching stage. The latter is still a rather rough process in creating grooves and boundaries between the photonic wires, so other fluctuations are unavoidably added. Tolerances of the order of $10nm$ are well accepted in microelectronic devices, but can strongly affect the performances of the photonic ones. This is due to the fact that most of them works with the interference of light of small wavelength (for SOI devices $1500 - 1600nm$), and interference effects are extremely sensitive to whatever can alter the light optical length. As a consequence, we expect that if we cover the whole surface of a wafer with a large number of nominally identical devices, everyone will show a different spectral response.

We divide the defects in 2 macro-categories:

- *Global disorder*: long range deviations of the structural parameters from the nominal values. These involve each wafer die. This kind of disorder manifests as small fluctuation of the effective index on the same die. The causes might be associated to the non uniform thickness of the BOX and of the silicon overlayer over whole wafer, that are crucial parameters in determining the effective index; core and cladding thickness are indeed given from the factory with standard deviations of $10nm$ and $25nm$ respectively. Variations could arise from a non uniform photoresist deposition or irregular oxygen ion implantation in the BOX, but also from non uniform oxygen thermal deposition on the silicon overlayer. All these fabrication steps process at slow rates, so fluctuations can be considered local but not random, a smooth sine like profile is expected.
- *Local disorder*: inter-die parameter fluctuations. Their origin is inherent in the finite precision of every lithographic production step: from sample cleaning at the beginning to photoresist removal at the end. Despite its effect generates structural variation of the order of $0.5 - 0.1\%$ ($\approx 5 - 10nm$), such variations are sufficient to modify, even heavily, the optical properties of a device. This topic will be studied in depth in the following chapters. Also this kind of defects depends on the position on the wafer: within the same die the dimension variation from a device to another is estimated to be of about $1nm$ while, within the wafer it grows to about $5nm$ and above.

Chapter 4

Side-coupled integrated spaced sequence of resonators (SCISSOR)

Complex photonic structures like CROW (coupled optical resonator waveguide) [174] and SCISSOR (side-coupled integrated spaced sequence of optical resonator) [174, 175] have been introduced to mold the light flow and to create slow light modes. Their strong dispersion allows engineering their optical properties by the coupling between waveguides and resonators, and by the number and spacings of resonators. In system like dual-channel (DC-) SCISSOR, there are two kinds of photonic bands, the resonator band (RB) and the Bragg band (BB) which satisfy independent resonance conditions [29]. The spectral positions of RB and BB are determined independently by the optical paths of the microring and their spacings, respectively. The two bands are coincident in the entire spectral response if the optical length of the side-coupled waveguide from center-to-center of adjacent rings is half that of a microring circumference (coherence condition) [26, 27]. But if their respective optical paths are slightly different (out of coherence), then the two bands occur at different resonance wavelengths. Due to index dispersion, they may be nearly coincident for few bands but tend to separate with either increase or decrease in their band-orders. However, if these two bands are in close proximity to each other (or coincident) and the single resonators have slightly different resonances, then one can expect sharp spectral resonance peaks (dips) in the through (drop) port signals which have similarities to the optical-analog of electromagnetically induced transparency (EIT) or to the coupled resonator induced transparency (CRIT) phenomena [11, 176, 177, 178]. When the two bands shift further apart, (lack of coherence) the CRIT resonances turn into localized states. These modes show unique spectral features and have the character of Fano resonances [179, 180, 181, 182]. They are more evident when the BB and RB are

well separated. As it will be shown in the following, these kinds of disorder can affect significantly the drop port transmission, featuring localized photonic states in RB.

The discovery of these localized modes means that even nanometre scale imperfections on the final geometry, introduced during the CMOS fabrication process, can completely compromise the correct functioning of the device. This dictates limitations of the reproducibility and of the reliability of high phase sensitive structures for DWDM applications. Since an high process yield is required, it is of great interest to have a method that allows to quantify the degree of structural disorder in a silicon photonics wafer in a very fast and accurate manner. Examples of current available techniques are ellipsometry and Critical Dimension - Scanning Electron Microscopy [183]. In the last part of this chapter, we propose a pure optical approach based on the use of the SCISSOR geometry in the Silicon On Insulator (SOI) substrate. The basic idea is that we can get information about the state of disorder by analyzing how it alters the spectral response of the device. It is designed to input and collect light by means of grating couplers, allowing to perform test experiments directly on the wafer without requiring further optical components except a broadband source and a detector.

The chapter is divided as follows: the first part describes the "ideal" SCISSOR structure both theoretically and experimentally. The second part focus on the discovery of the localized state in a SCISSOR and introduces to the theory of the *coupled resonator induced transparency*. The local nature of these states is demonstrated through a local optical tuning of the single cavity. In the last part, the reliability of the localized states as defect markers is experimentally demonstrated. Subsequently, the design of the test device is reported and its working principle is verified through simulations.

4.1 Some hints on the SCISSOR theory

In this section we are going to investigate the spectral response of a DC-SCISSOR device both theoretically and experimentally. The single channel (SC-) SCISSOR, in which different resonators are coupled to a single WG, is not being treated theoretically since, its transfer function is obtained by multiplying N times the transfer function of the single APF. From now on we let drop the prefix DC-SCISSOR using only SCISSOR. A SCISSOR is composed by N resonators (RR or RTR) indirectly coupled through the two WGs (Fig. 4.1).

A way to simulate the spectral response of such device is to use the TMM method as introduced in section 2.9.1. The derivation of the SCISSOR T and D response is straightforward: firstly we introduce a new matrix P_L^N to propagate the fields between

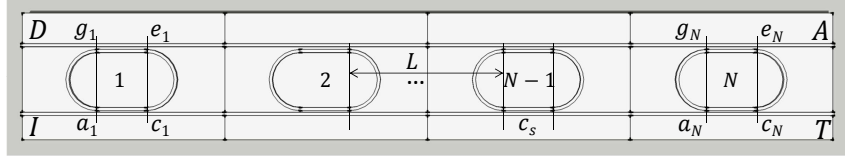


FIGURE 4.1: Sketch of a SCISSOR device composed of N resonator (RTR): L is the intra resonator distance.

the $(N - 1) - th$ and $N - th$ resonators.

$$\begin{pmatrix} a_N \\ g_N \end{pmatrix} = \begin{pmatrix} e^{-i\pi L\beta_s} & 0 \\ 0 & e^{i\pi L\beta_s} \end{pmatrix} \begin{pmatrix} c_{N-1} \\ e_{N-1} \end{pmatrix} \equiv P_L^N \begin{pmatrix} c_{N-1} \\ e_{N-1} \end{pmatrix} \quad (4.1)$$

where L is the distance between two resonators (see Fig. 4.1) and β_s is the propagation constant of the straight WG. The N suffix on the matrix symbols means that all the resonators could have different parameters. Now, using the matrix M^N (see eq. 2.44) that describes the in-out fields of the $N - th$ resonator we can write the total matrix S :

$$\begin{pmatrix} a_N \\ g_N \end{pmatrix} = M^N P_L^N M^{N-1} \dots P_L^1 M^1 \begin{pmatrix} c_{N-1} \\ e_{N-1} \end{pmatrix} \equiv S \begin{pmatrix} c_{N-1} \\ e_{N-1} \end{pmatrix} \quad (4.2)$$

To find the spectral response of the T and D ports of the SCISSOR it is sufficient to calculate the following ratios considering $e_N = 0$.

$$D = \left| \frac{g_1}{a_1} \right|^2 = \left| -\frac{s_{21}}{s_{22}} \right|^2 \quad T = \left| \frac{c_N}{a_1} \right|^2 = \left| -\frac{Det(S)}{s_{22}} \right|^2 \quad (4.3)$$

In the following, we are going to apply the code just derived to describe the optical properties of the SCISSOR and substantiate the experimental measurements.

We consider an ideal SCISSOR where all the resonators and their distances are identical. The first thing to be noted, when looking at figure 4.1, is its periodicity: each block is repeated after a distance L . In fact, the SCISSOR has, along the resonators band (RB), the so-called Bragg band (BB) generated by the DBR structure [27, 184]. Thus, the spectral positions of RB and BB are determined independently by the optical paths of the microresonator and their spacings, respectively. The two bands are coincident in the entire spectral response if the optical length of the side-coupled waveguide from center-to-center of adjacent rings is half of that of a microring circumference (coherence condition). But if their respective optical paths are different (out of coherence), then the two bands occur at different resonance wavelengths.

For the sake of simplicity, we are going to introduce the argument for a RR, and subsequently, the precise relation, valid also for the RTR, will be shown. The resonance

condition for RB is that the optical path in a RR is an integer multiple of wavelength ($m_R \lambda_R = 2\pi R n_{eff}^b$) with m_R the band order, λ_R the resonance wavelength, n_{eff}^b the effective index of the bent mode and R the radius of the RR. The resonance condition for BB is that the optical path in the waveguide between the center-to-center of two adjacent microrings is a half-integer multiples of wavelength, i.e. $m_B \frac{\lambda_B}{2} = L n_{eff}^s$ with m_B the band order, λ_B the Bragg band wavelength, n_{eff}^s the effective index of the straight mode, and L the separation between RRs. A first approximation is to consider $n_{eff}^s = n_{eff}^b$. This is commonly irrelevant for the final performances of a device but we will see that, for particular cases, is no more true. Under this assumption, for RB and BB to be coincident over an entire spectral range with $m_R = m_B$ requires $\lambda_R = \lambda_B$ thus $L = \pi R$.

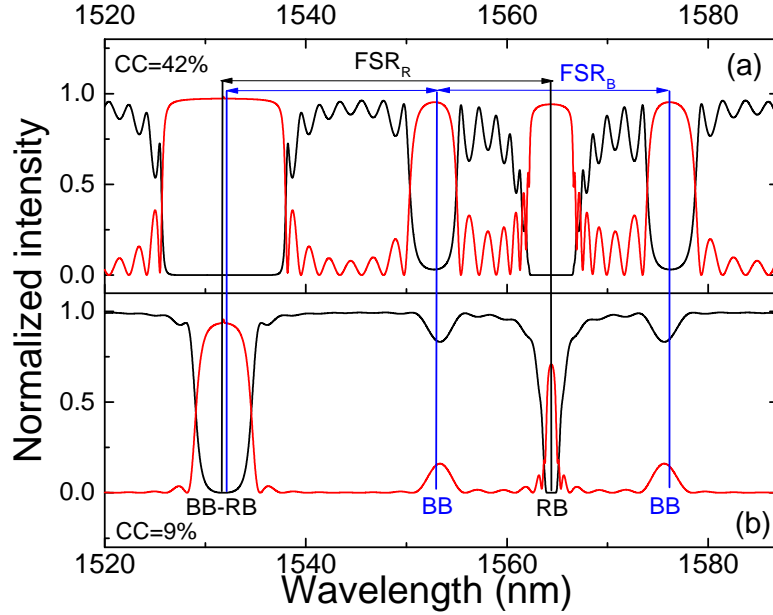


FIGURE 4.2: Simulated T (black) and D (Red) spectral response of a SCISSOR for two different values of CC, (a) 42% and (b) 9%. The blue (black) line identifies the Bragg band (resonator band). Simulation parameters: RR with, $R = 5\mu m$, $\frac{L}{\pi R} = \frac{m_B}{m_R} = 3/2$, $CC=9 - 42\%$ and $N = 8$; Ideal case with no dispersion.

Figure 4.2 shows the case of $\frac{L}{\pi R} = \frac{m_B}{m_R} = \frac{FSR_R}{FSR_B} = 3/2$ in which, the RB has a FSR greater than that of the BB. In this scenario, it is appreciated both the effect of the overlap of the two bands (blue and black lines) and the individual nature of the BB (blue line) and the RB (black line). The CC affects three main SCISSOR features. A greater CC leads to a greater spectrum ripple, larger stop band and higher extinction especially for the BB. The ripple problem can be limited by means of gap apodization (a sort of impedance matching) [26]. The overlap of BB-RB largely increases the total band width (more than doubled).

The general coherence length can be derived as follows. We write the equation for the RTR resonance and for the phase shifts of the resonator ϕ_R and the Bragg:

$$\lambda_m = n_{eff}(2c_s + 2\pi R)/m_R, \quad \phi_R = \frac{2\pi}{\lambda} n_{eff}\pi R, \quad \phi_B = \frac{2\pi}{\lambda} n_{eff}(\pi R + 2c_s + 2L) \quad (4.4)$$

In resonance condition, $\lambda = \lambda_m$, the following relation must be satisfied:

$$\phi_B - \phi_R = \frac{2\pi}{\lambda_m} n_{eff}(2c_s + 2L) = 2\pi n \quad n \geq 1 \text{ integer} \quad (4.5)$$

from which is derived

$$L = c_s \left(\frac{m_B}{m_R} - 1 \right) + \frac{m_B}{m_R} \pi R \quad (4.6)$$

What has been argued can be verified in the figure 4.3: when the difference between resonator phase shift (green path) and the bragg phase shift (red path) is a multiple of 2π the coherence condition is satisfied.

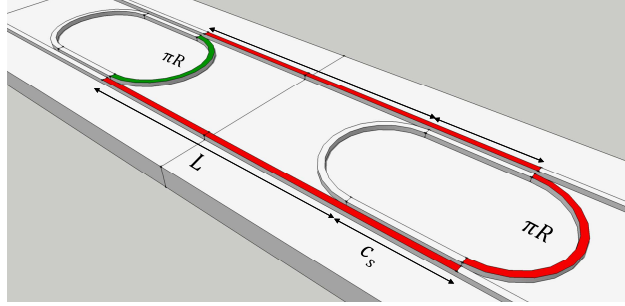


FIGURE 4.3: A sketch of the resonator phase shift (green path) and of the bragg phase shift (red path) for a RTR based SCISSOR.

It can be seen that, for $c_s = 0$, the band overlapping ($m_B = m_R$) is provided by the relation $L = \pi R$. The RTR preserves the former relation only for the case of $m_B = m_R$, otherwise it is necessary to use the full equation. For example, the case of $m_B/m_R = 3/2$ gives $L = c_s/3 + 3/2\pi R$.

4.2 SCISSOR experimental characterization

4.2.1 Racetracks based SCISSOR

Experimental investigations were made to verify these effects. We fabricated, as introduced in section 3, several SCISSOR, based on RTR, with different N: 1, 2, 4, 8. The other parameters were unchanged: $R = 3.25 \mu m$, $C_s = 10 \mu m$, $Gap = 0.16 \mu m$ and $L = 10.21 \mu m$. The used setup is found in appendix B.0.5.

The number of resonator N greatly influences the optical properties of the SCISSOR. In particular, from N it depends:

- The band edge slope measured as dB/nm . A SCISSOR with a large N behaves as a *flat-box filter*.
- The band width.

Figure 4.4 shows the effect of cascading several racetracks in a SCISSOR configuration. For these SCISSOR, the signal is recorded in a wavelength region where the RB and the BB overlap ($L = \pi R$). The stop-band due to the resonator resonance develops to a "flat box" lineshape as the number of racetracks increases: the slope at the band edge increases from $\simeq 6 dB/nm$, for 1 racetrack, to about $53 dB/nm$, for 8 racetracks. At the same time, the spectral width of the stop-band increases from $2.8 nm$, for 1 racetrack, to $6.6 nm$, for 8 racetracks.

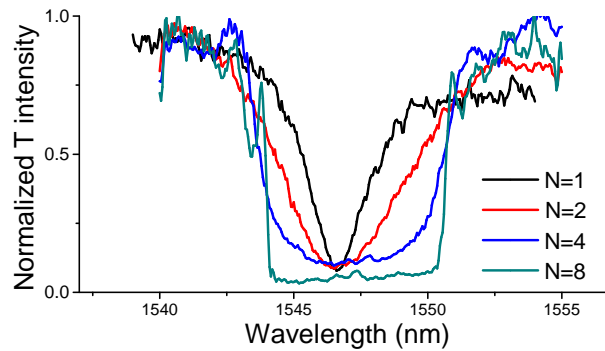


FIGURE 4.4: Transmission spectra of the through port for several SCISSOR composed of 1, 2, 4, 8 RTR. The RTR parameters are: $R = 3.25 \mu m$, $c_s = 10 \mu m$, $Gap = 0.16 \mu m$, $L = 10.21 \mu m$ and TE polarization.

Here we focus on the case of 8 RTR. Figure 4.5 shows the T and D port spectra, measured (black) and simulated (red) with the TMM code. The CC and dispersion were taken from the chapter 2. The simulation fits well the experiment but some little discrepancies were found:

- the gap used in the simulation is $180nm$ instead of $160nm$. This can be given by the fabrication tolerances, since such small gap is about at the limit of lithography accuracy (proximity effect).
- The spectra are not symmetric with respect to the band center. A possible explanation is the mismatch between the β_s and β_b that shifts the BB and the RB.
- The D port presents some features on the the pass band. The fabrication errors are here again involved. An in depth discussion of this phenomenon will be done in the following section.

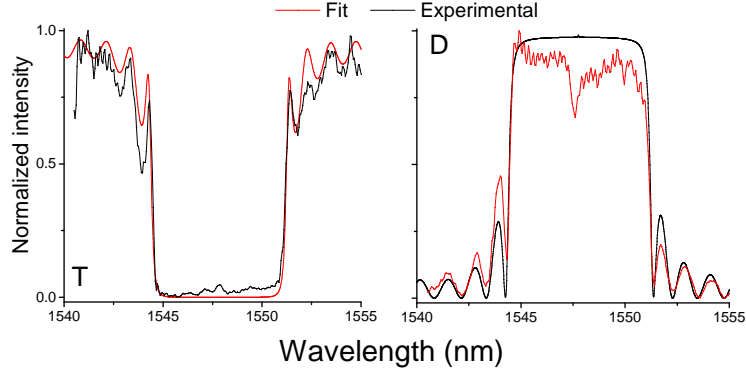


FIGURE 4.5: 8 RTR SCISSOR T and D port spectra: (black) experiment, (red) simulation. Simulation parameters: $R = 3.25 \mu\text{m}$, $c_s = 10 \mu\text{m}$, $\text{Gap} = 0.18 \mu\text{m}$ and $L = 10.21 \mu\text{m}$.

For completeness, we reports also the simulated behaviour of the group delay for the D port of the SCISSOR. Within the pass band of the SCISSOR the group delay is only

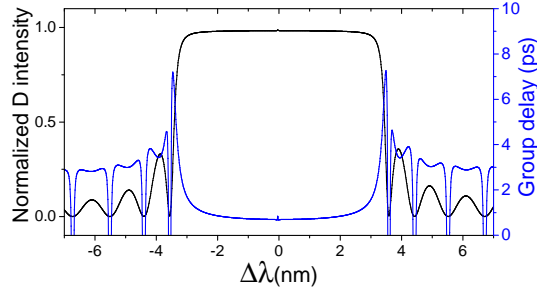


FIGURE 4.6: Simulated D port spectrum (black) and group delay (blu). Simulation parameters: $R = 3.25 \mu\text{m}$, $c_s = 10 \mu\text{m}$, $\text{Gap} = 0.18 \mu\text{m}$ and $L = 10.21 \mu\text{m}$.

0.7ps which is comparable (even lower) to that of an isolated resonator. Therefore, cascading multiple cavities, do not alter the global group delay of the pass band, except in the vicinity of the band edges: in the band edge the group delay reaches 8ps . A flat and low group delay is wanted in telecom applications as it allows the transmission of signals at high bit rate and low distortion. A group delay of approximately 0.7ps means a maximum bit rate of about 1THz .

4.2.2 Rings based SCISSOR

Here we are going to show an experimental proof of the existence of the two bands in a 8 RR SCISSOR device. The silicon wire dimensions for both rings and waveguides are 500nm wide and the used polarization is TM. The device parameters are: gap of 300nm that gives a CC of $9 - 20\%$, $R = 6.75\mu\text{m}$, $L = 22\mu\text{m}$.

The chosen values of L and R lead to a value of m_R/m_B equal to $\frac{\pi R}{L} = 0.96$. Since $L > \pi R$ we expect FSR_B to be greater than FSR_R at least by a factor of m_R/m_B . To

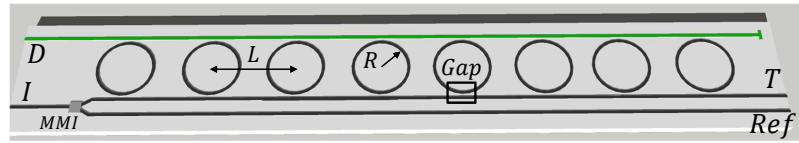


FIGURE 4.7: Sketch of the studied device. DC(SC)-SCISSOR with(without) the green WG. The port *Ref*, provided by an 1×2 MMI, is used to normalize the data.

highlight the RB and the BB we studied also the analogous SC-SCISSOR that, due to the absence of the feedback WG (Fig. 4.7 green WG), lacks of a BB.

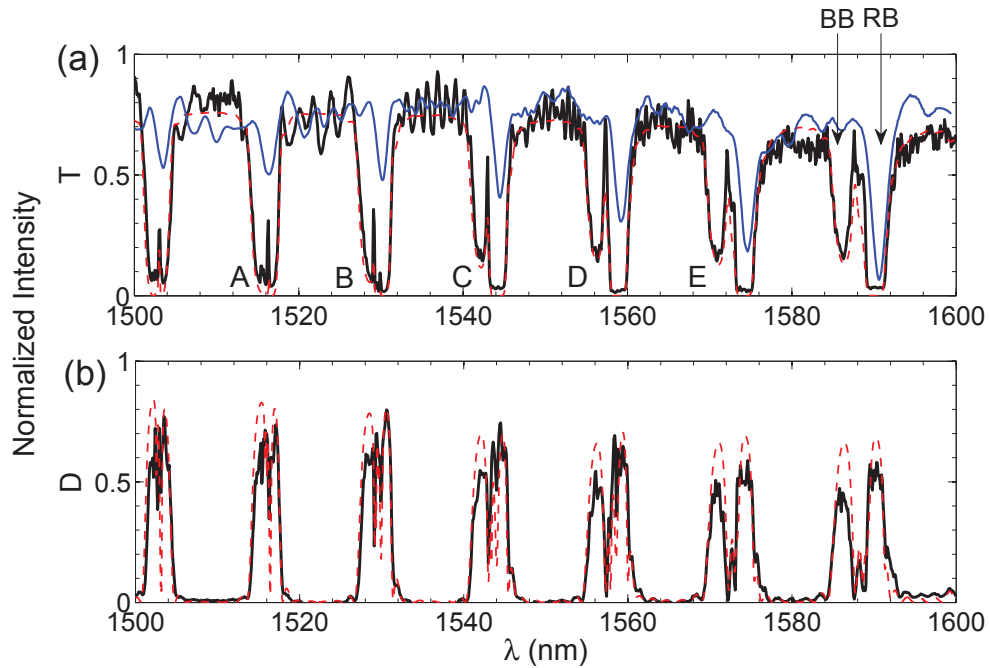


FIGURE 4.8: $1.5 \mu\text{m}$ to $1.6 \mu\text{m}$ spectrum of the T(a) and D(b) ports normalized to the *Ref* port of a (black) DC-SCISSOR, (blu) SC-SCISSOR. The dashed red lines are the simulated curves. [184]

The width of the resonance dip increases and the corresponding transmission value decreases, linearly, with the wavelength. This results from the increase in the coupling strength (CC) and resonator losses due to WG dispersion. The oscillations over the curve are due to Fabry-Perot resonances caused by reflections at input/output facets.

In the same Fig. 4.8, we show the transmission spectra of the through (Fig. 4.8(a), black line) and drop ports (Fig. 4.8(b), black line) of the DC-SCISSOR structure. Two distinct bands are observed due to the RB and BB. The comparison between the SC- and DC-SCISSOR transmission allows an easy identification of the RB, since they appear in both kinds of SCISSOR structures. In addition, the evolutionary features due to the BB are only observed for the DC-SCISSOR device. It is observed that the separation between the RB and BB increases with the wavelength. The RB, in the through port, have a flat band response with sharp roll-off edges (or box-like) and strong side lobes.

The BB lack such flat features and have weak side lobes as only few resonators are involved in creating the feedback. The transmission values related to RB vanish, while the transmission of BB does not. Thus BB need larger coupling constant and more resonators to vanish. It is worth to note that the RB and BB are nearly coincident or in close proximity in the wavelength range of $1500 - 1530nm$ as their respective resonance conditions are simultaneously satisfied. In this range, the spectra exhibit *narrow multiple spectral features*. At longer wavelengths, the RB and BB tend to move apart leading to an inhomogeneous broadening of the stop band in the through port signal and an appearance of well resolved multiple dips in the drop port signal. The top line of the transmission in the through and drop signal decreases with the wavelength due to an increase in modal loss, as it was observed in SC-SCISSOR. In Fig. 4.8 we have also reported the simulated transmission of the DC-SCISSOR in the through and drop ports (shown with red dashed line). A general good agreement is observed which substantiate the modelling and the interpretation of the results. The used simulation values are: CC is taken from the figure 2.16, n_{eff} is taken from the table 2.3 and the losses are $0.01 dB/90^\circ$.

Therefore, it is demonstrated the presence of two photonic bands, the BR and the BB, which derive from a global response of the system. In a SCISSOR there is, however, yet another spectral characteristic, that derives from the local response of the structure. The above-mentioned narrow peaks, that are visible in the figure, substantiate this claim. These spectral characteristics are generated from the multiple *coupled resonators induced transparency* (CRIT) effect that appears within the SCISSOR photonic band when process errors are present [11].

Before proceeding into the details of the multiple CRIT effect, the effect in a simpler system composed of two coupled resonators is introduced in the next section.

4.3 Introduction to the *coupled resonators induced transparency effect*

The CRIT effect is an interference phenomenon that occurs for particular conditions. Unlike a CROW device, where it is enough to have a coupling between to equal modes to generate CRIT [185], in a SCISSOR is necessary to have slightly detuned resonances and a coherent feedback between them (eq. 4.6). Under these conditions, a transparency window opens inside the two resonances.

Firstly, a simplified model, based on the CMT, is used to find the eigen frequencies of a 2 resonator SCISSOR system. Secondly, the CRIT effect is experimentally demonstrated in a 2 RTR system.

4.3.1 Theoretical description

The system under study is the following:

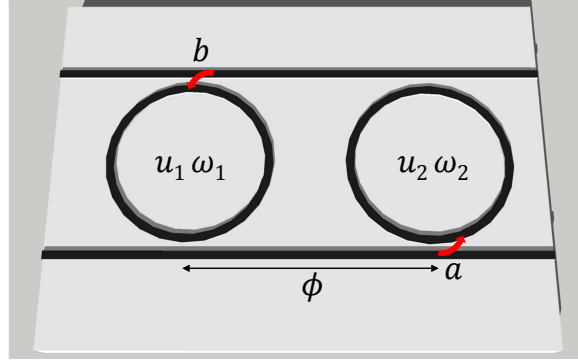


FIGURE 4.9: System under study.

The variables u_1 and u_2 are the field amplitude of the cavity, $\omega_{1,2}$ their resonance frequencies and ϕ is the phase relationship between them that sets the coherent condition. We approximate $\phi = i\beta_s L = \text{const}$ as frequency independent since we are working in the vicinity of a resonance, ie $\omega - \omega_{1,2} \ll \omega$. The variation of the parameter ϕ determines a dramatic change in the optical response of SCISSOR. This is one of the key points of the this work and one of the strengths of the SCISSOR. For the sake of simplicity, the cross coefficients $k_{1,2} = k$ are equal and small ($k \ll 1$) and the system is lossless, $\tau_0 = 0$

Using the CMT we write the equation for the two cavities as:

$$\frac{du_1}{dt} = (i\omega_1 - \frac{1}{\tau})u_1 - k_t^2 e^{-i\phi} u_2 \quad (4.7)$$

$$\frac{du_2}{dt} = (i\omega_2 - \frac{1}{\tau})u_2 - k_t^2 e^{-i\phi} u_1 \quad (4.8)$$

where k_t is related to the common k factor of the TMM through $k_t^2 = 2/\tau = k^2 v_g/p$ [186]. Notice as the two cavities are indirectly coupled through the phase factor ϕ . At this point we write the following matrix to calculates the eigenvalues Ω_{eig} :

$$\begin{pmatrix} 0 \\ 0 \end{pmatrix} = \begin{pmatrix} i(\omega - \Omega_{eig}) & -k_t^2 e^{-i\phi} u_2 \\ -k_t^2 e^{-i\phi} & (\omega - \Omega_{eig}) \end{pmatrix} \begin{pmatrix} u_1 \\ u_2 \end{pmatrix} \quad (4.9)$$

We define $\omega_{1,2} = \omega_c \mp \Delta\omega/2$ and the normalized frequency and decay rate as $\omega \rightarrow \frac{\omega}{v_g}p$, $k_t \rightarrow k$. The eigen frequencies are:

$$(1) \phi = \pi n \rightarrow \Omega_{eig} = ik^2 \mp \sqrt{-k^4 + \frac{\Delta\omega^2}{4}} + \omega_c$$

$$(2) \phi = \frac{\pi}{2}(2n + 1) \rightarrow \Omega_{eig} = ik^2 \mp \sqrt{k^4 + \frac{\Delta\omega^2}{4}} + \omega_c$$

with $n \geq 0$. We define the eigenfrequency as $\Omega_{eig} = \omega_{eig} + ik_{eig}$. The real part of the eigenfrequency ω_{eig} is related to the frequency of the eigen mode, while the imaginary part k_{eig} to the eigen mode lifetime.

Let's focus on the solution (1) $\phi = \pi n$, what we call *coherence condition* (ChC). In this case the determinant $\Delta = -k^2 + (\Delta\omega/2)^2$ assumes both real and imaginary solutions. All the possibilities are reported in figure 4.10 along with the spectrum of the most significant states. The normalized frequency used are valid for the third telecom window. $\Delta\omega$ is chosen by using $|\Delta\omega/\omega| = |\Delta\lambda/\lambda|$ and $\Delta\lambda$ 0.8nm, that is a typical value for this parameter (represent the spectral separation between the two resonances).

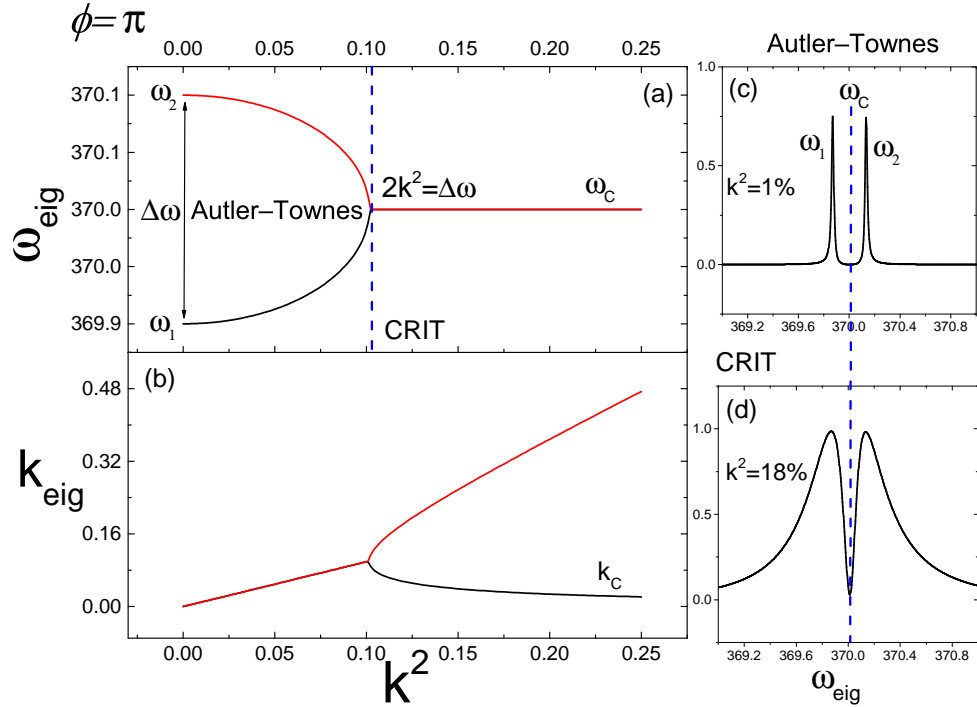


FIGURE 4.10: (a) Normalized real part of the eigen frequencies (red, black) as a function of k^2 . (b) Normalized imaginary part of the eigen frequencies (red, black) as a function of k^2 . (c) Transmission spectrum of the system for $k^2 = 0.01$: Autler-Townes doublet. (d) Transmission spectrum of the system for $k^2 = 0.18$: CRIT condition. Used parameter: $\phi = \pi$, $\omega_c = 370$, $\Delta\omega = 0.2$.

When the resonance separation is zero, the system is trivial and behaves as a single resonance with a doubled width $k_{eig}^2 = 2k^2$. But for a $\Delta\omega > 0$, two conditions arise, the state of CRIT and the state of doublet that are discriminated by the condition:

- for $\Delta\omega < 2k^2$: CRIT condition.
- for $\Delta\omega > 2k^2$: Autler-Townes like doublet.

The system is studied varying k . For a low coupling, the eigenfrequencies correspond to the resonance frequencies $\omega_{1,2}$ (whose spectrum is shown in figure 4.10(c)). The eigenfrequencies get close as k is increased until to the condition of CRIT (dashed blue line), where they become degenerate and assume the value ω_c (CRIT frequency). Conversely, k_{eig} increases linearly with k until the CRIT condition where there are two modes with a different decay rate that coexist. It's important to remark that one of the k_{eig} (whose spectrum is shown in figure 4.10(b)) (black line) decreases its decay rate as k gets larger until 0 (for a lossless system). In fact, in figure 4.10(d) there are two modes with the same frequency but a different width. The narrower one is the transparency peak associated to a lifetime of $\tau = 2/k_c^2$. Obviously, in a real system k_c has a minimum value that corresponds to the mode losses.

Summarizing, we write the conditions for CRIT creation:

- $\phi = \pi n$, coherence condition.
- $\Delta\omega \neq 0$, detuned resonances .
- $\Delta\omega < k^2$, a coupling greater than the resonances separations.

Let's focus on the solution (2) $\phi = \pi/2(3n + 1)$, what we call *out of ChC*.

In this case, Δ is always real, thus only ω_{eig} is affected by a k variation. The eigenfrequencies ω_{eig} remain separated and their separation increases with an increase of k (Fig. 4.11 (a)). The eigenmodes decay rates corresponds to that of the unloaded system $k_{eig}^2 = k^2$ (Fig. 4.11 (b)). An example of transmission spectrum is reported in figure (Fig. 4.11 (c)). For $\phi = \pi/2$, the lack of feedback between the cavities, prevents the transparency peak creation.

The used frequency parameters ω_c and $\Delta\omega$ correspond to a $\Delta\lambda = 0.8nm$, for a RR system with $p = 2\pi R$, $R = 7\mu m$ and $v_g = c/n_g$, $n_g = 4$ and $\lambda_C = 1536 nm$ (the CRIT wavelength, Fig. 4.10(c)).

Here we focus only on the region around λ_C . Through the TMM code, the transmission for the T and D port and the losses, defined as $1 - (T + D)$, as a function of the bent

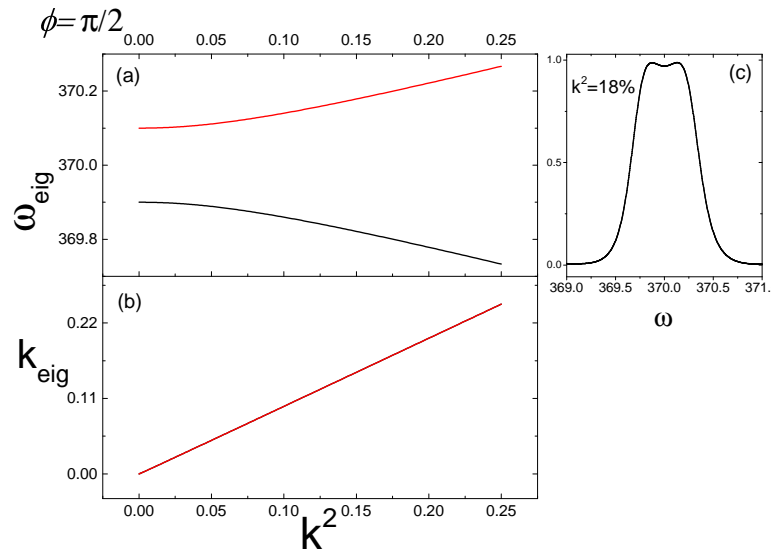


FIGURE 4.11: (a) Normalized real part of the eigen frequencies (red,black) as a function of k^2 . (b) Normalized imaginary part of the eigen frequencies (red,black) as a function of k^2 . (c) Transmission spectrum of the system for $k^2 = 0.18$. Used parameter: $\phi = \pi/2$, $\omega_c = 370$, $\Delta\omega = 0.2$.

losses (Fig. 4.12(a)) and of the phase (Fig. 4.12(b)) are calculated and reported in figure 4.12 . Note that the losses α are defined as:

$$\gamma = e^{-\alpha x} \quad \frac{1}{\tau_0} = \alpha v_g$$

where γ is the term used in the TMM theory and τ_0 is a lifetime linked to the losses used in the temporal CMT.

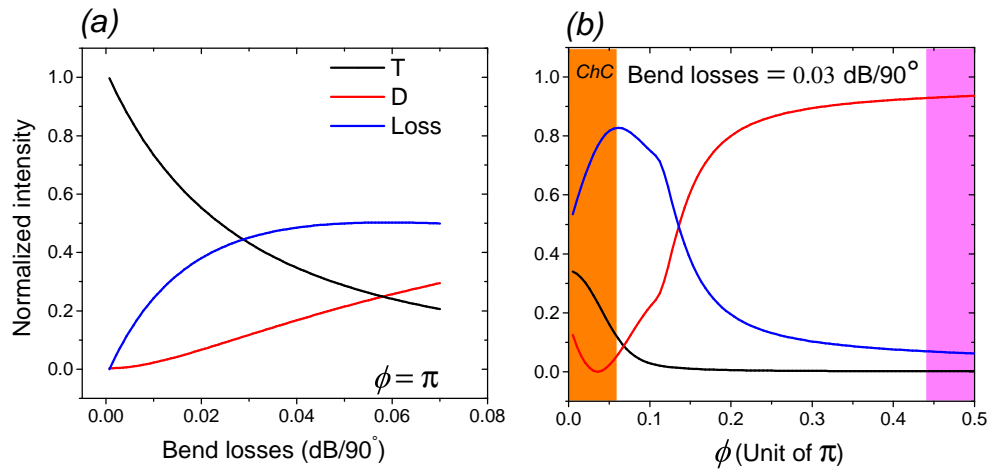


FIGURE 4.12: Simulated intensity at λ_C in the transmitted (black) and dropped (red) signal as a function of bending losses. Simulation parameters are the same as used for simulating the racetrack in figure 4.15. Simulation parameters: $\lambda_C = 1536 \text{ nm}$ and $\Delta\lambda = 0.8 \text{ nm}$, $k^2 = 0.4$

Despite the observed region is within the stop band, the transmission is high (black

line) for the ChC ($\phi = \pi$), especially for low losses (panel (a)). On the contrary, the drop signal (red line) is low. The transmitted signal is the most sensitive to the bend losses compared to the drop signal: this discrepancy means that the remaining signal has to be lost through scattering (blu line). Through the phase parameter is possible to control the formation of the transparency state, going, for example, from a $\phi = \pi$ to $\phi = \pi/2$ (Fig. 4.10 and 4.11). The panel (b) show how fast is this transition in term of transmitted (black line), drop (red line) and scattered signal (blu line). Initially, the system is in a transparency state (high transmission) identified by the orange region. As the system is moved to an out of ChC state ($\phi \rightarrow \pi/2$), pink region, the transparency disappear. The transmission is by far more sensible to this transition with respect to the drop signal. In fact, the presence of the localized state still remains in the dropped signal giving rise to a lossy state: there is no transmitted signal, no signal dropped but only scattered signal. We call this lossy state *localized state*. The lossy state can be verified by performing a spectrum of the D port of a SCISSOR in non-perfect ChC, as done in figure 4.14.

So we saw the conditions for the creation of CRIT and the great influence that the phase of the feed-back has on it. In particular, a switch of the CRIT can be obtained with a variation of phase from π to $\pi/2$. Moreover, a lossy localized state appears for a $\phi \sim 0.1\pi$ in the presence of cavity losses $\tau_0 \neq 0$.

All the calculations are also valid for an RTR assuming the use of the right ChC described by the equation 4.6.

4.3.2 Experimental investigation

To investigate the CRIT effect in a SCISSOR we have designed the device in figure 4.13. It is based on two RTR that differ for their radius by a quantity of $\Delta R = 5nm$. Thus, one of the conditions for the CRIT is satisfied. A $\Delta R = 5nm$ corresponds to a $\Delta\lambda = 0.8nm \rightarrow \Delta\omega = 0.18$, calculated using the RTR perimeter and a group index of 4.1 (extracted from the table in 2.3). Since we have roughly a $CC(k^2)$ of 40% (extracted from the table in 2.6), the condition of $\Delta\omega < 2k^2$ is also satisfied.

The ChC was derived with eq. 4.4 using the approximation of $n_{eff}^b = n_{eff}^s$. We fabricate several samples with different L (from $10.100\mu m$ to $10.300\mu m$ with a step of $5nm$) in order to find which L gives the best ChC, defined as the L that maximizes the CRIT transmission and the spectrum symmetry. The coherence length L_c for this system is:

$$L_c = \left(R + \frac{\Delta R}{2}\right)\pi = 10.218\mu m$$

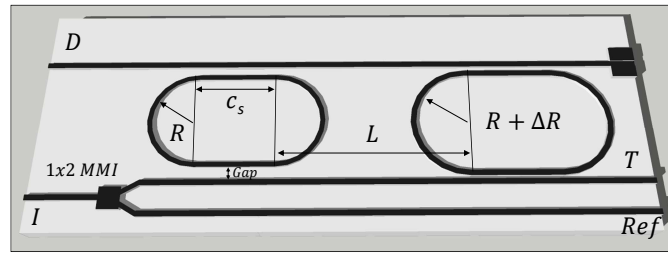


FIGURE 4.13: Schema of the studied device. The size difference of the RTR is exaggerated. Device parameters: $R = 3.25\mu\text{m}$, $c_s = 10\mu\text{m}$, $\text{gap} = 180\text{nm}$, $\Delta R = 5\text{nm}$ and $L = 10.16, 10.21, 10.26\mu\text{m}$. TE polarization.

The measurements reported in figure 4.14 are taken using the setup described in appendix B.0.5.

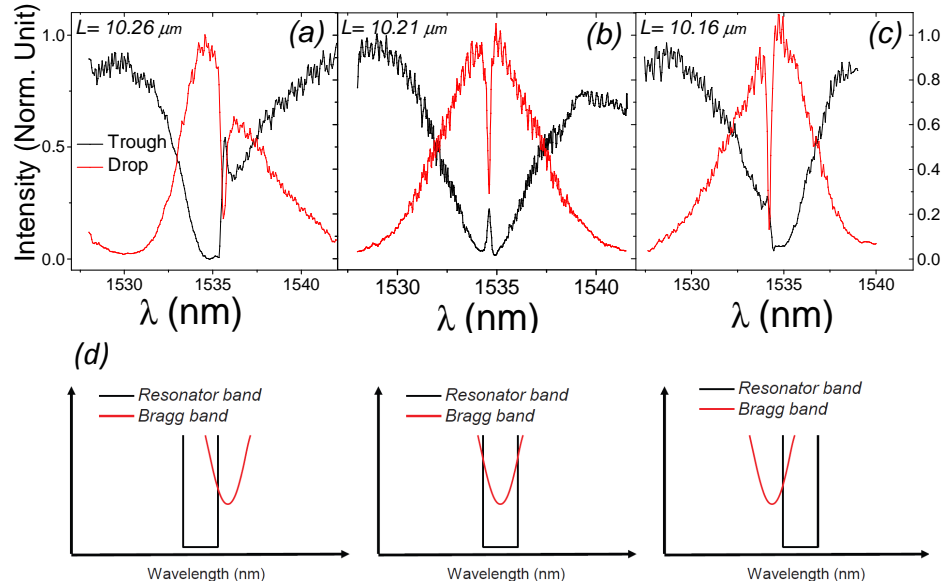


FIGURE 4.14: Transmission spectra of the through (black line) and drop (red line) ports for several L : (a) $10.26\mu\text{m}$, (b) $10.21\mu\text{m}$ and (c) $10.16\mu\text{m}$. (d) Schematic representation of the position of the BB and RB that refers to the graphs above.

When $L = 10.21\mu\text{m}$, the BB and RB overlap and CRIT appears as a sharp feature in the stop band (Fig. 4.13(b)). Under these conditions, both through and drop ports show a CRIT features with a transmission of 0.23. When $L = 10.26\mu\text{m}$ the BB is red shifted with respect to the RB (Fig. 4.13(c)) while when $L_c = 10.16\mu\text{m}$ the Bragg resonance is blue shifted with respect to the resonator resonance (Fig. 4.13(a)). The through resonance signal is strongly deformed and an asymmetric stop band is observed. Under these conditions the CRIT behaves as lossy localized state. It is also worth noticing that in Fig. 4.13(a)(c) the Bragg resonance is less deep than the resonator resonance because

of the few number of RTR in the SCISSOR. From the measurements, results that the best L is $L = 10.210\mu m$. The discrepancy between the expected and measured L to observe CRIT, is of the order of the 0.07%. Such small variation could be due to both fabrication defects and to the bend-straight index mismatch.

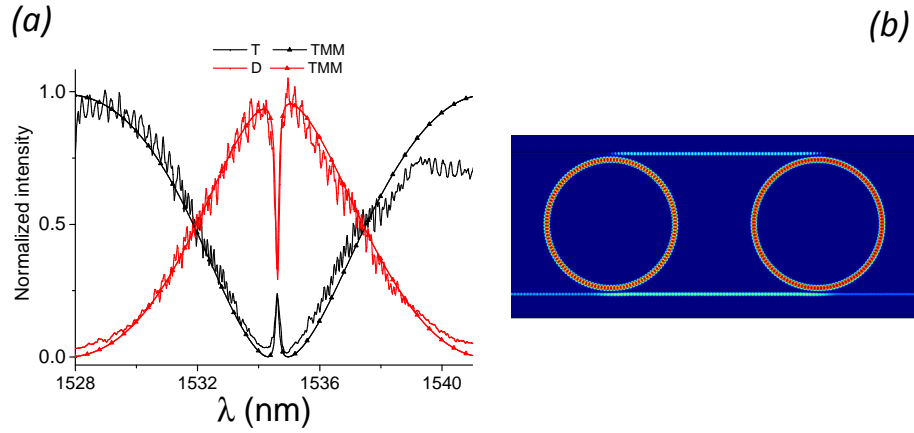


FIGURE 4.15: (a) Transmission spectra of the T and D ports: (black line, red line) measured data, (black, red triangles) simulated data. Simulation parameters: $CC = 40\%$, losses $0.045dB/90^\circ$ and $L = 10.216\mu m$. (b) FEM simulated field distribution for a system of 2 RR in the transparency condition, $\lambda = \lambda_c$.

The fact that the linewidth of the CRIT mode is narrower than the single isolated cavity is evident. The measured Q of the isolated RTR (see Fig. 4.4) is about 500 while the CRIT in figure (b) has a Q of 11000. Such high Q factor makes the CRIT very sensible to any cavity losses (see Fig. 4.12). This is not only a disadvantage since this feature allows a good estimate of the losses by fitting the peak of CRIT with the TMM code. By fitting the data with the TMM code we extract a bend losses of $0.045dB/90^\circ$ and an L_c of $10.216\mu m$.

The phenomenological behaviour of CRIT can be understood by looking at the top scattering of the system. The simulated field distribution of a 2 RR SCISSOR, for a probe wavelength centered at λ_c , is reported in figure 4.15(b). It is clear that the effective cavity involved in the process is composed by the two RR plus the WGs in between. The two RR act as a mirrors that traps the light between them. This "light trap" finds place in slow light applications because of its group delay and geometry [84, 85].

On the contrary with what it happens an APF, an increase of the CC leads to an increase of the group delay in the CRIT resonance.

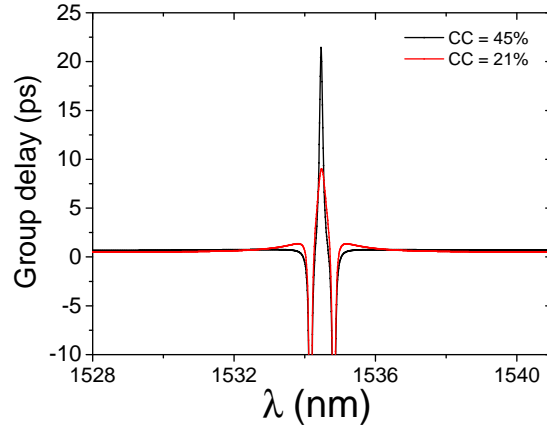


FIGURE 4.16: Simulated group delay of the structure in figure 4.15 for two values of coupling coefficient, 45% (black) and 21% (red).

4.4 Localized states in a SCISSOR structure

In chapter 3, it was introduced the technique of optical Lithography. The series of processes involved in this technique have a limited accuracy. This limit is found in the fabricated devices as process errors, that is, the real device dimensions differ from the nominal ones. Since integrated photonic devices have typical footprint of a few microns, the relative error induced by the defects is approximately 0.1%. As anticipated in section 4.2.2, the presence of these defects in SCISSOR manifests itself with CRIT resonances. In fact the effect of the errors is to induce a $\Delta\omega$ through the variation of the optical paths of the resonator. Errors of about $5nm$, as seen in the preceding section, are enough to generate this phenomenon.

First, the local nature of the CRIT resonances will be proved. Afterwards, the relation of the CRIT phenomena with manufacturing defects will be highlighted.

4.4.1 Localized states in a SCISSOR structure

Let us start from the 8 RR SCISSOR characterization 4.2.2. We know that one of the CRIT feature is the narrow line width, thus in order to resolve these resonances, a fine spectral measure is performed (tunable laser step of $0.02nm$).

We measured the resonances labelled ‘A’, ‘B’, ‘C’, ‘D’ and ‘E’ in Fig. 4.8 (a) with higher resolution (wavelength step of $0.02nm$). The results are shown in Fig. 4.17.

Each row represents results of one particular resonance band. We have also reported in the third column the spectra of out-of-plane scattered light. In the band ‘A’, we notice multiple resonance peaks(dips) in the T(D) port signal which are closely related to

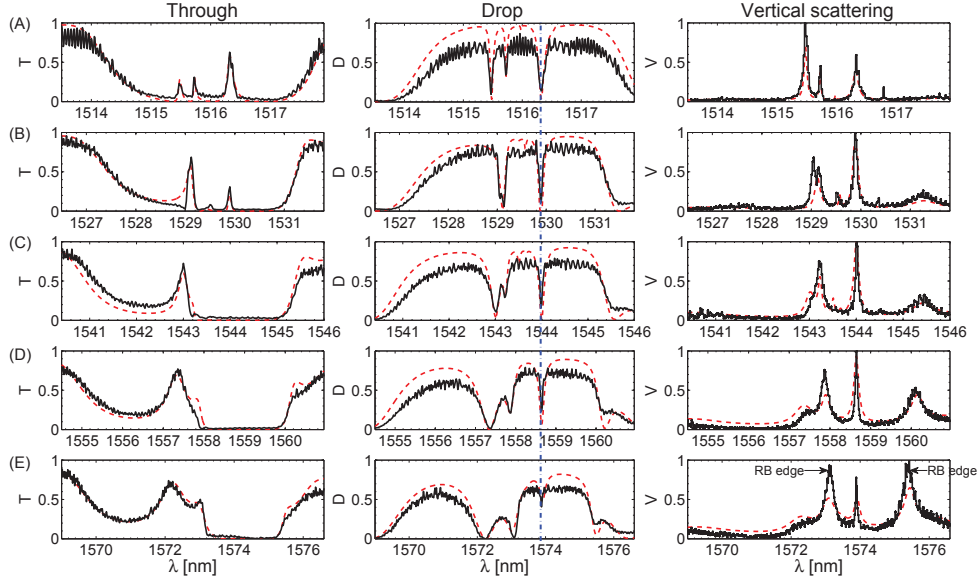


FIGURE 4.17: Fine resolution spectra of bands ‘A’, ‘B’, ‘C’, ‘D’ and ‘E’ (for labels refer to Fig. 4.8). Panels in columns 1, 2, and 3 represent transmission signals in through (T), drop (D) ports and out-of-plane scattering (V, spatially integrated), respectively. Black (solid) and red (dashed) curves are experimental and simulation results, respectively. The vertical scattering spectra are normalized to the maximum value while the simulation data are obtained by using the relation $(1 - |T| - |D|)$. Hence their comparison is only qualitative. [33]

multiple-CRIT as recently discussed in chains of resonators [187] and also demonstrated experimentally in photonic crystals [178]. We interpret them as CRIT since we observed signatures of the resonances both in the drop as well as in the through port signals. In particular, the appearance of resonance peaks in the through port signal substantiates the CRIT name. This spectral feature becomes more evident in the vertical scattering spectrum. In fact, we observe very intense peaks at the same wavelengths of the CRIT resonances as those observed in the through/drop port signals. As these peaks are also a signature of propagating modes with large group index (n_g), i.e. slow light modes, the signal in the through/drop port will be affected by large scattering losses. The top scattering spectrum is very sensitive to slow modes, indeed, we are also able to observe some peaks which are not resolved, or have very small amplitude, in the through/drop transmission.

It is known that slow modes occur also at the band-edges of a RB (as shown in Fig. 4.6). Indeed, we also have scattering bands with strong and broad features near RB edges and very weak feature around BB edges. In the drop port, the sharp and narrow spectral dip (see Fig. 4.17 marked with blue dash-dot line) in RB is caused by the defects in the radius of the RR leading to localized modes. The Q-factors (calculated with the drop port signals) of these modes are $Q \approx 16000, 19500, 23000, 23600, 37000$, for panels ‘A’, ‘B’, ‘C’, ‘D’, ‘E’ bands, respectively. At the corresponding wavelengths, in

TABLE 4.1: Ring radius error distribution used in the simulation. The radius error is define as $R_{eff} = R + \Delta R$ The value $R = 6.75\mu m$ is used in the simulations.

Ring number	1	2	3	4	5	6	7	8
ΔR (nm)	6.2	6.1	2.0	6	0.5	0.0	5.0	4.0

the transmission of the T port we observed a transparency peak in the stop bands of ‘A’ that progressively disappears in the the other panels. This is due to the fact that the BB and RB are overlapped only in the panel A. Their overlap indicates that the difference in phase shift induced by the two bands is a multiple of π (in this case is precisely π since $m_B \sim m_R$) i.e., the ChC is achieved. As the bands start to separate, the ChC is no more satisfied and the CRIT contrast decreases. When the separation is enough to induce a phase relation of 0.1π the CRIT state becomes a localized state (Panel (C)) . This is the exact behaviour found in the system of 2 coupled cavity and it is confirmed by this experiment (Fig. 4.12). As the separation increases the system goes to the condition of $\phi = \pi/2$ where no more localized states are allowed (panel (D)).

Simulations confirm this interpretation. In fact, red lines in figure 4.17, which were computed with the ring parameters reported in table 4.1, match almost perfectly the experimental data. Note that the nanometer scale variation in the ring radii is aligned with what said at the begin of the section.

To distinguish between bandedge and localized modes, we looked at the spatial intensity distribution of these modes by recording the wavelength resolved out-of-plane scattered images. Fig.4.18 shows IR camera snapshots at resonances and bandedges as indicated by arrows in the associated drop port/scattering spectra of band labelled ‘D’.

The snapshot of scattered light at RB bandedge (at longer wavelength, in Fig. 4.18(c)), shows that the light is distributed and scattered among all 8 rings of the SCISSOR structure.

On the contrary, at the localized wavelengths (a,b) (see Fig. 4.18) the mode is localized and scatters from only few RRs: for the localized mode (a) the RRs ‘1’ and ‘2’, for the localized mode (b) the RRs ‘3’ and ‘4’.

4.4.1.1 Local optical tuning of a localized state

Here we are going to prove the localized nature of the defects modes by means of local free carriers injection (for more details refer to chapter 7). The free carriers are generated by focusing a CW Nd:YAG green laser on a single RR as shown in figure 4.19. Is well know that free carrier generation induces free carriers dispersion (FCD). The refractive

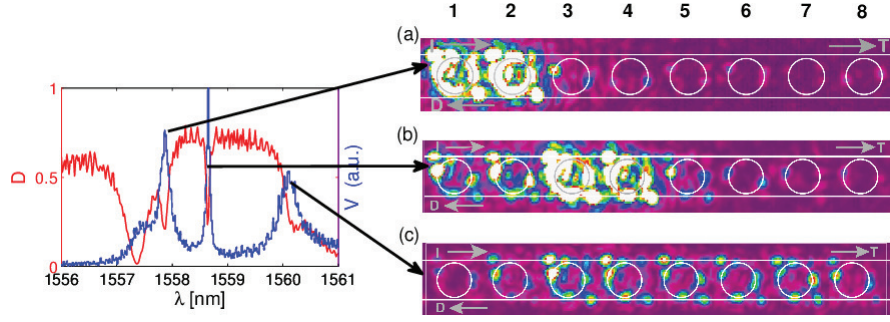


FIGURE 4.18: Snapshots obtained from an IR camera placed over the top of the sample and shown for three distinct spectral peaks at $1557.86nm$, $1558.65nm$, and $1560.11nm$ for images (a), (b), (c), respectively, in the response of drop(red)/out-of-plane scattered light(blue line) for band labelled 'D'(see Fig.4.17). For the sake of clarity, the images are outlined (in white line) with RRs and WGs of the SCISSOR. Note that the normalization used for the drop signal is with respect to the reference signal whereas the out-of-plane scattering is normalized to the maximum value in the relevant spectral range. [33]

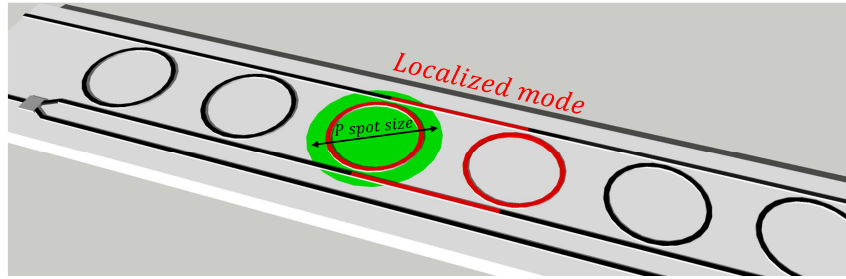


FIGURE 4.19: Sketch of the optical tuning of a cavity through a green laser.

index variations is negative, thus a blue shift of resonance is expected as described by the following law:

$$\Delta n = -\frac{dn_{Si}}{dN} \Delta N$$

where Δn is the refractive index variation, $\frac{dn_{Si}}{dN}$ is the FCD coefficient and ΔN is the carriers concentration.

The used setup is reported in appendix B.0.6. The spot size of the pump laser on the sample is about $20\mu m$, therefore the refractive index change is practically limited on a single RR (Fig. 4.19).

We focus the laser on each RR, from 1 to 8 with a maximum pump power of $30mW$ (see labels in Fig. 4.18), and measure the drop signal for band 'D'. The estimated blue shift induced by the pump is about $0.1nm$ that corresponds to a $\Delta n \sim 2 \times 10^{-4}$. The pump greatly influences the shape of the localized states, while leaves unaltered the whole SCISSOR band.

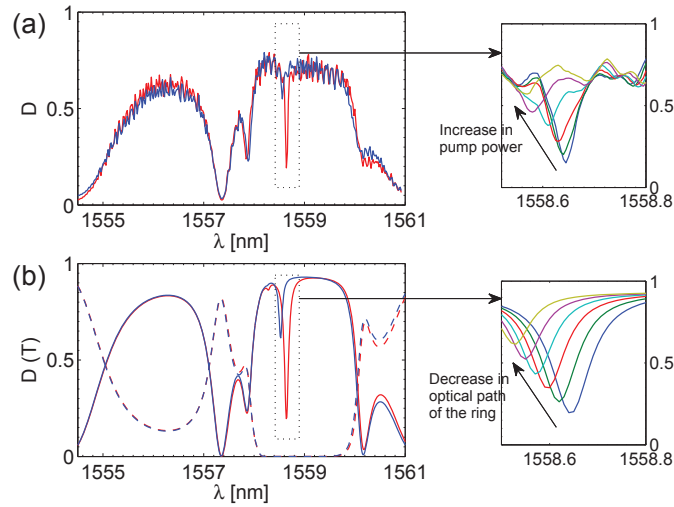


FIGURE 4.20: Optical tuning of localized mode for band ‘D’ observed in the drop signal for different pump powers that are focused on the 3rd ring in the DC-SCISSOR structure. (a) Experimental results: Drop transmission when the pump power is turned on(off) shown with blue(red) line. Inset: Enlarged view for different pump powers going from 0 to maximum(30mW). (b) Simulation results: The transmission in the drop(through) port is shown with solid(dashed) lines and for two different values of the ring radius $6.756 \mu\text{m}$ (red line) and $6.754 \mu\text{m}$ (blue line). Inset: Enlarged view of the drop transmission for a gradual change in the ring radius with ΔR decreasing by steps of 0.4nm [33].

We focus for example on the ring ‘3’. When the pump is focused on such ring, we noticed a significant change in the high-Q mode at the 1558.65nm . The drop signal changed by $\Delta T=0.46$ and the resonance wavelength is blue-shifted by $\Delta\lambda=-0.08\text{nm}$ which is more than its FWHM. The results are shown in Fig. 4.20(a) for the drop signal. The inset in Fig. 4.20(a) shows the pump power dependence of the resonance transmission. Since we observed a blue-shift we attribute the effect to pump excited FCD. We also note a change in the resonance lineshape from nearly symmetric to an asymmetric lineshape as the pump power is gradually increased. In Fig. 4.20(b) we show the simulation results obtained using the TMM by reducing the radius of the ring ‘3’ in steps of 0.4nm , in order to simulate the pump induced changes in the optical path.

4.5 Fabrication defects and localized states

The link between the fabrication defects and the creation of localized states is easily demonstrated. Since the errors are normally distributed, two different samples should show a different localized modes distribution. We are working on the same 8 RR SCISSOR used previously and shown in figure 4.7.

As expected, three different samples, taken from different positions on the wafer, show a different localized mode distribution while the global characteristic of the bands, BB

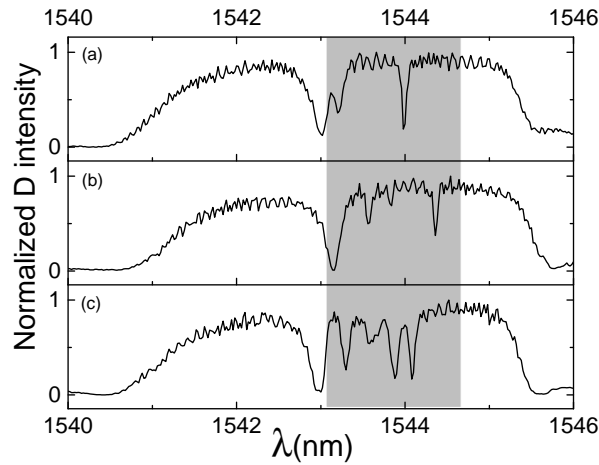


FIGURE 4.21: D port spectrum of three samples coming from different positions on the wafer. The grey area highlights the localized states

and BR, remains the same. Moreover, we note that the randomness of defects changes both the number, the ER and the FWHM of the spectral features associated to localized modes.

In the following, we demonstrate that there is a strong correlation between the localized states and the short range disorder distribution. By exploiting this fact, we numerically simulated the presence of disorder through a TMM code, by treating the device parameters as random variables with normal distribution, and we estimated the set of standard deviations that statistically reproduces the experimental data.

4.5.1 Statistical investigation of the localized states

The LETI fab, which produced the samples, suggests a standard deviation value of defects of 5nm [47]. Our goal is to find the statistical relationship between localized modes and disorder.

We refer to these random fluctuations, that break the correlation on the device scale, as short range or *local disorder*. Number, intensity and full width half maximum (FWHM) of the localized states possess a strong correlation with the degree of local disorder. In particular, their values increase as the resonators radii fluctuate with an higher standard deviation i.e., an higher defects-induced detuning. The measures are performed in the band in which the BB and RB are overlapped to maximize the number of localized states and CRIT (Fig. 4.17, band 'A'). We adopted the following scheme:

1. Localized state peaks (deeps) from the Through (Drop) port of several samples have been characterized. The characterization includes the number of peaks, their

FWHM and their ER. The number of measured samples must be large enough to perform a statistical analysis. We choose a number of 35 samples.

2. A statistical average is performed on the previous measured quantities. Results are shown in table 4.2.
3. Numerical simulations are performed: RR radii, separations and coupling coefficients are set by taking their design values and adding normally distributed random variables with zero mean values and known standard deviations (STD) σ_k . This simulates the presence of disorder. The choice of a normal distribution is dictated by the fact that the final dimensions are the sum of a large number of weakly correlated fabrication processes, so the central limit theorem holds. A number of 35 iterations is done for each parameter set, and, at the end, the averaged quantities listed in step 3 are calculated. Simulation parameters are indicated in table 4.3. RB and BB are overlapped in the simulated wavelength range.
4. A comparison with the experimental data is performed to find the set of standard deviations that best reproduce the measured localized states features.

TABLE 4.2: Experimental results for the localized modes features.

Parameter Averaged Quantity	Value
Number of peaks	4.22 ± 0.19
FWHM	$(0.060 \pm 0.003)nm$
Through relative intensity	0.256 ± 0.016
Drop relative intensity	0.401 ± 0.019

TABLE 4.3: Simulation parameters used to statistically reproduce the observed localized modes features.

Simulation parameters	Value
Wavelength range	$1500 - 1510nm$
Wavelength step	$0.02nm$
Ring radius R	$6.75\mu m$
Ring separation L	$22\mu m$
Effective index dispersion	$1.845 - 1.23 \cdot (\lambda - 1.534)$
Coupling coefficient dispersion	$9 - 20\%$
Bend losses	$0.01 \frac{dB}{90}$
σ_k^R	From $2nm$ to $10nm$ with $0.2nm$ step
σ_k^L	From $2nm$ to $10nm$ with $2nm$ step
Coupling coeff. randomization	5%

Simulation results are shown in figure 4.22. As expected, simulations confirm that the average number of CRIT peaks, their FWHM and their intensity grow as the ring radius standard deviation increases. The curves, practically, are not influenced by a σ_k^L variation. It is the σ_k^R that plays the most important role. This is due to the fact that,

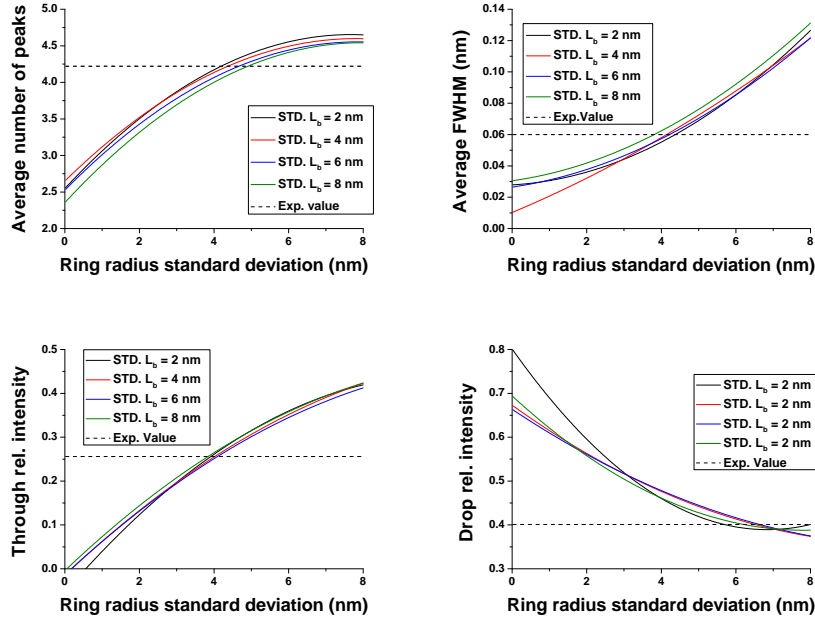


FIGURE 4.22: Simulation results: Average number of peaks (deeps), FWHM and intensity as a function of σ_k^R for several values of σ_k^L . Dashed lines indicates the experimental values reported in table 4.2.

in order to shift from a ChC, which enhances localized modes (see Fig. 4.12), to an out of ChC, an additional propagation phase shift of $\pm\frac{\pi}{2}$ between two adjacent rings is required. This is possible only if L is changed by a quantity $\Delta L = \pm\frac{\lambda_m}{4n_{eff}} \approx 200\text{ nm}$, that can not occurs through disorder. STDs higher than 10 nm are not investigated since they don't reproduce the experimental data. Simulations performed with and without a randomization of 5% in the coupling coefficient give no substantial differences, so they are not shown in the final results. However, it's expected that deviations in the coupling gaps are of the same order of the ring radius ones because they arise from the same fabrication steps. A good agreement with the experimental data is found in the 4–5 nm range of radius STD, while the mutual separation can not be determined with the same precision.

The σ_k that represents the experimental σ is the one that generates an average number of peaks, FWHM and Through relative intensity that are compatible within a standard deviation with the experimental data. Drop relative intensity has not been considered as a reliable parameter since the Fabry Perot noise, in the Drop port, hides the small deeps. The values of STDs that fulfil the compatibility criteria are listed in table 4.4, both are compatible with the photolithography standards.

The STD of the radius is found with a relative error $< 12\%$. Given the high interdependence between the localized states and local disorder on the wafer, in the next section

TABLE 4.4: Best estimations of the fabrication defects, given in terms of the standard deviations.

Parameter	Mean+STD	Relative error (%)
σ_k^R	$(4.3 \pm 0.5)nm$	11.6%
σ_k^L	$(6.3 \pm 2.8)nm$	44.4%

we propose the design of a test structure that exploits the localized states to determine the magnitude of local errors in a wafer.

4.5.2 Test device for fabrication process errors estimate

As shown in figure 4.22, the Drop intensity of the localized mode dips quadratically decreases as the defect STD increases. The error done on estimating the mean value of the defect population scales with the square root of the number of Drop signal measured.

We start from these considerations to develop a quick, simple and precise device that estimates the magnitude of the fabrication errors (for any fabrication techniques) with a single measurement in order to be applied in wafer defects control. Figure 4.23 shows

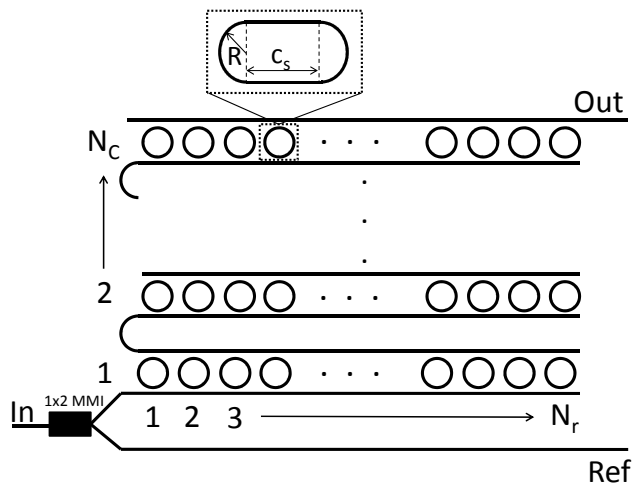


FIGURE 4.23: The proposed design. There are 3 ports: the input (In), Out and the reference (Ref). N_r , number of resonators that compose a SCISSOR. N_c , number of cascaded SCISSORS.

the proposed design. It is composed of several cascaded SCISSORS. N_c is the SCISSOR number and N_r is the number of resonators that compose the SCISSOR (RR or RTR). The acronym $N_r \times N_c$ stands for a device composed by N_c SCISSORS of N_r resonators. The behavior of this device is investigated using the parameters in Tab 4.5.

TABLE 4.5: Device simulation parameters

Parameter	Gap	R	c_s	L	w	Polarization
Racetrack	160nm	3.25 μ m	7 μ m	10.210 μ m	450nm	TE

This configuration acts as an optical mediator by summing the effect of the defects in each SCISSOR. As a consequence the transmission band of the Out port presents several dips and its mean value decreases as the magnitude of defects increases. This trend is clearly shown in figure 4.24.

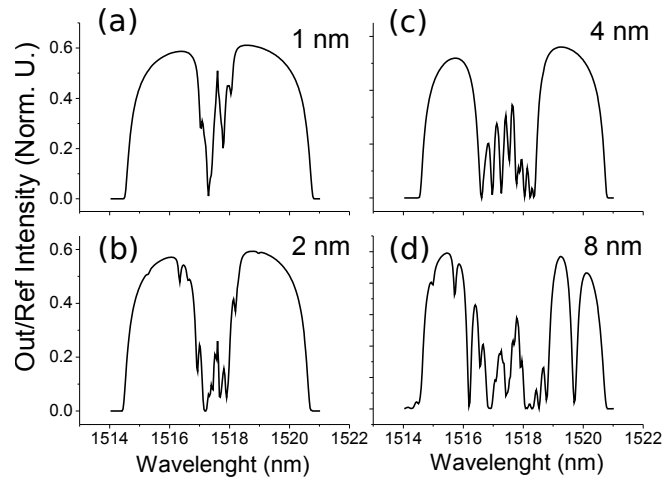


FIGURE 4.24: 14x10 device Out port transmission spectrum normalized by Ref port for different values of radius STD.

Without performing any spectral measurements, it is possible to get information about the defects STD by spectrally integrating the intensity of the Out port. The optimal value of N_c has to be found as a tradeoff between the device footprint and its sensitivity. Figure 4.25(a) reports the normalized Out intensity, spectrally integrated in the 1514 – 1521nm range, for 3 values of radius STD. We can notice that the sensitivity ($1/nm$) increases with the number of cascades.

To investigate the accuracy of the device, the statistical distribution of the Out spectrally integrated intensity is simulated for 50 times. Figure 4.25(b) reports the relative STD (calculated as $STD/MeanValue$) as a function of defects STD for 3 values of N_r . N_c is fixed to 10. It can be seen that it is important to have a large N_r to maintain a good accuracy even for large process errors. Figure 4.26(a) reports the design for a 14×10 test structure. It uses a broadband source (i.e an ASE source), as input. Two input-output gratings inject and collect light from two single mode optical fibers. The Out signal can be measured using a photodiode. The Ref port is used to normalize the data.

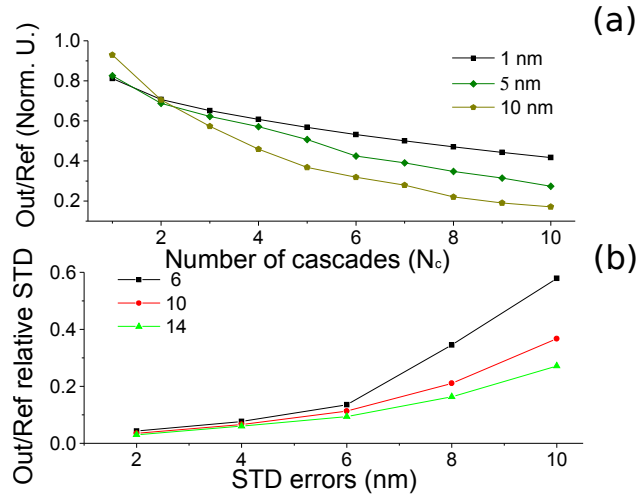


FIGURE 4.25: (a) Out/Ref spectrally integrated intensity as a function of N_c for different values of radii STD. $N_r = 14$ (b) STD of 50 simulated value of the Out/Ref spectrally integrated intensity as a function of radius STD deviation for different values of N_r . $N_c = 10$.

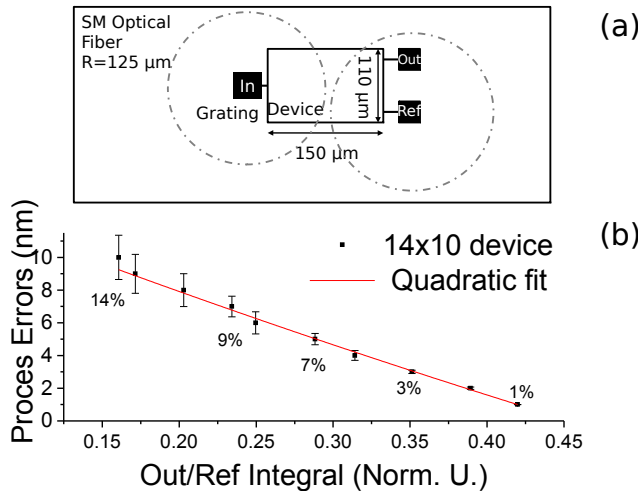


FIGURE 4.26: (a) Real device proposal. (b) Calibration curve for a 14x10 device: (black) Mean value and relative error of the process errors as a function of Out/Ref ratio, (red) quadratic fit.

The error estimation process is done by aligning the fibers and then measuring the ratio between the Out and the Ref port. This value has to be compared with the pre-calibrated curve in figure 4.26(b) that yields the errors and the accuracy of the process. The calibration curve is generated by simulating the test device starting from the geometrical parameters in table 4.5. The calibration curve fits very well a quadratic polynomial, as shown in Fig 4.22. The equation is $err[nm] = 9.5 x^2 - 37.4 x + 15$. The total device footprint, using the parameters in table 4.5, is roughly $150 \mu\text{m} \times 100 \mu\text{m}$. This value is limited by the fibers, so even if a high number of resonators are used, the device footprint remains smaller than the area covered by the two optical fibers used to

couple and extract the light. It is convenient to use this area to maximize the resonator number and have a better accuracy.

Chapter 5

Coupled resonator induced transparency for routing application

5.1 Introduction

Silicon photonics is the technology to develop next generation opto-electronic and all-optical integrated devices [188]. It allows increasing the integration level of photonic circuits at the levels required by complex network on chip or signal optical processing systems for chip-to-chip and on-chip applications [189]. A key element for any of these applications is the switching port. The most successful switching ports are based on single microring resonators where the ring resonance rules the behavior of the port. Single switches and complex resonator fabrics have shown very high performance, very large bandwidths as well as extremely low power consumption [190].

SCISSORs have a rich optical phenomenology due to the interplay between the coherent feedback of all the rings, when the wavelength of the signal satisfies a Bragg-like condition, and the resonant behavior of the rings which form a resonator stop-band [82, 83].

In the first part of this chapter we carried out a study of the CRIT effect in SCISSOR devices, using simulations, in order to demonstrate a novel way to exploit it for signal routing. A new design will be presented where a modified tapered SCISSOR structure, called CRITAD, is used to control the spectral position of the CRIT resonance. The coherent interference among the resonators will be carefully detailed. Two methods to control the CRIT, which are based on different principles, will be studied. In addition, we

will consider the consequence of the limited resolution in current lithographic processes on the router performances, in particular on the insertion losses and crosstalk. We will see that the controlled breaking of the periodicity of the structure helps to make it robust to errors in the structure. Finally, a direct comparison between the ADF and the CRITAD structure, used as a building block for an 1×4 multiplexer, will be reported .

The second part reports all the experimental results which include both a stationary and a dynamical investigation of the CRITAD design. The former includes transmission and switching measurements with also the robustness test to fabrication errors. The latter, concerns the CRITAD time switching response under a local perturbation provided by a pulsed $Ti : Sa$ laser. The results show that the CRITAD structure could be a good substitute for the simple ADF in some applications, and can be used to engineer devices robust against fabrication defects, fully supporting DWDM channel spacing and easily extendible to UDWDM. CRITAD operates in an over-coupled regime, that in principle, should avoid the mode splitting due to the counter-directional propagating modes but still preserving high Q-factor resonances [167]. Furthermore, we experimentally demonstrate that CRITAD is capable to address single channel I/O operation and it shows a fast, efficient and hitless switching mechanism [35].

All the results are obtained through numerical simulations based on a Transfer Matrix algorithm (refer to chapter 4). The input parameters are the geometry of the SCISSOR (ring radii, coherence length and ring number), the effective index of the waveguides and the coupling coefficient between the waveguide and the resonator. All the discussions derived in the following, are valid for whichever single mode optical microresonator, RR or RTR for example, provided that the orders of magnitude of the coupling coefficient and the resonators detuning are compatible with those suggested here.

TABLE 5.1: Hypothetic parameters for two different systems, to comply the CC requirement

Parameter	Gap	R	c_s	L	w	Polarization
Ring	250 – 300nm	7 μ m	–	$\sim 21.205\mu$ m	500nm	TM
Racetrack	160nm	3.25 μ m	7 μ m	$\sim 10.210\mu$ m	450nm	TE

The effective indexes used in the simulation are extracted from the dispersion law simulated and measured in the chapter 2 for the TE ($w = 450nm$) and TM mode($w = 500nm$). In the discussion we will use the CC parameter to describe the resonator-WG coupling strength. Starting from the suggested value, an estimate of the actual size of the gap to be used in a RR, or in a RTR system is found in chapter 2. Table 5.2 gives the simulation code parameters.

TABLE 5.2: Optical parameters used in the transfer matrix (TMM) simulations.

Wavelength	Coupling Coefficient	Round Trip Loss
λ (nm)	κ^2	dB/90°
From 1500 To 1600	From 10% To 80%	0, 0.008 or 0.015

5.2 Exploiting CRIT in a tapered SCISSOR

5.2.1 Working principle

Figure 5.1(a) reports the *new* SCISSOR design which is composed by 7 resonators with a tapering in the radii. In a chain of n resonators, the one in the middle ($\frac{n+1}{2}$ for an odd n) has a radius R , while the others have either decreasing or increasing radii. Each resonator differs from its neighbor by ΔR (detuning). All the resonators are coupled to the input and drop waveguides with the same coupling coefficient. Even for the RTR, it is better to induce the detuning using the parameter R instead of c_s in order to maintain a constant CC along the chain.

The difference in radii between nearby resonators leads to a spectral shift of the single ring resonance and creates the condition for the creation of CRIT (refer to section 4.3.1). Indeed, if two resonators have the same radius, the signal is channelled into the drop waveguide by the first one. In this case, no signal reaches the second resonator preventing the formation of the coherent feedback which yields the CRIT. One needs to slightly detune ($\Delta R \neq 0$) the resonances so that enough signal reaches the second resonator allowing a significant coherent feedback. The detuning, on the other hand, must be small enough in order to keep the spectral overlap of two adjacent ring resonances ($\Delta\omega < 2k^2$ that corresponds to one of the condition required by the CRIT effect as shown in section 4.3.1)).

Three ports are present: input (I), through (T) and drop (D). The colored arrows indicate the coupling between the cavities. Having different radii, each resonator is characterized by a different resonant wavelength. If we consider the through signal when all the resonators are acting independently, i.e. are isolated, we find the sequence of spectra shown in Fig. 5.1(b). However in the SCISSOR structure, the single resonators are coupled through the drop waveguide: it is the choice of the coupling length which determines the coherent interaction between the signal resonant to the various resonators. In fact L_c is directly related to the ChC previously introduced. If L_c satisfies the constructive interference condition we have CRIT. If not, we do not have any through signal. This is demonstrated in figure 5.2 where we plot, with the black line, the T signal when the coherence condition is satisfied and, with the red line, the T signal when the coherence condition is not satisfied.

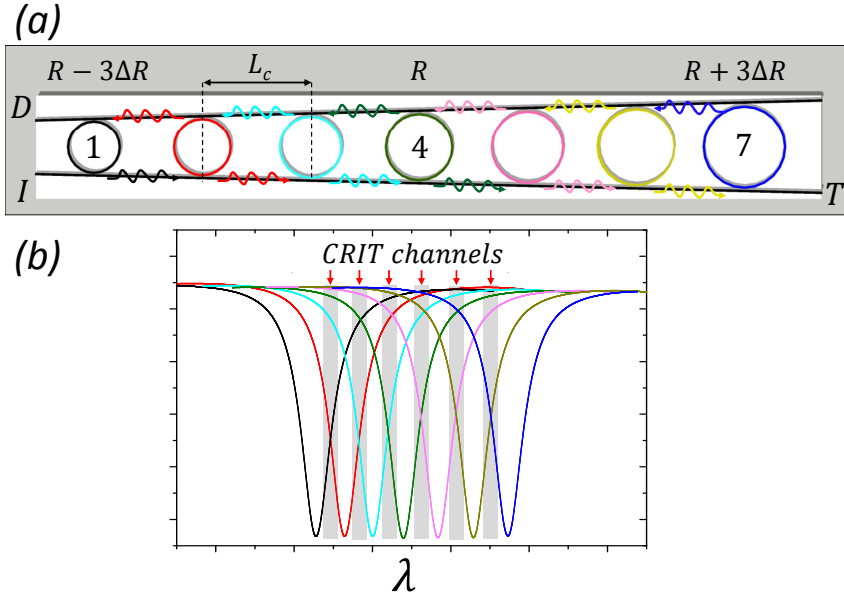


FIGURE 5.1: (a) Schema of the new SCISSOR for $n = 7$: R represents the radius of the central resonator, ΔR the detuning and L_c the coherence length. The resonators are labelled from 1 to 7 starting from the left. (b) Simulated spectra of the through signal for each isolated resonator. The gray rectangles and red arrows correspond to the possible wavelength where CRIT might occur.

Note that since the radii of the resonators are all different, L_c is different for each pair of rings. The coherence length is obtained using the mean radius between two nearby resonators:

$$L_c(n) = c_s(n) \left(\frac{m_B}{m_R} - 1 \right) + \frac{m_B}{m_R} \pi R_m(n) \quad (5.1)$$

$$R_m(n) = \frac{R(n) + R(n+1)}{2}$$

where $R_m(n)$ is the mean radius of the n -th pair of resonators, $R(n)$ is the radius of the n -th resonator and $L_c(n)$ is the distance of the n -th pair of resonators that regulates the feedback between the cavities. The ChC is imposed by fixing the ratio of the BB and RB order:

- Coherence Condition: $m_B/m_R = j$ with $j \geq 0$ and integer
- Out of Coherence Condition: $m_B/m_R = (j+1)/2$.

It is important to note that when $m_B/m_R \neq 1$, i.e. non-overlapping bands, the L_c for a RTR differs from that of a RR because it has a dependence also on the c_s . From now on we focus only on ring resonators without losing generality, thus $c_s = 0$.

Then, $L_c(n) = \pi R_m(n)$ is the ChC and $L_c(n) = \frac{3}{2}\pi R_m(n)$ is the out of ChC.

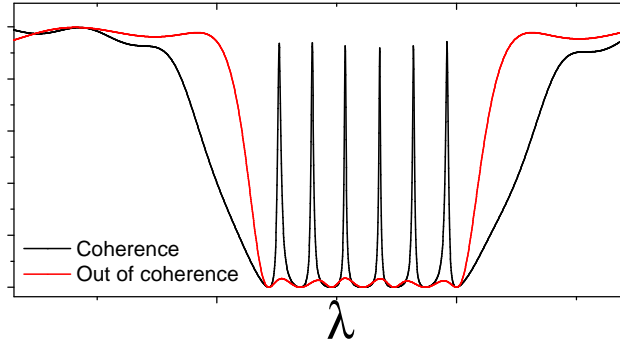


FIGURE 5.2: Example of the through port response for a CRITAD made with 7 ring resonators in which all pairs are in the ChC condition (red line) and out of ChC (black line) condition.

For an out of ChC, we have a flat stop-band which is typical of a sequence of rings. Note that the spectral position and the presence of each one of these CRIT peaks is carefully controlled by the choice of ring radii and of ChC in this new tapered design: each single CRIT peak is formed only via the coupling of a single pair of resonators. This avoids the random formation of CRIT peaks which might occur in more complex situations where more than two rings might be coupled (see section 4.4.1).

Since only one pair generates a single CRIT resonance, the maximum number of available CRIT resonances for N resonators will be $N - 1$. In addition, in the proposed structure, all pairs are formed by adjacent rings to minimize the effective length of the cavity that generates the CRIT.

Figure 5.3 compares an ADF based on a single resonator with CRITAD. The design parameters are the same in the two case, i. e. the same average ring radius, coupling coefficients, losses etc. Note that, for the CRITAD, the CRIT condition has been imposed only on one pair of rings in order to have a single CRIT resonance. In Fig. 5.3, the through signal is reported in the two cases.

It is interesting to note that:

- the ADF has a blocking characteristic when in resonance, while the CRITAD is transparent;
- even if the Q factor of individual rings are the same, CRITAD has much narrower linewidth ($\sim 0.1 \text{ nm}$) if compared with ADF (2 nm).
- the series of coupled rings in the CRITAD form a large stop-band whose width can be controlled by the number and sizes of the rings;

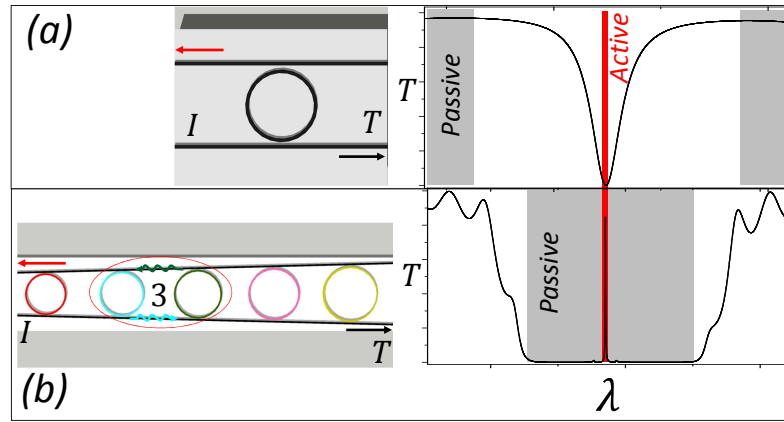


FIGURE 5.3: Schematic representation of the two types of structure, ADF (structure a) and CRITAD (structure b) with the wavelength response of the through signal in equal simulation conditions. The black (red) arrow represent the passive (active) state. The CRITAD is composed by 7 resonators in which the active couple is the third. [34]

- the single CRIT resonance can be understood as the single channel in the add-drop while the other wavelengths within the stop-band are channelled into the drop ports.

Finally, let us remark that the spectral characteristics of the single CRIT channel depends on the propagation losses, the coupling coefficient CC , the ChC and on the detuning of the resonances (Fig. 5.1). In particular, the insertion losses (losses of the signal in resonance with the CRIT channel) are mainly due to the radiative losses of the cavities that are related to the fabrication imperfections (surface roughness).

5.2.2 Two different ways to control the coherence condition

Two different ways to control the coherence of a pair exist: the Bragg method, that changes the BB position (i.e. the L_c of the entire chain is modified) to select the pair and the Local method, that acts on the ChC of a pair by changing only its L_c .

5.2.2.1 Local method

Consider the case where all resonators are in a out of ChC ($L_c = 3/2 \pi R_m$) and let us "open" a CRIT channel by imposing the ChC only to one pair of resonators ($L_c = \pi R_m$). This method will be called the *local* method.

Figure 5.4 shows how to create two different transmission channels in two different CRITAD by using the *local* method. We start from a basic block made by 3 resonators

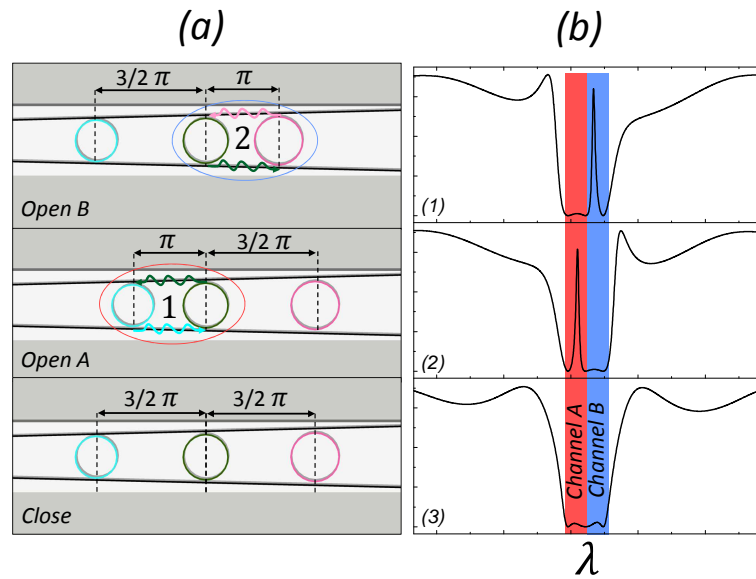


FIGURE 5.4: Schema of the 3 rings *local* CRITAD structure (a) and spectrum of the through signal (b) for: (3) out of ChC, (2) ChC for the first pair, (1) ChC for the second pair.

in a out of ChC. The effect of changing the phase from $3/2\pi$ to π on a single pair allows the creation of one CRIT channel (Fig. 5.4 for channel A (red region) and channel B (blue region)). Since L_c is different in each couple of resonators, the Bragg band is not well defined in this structure.

The choice of $L_c = 3/2\pi$ for the out of ChC is dictated by design limits, since an $L_c = \pi/2$ would give a physical overlap of RR or RTR circumference. This leads to an odd relation between the RB and the ChC as shown in figure 5.5.

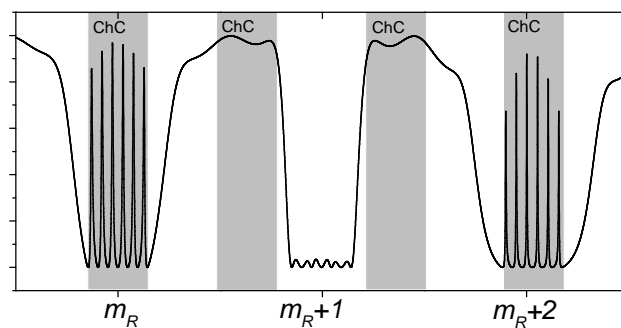


FIGURE 5.5: (Black line) Local CRITAD T spectrum with highlighted in grey the area of ChC. m_R is the resonance order .

As a consequence, not all the bands are available for routing signal or, by another point of view, we will have an alternation of bands with open (m_R and $m_R + 2$) and closed channels ($m_R + 1$). Anyway, all the bands became available by using, for example, an elliptic resonator with the shorter radius along the WGs direction.

Below, the characteristics of the local method are summarized:

- from 0 to n open or closed channels
- Independent control of the state of each channels through an $L_c(n)$ variation
- For an RR or RTR, there are $m_R/2$ available bands. Full availability for elliptical resonators.

5.2.2.2 Bragg method

The ChC condition can also be changed under a global variation of the structure. Another way to define the ChC is $\lambda_B = \lambda_{R_m(n)}$, that in turn means a global $L_c(n) = L_c$ that centers the BB position on the chosen CRIT channel. Unlike the *local* method, now L_c is equal along the chain in order to establish the conditions of periodic reflection that generates the BB. In fact, the *Bragg* stop-band is centered at the wavelength λ_B defined by:

$$\lambda_B = \frac{2L_c n_{eff}}{m_B}$$

where m_B is the order of the Bragg band and n_{eff} is the effective index of the optical mode in the waveguide. This method will be called the *Bragg* method.

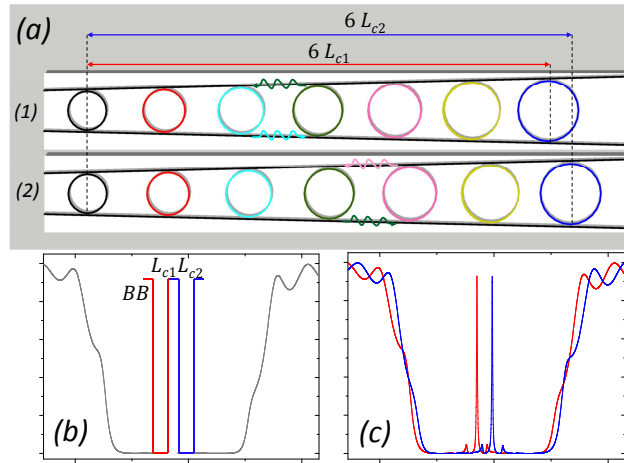


FIGURE 5.6: Schema of the 7 rings *Bragg* CRITAD structure (a) and spectra of the T signal for different coherent length L_{c1} (red) and L_{c2} (blu). (b) Schematic view of the position of the Bragg band inside the stop-band and (c) spectral response of the through port for the 2 different L_c .

In order to understand the *Bragg* method, we show in Fig. 5.6 (a) the schematic of the CRITAD and in Fig. 5.6 (b) a sketch of the through response for two different values

of the Bragg stop-band determined by two different values of L_c equal along the chain. Note that also in this case the radii of the various rings differ by ΔR .

Within this method, to have a CRIT channel, the spectral position of the Bragg stop-band has to overlap with the CRIT condition of a pair of neighboring rings, i.e. $\lambda_B = 2\pi R_m n_{eff}/m_B$. This is demonstrated in Fig. 5.6(c) where the through signal is reported for two CRITAD structures which differ only for L_c .

Unlike the local method, all the bands are available for signal routing even for a RR or a RTR since, $m_R = m_B$ by imposition. This is confirmed in figure 5.7.

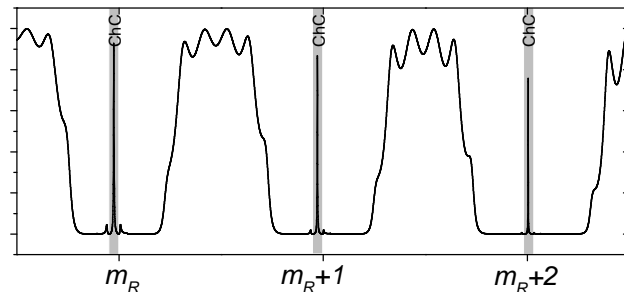


FIGURE 5.7: (Black line) Bragg CRITAD T spectrum with highlighted in grey the area of ChC. m_R is the resonance order .

Below, the characteristics of the Bragg method are summarized:

- Only one open or closed channel.
- Control of the state of each channel through an L_c variation.
- Full bands availability.

5.3 Performances of the CRITAD: spectral investigation

We compare the two methods to form a CRITAD by computing:

- the channel bandwidth, defined as the resonance linewidth at -3 dB in GHz
- the channel losses, defined as maximum intensity of T port in dB inside the selected channel Ch_n (see Fig. 5.8)
- the crosstalk, defined as the difference between the channel losses of Ch_n and the intensity in dB of the T signal in the closed nearby channels $Ch_{n\pm 1}$.

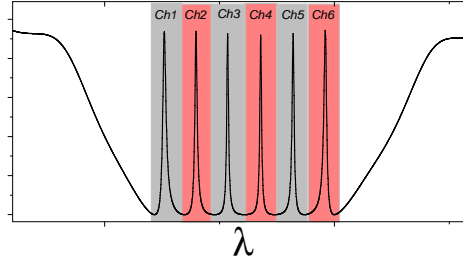


FIGURE 5.8: The channels are defined by the grey and light red regions.

For both cases, the schemes of the structures are similar to the one shown in Fig. 5.1. Both have 7 rings of radius $R_3 = 6.75 \mu m$, and for each method, we used two values of ΔR : 5 and 10 nm. The coherence length L_c is equal to πR_m or $3/2 \pi R_m$ depending on the design. As it was discussed in chapter 2, a common value for the bend losses of a SOI based microresonators with a radius of $5 \mu m$ are of $0.005 - 0.01 \text{ dB}/90^\circ$. Thus, the simulations are computed for 3 different value of bend losses: $0 \text{ dB}/90^\circ$, $0.008 \text{ dB}/90^\circ$ and $0.15 \text{ dB}/90^\circ$.

Since in the microring resonator the coupling section (the section of the bus waveguide coupled evanescently with the resonator) is very short, almost punctiform, we have neglected the coupling losses.

In addition, we changed also the bandwidth of the CRIT channel, which is mainly controlled by the CC. This is shown in Fig. 5.10(a). The over-coupling regime (it must be $CC > K$ where K is the *roughness-induced reflection*) allows to limit the problem of the mode splitting induced by surface-roughness that becomes critical when using resonators in the under-coupling regime (see section 2.11 and the reference [191]). Values of coupling coefficient from 10% (wider gap width) to 50% (narrower gap width) were used for the $\Delta R = 5 \text{ nm}$ design and from 20% (wider gap width) to 80% (narrower gap width) for the $\Delta R = 10 \text{ nm}$ design.

Figure 5.9 reports the values of channel losses and crosstalk as a function of the channel bandwidth for different values of bending losses. Figures 5.9(a) and 5.9(b) refer to the *local* method for two different values of ΔR . Figures 5.9(c) and 5.9(d) refer to a structure designed by using the *Bragg* method for two different values of ΔR .

We found that:

1. if the losses are different from zero, the channel losses depend on the bandwidth;
2. the dependence on the channel losses of the bandwidth is stronger for the *local* than the *Bragg* method;

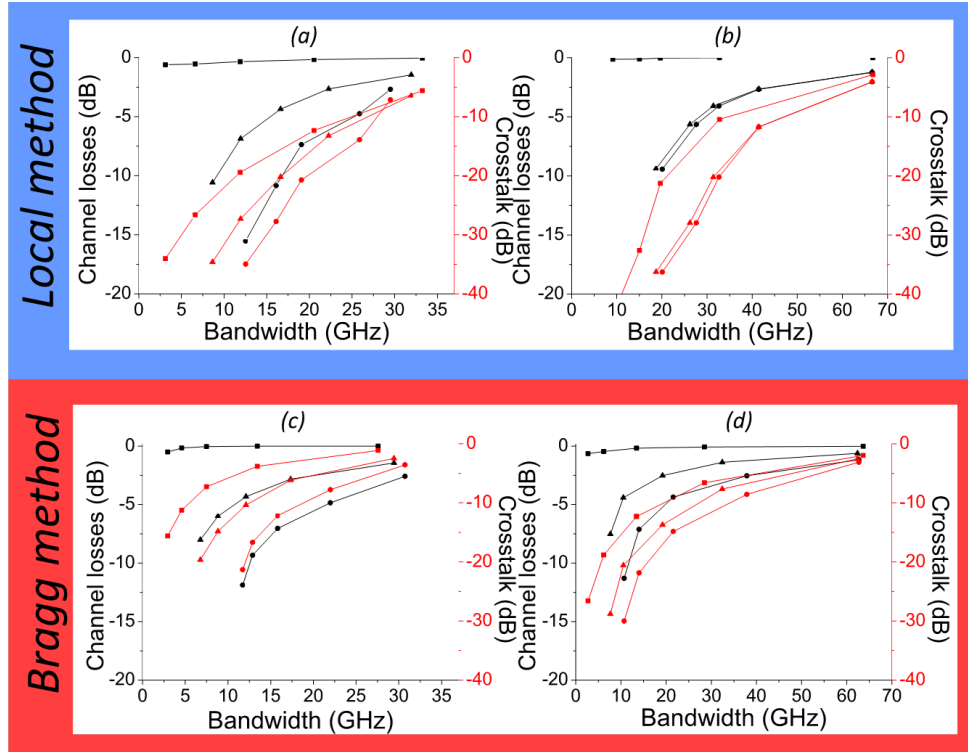


FIGURE 5.9: Cross talk (red line) and losses (black line) of CRIT channel as a function of the bandwidth for 3 different values of the bend loss: $0dB/cm$ (Square), $0.008 dB/90^\circ$ (Triangle) and $0.015 dB/90^\circ$ (Circle). (a) Local method with $\Delta R = 5 nm$ (b) Local method with $\Delta R = 10 nm$ (c) Bragg method with $\Delta R = 5 nm$. (d) Bragg method with $\Delta R = 10 nm$. Other parameters are detailed in the text.

3. the cross talk is larger for the *Bragg* than for the *local* method;
4. the crosstalk depends only slightly on the losses;
5. once fixed the process (i. e. fixed the losses), both designs are able to achieve the same bandwidth;
6. the *local* method shows a significant lower crosstalk but higher channel losses;

These results show that the choice of ΔR and coupling coefficients allow to adapt the performance of the CRITAD to the different routing requirements, e. g. for coarse wavelength division multiplexing (CWDM, bandwidth $> 500 GHz$), dense WDM (DWDM, bandwidth $\sim 100 GHz$) or ultra dense WDM (UDWDM, bandwidth $< 50 GHz$) [192].

The crosstalk of CRITAD designed by the *Bragg* method can be decreased by increasing the number of rings in the SCISSOR while that of CRITAD designed by the *local* method is almost insensitive to the number of rings in the SCISSOR (see Fig. 5.10(b)). This is due to the fact that an increased number of rings in the SCISSOR sharpens the Bragg stop-band. Hence, the crosstalk is decreased for the CRITAD designed by the *Bragg* method where the Bragg stop-band rules its behavior.

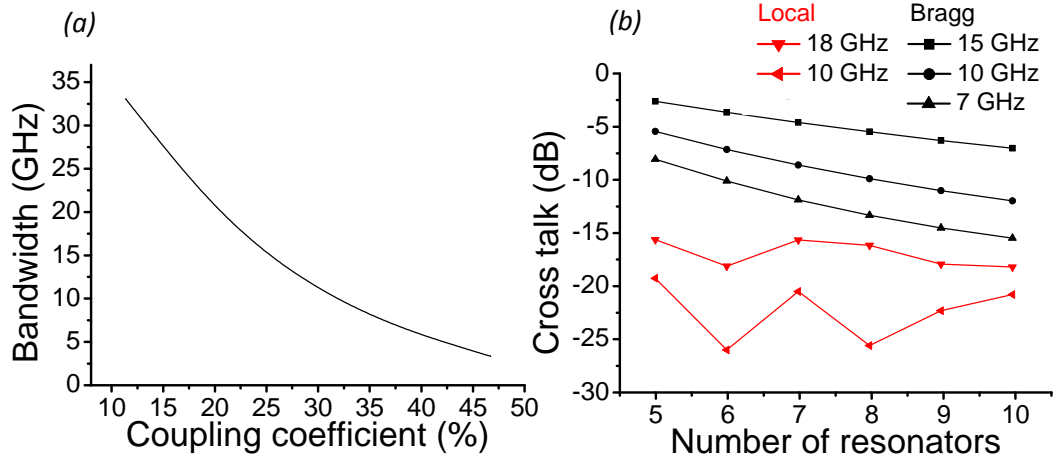


FIGURE 5.10: (a) Bandwidth of a CRIT channel versus the coupling coefficient used in the simulation. These values are for the local method and a ΔR of 5 nm . (b) Crosstalk versus the number of rings that compose the CRITAD for different values of channel bandwidth (reported in the legend) and different design: (black) Bragg method, (red) local method. The losses were fixed to $0.008 \text{ dB}/90^\circ$.

A final comment is about the footprint of the CRITAD: for the same number of rings, the *local* method yields SCISSOR which are $1/3$ longer than SCISSOR obtained by the *Bragg* one, since in the *local* method the coherence length is $3/2 \pi R_m$ instead of the πR_m length needed for the *Bragg* method.

5.4 Performances of the CRITAD: Switching capability

The switching capability of the CRITAD is here investigated for both *local* and *Bragg* method. Two switching methods are offered by the CRITAD: the first, acts to cancel the ΔR between a pair of resonators while the second, acts on the L_c in order to broke the ChC. Practically, this could be achieved by using a local refractive index variation through an integrated heater or a p-n junction. The performances are reported as a function of the relative variation of $\frac{\Delta R_{eff}}{R}$ and $\frac{\Delta L_{eff}}{L_c}$ that are related to the refractive index variation as follows:

$$OP = 2\pi(n_{eff} + \Delta n)R = 2\pi(n_{eff}R + \Delta nR) \quad (5.2)$$

where OP is the optical path of the ring and Δn in the local refractive index change. Dividing by n we get:

$$p_R = 2\pi \left(R + \frac{\Delta n}{n_{eff}} R \right) = 2\pi(R + \Delta R_{eff}) \rightarrow \frac{\Delta n}{n_{eff}} = \frac{\Delta R_{eff}}{R} \quad (5.3)$$

We examine the case of the thermal tuning in a CRITAD made of 7 resonators with only the *Ch3* opened. The following parameter are used: $\delta R = 5nm$, $CC = 32\%(44\%)$ for the local (Bragg) case and losses of $0.008dB/90^\circ$. The CRIT resonance of the *Ch3* has these characteristics: $Q = 13000$, $FWHM = 0.13nm$ and a bandwidth of about $20GHz$. The simulated values of channel ER, defined as the maximum intensity inside the *Ch3* minus the channel loss (at $\Delta n = 0$), and the cross talk, defined as the maximum values inside channels of *Ch2* and *Ch4* minus the *Ch3* loss, will be reported for several ΔR_{eff} . the same applies for the L_{eff} defined as $L_c \frac{\Delta n}{n}$

5.4.1 Switching through an R variation

Figure 5.11(a) reports a sketch of the thermal tuned system. The 'omega' heater (red sketch) acts on the third resonator, since that is the blue detuned one compared to the CRIT resonance that supports. The local tuning has to be applied on the fourth resonator for an FCD based tuning method.

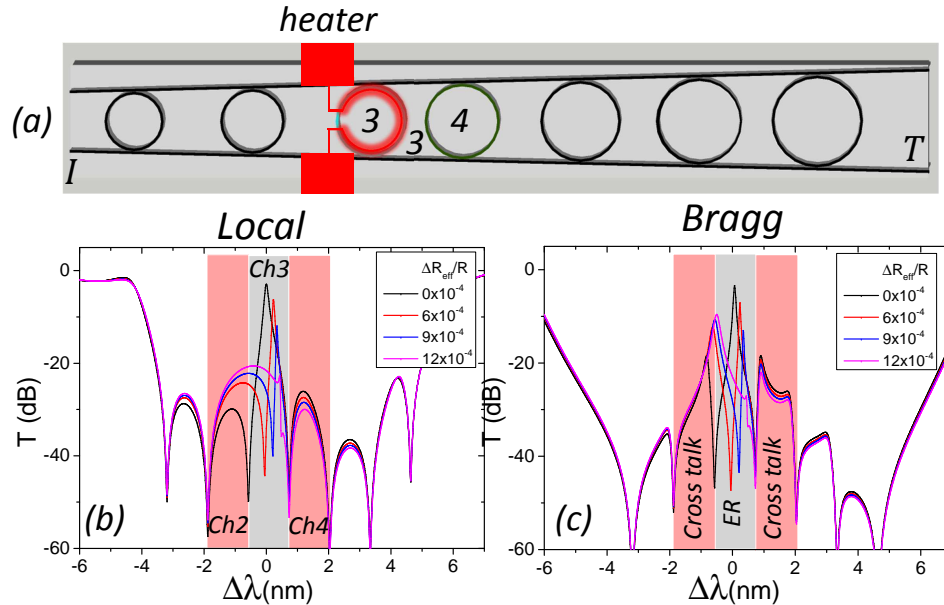


FIGURE 5.11: (a) Scheme of the switching configuration: metal heater (red) above the third resonator. Transmission spectrum of the T port in dB for several $\frac{\Delta R_{eff}}{R}$: CRITAD based on (b) local ((c) Bragg) method. The x scale is centered on the *Ch3* wavelength. The legend reports the used values of $\frac{\Delta R_{eff}}{R}$. The grey rectangle highlight the open channel while the light red rectangles highlights the two nearby closed channels, *Ch2* and *Ch4*.

The graphs 5.11(b,c) report the spectra for several values of relative refractive index variations $\Delta R_{eff}/R$ (the used values are reported in the legend) simulated for the *local*(b) and *Bragg* method (c). Note that, as the CRIT resonance starts to being switched off, it never exits its channel area (grey). This is called hitless switching [35]. The

Bragg method cross-talk performances are limited by the low number of resonators in the chain. A $\frac{\Delta R_{eff}}{R} = 12 \times 10^{-4}$ corresponds to a $\Delta R_{eff} = 4 \text{ nm}$. As a consequence the ΔR between the active pair is changed to $\Delta R = 1 \text{ nm}$.

A summary of the performance in term of ER and cross-talk is reported in figure 5.12.

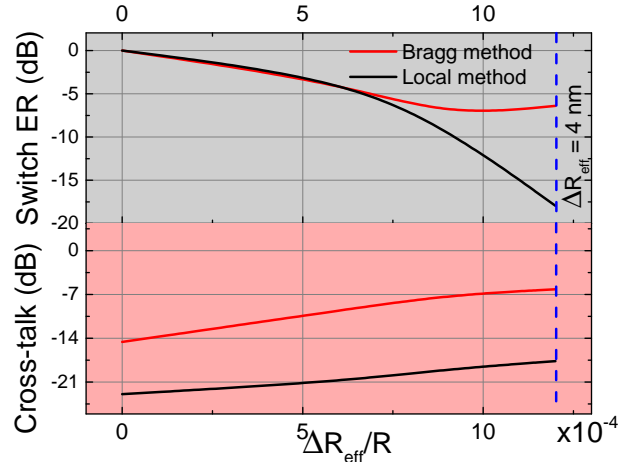


FIGURE 5.12: The grey (light red) panel reports the switching ER (cross-talk) as a function of $\Delta R_{eff}/R$. The blue dashed line represents the value of $\Delta R_{eff} = 4 \text{ nm}$ related to the maximum used value of the $\Delta R_{eff}/R$.

5.4.2 Switching through an L_c variation

The figure 5.13(a) reports a sketch of the thermal tuned system. The heater (red) acts on the WGs between the third and the fourth resonators in order to increase the effective length, L_{eff} , of L_c and thus, change the ChC. Note that, since the illustrated system induces a local perturbation, it works only for the local method. For a CRITAD based on the *Bragg* method (structure not shown in figure), a series of similar heaters have to be placed along the whole WG in order to shift coherently the BB. In this case, the same tuning system can be applied in the case of a p-n junction modulation.

The graphs 5.13(b,c) report the spectra for several values of relative refractive index variations $\Delta L_{eff}/L_c$ (the used values are reported in the legend) simulated for the *local*(b) and *bragg* method (c). Note that also in this case, as the CRIT resonance starts to being switched off, it never exceeds its channel area (grey). This is called hitless switching [35]. In general, this switching method has a lower efficiency compared to the ΔR based one. In this case, the scenario is a bit different for Bragg based CRITAD. In fact, in figure 5.13(c) it is seen that, switching off the Ch3 implies to open the Ch4 (Ch2 for a p-n junction). That means that, the Bragg structure does not allow to switch off independently a channel by only changing ΔL_c .

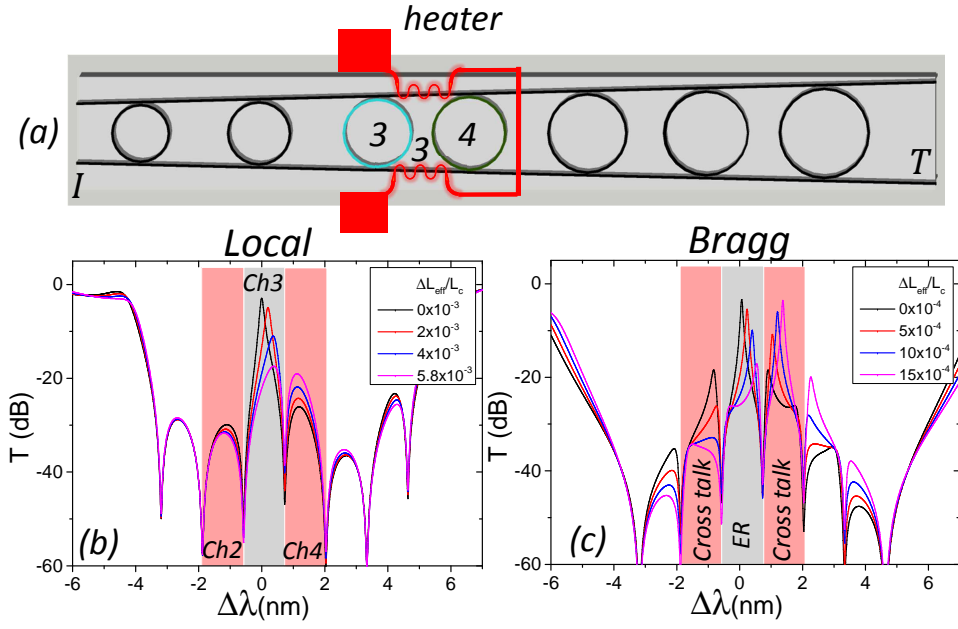


FIGURE 5.13: (a) Scheme of the switching configuration: metal heater (red) above the WG section of the third pair. Transmission spectrum of the T port in dB for several $\frac{\Delta L_{eff}}{L_c}$: CRITAD based on (b) local((c) Bragg) method. The x scale is centered on the Ch3 wavelength. The legend reports the used values of $\frac{\Delta L_{eff}}{L_c}$. The grey rectangle highlights the open channel while the light red rectangles highlight the two nearby closed channels, Ch2 and Ch4.

A $\Delta L_{eff}/L_c = 5.8 \times 10^{-3}$ corresponds to a $\Delta L_{eff} = 60 \text{ nm}$. A summary of the performance in term of ER and cross-talk is reported in figure 5.14.

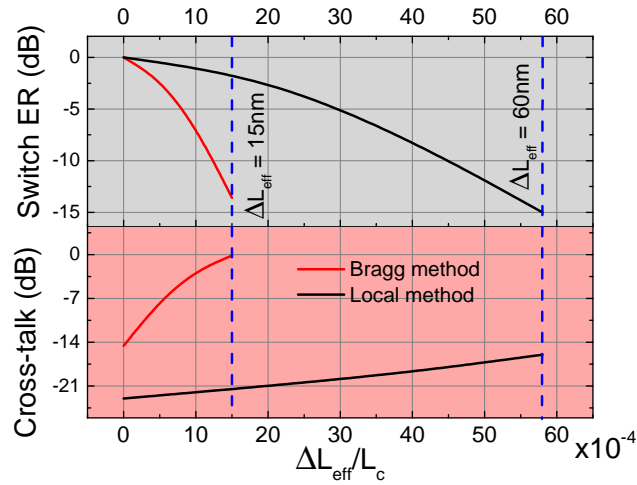


FIGURE 5.14: The grey (light red) panel reports the switching ER (cross-talk) as a function of $\frac{\Delta L_{eff}}{L}$. The blue dashed line represents the value of ΔR_{eff} related to the maximum used value of the $\frac{\Delta R_{eff}}{R}$: 15 nm for the Bragg method, 60 nm for the local method.

5.5 Performances of the CRITAD: delay investigation

The very narrow bandwidth of the CRITAD is reflected in short pulse dispersion. Figure 5.15 reports the phase shift and the group delay for the T port of a CRITAD. The group delay is related to the group velocity ($v_g = L_{tot}/\tau_g$, where L_{tot} is the SCISSOR length) and, in turns, to the temporal broadening that a pulsed signal suffers while being transmitted by the CRITAD to the through port. Therefore, τ_g limits the data rate that can be sent in the CRITAD.

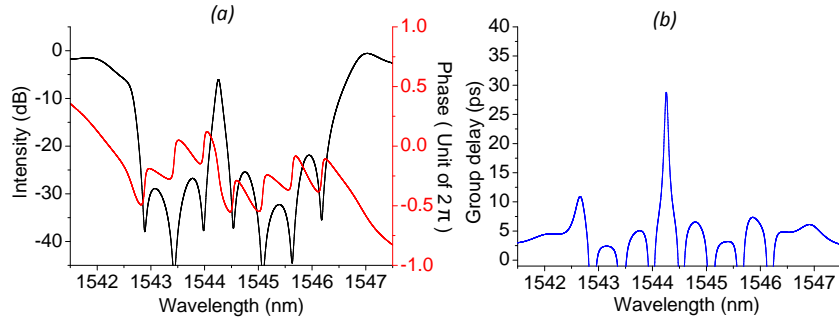


FIGURE 5.15: (a) Spectral response of the T port for a CRITAD with the *local* design and a $\Delta R = 5 \text{ nm}$: signal intensity (black) and signal phase shift (red). (b) Group delay (blue) of the through signal.[34]

Figure 5.15 shows the results for a CRITAD designed by the *local* method with a 7 ring SCISSOR where the pairing occurs between the 3rd and 4th rings (Fig. 5.2). The various parameters are: bend losses of $0.008 \text{ dB}/90^\circ$, coupling coefficient of 25% and $\Delta R = 5 \text{ nm}$. It is observed that the phase changes by $0.8(2\pi)$ across the CRIT resonance and that the maximum τ_g is 28 ps with a bandwidth of 12 GHz . This value of group delay limits the bit rate to 30 Gb/s . If we increase the bandwidth to 22 GHz by using a coupling coefficient of 55% and a $\Delta R = 10 \text{ nm}$ the maximum τ_g decreases to 17 ps , which in turn means a maximum bit rate of 50 Gb/s .

5.6 Performances of the CRITAD: errors robustness

The CRITAD is a building block which needs to be repeated for multi-channel routers. The fabrication processing errors during the manufacture of the router can become relevant. It is therefore necessary to look at their influence on the proposed designs.

Just for a matter of sum of normally distributed random variables, the CRITAD channel position shifts by a smaller factor of 0.7 than a ADF made by a single resonator. In

fact, the CRITAD channel position is fixed by the mean of the radii of the active pair:

$$R_m(n) = \frac{R(n) + R(n+1)}{2}$$

Since each R varies as a normal distributed variable, considered independent, the σ_m on the R_m is the sum of the quadrature of the $\sigma_{1,2}$ divided by 2.

$$\sigma_m = \frac{\sqrt{\sigma_1^2 + \sigma_2^2}}{2} \text{ for } \sigma_1 = \sigma_2 \rightarrow \sigma_m = \frac{\sqrt{2}}{2}\sigma_1$$

from which we obtain $\sigma_m/\sigma_1 \sim 0.7$.

Probably, the situation in the CRITAD chain could even improve thanks to the feedback provided by the other cavities. To investigate on this, we added random lengths to the nominal radius R and coherence length L_c of each ring and ring spacing in the CRITAD. These random lengths are normally distributed with zero mean and with a standard deviation σ of the order of few nanometers. Note that in processing, the length specification errors are usually given as 3σ from the average.

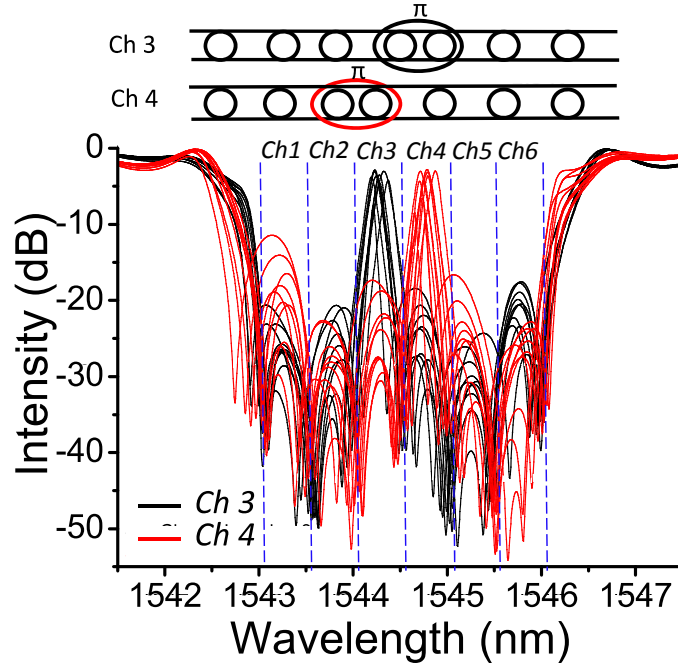


FIGURE 5.16: T port response for 2 CRITAD devices based on local method: (black) third channel open, (red) 4 th channel open. The multiple red (black) curves represent the effect of $3\sigma = 3\text{ nm}$ fabrication error. The blu dashed lines delimit the 6 channels of the CRITAD. The parameters used are $R = 6.75\mu\text{m}$, coupling coefficient 20%, $L_c = 3/2\pi R_m$. [34]

Figure 5.16 shows the results of various simulations where the random errors have a standard deviation of 1 nm . Here two CRITAD with two different channels and ΔR

TABLE 5.3: Table showing the average value for channel losses and crosstalk with relative standard deviation for 3 different values of structural errors, 3, 6, 9 nm, and two ΔR , 5 and 10 nm. The parameters obtained with 0 nm of error represent the values obtained from the ideal structures. The parameters were obtained from a sample of 100 CRITAD.

Error (3σ) (nm)	Bandwidth 11 GHz ($\Delta R = 5$ nm)		Bandwidth 22 GHz ($\Delta R = 10$ nm)	
	Losses (dB)	Crosstalk (dB)	Losses (dB)	Crosstalk (dB)
0	-04.44 ± 00.00	-19.56 ± 00.00	-01.61 ± 00.00	-18.56 ± 00.00
3	-06.45 ± 03.77	-17.80 ± 06.74	-01.70 ± 00.41	-18.59 ± 02.43
6	-12.48 ± 07.98	-12.86 ± 12.11	-02.37 ± 01.74	-19.32 ± 05.98
9	-13.39 ± 09.48	-13.18 ± 13.90	-04.50 ± 04.86	-16.50 ± 09.45

of 5 nm were simulated. Unwanted peaks or spectral shifts caused by the pairing of other rings are avoided by imposing the condition of destructive interference between the resonators. In fact, to have a pairing the coherence length between adjacent rings should change by $1/2\pi R = \frac{\lambda}{4n_{eff}^2}$, that in the telecom window and for a TM polarization means $\simeq 200$ nm. If a non tapered structure would have been used, random pairing of rings would have occurred and unwanted CRIT resonances would have appeared in the stop-band, as experimentally observed in section 4.4.1.

A summary of a statistical analysis over 100 realizations of CRITAD with different randomness and several ΔR is reported in Tab. 5.3. Here we show the losses and crosstalk induced by fabrication errors. By increasing the fabrication errors we note an increase in the channel losses due to the random fluctuations of the CRIT resonance. The channels are completely smeared out when the losses and crosstalk have the same value.

A good robustness to fabrication errors of 3 nm is observed for both bandwidths. The 22 GHz one shows a very good strength up to 9 nm of error. The performances deteriorate for larger fabrication errors, especially when small bandwidths are required. These simulations show that the application of these devices in UDWDM requires an extremely accurate and stable processing.

5.7 CRITAD based multiplexer/demultiplexer

The possibility given by the CRITAD to have multiple narrow channels inside the same stop-band suggests to look for applications in Wavelength Division Multiplexing. Here, we discuss a design which yields a mux/demux.

Figure 5.17(a) shows a schema of a $4 \times 1/1 \times 4$ mux/demux. This structure consists of a combination of 4 cascaded CRITAD. Each one is designed to have only one CRIT channel by pairing only two resonators in ChC ($L_c = \pi R_m$) while all the others are coupled in

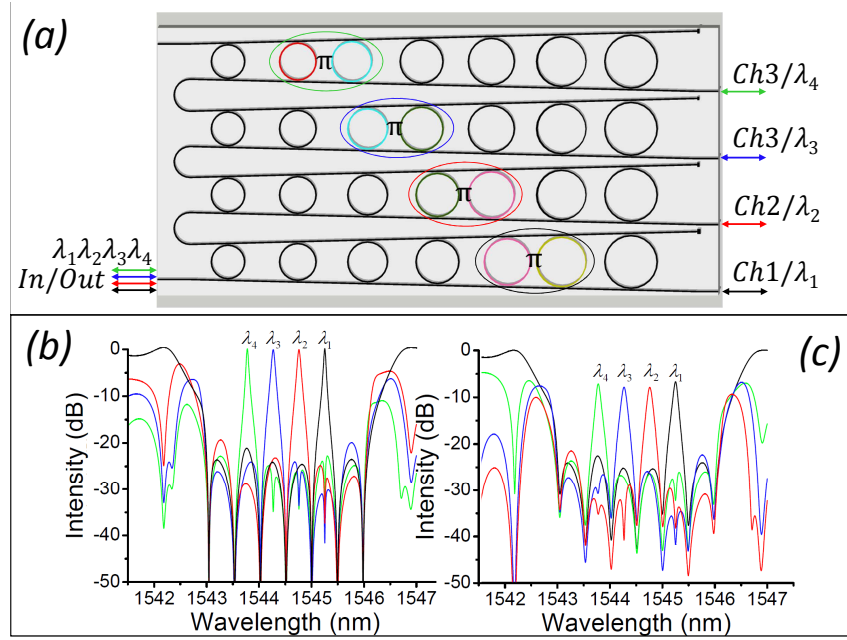


FIGURE 5.17: (a) Schema representing a 4×1 (1×4) multiplexer (demultiplexer) based on *local* method CRITAD, composed by 7 resonators, in which the colored circles identify the pair that does CRIT and then creates a channel. (b) Simulated spectral response, without considering losses, of the 4 channels in which the colors are linked to the schema of the structure. (c) Simulated spectral response, considering losses of $0.008 \text{ dB}/90^\circ$. The parameters used are $R = 6.75 \mu\text{m}$, $\Delta R = 5 \text{ nm}$, coupling coefficient 23% .

an out of ChC ($L_c(m) = \frac{3}{2}\pi R_m$). Figure 5.17(b) shows the transmitted signal out of the four output ports when no propagation and bending losses are considered. Figure 5.17(c) shows the same when $0.008 \text{ dB}/90^\circ$ of bending losses are assumed. When the input signal has a wavelength within the stop-band but different than the CRIT condition, it crosses all the CRITAD. On the contrary, when the input signal has a wavelength which satisfies the CRIT condition for anyone of the 1-4 channels it is transmitted in the corresponding output channel. Clearly, the structure can also work as multiplexer if the four outputs are used as inputs: in this case four different wavelengths within the CRITAD stop-band are channelled into the single output waveguide (from right to the left in the figure).

Note that the channels have similar insertion losses (channels balanced) and also that the effect of losses is to slightly increase the crosstalk ($< 20 \text{ dB}$) while keeping acceptable insertion losses of $7-8 \text{ dB}$. These figures are obtained for channel separations $< 60 \text{ GHz}$ and a channel bandwidth of 12 GHz . If larger bandwidths are acceptable, (e. g. 38 GHz which is obtained by a $\Delta R = 10 \text{ nm}$), similar crosstalk values are obtained but the channel losses decrease to about 3 dB . It is straightforward to expand this design to a $1 \times N$ mux/demux by increasing the number of rings and CRITAD. Note that the channel spacing is related to the ratio $\frac{\Delta R}{R}$ thus, since nowadays the minimum ΔR is

fixed by the lithography accuracy to 5 nm , the only way to increase this value is to enlarge the ring radius or to use an active tuning system.

Finally, it is also possible to turn on/off one channel, without disturbing the others (hitless), by changing locally the refractive index of a ring in the pair that does CRIT as shown in section 5.4. Control of the ring refractive index, can be achieved with an integrated heater or an integrated p - n junction.

5.8 CRITAD based 2x2 router

Another possible application of the proposed CRITAD design is the realization of a hitless 2×2 router.

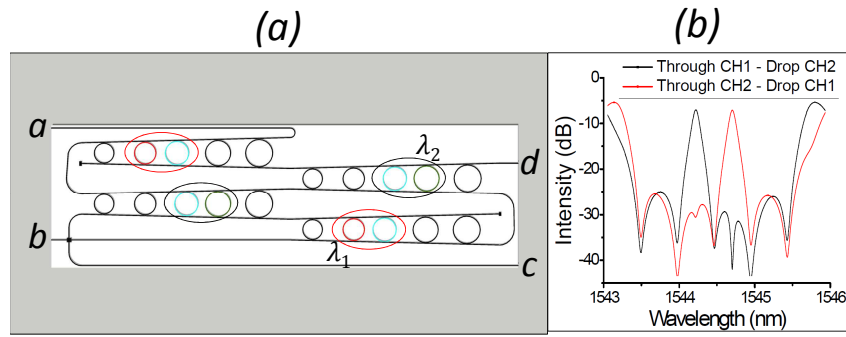


FIGURE 5.18: (a) Schema representing a 2×2 router based on local method CRITAD, composed by 5 resonators, in which the colored circles identify the pair that does CRIT and then creates a channel. (b) The black (red) curve represents the simulated spectra obtained with $\lambda_{1(2)}$ that passes through the transparency of CRITAD 1(2) and the resonance of CRITAD 2(1).

TABLE 5.4: Table of routing of the structure. The parameters used are $R = 6.75\ \mu\text{m}$, $\Delta R = 5\text{ nm}$, coupling coefficient 23% and bend losses $0.008\text{ dB}/90^\circ$.

		Out			
		a	b	c	d
In	a	\times	\times	λ_2	λ_1
	b	\times	\times	λ_1	λ_2
	c	λ_2	λ_1	\times	\times
	d	λ_1	λ_2	\times	\times

To build a 2×2 bidirectional router one needs four CRITAD, each couple of which has the same CRIT resonance. The four CRITAD are arranged as in Fig. 5.18(a). Each CRITAD is composed by 5 rings and, in this implementation, it is designed by using the *local* method. In the sketch, the CRITADs which have the CRIT resonant on channel 1 (λ_1) are circled in black while the other two in resonance with channel 2 (λ_2) are circled in red. All the inputs a , b , c , d are bidirectional. For each input is associated only

one output where the selection is determined by the input signal wavelength. If the signal is injected at input b with a wavelength λ_1 , it is dropped by the first SCISSOR it encounters and it is transmitted to output c by the next CRITAD. Figure 5.18(b) shows the transmitted signal from port a and b to port c and d as a function of the wavelength. It is observed that only a specific wavelength entering in a given input port can be routed to a given output port.

The Table 5.4 shows the correspondence among the various inputs/outputs. This structure is bidirectional and antisymmetric with respect to a change of the inputs with the outputs. For the assumed parameters, it can handle signals of 12 GHz bandwidth with channel losses of 7 dB and crosstalk of less than 21 dB .

Also here, it is possible to modify the router into an active one by changing locally the refractive index of a ring in the pair that does CRIT as shown in section 5.4.

5.9 CRITAD vs ADF

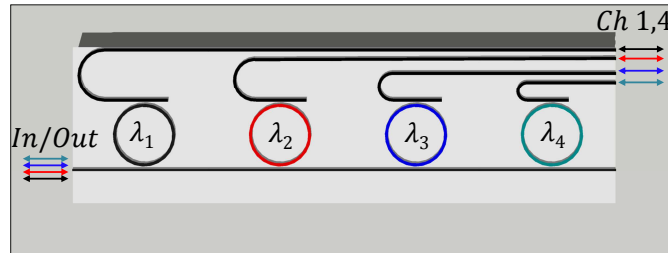


FIGURE 5.19: Schema representing a 4×1 (1×4) multiplexer (demultiplexer) based on ADFs.

We are going to make a detailed comparison between the multiplexer shown in section 5.7 and the multiplexer based on ADF sketched in figure 5.19. The simulation parameters are the same used in the lossy CRITAD multiplexer: the most important are $\Delta R = 5\text{ nm}$, $CC = 23\%$ and $\alpha = 0.008\text{ dB}/90^\circ$. The mux based on ADFs uses equal parameters, included the ΔR to shift the resonances, apart from the CC : the CC is reduced to the value of 0.7% in order to reach the same bandwidth of the CRITAD, 0.06 nm . The spectral response of the ADF multiplexer is always showed with a grey dashed line while that of the CRITAD mux by colored lines (for each channel). The spectra of both structure, ADF and CRITAD, for the case of, $\Delta R = 5\text{ nm}$ (a) and $CC = 10\text{ nm}$ (b) are reported in figure 5.20.

Essentially, the two designs are equivalent in terms of channel loss ((a) -6 dB , (b) -3 dB). Regarding the cross talk, it depends on how this is defined: if it is defined as the

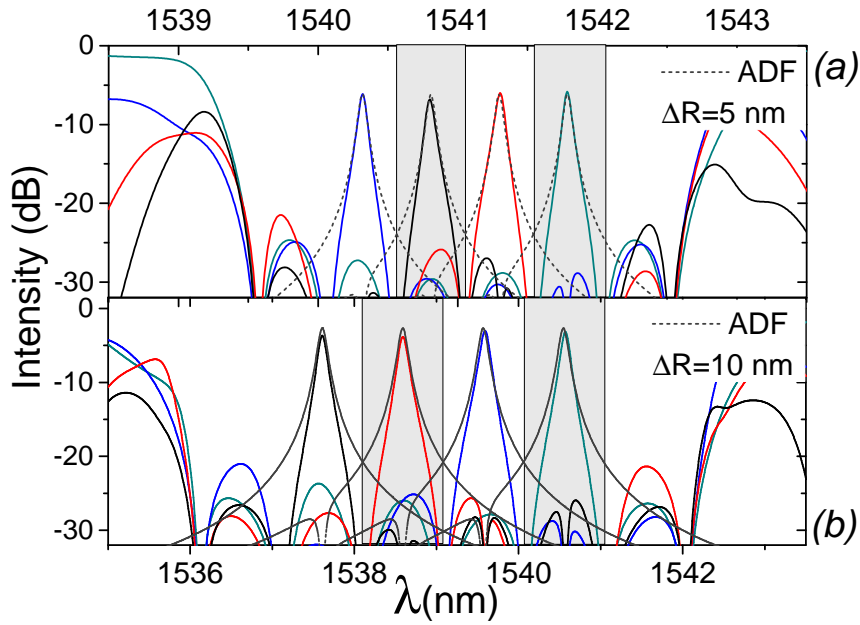


FIGURE 5.20: Transmission spectra in dB of T port for CRITAD mux (colored lines) and for the ADF mux (grey dashed lines) for a $\Delta R = 5$ nm (a) and $\Delta R = 10$ nm (b). The grey rectangles define the channel width: (a) 0.5 nm, (b) 1 nm.

maximum intensity inside the adjacent channel, the cross-talk is then slightly better for the CRITAD. If it is defined only at the center wavelength of the channel, then the cross-talk better for the ADF mux.

The switching is where the CRITAD is superior because of the feedback by the other cavities. In the ADF case the switching is performed through a variation of the radius of the second resonator, that in this case is chosen positive. A comparison between the ADF and CRITAD switching behaviour as a function of the relative variation of L_c , $\Delta L_{rel} = \frac{\Delta L_{eff}}{L_c}$, and of R , $\Delta R_{rel} = \frac{\Delta R_{eff}}{R}$ is reported in figure 5.21. The same ΔR_{rel} is chosen for both the cases of ADF and CRITAD. The "open" channels are in grey while the "closed" is in light red.

The following points can be highlighted :

- Fig. 5.21(a): despite the switched CRIT (red line) is pushed to the red, it falls off before reaching the channel 3. In the meanwhile, an hump ruins the crosstalk in the channel 1. A possible enhancement of this method can be achieved by an increases of the CC during the switching procedure only on the involved resonator. Going from a CC of 26% to a CC of 36% gives a improvement of 4dB in both the ER and the crosstalk (refer to table 5.5 for the details). On the contrary, the second resonance of the mux ADF (grey line) is shifted linearly to the red and crosses the

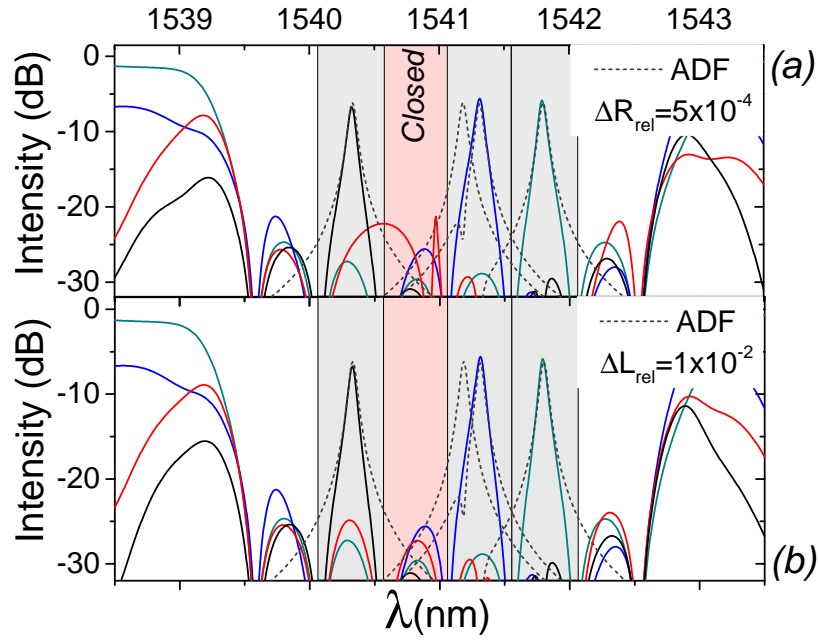


FIGURE 5.21: Transmission spectra in dB of T port for CRITAD mux (colored lines) and for the ADF mux (grey dashed lines). Switching of the channel 2, light pink rectangle, under a ΔR_{ref} variation (a) or a ΔL_c variation (b).

channel 3. For a given relative variation ΔR_{rel} , the ADF moves much more. Also this fact contributes to the robustness of the CRITAD to the fabrication defects.

- Fig. 5.21(b): In this case the ChC of the channel 2 is changed. For a complete shift of π to $\pi/2$, that corresponds to a $L_{rel} = 10^{-2}$, the channel is completely switched off with a minimum influence on the other channels. In this case the spectrum remains very clean and the switching process is far better than the ADF one. The drawback is that the switching efficiency, as already shown in section 5.4.2, is low (Tab. 5.5). However, if we accept a crosstalk increases of $3dB$, the required ΔR_{rel} drops to 4×10^{-3}

The ER, crosstalk and switching efficiency are summarized in the table 5.5. Values were calculated at the wavelength of the center of the resonances (i.e. the wavelength at the half of a channel) which is the worst case scenario for the CRITAD. For the crosstalk calculation, it has been considered the channel nearby the second that shows the worst performance.

5.10 Experimental investigation

In this section, we will show the measured performance of the CRITAD device. We will investigate on a device based on RTR that exploits the Bragg method. Several

TABLE 5.5: Performances comparison between the mux CRITAD and the mux ADF. ER: minimum at the resonance wavelength of the close channel 2 minus the maximum at the same wavelength for open channel. Crosstalk: minimum at the resonance wavelength of the channel 3 or 4 minus the maximum at the wavelength of open channel 2

Ch2	Switch ER (dB)	Crosstalk (dB)	Δx_{rel}
ADF	-21	-12	5×10^{-4}
CRITAD ΔR_{eff}	-20	-19	5×10^{-4}
CRITAD ΔL_{eff}	-21	-19	$10 - 4 \times 10^{-3}$

samples were fabricated which were based on both the local method and the Bragg method. Unfortunately, only devices based on the Bragg method were working due to a manufacturing error. All the local devices were based on RR to work in TM polarization but the SOI wafers on which they were built was found to have only $1\mu m$ of BOX. Consequently, the TM mode appears to have high losses because of the coupling with the substrate. Since theoretically, the local method shows superior performance, wide margins of improvement are expected to the results that are here reported.

First it will be shown the spectrum of the Bragg CRITAD, after that its switching behaviour will be tested by using both ΔR and ΔL_c method. By carrying out several measurements on different samples, the robustness of the structure to the fabrication defects will be studied. Finally, we show the proof of concept of the multiplexer proposed in section 5.7 .

After these series of stationary measurements, the dynamical switching capability will be investigated using a visible pulsed laser as perturbation medium.

5.10.1 Bragg based CRITAD: Transmission spectrum

The studied device is reported in figure 5.22 . It is a CRITAD based on the Bragg method. It consists of seven RTR that differ for a ΔR of $10 nm$. It integrates also a metallic "omega" heater placed above the third RTR . The red square identifies the active RTR pair that provides the open channel $Ch3$ through the correct choice of $L_c = \pi R(3) + \Delta R/2$. The fabrication parameters are reported in table 5.6.

TABLE 5.6: Device parameters

Parameter	Gap	R	ΔR	c_s	L_c	w	Polarization
Racetrack	$160nm$	$3.25\mu m$	$10 nm$	$7\mu m$	$10.195\mu m$	$450nm$	TE

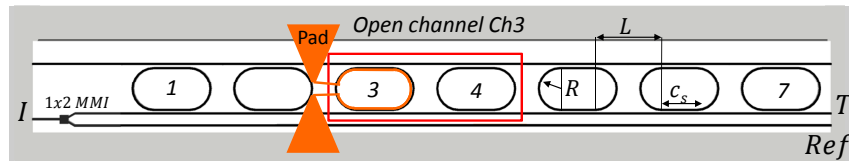


FIGURE 5.22: Sketch of the studied device, composed of 7 RTR numbered from left to right. The orange layer identifies the metallic omega heater above the third RTR. The red square identifies the active RTR pair that provides the open channel *Ch3*. The construction parameters are reported in table 5.6. The differences between the RTR, due to the ΔR , are not reported in figure.

The transmission spectrum for the T port normalized to the reference is shown in figure 5.23 . The spectral measurements are performed as usual using the transmission setup reported in the appendix B.0.5.

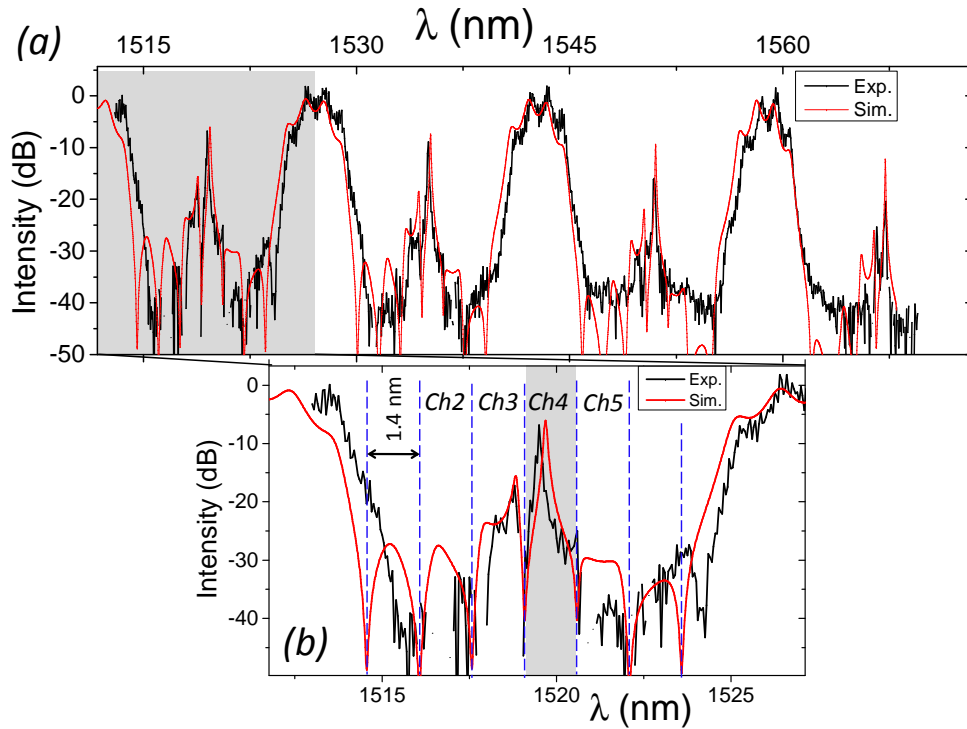


FIGURE 5.23: (a)(Black) Measured spectrum of the T port normalized to the Ref port performed in the spectral range of $1510\text{nm} - 1570\text{nm}$. (Red) TMM simulation. (b) Zoom of the grey area in (a): the blu dashed lines delimits the channels from Ch2 to Ch5. Simulation parameters are reported in table 5.7.

The spectrum in Fig. 5.23 indicates that the BB is shifted to the red, since the open channel seems to be the Ch4. In reality it is the RB that undergoes a blue shift caused by the bend-straight index mismatch. This fact was not taken into account during the design of the device. From the TMM code it is extracted an index variation for the bent mode of -0.006 that is comparable with the values reported in section 2.4 . Thus, a

lower coherent length, $L_c - \delta L_c$ with $\delta L_c \sim 26 \text{ nm}$, should be used in order to take into account this effect and to correct the optical response of the device. It is important to note, how there are no more localized states, as it was in the case of SCISSOR, other than that selected by the BB despite the random 5 nm error of the lithographic process.

TABLE 5.7: TMM simulation parameters

	Gap	R	ΔR	c_s	L_c	w	n_{eff}	δn_b
TE	140 nm	$3.25 \mu\text{m}$	10 nm	$7.2 \mu\text{m}$	$10.195 \mu\text{m}$	450 nm	$2.315 - 2.309$	-0.006

With a CC that spans from 49% to 67% the resulting line width of CRIT goes from 0.11 nm (12 GHz) to 0.07 nm (9 GHz). The channel loss is about -7 dB and the cross talk -12 dB . It has to be considered that these values are obtained for a non optimized structure and that the local method should provide superior performance. Despite the relatively high Q of 22000 and the TE polarization, no sign of mode splitting is visible.

In the next section, we will demonstrate the switching through ΔR variation.

5.10.2 Switching capability: ΔR method

The electrical connection to the optical chip is provided by two metal tips that are placed in contact with the pads. The heating power is then measured by looking at the current and the voltage provided to the chip by the power source and calculated using the Ohm's law (setup details are shown in appendix B.0.7).

To calibrate the modulation efficiency of the heater, we measured a test device based on a simple RR as shown in figure 5.24. A linear fit of the resonant wavelength as a function of heating power gives a slope of $0.2194 \pm 0.0007 \text{ nm/mW}$. Dividing by λ the relative variation is derived, $\frac{\Delta\lambda}{\lambda}/\text{mW} = 1.4 \times 10^{-4}$. Using the thermo-optic coefficient of silicon $1.86 \times 10^{-4} \text{ K}^{-1}$ an estimate of the ring temperature can be obtained, $\sim 2.5 \text{ K/mW}$. This is an approximate value since the resonance shift is linked to a mode effective index variation.

In the previous section we showed that the structure was designed to switch off the Ch3 through a modulation of the third RTR. But, because of the bend index mismatch, the open channel is the fourth. Thus, in order to switch the Ch4, through a modulation of the third RTR, an extra heating power is needed. The measures show a switching threshold of about 1.8 mW . Thus this value is subtracted from the estimated power necessary to switch the channel. In the simulations, the effect of the thermal tuning is

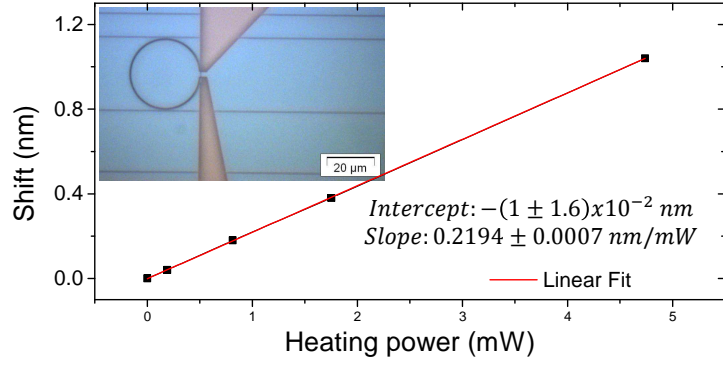


FIGURE 5.24: Calibration curve for the omega heater: resonance shift as a function of heating power (black squares) . (Red line) linear fit. The insert contains a photo of the fabricated device.

treated as a change in the optical path of the RTR, Δp . The variation is distributed along the radius and the coupling section through a weighted mean calculated as follows:

$$\frac{\Delta p}{p} = \frac{\Delta p \frac{2c_s}{p} + \Delta p \frac{2\pi R}{p}}{p} \quad (5.4)$$

The new functionality introduced by the CRIT is the fact that the resonance is switched off without a significant wavelength shift. Typically, with 1.6 mW of electrical power injected in the heater, we fully switch off the resonance with an estimated variation in the refractive index of $\Delta n = 7 \times 10^{-4}$. This is shown in figure 5.25.

As done before, we define the transmission channel as the spectral region centered on a CRIT resonance and with a width equal to the separation between two nearby CRIT resonances (spectral width $1.4 \text{ nm} \sim 180 \text{ GHz}$ fixed by $\frac{2\pi\Delta R}{p}$). This channel is named Ch4, while the adjacent channels Ch3 and Ch5. Figures 5.25(a) and 5.25(b) show that the CRIT resonance attenuates within its transmission channel as the heater power increases. The maximum transmission intensity at the CRIT wavelength decreases by more than 10 dB. If we define extinction ratio as the ratio of the integrated transmitted signals in the on and off states, an extinction ratio of 4 dB is observed due to the appearance of side peaks. On the other hand, the cross talk, defined as the ratio between the integrated transmission on Ch5 to that of Ch4, shows a weak dependence on the heater power and starts from a value of 15 dB to reach a value of 13 dB at the maximum extinction ratio (data shown in Fig. 5.26). The CRITAD allows addressing the single resonator without significant changes in the collective behavior of the resonator sequence. The thermal tuning of a single resonator does not affect the spectral position of the CRITAD stop-band (inset of Fig. 5.25 the blue edge shifts only by 0.1 nm, while the red edge does not shift). Furthermore, even using a non optimized heater, the power

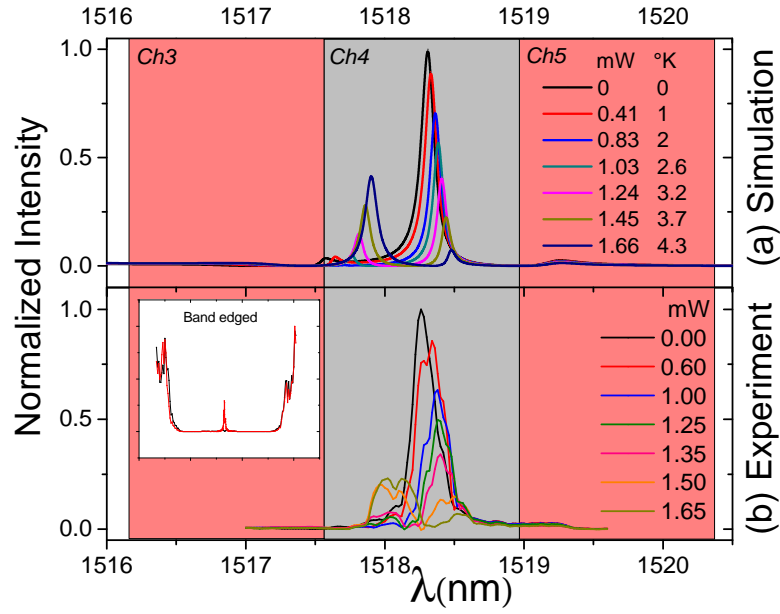


FIGURE 5.25: Simulated (a) and Experimental (b) T port transmission spectra for various heating power. The grey area defines the active channel, *Ch4*, while the light red area define the two nearby closed channel, *Ch3*, *Ch5*. The inset shows the position of the band edges at $0mW$ (red) and $1.5mW$ (black).

required to switch a CRIT resonance is of the order of $1.5mW$ (without considering the power threshold since it is present for a design mistake).

The measured and simulated switching performances are reported in figure 5.26.

In general there is a good agreement between simulation and experiment. Small discrepancies may be due to the presence of manufacturing defects that can not be included in the TMM code with a deterministic approach.

5.10.3 Switching capability: ΔL_c method

The other tuning possibility offered by the CRITAD geometry is the L_c switch. In fact, the CRITAD based on the Bragg method is affected by the collective properties of the SCISSOR sequence, i. e. by the Bragg condition. Figure 5.27 shows a CRITAD where serpentine heaters are overlapped with the side WGs (coupling section excluded). In this way, the L_c of the WGs is modified and, therefore, the Bragg stop-band is shifted within the stop band of the structure (Fig. 5.27(a)).

Since the TOE is used as a method of tuning, the BB undergoes only to red shifts (sketch of Fig. 5.27 (a)). Therefore, we looked for a structure that, despite the design error on L_c , it shows the Ch3 at least partly open. This is possible because of the dose sweep

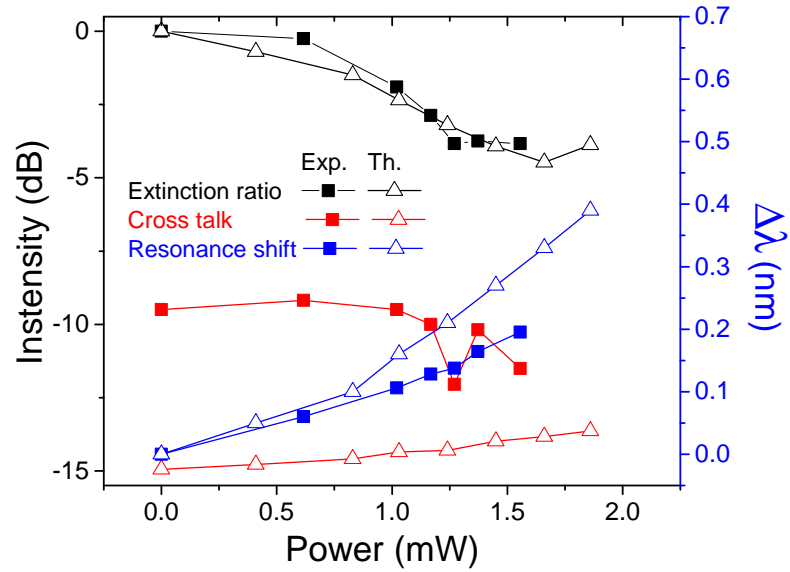


FIGURE 5.26: Extinction ratio of Ch4 (black squares), cross talk of Ch4 to Ch5 (red squares) and shift of the CRIT resonance in Ch4 (blue squares) as a function of the heater power (open triangle symbols refer to simulation values).

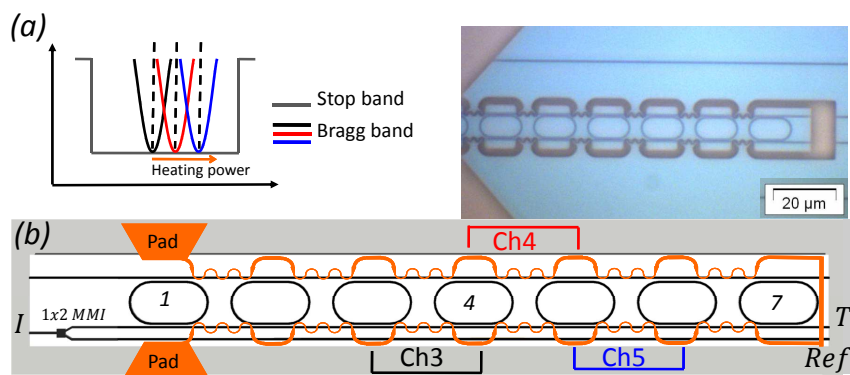


FIGURE 5.27: (a) A sketch of the operating principle is shown. (b) Scheme of the device under study and its photo: the orange drawing represents the heater serpentine. The black, red and blu lines indicate the pairs involved in the creation of the channel Ch3, Ch4 and Ch5 respectively.

along the wafer and the manufacturing defects that together mixes up the structure parameters around its nominal value. In this way, the selectable channels by means a small shift of the BB are maximized. This is convenient from an experimental point of view since, the larger the shift the greater the possibility to burn out the metal tracks. In fact, a fit on the "cold state" spectrum in figure 5.28 suggests an L_c of $10.185\mu\text{m}$ that lacks of 16nm the target optimal value.

Shifting the Bragg resonance selects a different racetrack pair for the CRIT resonance. This effect is confirmed in Figs. 5.28(a) and 5.28(b) where, by increasing the injected power in the heater, we switch different channels. Experimentally, the n -th channel is switched by changing the heating power until the transmission is maximum in the channel $n + 1$ and minimum in the channel n .

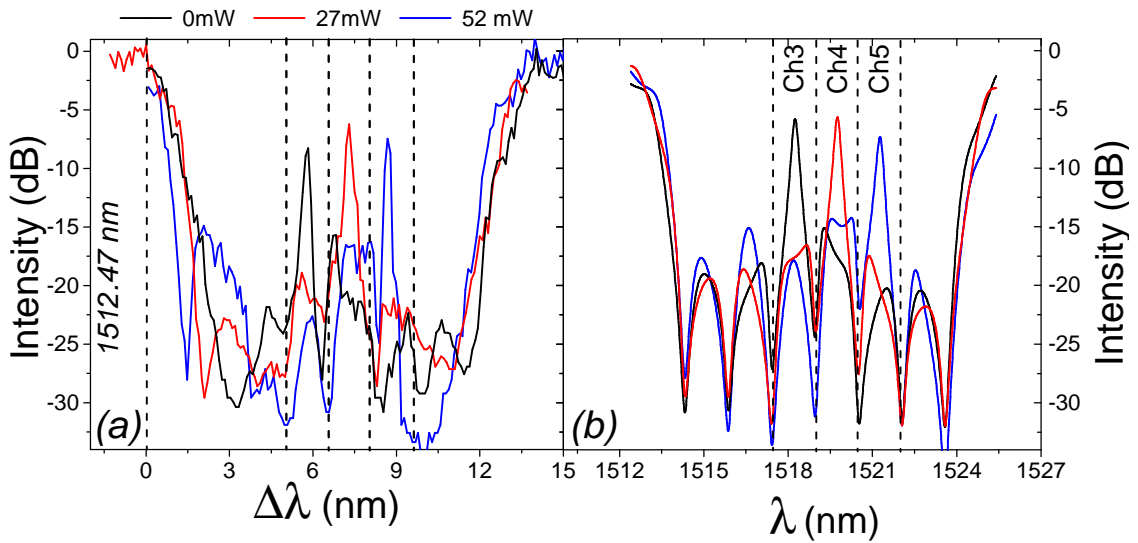


FIGURE 5.28: Through port transmission for different heater powers: 0 mW (black), 27 mW (red), 52 mW (blue). Dashed lines delimit the widths of the channels. (a) Experimental T port transmission for the CRITAD. (b) Simulated data. The different lines correspond to $L_c = 10.185\mu\text{m}$ (black line), $10.205\mu\text{m}$ (red line) and $10.220\mu\text{m}$ (blue line).

It has to be noted that because of the proximity of the thermal heater to the cavities, the resonators are heated too. This causes a rigid shift of the entire resonator stop band of about 2 nm . Therefore, to clearly underline the effect of heating on the single channel we rigidly shift the spectra and assume the low energy resonator band edge as the zero of the wavelength axis .

Normalized spectra are then reported as a function of the wavelength shift from this common point(Fig. 5.28). It is clear that the main spectral features are largely unaffected by the resonator heating. The heat diffusion can be easily solved by using a larger separation between the resonators or a better heater design.

The switching efficiency, $26mW/Ch$, is rather high, respect to the ΔR case, because of the large area covered by the heater. There is an optimal agreement between the experiment and the simulations. The performances of the device in terms of channel loss and cross talk are reported in table 5.8

TABLE 5.8: Bragg CRITAD switch performances: ΔL_c method

	<i>Ch3</i>	<i>Ch4</i>	<i>Ch5</i>
Loss (dB)	-8.3	-6.2	-7.5
Crosstalk on Ch3 (dB)	-	-10.6	-14.4
Crosstalk on Ch4 (dB)	-9.6	-	-10.5
Crosstalk on Ch5 (dB)	-15.3	-14.8	-

5.10.4 Robustness to fabrication defects

Figure 5.29 reports data of ten nominally identical CRITAD taken randomly on various wafer dies. In all the spectra, the CRIT resonance is observed. Even if, we claim that this structure is robust to the local fabrication defects (that acts on a local parameter of the structure) this is not true for the medium range defect, as the variation of the SOI thickness. This is a global variation and acts in equal manner on all the structure parameters caused by the modification of n_{eff} . This problem can be fixed only by using an active approach or a permanent post-trimming process [89]. However, since this effect has a long range variation (about a couple of mm), nearby devices are not affected by this problem. Since now we are interested in the local robustness, we align the low wavelength edge (maximum shift of $\sim 5nm$) of the T transmission stop band of the various CRITAD to take into account the typical variation of the silicon thickness in a SOI wafer.

The design seems to be quite robust against the local defects. The transparency peak instead of moving out of its channel space, the grey area of figure 5.29, it is rather attenuated. Also the rest of the stop band remains free of unwanted localized state. Considering that this device is affected by a design error and that the local method should provide better performance, the results reported in table 5.9 are widely improvable.

TABLE 5.9: Statistical analysis results: parameter given as $mean \pm STD$

Channel center dispersion (nm)	Channel loss (dB)	Cross talk (dB)
0.13	-5.4 ± 2.5	-10 ± 4

The value of the channel center dispersion of the CRIT resonance could be affected by the post-process trimming of the resonators.

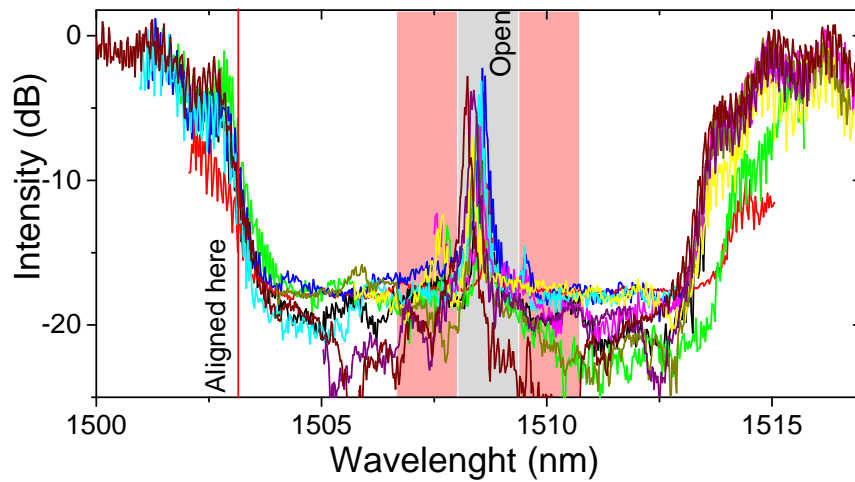


FIGURE 5.29: T port transmission spectra of ten equal CRITADs chosen randomly on a 200 mm wafer. Open channel area is highlighted in grey.

5.10.5 Proof of concepts of the 1x4 CRITAD based multiplexer

Finally, we demonstrate a 1x4 demultiplexer by using a cascaded sequence of CRITAD (Fig. 5.30). Each CRITAD has the same racetrack sequence but different L_c . The device was already explained in section 5.7.

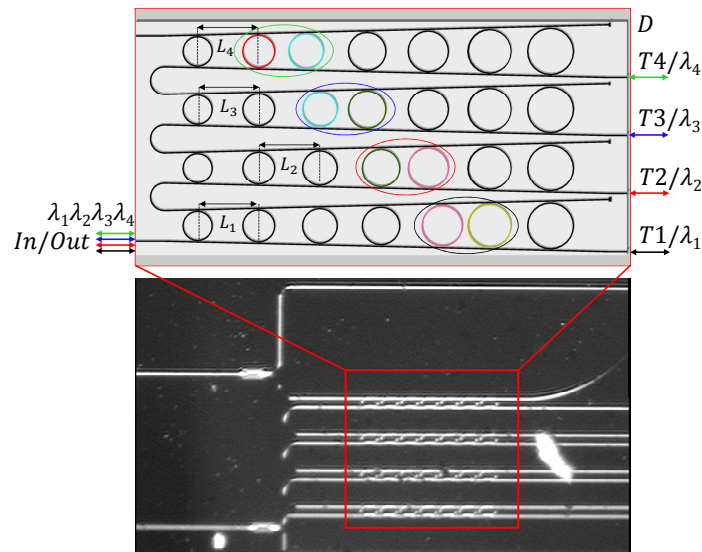


FIGURE 5.30: Sketch of the 1×4 mux/demux composed by 4 CRITAD cascaded via the drop waveguide. For the sake of simplicity, the sketch shows RR instead of RTR. The design parameters are $R = 3.250\mu m$, $C_s = 7\mu m$, $gap = 160nm$, $R = 10nm$, $L_1 = 10.265\mu m$ (T1, black), $L_2 = 10.225\mu m$ (T2, red), $L_3 = 10.195\mu m$ (T3, blue), $L_4 = 10.155\mu m$ (T4, green). Below, a photo of the sample.

Therefore four different CRIT channels open. Since the four CRITAD differ solely for a 0.3% variation in L_c , the wide resonator stop band of each CRITAD remains

largely unaffected and they overlap each others. When the signal wavelength is resonant with the CRIT resonance of a particular CRITAD, the signal is transmitted out of the demultiplexer (ports T1-T4 in Fig. 5.30). Otherwise it is dropped as input to the following CRITAD. Clearly, if the signal wavelength is not resonant with any CRIT resonance it emerges in the output D port. The same structure works as a multiplexer if the input are mirrored.

Figures 5.31(a) and 5.31(b) show the experimental as well as the simulated transmissions of each T1-T4 ports of the 1x4 demultiplexer. Within the overlapping stop-bands, four CRIT channels open (linewidth 8 GHz and channel spacing 155 GHz). Despite non negligible value of insertion losses, CRITAD shows rather low cross talk values. No performance degradation along the sequence is observed which indicates that more CRITAD can eventually be cascaded. It is remarkable that no trimming of the various racetrack resonances is needed and all CRITAD channels are aligned. Considering that, this is the best result of 4 samples measured, it gives us an indication of the device robustness versus fabrication tolerances. In figure 5.31(c) is shown the $T_{1,2,3,4}$ ports spectra of a not working sample. In any case, to achieve an high yield fabrication, a post trimming function has to be applied on the structure with which it is possible to counterbalance the fabrication errors and to switch the channels through the ΔR method.

The 4 channels performances, in term of losses and crosstalk, are reported in table 5.10.

TABLE 5.10: Multiplexer channels performances

	Ch1	Ch2	Ch3	Ch4
Channel loss (dB)	-7.7	-8.1	-9.7	-8.6
Crosstalk to Ch1 (dB)	-	-9	-15	-18
Crosstalk to Ch2 (dB)	-10.5	-	-11.8	-13
Crosstalk to Ch3 (dB)	-11.8	-7.3	-	-12.8
Crosstalk to Ch4 (dB)	-15	-8	-10	-

Compared to other ring resonator based routers our implementation has important advantages:

1. it allows a single channel addressing capability based on a hitless switching mechanism, rather than wavelength shift.
2. it is robust to the fabrication errors.

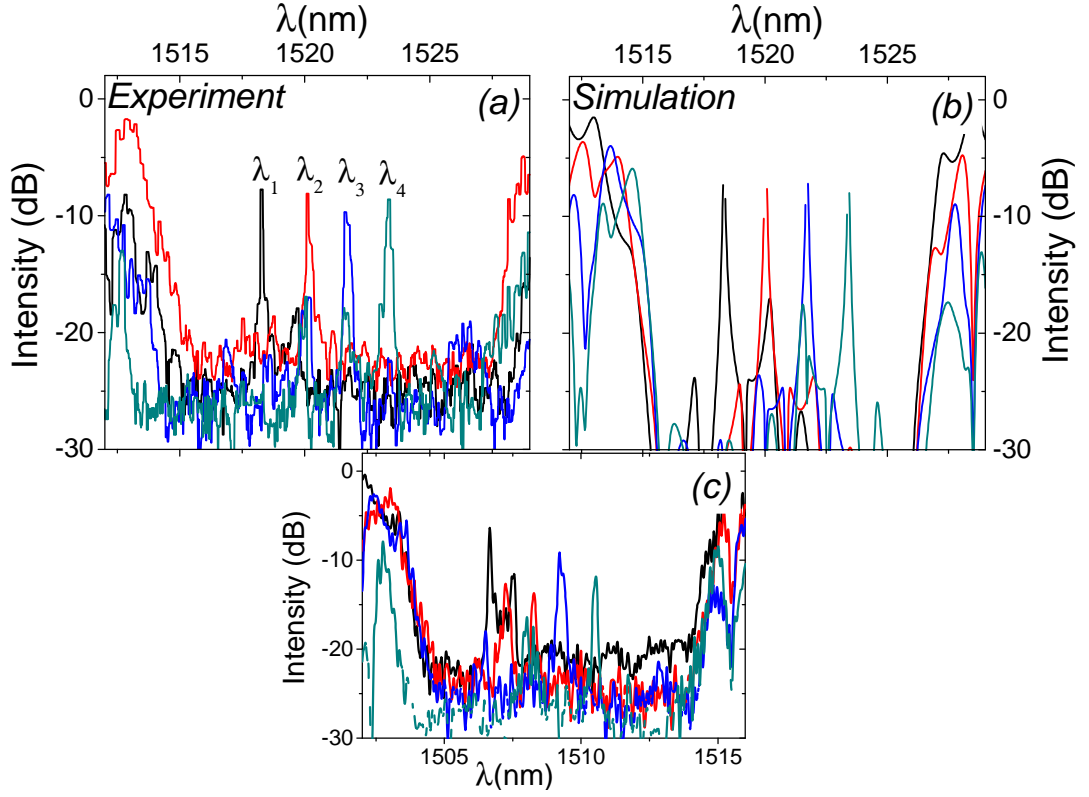


FIGURE 5.31: Each CRITAD is designed to have different CRIT resonances. (a) Experimental transmission spectra for the Through ports: T1 black, T2 red, T3 blue and T4 green; (d) Simulated spectra.

5.11 Dynamic switching capability of the CRITAD

The switching here is provided by an external $Ti : Sa$ visible laser. The measured mean power is about $P_{avg} = 4 mW$ and the repetition rate is $f_{rep} = 1 kHz$ (obtained by means of an acousto-optic bragg grating). Thus, the energy carried by one impulse is $E_p = P_{avg}/f_{rep} = 4 \times 10^{-6} J$. Now, a scale factor A_{tot} , that depends on the geometrical parameters of the structure, has to be included. The silicon absorption coefficient at $800 nm$ is $\alpha_{lin} = 1.02 \times 10^3 dB/cm$. We are interested in the absorption provided by the RTR waveguides that are $220 nm$ tall. The absorbed percentage is found to be only $\Delta P_{abs} \sim 0.5\%$. Also the ratio between the racetrack area and the spot is considered through the factor $A = A_{RTR}/A_{spot} \sim 6\%$.

The total geometrical factor is $A_{tot} = A P_{abs} = 4 \times 10^{-4}$. The energy absorbed by the RTR is then $E_{RTR} = E_p A_{tot}$. If each photon generates a free carrier, the generated free carrier density is

$$\Delta N = \frac{E_{RTR}}{\hbar\omega_p} \frac{1}{V_{RTR}}$$

where ω_p is the frequency of the *Ti : Sa* light emission and V_{RTR} is the RTR volume. In the literature [144] an equation relates the free carrier density ΔN to the silicon refractive index variation Δn , and free carrier absorption $\Delta\alpha_{FCA}$ at $1.55\mu m$:

$$\Delta n = -8.8 \times 10^{-22} \Delta N + 6 \times 10^{-18} (\Delta N)^{0.8}$$

$$\Delta\alpha_{FCA} = 6 \times 10^{-22} \Delta N + 4 \times 10^{-18} \Delta N$$

A $\frac{\Delta n}{n} \sim 0.3$ and a $\Delta N \sim 8 \times 10^{20} 1/cm^3$ are found. The value of ΔN is more than enough to induce a switch-off of a CRIT resonance in a system that requires a $\frac{\Delta n}{n} \sim 10^{-4}$.

Probably this value is overestimated because of:

- the reflections on the sample surface
- the losses that exist along the *Ti:Sa* path to the sample (refer to the appendix B for more details on the set-up)
- the uncertainty on the spot dimension of the *Ti:Sa* laser.

During the experiment, neutral filters are used to regulate the power of the *Ti:Sa*.

5.11.1 Experimental setup

Here we want to observe the switching speed of a CRITAD channel, by using the ΔR method, through free carriers injection (negative refractive index variations). This is achieved by focusing a *Ti : Sa* laser on the 5-th RTR.

The setup is divided into a transmission setup (B.0.5), to probe the device, plus a pump setup (B.0.6), to perturb the local refractive index of the 5-th racetrack.

- Transmission setup. We probe the system with the infrared tunable laser Tunics BT, which has a tunable range from $1510nm$ to $1630nm$, with $5mW$ of maximum power. The laser is interfaced to a single-mode fiber coupled to a polarizer and, then, to a tapered fiber tip to inject the signal into the device. We use a nanometer piezoelectric XYZ positioning system to align both fiber tip and sample. Firstly, a spectrum is performed to find the position of the CRIT resonance. Then, we maximize the signal to center the CRIT resonance. The detection is provided by a fast APD connected to an oscilloscope characterized by a bandwidth of $7GHz$ and $6GHz$ respectively.

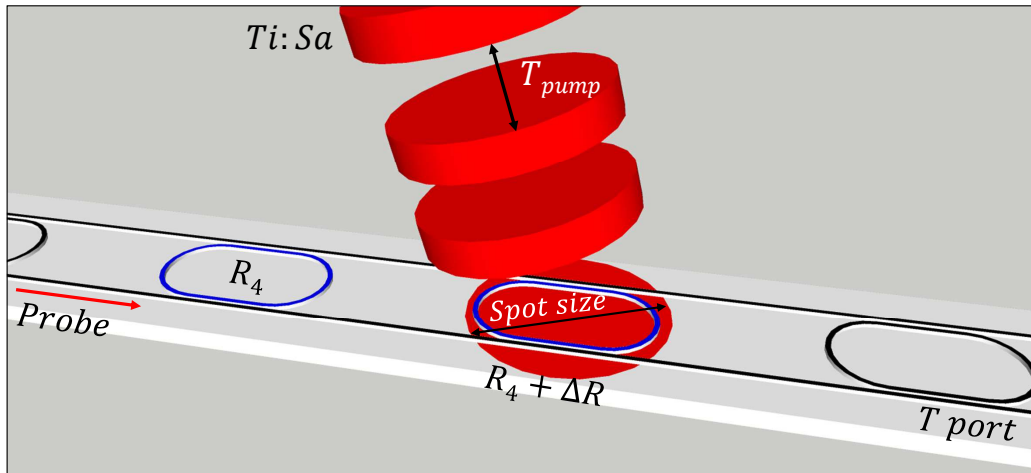


FIGURE 5.32: Sketch of the experimental setup. The blue RTR identifies the pair that generates the CRIT. *Ti:Sa* repetition rate $1/T_{pump}$.

- Pump setup. The in-air laser beam of the Ti:Sa laser is focused by means of an infinity corrected objective onto the 5-th resonator of the CRITAD (blue pair in Fig. 5.32). The Ti:Sa laser is characterized by a wavelength of $800nm$, a pulse width of about $6ps$, a repetition rate of $1/T_{pump} = 1kHz$ and a mean power of $4mW$. The coarse alignment is performed using a visible camera plus an objective aimed to the CRITAD position. Then, the optimal focus position is found by moving the $10\mu m$ laser spot around the RTR and by maximizing the induced perturbation by looking at the oscilloscope signal.

5.11.2 Experimental results

Once that all the free carriers are generated by the laser pump, their relaxation induces an heating of the sample that in turn modifies the silicon index as a consequence of TOE effect. The two phenomena have very different time scales as shown in figure 5.33: the former is on the ns time scale while the latter in the μs . In fact, we use a repetition rate of $1kHz$ in order to let the system relax, and to avoid cumulative thermal effects.

The thermal fall time is found to be $\sim 20ns$ while the rise time is $\sim 140ns$. It emerges that the thermal dynamic does not just depend on the RTR volume, since the used racetrack should have a fall time of the order of $60 - 80ns$ due to its low mass (for details refer to section 7.5.2). Probably, the pump laser beam can reach also the substrate through the silica layer in the middle of the RTR thus increasing the effective heated volume. The FCD fast dynamic, illustrated in the inset to figure 5.33, is investigated in what follows.

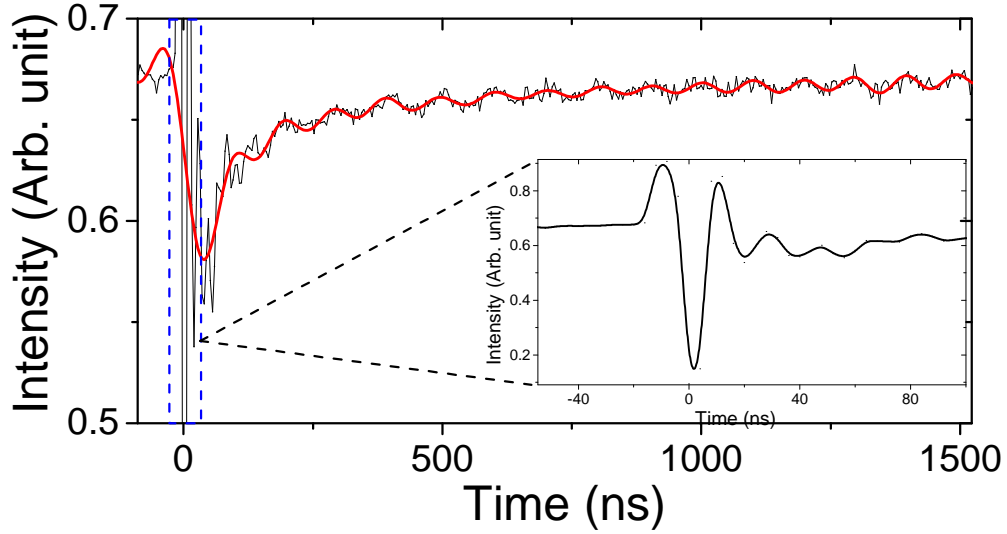


FIGURE 5.33: (Black line) Probe signal as a function of time for a single pulse of the laser pump. (Red line) Filtered signal extracted from the probe detected signal. Inset: zoom of the area inside the dashed blue line.

Here we introduce a very simplified model to describe the time response of a CRIT resonance subjected to refractive index perturbation generated by phenomena with two different time scales. We neglect the FCA for the sake of simplicity. We approximate the system by only two coupled cavities (blue racetracks) considering that we are studying the system close to the CRIT resonance. We neglect also the pump crosstalk between the two cavities due to the finite size of the pump spot.

The model is analogous to that used in section 4.3.1 to describe the eigenmodes of a 2 cavities SCISSOR. Here we inject a CW signal to the input WG, the probe signal, and we model the pump laser as a time dependent variation of the resonant frequency ω_2 of the second cavity (i.e the 5-th RTR) that follows this law:

$$f(t) = (e^{\frac{t-t_0}{\tau_G}} + e^{-\frac{t-t_0}{\tau_R}})^{-1} \quad (5.5)$$

where t_0 is the time at which the perturbation starts, τ_G is the generation time constant of the free carriers and τ_R is the recombination time constant of the free carriers. Through this formula we write the new ω_2 as:

$$\omega_2 \rightarrow \omega_2 \left(1 + \frac{\Delta n}{n} f(t)\right) \quad (5.6)$$

where the term $\frac{\Delta n}{n}$ takes into account the free carrier coefficient dispersion and the number of generated carriers by the Ti:Sa pump. This equation is a sum of two exponentials with different time constants that represents how fast the carriers are generated

and then recombine. The function $f(t)$, calculated with the parameters in table 5.11, is shown in figure 5.35.

TABLE 5.11: CMT simulation parameters

CC	R	ΔR	c_s	ϕ	n_g	$\frac{\Delta n}{n}$	τ_G	τ_R
70%	$3.25\mu\text{m}$	10nm	$7\mu\text{m}$	π	4.1	2.8×10^{-4}	0.13ns	3.8ns

We use, practically, the same geometrical parameters of the RTR, apart for an higher CC to compensate for the lack of feedback given by the other cavities when the probe is out of the CRIT resonance. The complete description of the model, together with the used equations, is reported in the appendix C.

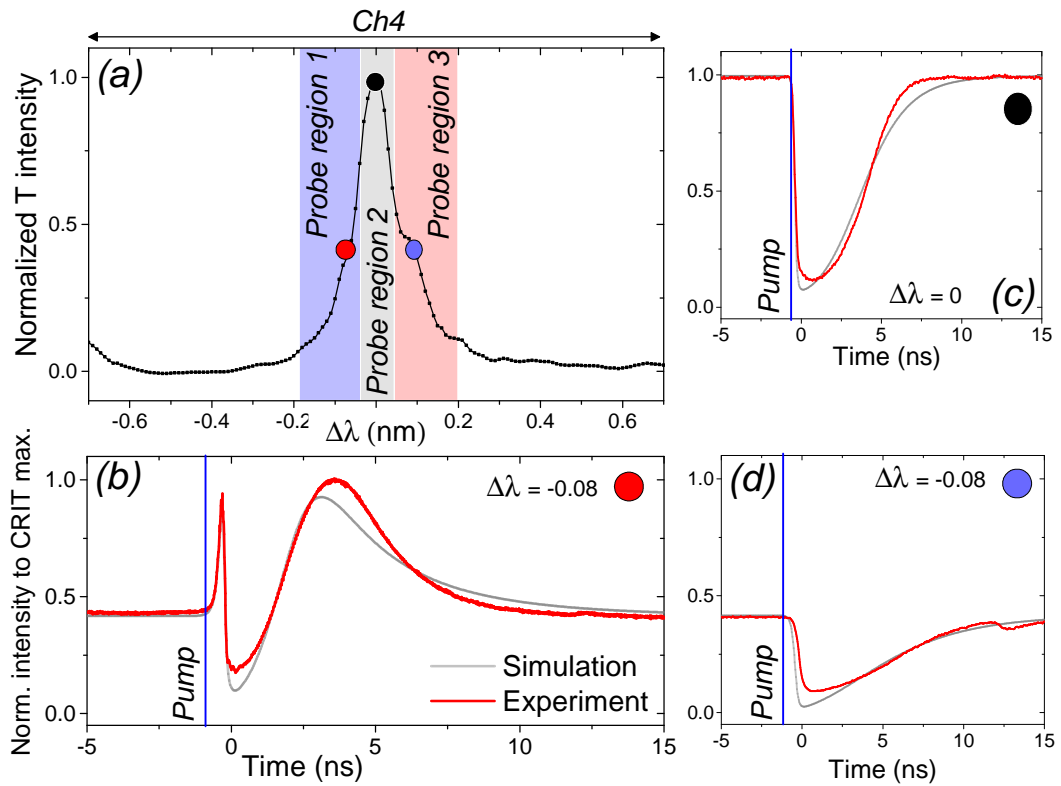


FIGURE 5.34: (a) CRITAD T port transmission spectrum as a function of the detuning to the CRIT center: fine scan on the spectral range of the open Ch4, $\lambda_0 = 1538.35\text{nm}$. (Red line) Experimental and (Grey line) simulated time response of the CRIT for 3 different probe detunings: (b) -0.08nm , (c) 0nm , (d) $+0.08\text{nm}$. The 3 circles identify the spectral points in which the time response is observed. The blue line indicates the point at which the pulse hits the sample. All the spectra are normalized to the CRIT maximum.

In figure 5.34 both the spectrum of the CRIT inside the Ch4 and the dynamic response of the system for 3 different probe detunings (b,c,d) are reported. The system behaviour is characterized by 3 main distinct regions:

- Probe region 1: The probe is blue shifted from the CRIT center wavelength. The time dynamic presents two maximums and one minimum.
- Probe region 2: The probe is in the middle of the CRIT resonance. The time dynamic presents one minimum that represents the switching ER.
- Probe region 3: The probe is red shifted from the CRIT center wavelength. The time dynamic presents one minimum.

Note that the CRIT is switched from the right. The simulations fits well the experiment even if, a very simple model is used. The lack of FCA in the model can be observed in the minimum present in all three temporal dynamics: the minimum point is linked to the ER of the second cavity. The effect of FCA is to lessen the cavity ER. Thus, our model will always overestimate the ER. Also the absence of thermal effect could be the responsible of the other small discrepancies.

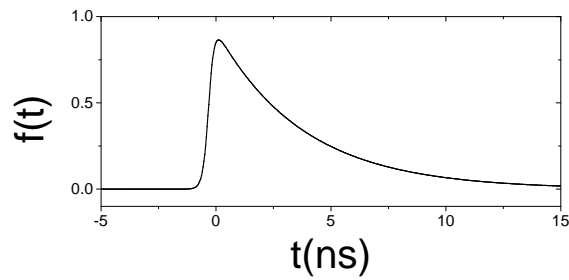


FIGURE 5.35: Shape of $f(t)$ as a function of time calculated with the parameters in table 5.11.

The τ_G was chosen equal to the electronic response time in order to fit the experimental data. In principle, τ_G could be much faster, even of the order of ps . The other two free parameters are adjusted to fit the experimental decay time and the ER. The τ_R is found to be of the order of $3ns$, that is a reasonable value for this kind of system (this value will be used also for the simulation in the section 7.5.2). From the $\frac{\Delta n}{n}$ value we can estimate a carrier density of $1.6 \times 10^{14} 1/cm^3$.

The shape of figures 5.34(b,c,d) can be explained as follows. Take as reference the figure 5.36:

- Panel 1. The system is stationary, and the level of the probe is determined by its detuning from the CRIT (red circle). At a time t_0 (red line, top) the Ti:Sa pump shines on the RTR and therefore, carriers are generated and, in turn, FCD.
- Panel 2. The resonance starts to shift to the blue and begins to approach the CRIT. The CRIT is shifted as well and at this point the probe is in the maximum transmission (blu circle 2).

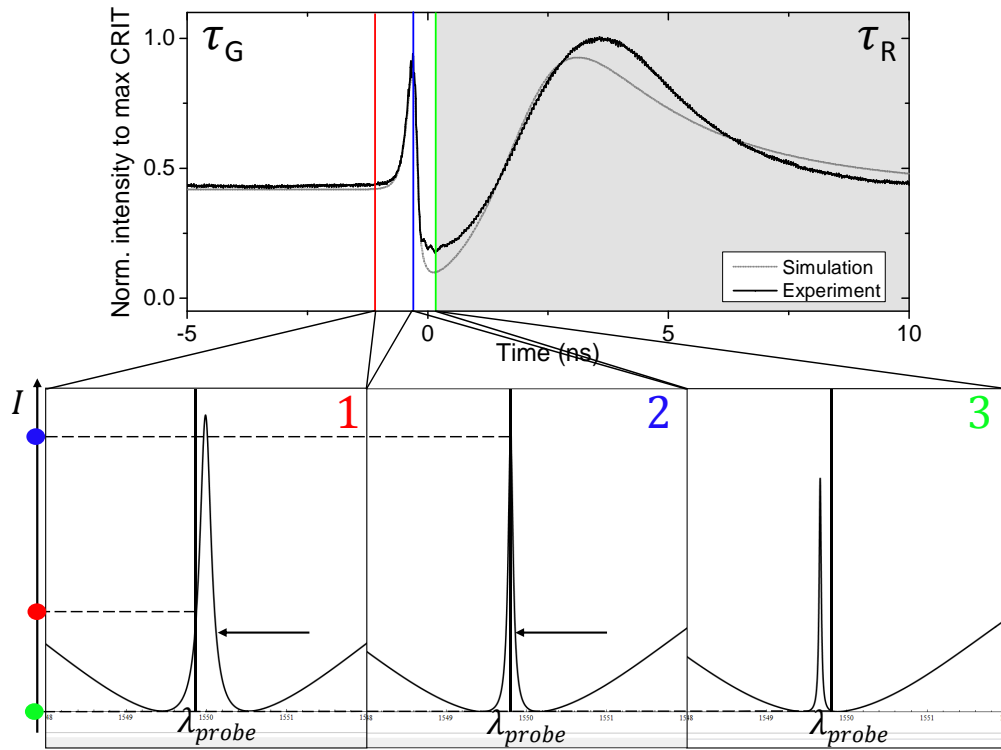


FIGURE 5.36: (top) Probe level as a function of time: (red line) pump on, (blue line) first max of transparency, (green line) end of the forward path. (1,2,3) Panels indicate the spectrum position for three different times.

- Panel 3: The CRIT continues to shift to the blue and the probe now is resonant with the second cavity, i.e. at a minimum of transmission (green circle). This is also the point in which the system stops shifting further and starts to return back, using the same path but with a different time constant τ_R (green line)

The time distance between the two maximums of figure 5.34 (b) as a function of the pump power is expected to be linear. That is because, ΔT_{bf} , that is the time that the cavity takes to go back and forth, depends on two parameters: the $\tau_{G,R}$ and the Δn . Δn is related to how far the cavity is pushed away from the stationary point. Since $\tau_{G,R}$, as a first approximation, does not depend on the power, only Δn is responsible for the variation of ΔT_{bf} . Thus, since the absorption of silicon is a linear process, this relation has to be linear:

$$\Delta n(P) \propto P \propto \Delta T_{bf} \quad (5.7)$$

This is confirmed by the inset of graph 7.24. The figure 7.24 reports several curves taken with a probe in negative detuning and for several pump powers.

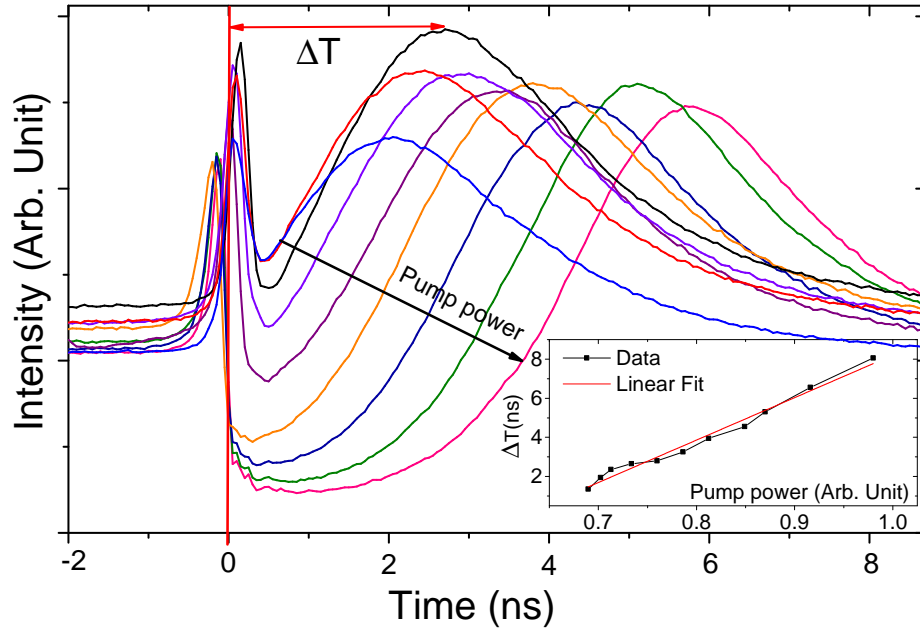


FIGURE 5.37: Probe intensity, in arbitrary unit scale, as a function of time for several pump power. The inset shows the ΔT as a function of the pump power. Probe wavelength: $1518.27 \pm 0.01 \text{ nm}$.

It is clear that ΔT_{bf} increases as the pump power increases and this increase is linear (inset of Fig. 7.24). Another interesting observation is that the narrow spectral shape of the CRIT allows to make a cycle of switch on-off in $< 500 \text{ ps}$, exploiting both the fast free carriers generation time and the non linear lineshape of CRIT [193]. Note that the measured switching time and ER are limited by the used electronics (Fig. 5.38(a), grey rectangle). The switch ER should correspond to the ER of the static CRIT that is about -10 dB .

In any case the total decay time of the system is limited by the free carrier recombination [194]. In the figure 5.38(b), the case of a probe centered into the CRIT channel is illustrated. The total switch time is 4 ns .

5.11.3 CRIT channel eye diagram

The data transmission capability of the CRIT channel is also tested by means of a transceiver and a pseudo-random bit generator. The wavelength of the transceiver transmission was centered on the CRIT channel at $\lambda_0 = 1518.35 \text{ nm}$ through a peltier cell. Then, a 3 GBit/s pseudo random data stream is transmitted through the CRIT channel while the eye diagram is measured by the oscilloscope.

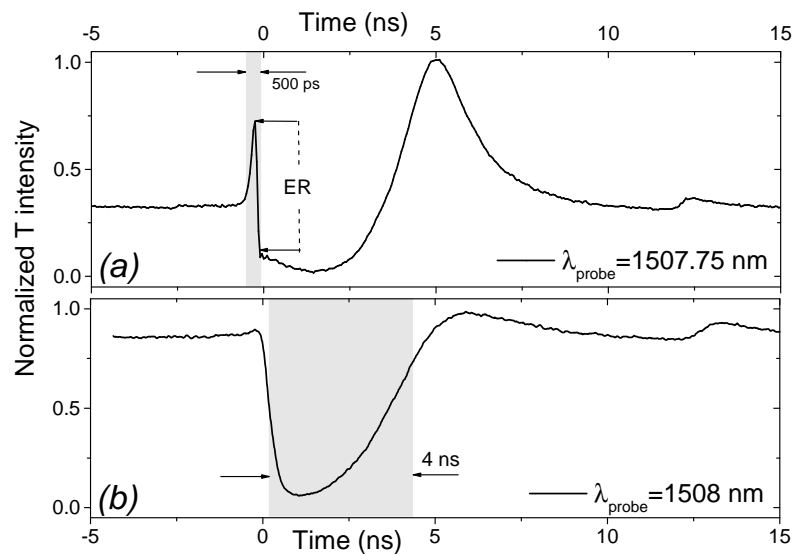


FIGURE 5.38: Probe intensity as a function of time under a pump pulse perturbation. (a) The probe is negative detuned to the CRIT. (b) Probe centered in the CRIT channel.

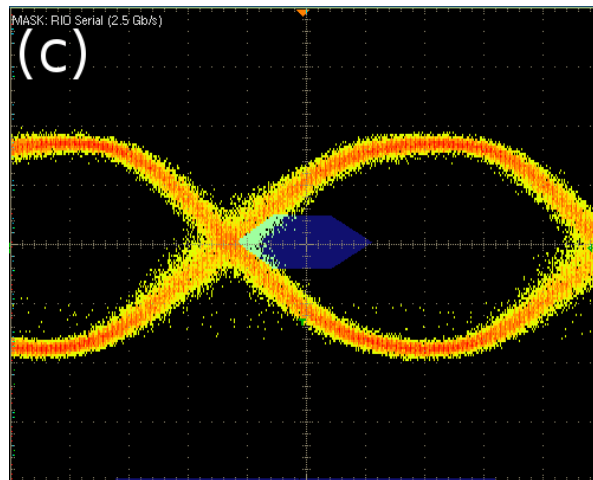


FIGURE 5.39: 3 GBit/s eye diagram.

The clearly open eye diagram confirm the good data transmission, at least at 3 GBit/s limited by our experimental setup. Much faster rate is envisioned.

5.12 Conclusions

The presence of CRIT effects in a tapered SCISSOR can be exploited to realize new designs for reliable add/drop filters, multiplexers/demultiplexers and routers.

In addition, CRITAD allows:

- to achieve a sub-nanometer linewidth in the over-coupled regime while a ring resonator would have to work in an under-coupled regime to have the same linewidth. However, in this working regime, ring resonators are affected by a mode splitting nuisance which is induced by surface roughness [167, 191];
- to define a transmission channel which is robust to fabrication errors. In the worst case of many fabrication errors, the CRITAD resonance is mainly depressed without moving out of the given channel;
- just for a matter of sum of normally distributed random variables, the random error shifts the CRITAD channel of less than 30% compared to a single microresonator channel.
- hitless and independent switch of each channel offered by CRITAD configuration.
- to use two different hitless methods, one based on the variation of R and the other on the L , to switch a channel.
- to reduce the channel crosstalk since the sharp CRIT resonance lineshape cuts out the tails of the typical lorentzian lineshape of the single microresonator resonance;

The experimental results have shown that:

- the Bragg CRITAD design works
- the channel switches with a power of about $2mW$
- the channels reconfigure with a power of about $27mW/ch$
- the switching speed is limited by the free carrier recombination to the values of about $4ns$, while the rise time indicates that, the structure do not limits the switching time, at least up to $130ps$
- we demonstrate a 1×4 CRITAD multiplexer design that works without any post-trimming technique.

Although this is a very peculiar system, which differs from what found in literature, here, we are going to make a comparison between 2 devices that, in my opinion, share similar characteristics with the *local* CRITAD structure, first of all the hitless switching.

The first one is found in the article "*Transparent wavelength switching of resonant filters*" [195]. We call this device ADF_1 . It is based on an ADF in which one coupler integrates a MZI. By changing the phase on the MZI it is possible to switch the resonance without any spectral shift. Thus, the working principle of the ADF_1 relies on the phase variation

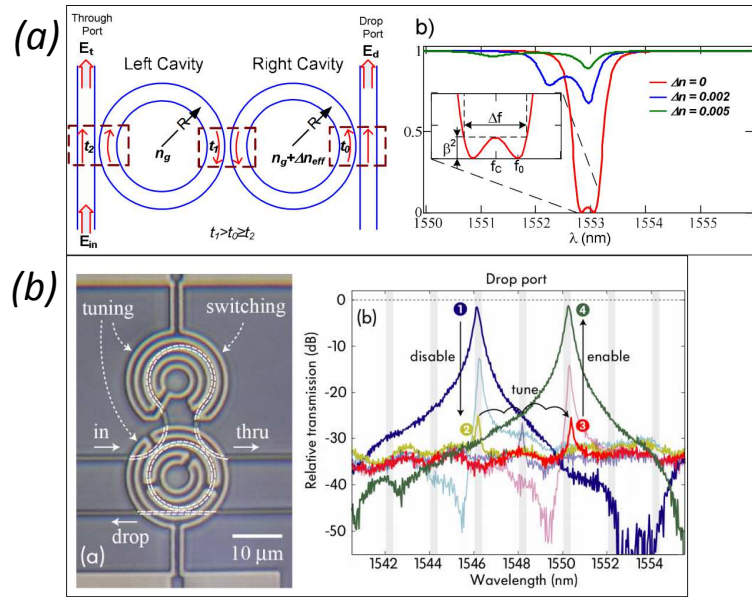


FIGURE 5.40: (a) Device described in this article "Broadband hitless silicon electro-optic switch for on-chip optical networks" [35]. (b) Device described in this article "Transparent wavelength switching of resonant filters" [195].

induced in the MZI. Since the phase rules the switching process, this device is comparable with the CRITAD in which the channel is switched through the ΔL method. In fact, the required switching power is very similar as well as the switch contrast. By cascading N of these devices, a device close to a CRITAD with $N + 1$ resonators is obtained. We obtain 8 channels each of which independently switchable. A difference is that, while the ADF_1 , during the switching process, should change the resonance linewidth (not shown in the article), a CRITAD preserve the initial channel bandwidth.

The second analogy refers to the case of switching through the ΔR method. This article "Broadband hitless silicon electro-optic switch for on-chip optical networks" describes the device [35]. We call this device ADF_2 . It consists of a 2 resonators CROW. The hitless operation of the switch is achieved by changing the resonance of the cavity coupled to the drop waveguide while leaving the other unperturbed. Also in this case the switching efficiency of the ADF_2 is comparable to that of CRITAD but the ER of the latter should be better.

In order to make a comparison table, considering the same index variation method, the values of Δn , required to switch the channel, are taken from the two articles. Then, by means of the heater efficiency extracted in the section 5.24, we calculate the power required to the switch using the same heater scheme for all the structures. The table is shown below.

TABLE 5.12: Devices comparison

	ADF_1	ADF_2	$CRITAD_{\Delta R}$	$CRITAD_{\Delta L}$
R (μm)	7	8	6.75	6.75
BW (GHz)	40	80	20	20
ER (dB)	-27	-13	-20	-30
P_{switch} (mW)	39	25	3.8	67

Although the comparison made can be said to be "forced", what emerges is that, the CRITAD channel could be switched using both the effects of the $ADF_{1,2}$ leaving more design flexibility as an ONC component.

In this work [196] a modified version of the CRITAD, to handle large channel width, is presented. They reach a channel bandwidth of about $100GHz$, without compromising the performance, by multiplying by j the single resonator that composes the CRITAD. For example, $j = 3$ gives a CRITAD radii sequence of $R_1 R_1 R_1 R_2 R_2 R_2 \dots R_n R_n R_n \dots$

Since the small BOX of the SOI wafer causes high losses on the TM mode (estimated as $10 - 15dB/cm$), it was not possible to measure the local design, that indeed promises higher performance. We are planning another mask, to investigate on the performance of the other design.

Chapter 6

Interferometric switching in reconfigurable optical device

6.1 Introduction

Switching in an optical ONC is usually performed by MZI or RR [197, 198]. Another functionality of interest in modern ONC is interleaver, which is used to combine (separate) different wavelength channels in a network [97, 199].

The transmission spectra of microresonator usually exhibit symmetric line shapes. However, it has been shown that an asymmetric shape can be generated in the transmission spectra by a ring enhanced MZI [200, 201, 202, 203]. This is the manifestation of the *Fano resonance* that arises from interference phenomena that can be related to the interaction of a discrete resonator state and the waveguide continuum of propagation modes [181, 182]. Recent studies highlighted its applications also for optical micro-resonators [204] and in ring enhanced Mach-Zhender interferometers .

Here we are going to use a similar concept in a CROW system, to exploit both the functionalities of the selective wavelength routing of an ADF and the phase switching offered by an interferometric system. We will also show that the structure is robust to the process errors. The TMM approach for this system has already been introduced in these theoretical articles [205, 206].

In the first part of the chapter, the transfer matrix approach for a CROW structure is introduced and its spectral response and group delay are reported. Afterward, the condition of single input used so far in the transfer matrix will be replaced by that of two inputs. In this way, the principle of operation of the switch, based on the phase between the two inputs, is shown.

$$\begin{pmatrix} a_N \\ c_N \end{pmatrix} = K^n \prod_m^{m-1} P^n \cdot K^n \begin{pmatrix} a_1 \\ c_1 \end{pmatrix} \equiv S^c \begin{pmatrix} a_1 \\ c_1 \end{pmatrix} \quad (6.1)$$

with $m = 2, 3, 4, \dots$. The dependence on the resonator number of the output direction is included into the matrix exponent. Once the fields a_1 , I port, and the field c_N , A port, are defined, the T and D ports are obtained by calculating the ratios c_1/a_1 and a_N/a_1 respectively (for $c_N = 0$):

$$\begin{pmatrix} c_1 \\ c_N \end{pmatrix} = 1/S_{12}^c \begin{pmatrix} -S_{11}^c & 1 \\ 1 & S_{22}^c \end{pmatrix} \begin{pmatrix} a_1 \\ a_N \end{pmatrix} \quad (6.2)$$

In figure 6.2 we show an example of how the CROW T and D port, phase shift and group delay behave as a function of the detuning from the center of the band. Here we use equal CC for each resonator and this is the reason why the ripples inside the stop band appear.

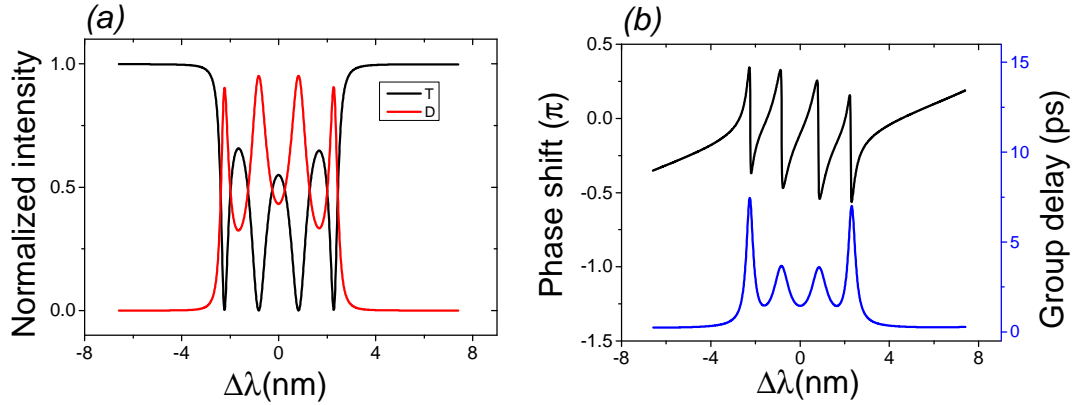


FIGURE 6.2: (a) T(black) and D(red) port spectra as a function the detuning, $\Delta\lambda$, from the resonance center. (b) Phase shift (black) and group delay (blu) as as a function the detuning. Simulation parameters: $R = 3.25\mu m$, $c_s = 10\mu m$, $gap = 200nm$ ($CC = 46\%$), $N = 4$, $w = 450nm$ and losses $0.01 dB/90^\circ$.

The number of ripples is equal to the number of cavities in both the T and D port (Fig. 6.2 (a)). The phase shift of the T port, reported in panel (b) is characterized by a total of 4 jumps that correspond to the crossing of the 4 ripples (resonances). In panel (b), blue line, is reported the group delay. The ripples are due to the mode splitting induced by the large coupling existing between the cavities. Despite the equal radii, the spectral position of the modes is not equal and is distributed along the CROW band. The position of these modes are only in part determined by the radius of the cavities but especially by the cavity-cavity CC. Infact, the larger the CC, the greater the modes separations. This concept will be used later (section 6.3.3).

An engineering of the coupling gaps, i.e CC, can turn the stop band in figure 6.2 into a box like stop band as reported in figure 6.3. The nine gaps values are reported in table ??.

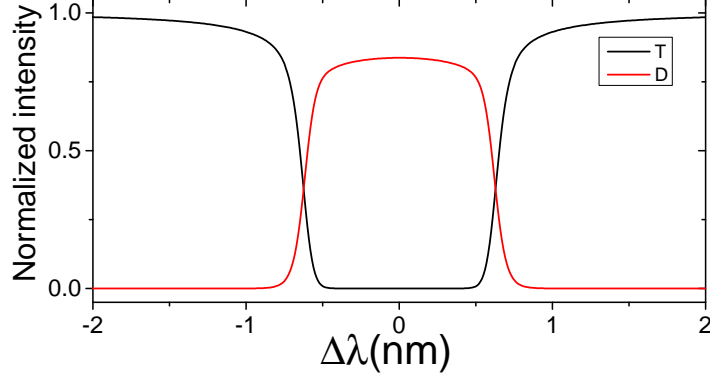


FIGURE 6.3: (a) T(black) and D(red) port spectrum as a function the detuning, $\Delta\lambda$, from the resonance center. Simulation parameters: $R = 3.25\mu m$, $c_s = 10\mu m$, $N = 8$, $w = 450nm$ and losses $0.01 dB/90^\circ$. The gaps are reported in table 6.1.

TABLE 6.1: CROW gaps values (nm)

Gap_1	Gap_2	Gap_3	Gap_4	Gap_5	Gap_6	Gap_7	Gap_8	Gap_9
160	280	360	390	400	390	360	280	160

The response of the CROW is assimilated to that of higher order electronic filters. Changing the tapering of the gap involves a switch from a transfer function "butterworth" maximally flat to, for example, a "Bessel" with minimum group delay as shown here [174].

6.2.1 Interferometric ADF

Here we are interested to know what happens if another input signal, phase shifted with respect to the first one, is injected in the A port. As we can see from figure 6.4 , the Add signal has a phase shift of $\Delta\phi$ and is co-propagating with the one in the port I. Under this condition we can use the scattering matrix of the CROW (in this case with $m = 2$) with $a_1 = c_N \neq 0$.

We define the input fields in the I and A port as:

$$\sqrt{I} = |in e^{i\phi_{in}}| \quad \sqrt{A} = |a e^{i\Delta\phi}| \quad (6.3)$$

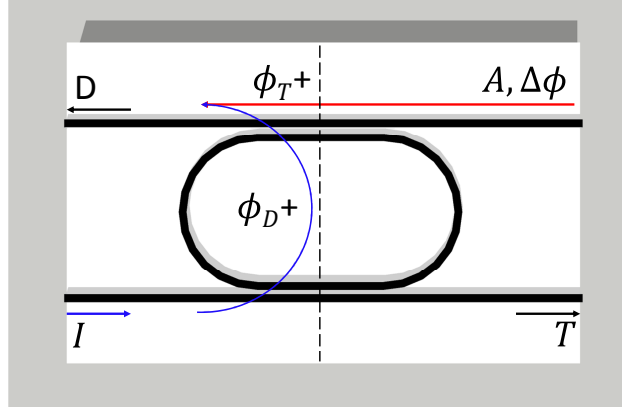


FIGURE 6.4: Sketch of a racetrack resonator with two input signals, one in the I port the other in the A port with a phase $\Delta\phi$. $\Delta\phi_R$ is the phase difference between the T and the D ports of an add drop filter. All the phases are referred to the phase of I port.

The phase of the input is considered zero thus, $\phi_{in} = 0$. In fact, if we focus only on the D port in figure 6.4, we can see that it is the result of the A port that passes straight the RTR (red arrow), plus the I port that crosses the RTR (blue arrow). The former signal is associated with the phase shift of the ADF T port, ϕ_T , while the latter is associated with the phase shift of the D port, ϕ_D . Thus, the spectral response of the interferometric ADF is governed by the phase difference between the T and D port, $\Delta\phi_R = \phi_T - \phi_D$, plus the $\Delta\phi$. By neglecting, only for now, the fact that RTR modulates also the intensity of the signal we can write:

$$D = |in(\lambda) + a(\lambda)e^{i\Delta\phi_R + \Delta\phi}|^2 \quad (6.4)$$

The value of the exponent is reported in figure 6.5 (blue line) for two cases, $\Delta\phi = 0$ (a) and $\Delta\phi = \pi/2$ (b) together to the T port transmission spectrum of an ADF (black line).

With reference to figure 6.5, we can see that for a $\Delta\phi$ of 0 the D port is the sum of the square of the 2 inputs, $D = |in(\lambda)|^2 + |a(\lambda)|^2$, thus they do not interfere and the system is (almost) insensitive to the wavelength. In fact if we consider unit inputs in a lossless system we can write:

$$|in(\lambda)|^2 = 1 - |a(\lambda)|^2, \quad \Delta\phi = 0 \rightarrow D = 1$$

where we can see that the port D is always equal to 1. Instead, for a $\Delta\phi$ of $\pi/2$, the D signal characterized by two different behaviours which are defined by the RTR resonance (black line):

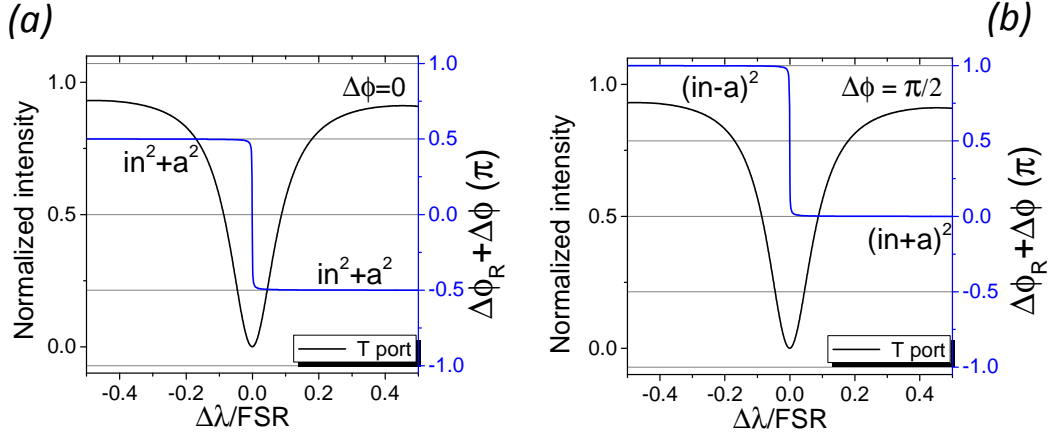


FIGURE 6.5: (black line) T port of an ADF as a function of $\Delta\lambda/FSR$. (blu line) Phase difference of the ADF T and D ports plus the external $\Delta\phi$ (unit of π) as a function of $\Delta\lambda/FSR$. (a) $\Delta\phi = 0$, (b) $\Delta\phi = \pi/2$.

1. for smaller wavelength than resonance, D is the square of the difference of the 2 inputs, $D = (|in(\lambda)| - |a(\lambda)|)^2$ (destructive interference)
2. for largeer wavelength than resonance, D is the square of the sum of the 2 inputs, $D = (|in(\lambda)| + |a(\lambda)|)^2$ (constructive interference)

Again, by considering unit inputs and a lossless system we can write :

$$|in(\lambda)|^2 = 1 - |a(\lambda)|^2, \quad \Delta\phi = \pi/2 \rightarrow (1) D = 1 - 2|in(\lambda)a(\lambda)| \quad (2) D = 1 + 2|in(\lambda)a(\lambda)|$$

For an inversion of the phase from $\pi/2$ to $-\pi/2$, the cases (1) and (2) are exchanged thus, they are completely symmetric.

These are 2 states of the system. An inversion of the input phase from $\pi/2$ to $-\pi/2$ gives the third state: this is completely symmetric compared to the case of figure (b).

Summarizing, we found that the interferometric ADF (IADF) is characterized by 3 states: one insensitive to the wavelength, for $\Delta\phi = 0$, and the other two in which occurs the interference of the inputs with a π symmetry. All the discussions done for the D port are valid also for the T port by considering the system symmetry that is, $\phi_T \rightarrow \phi_D$ and viceversa.

By means of the transfer matrix approach, we plot the 3 states of the IADF in figure 6.6 . Here we consider $I = 1$ and $A = 1$. The panel (a) reports the transmission spectrum of the T(black) and D(red) ports of the IADF for a $\Delta\phi = \pi/2$. As we predicted, after each resonance, identified by the dashed rectangle, there is a transition between a destructive-constructive (constructive-destructive) condition. Note that, the system is symmetric

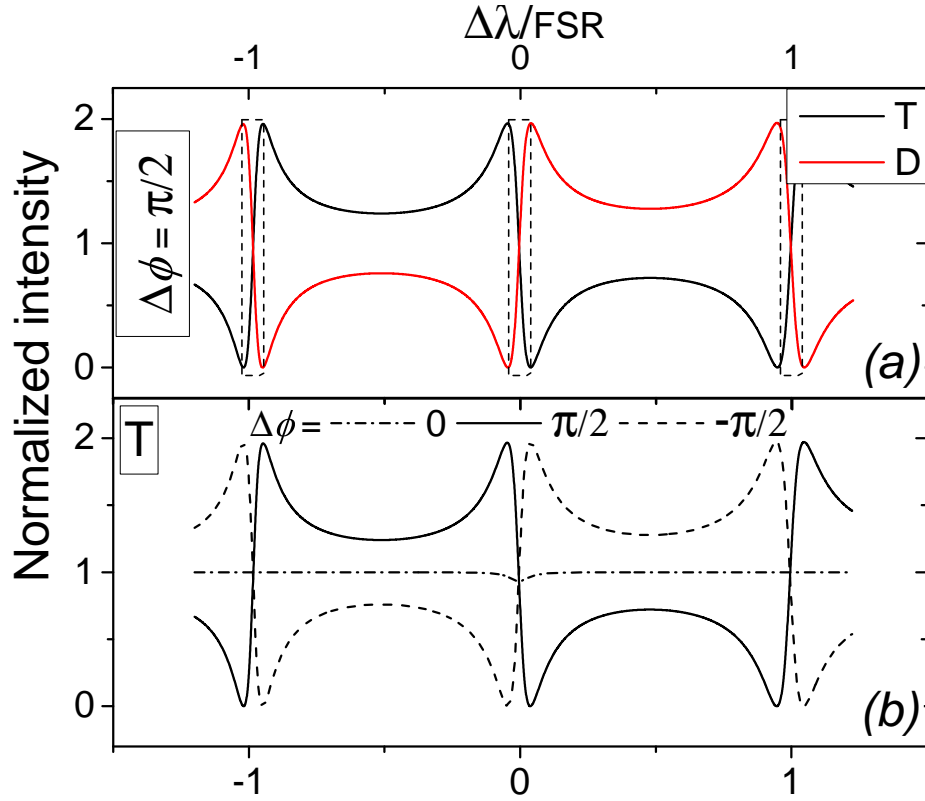


FIGURE 6.6: (a) IADF transmission spectrum of the T (black) and D (red) ports for a $\Delta\phi = \pi/2$. (b) Transmission spectrum of the T (black) port for several $\Delta\phi$: $0, \pi/2, -\pi/2$. the input values are $I = 1$ and $A = 1$.

for a T-D exchange. The panel (b) reports the transmission spectrum of the T (black) port for several $\Delta\phi$:

- $\Delta\phi = 0$: splitter state (dash-point line). The T(D) port is wavelength independent and equal to 1 .
- $\Delta\phi = \pm\pi/2$: normal and reverse state (solid and dashed line). The T(D) port is wavelength dependent.

Note that shapes of the D and T ports become asymmetric. The asymmetric line shapes of Fano resonances are due to interference phenomena that can be related to the interaction of a discrete resonator state and the waveguide continuum of propagation modes. Fano resonances attracted renewed attention in several fields of physics [182] . Recent studies highlighted its applications also for optical micro-resonators [181, 204] and in ring enhanced Mach-Zhender interferometers [200].

In the following we will show the experimental proof of what it was said above. The concept of the phase switch will be extended to a greater resonators number. From now on we makes use of balanced inputs, i.e. $I = A$.

6.3 The proposed interferometric band interleaver (BIL)

In a standard Add/Drop filter based on CROW sequence[207], four ports exist. Signals are routed to either the T or the D ports depending on their wavelength. In our device the input port feeds two arms (equivalent to the In and Add ports) and it realizes an interferometer based on a CROW sequence. Depending on signal phase relations and wavelengths, they are either routed in one port or split across both ports. Figure 6.7(d) shows the design of the proposed device. Before entering into the device (black stripes), the signal is split by an MMI to obtain a reference channel used to normalize the measurements (blu stripes). The signal is then fed into the In port and split by another MMI. The MMI2 splits the input signal (50/50 ratio) in the two input arms of an interferometric CROW. The phase difference ($\Delta\phi$) between the two in the MZI is ruled by an heater (drawn in orange in Fig 6.7(d)). The two beams are then recombined by means of the CROW. The panels show:(b) a mask design detail of the heater, (c) a photograph of the RTR sequences and (a) a photograph of the metal pads and MMIs .

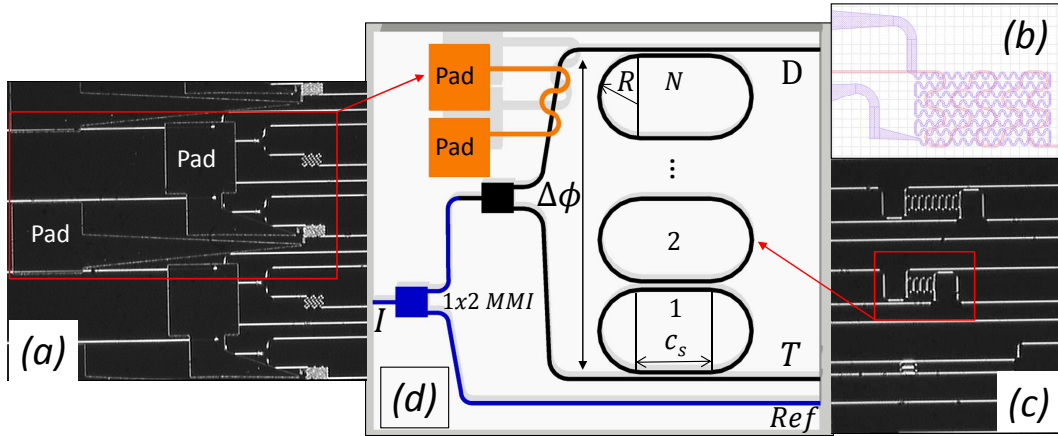


FIGURE 6.7: (d) Design of the reconfigurable interleave. Reference part (blue): an MMIs as 50/50 splitter, one output is the reference the other output feeds the device. Interferometric device(Black): interferometric device composed of an input channel and two outputs: the T and the D ports. The metallic heater is shown in orange: its task is to heat one arm of the interferometer to induce a $\Delta\phi$ on the propagating signal. See text for other symbol explanation.

Optimum device properties require large coupling coefficients and since, we want to use TE polarized light, we then uses the RTR geometry. The fabricated CROW sequences are composed by 2, 4 or 8 racetracks with radius R of $3.25 \mu m$, gap of $200nm$ and coupling section c_s of $10 \mu m$ (symbols are defined in Fig. 6.7(d)). We chose sequences with an even N in order to have co-propagating outputs. We uses equal gaps, thus the transmission spectrum of the CROW with a single input would be as the one shown in figure 6.2. We performed the transmission spectra using a broadband ASE source

(range $1520\text{nm} - 1570\text{nm}$) and by detecting with an OSA. Two micrometer metal tips were used to contact the pads and inject current, as shown in appendix B.0.7.

The device is called interferometric band interleaver (BIL) because, while a standard interleaver is designed to divide a whole telecom window in smaller bands, this device acts as interleaver only around the resonances of the racetracks that composes the CROW.

6.3.1 Experimental test

Figure 6.8(b) shows the transmission of the T port of a BIL composed by 4 resonators. The bands, highlighted by the grey rectangle, are spaced by a free spectral range (FSR). The width of the bands is determined by the optical path of the resonator and by the gap, thus it can be modified by a proper device design.

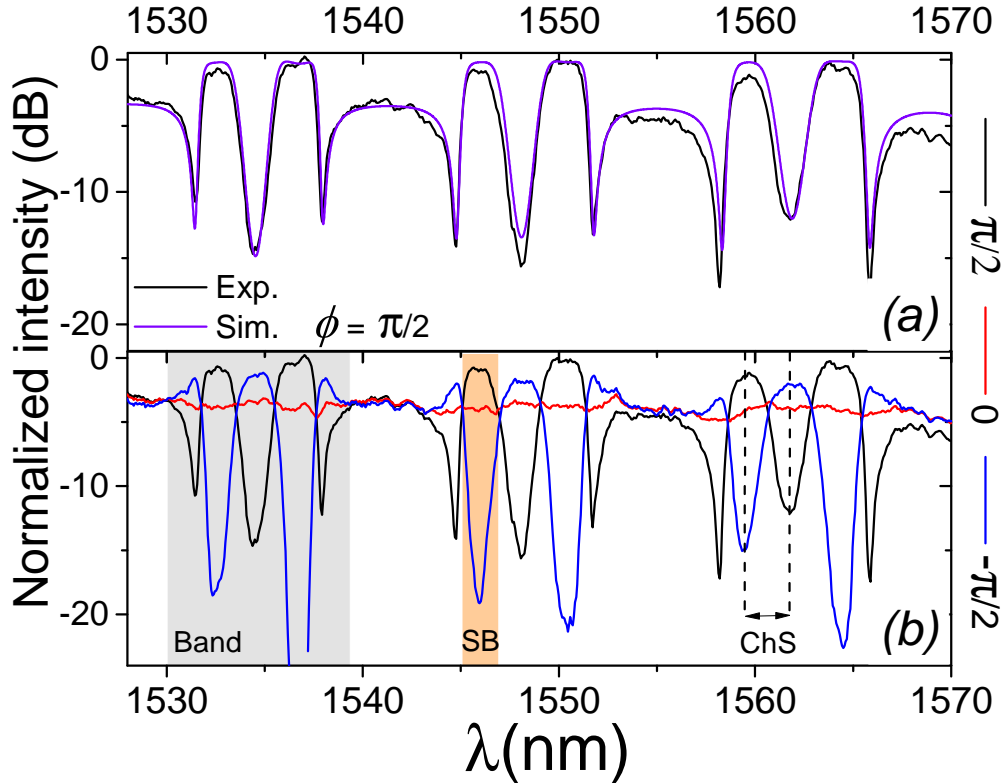


FIGURE 6.8: (b) 4 resonators BIL transmission spectra of the T port showing several resonance orders for several heating powers (or $\Delta\phi$): (black) $1\text{mW}(\pi/2)$, (red) $7.7\text{mW}(0)$, (blue) $14.2\text{mW}(-\pi/2)$. (a) Experimental T port spectrum (black) superimposed with the simulated response (violet curve) for a $\Delta\pi = \pi/2$. The simulation parameters are reported in table 6.2.

As we can see each band is divided into $N + 1$ sub-bands (SB). Each band is generated by a π phase shift induced by the CROW inside its photonic stop band. In fact, as was shown in figure 6.2, a 4 resonator CROW featured 4 π jumps in the phase shift. Each

jump, in this interferometric device, involves an exchange between a state of constructive interference to a state of destructive interference (refer to the black curve). By changing the heating power is possible to switch the state of each SB. Let us concentrate only on the orange SB: for $\Delta\phi = \pi/2$ (black line) the signal is routed to the T port (normal state) while for $\Delta\phi = -\pi/2$ (blu line) the signal is switched off (reverse state). As we will see in a while, the reverse state implies a redirection in the D port for symmetry reason. Therefore the device is fully reconfigurable depending on the phase difference of the incoming signals, that is regulated by the external heater. A new functionality is observed for $\Delta\phi = 0$ (red line): the device is in the "splitter" state, i.e. the incoming signal is redirected in both the output ports. Moreover, this state is completely insensitive to the wavelength of input signal. The $\Delta\phi$ values that represent the experiment are: $\pi/2, \pi, 3/2\pi$ for the normal, splitter and reverse states respectively. The splitter state has a π periodicity while, the normal and the reverse states have a 2π periodicity.

TABLE 6.2: CROW simulation parameters

	$R(\mu m)$	$c_s(\mu m)$	$Gap(nm)$	$BendLoss(dB/90^\circ)$
Nominal	3.25	10	200	0.02 – 0.03
Simulation	$3.25 \pm 4 \times 10^{-3}$	10	180	0.03

The simulation and the experiment are in excellent agreement (Fig. 6.8(a)) but, to obtain that nice overlap it was necessary to add a random perturbation in the RTR radius with a standard deviation of $4nm$ (as measured in the section 4.5.1). In fact, the simulated "perfect" device exhibits a SB extinction ratio that exceeds by $-10dB$ the measured one. A more in depth investigation will be carried out in the next section. A little discrepancy in the long wavelength region is present. As the wavelength increases the confinement factor decreases as well, thus there could be some extra losses generated from the coupling between the optical mode and the metal above the ΔL section (see Fig. 6.7(b)).

Figures 6.9 show an high resolution spectra of a single band for the T and D ports for different heating power. We can immediately see the symmetry of the T and D ports. In fact:

- normal state (black line): there are 2 "on" SBs in the T port and 3 "on" SBs in the through (grey rectangles).
- reverse state (blu line): there are 3 "on" SBs in the T port and 2 "on" SBs in the through (light orange rectangles)
- splitter state (red line): no SBs.

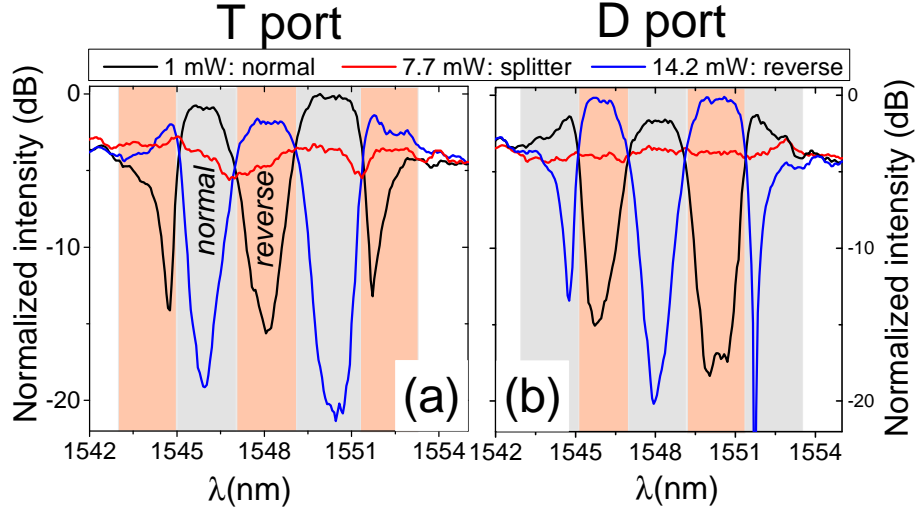


FIGURE 6.9: T and D ports transmission spectrum for several heating power: (black) $1mW$, (red) $7.7mW$ and (blue) $14.2mW$. The grey (light orange) rectangles indicates the normal (reverse) state. The simulation parameters are reported in table 6.2.

In this case, a power of $1mW$ is required to maximize the extinction of the normal state because of the fabrication errors. The SBs reconfiguration, i.e. normal to reverse transition, is achieved with a power of $13.2mW$. The splitter state require $7.7mW$. Therefore, about $7mW$ is required to induces a phase shift of $\Delta\phi = \pi/2$. The effective index variation Δn induced by the heater can be calculated knowing the length of the heated length $\Delta L = 132\mu m$ (see Fig. 6.7(b) pink stripe). By approximating the two input arms as equal (fabrication defects) the $\Delta\phi$ is:

$$\frac{2\pi}{\lambda} \Delta n \Delta L = \Delta\phi = \frac{\pi}{2}$$

thus, we can solve for Δn obtaining the values in table 6.3.

TABLE 6.3: Heater effects: efficiency, local temperature and relative refractive index variation

$$\frac{\frac{\Delta n}{7mW} (1/mW)}{4 \times 10^{-4}} \quad \frac{\Delta T (K)}{16} \quad \frac{\frac{\Delta n}{n}}{8 \times 10^{-4}}$$

The approximated temperature variation is derived from the Δn using the TOE coefficient (this is an approximation since the TOE refers to the silicon refractive index variation). The power dissipated to reconfigure the device is comparable to the state-of-the-art results obtained in thermo-optic Add/Drop devices based on single resonator. [202, 203]. Reconfigurability efficiency can be further improved by a finer optimization of the heater design.

Finally we shows the group delay of the T and D port simulated starting from the parameters in table 6.2. As expected, inside of the routed SBs (grey rectangles), the

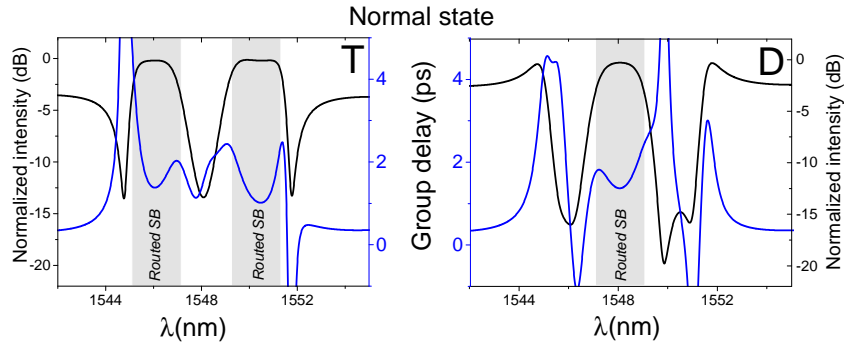


FIGURE 6.10: T and D port spectrum (black line) and relative group delay (blu line). The grey rectangles are the active SBs . Simulation parameters in table 6.2.

group delay is about $2 - 3$ ps, thanks to the low Q of the RTR that composes the CROW.

6.3.2 Influence of the resonators number

A number N of resonators implies $N + 1$ SBs (light orange rectangle in figure 6.8(b)). Thus, by increasing the number of resonators a larger number of SBs can be managed within the same resonance band.

Figure 6.11(a,b,c) reports the behavior of BILs composed by 2,4 and 8 coupled resonators for $\Delta\phi = \pi/2$. Note how the total width of the CROW band (grey region) remains the same for all the devices thus, does not depends on N . The larger the N , the larger the SBs number in which the CROW stop band is divided. Thus higher N means narrower SBs and a lower channel spacing (ChS Fig. 6.8) as is found in table 6.4. The average SB extinction is about -16 dB and remains constant across the device bandwidth up to the 4 resonators BIL. Devices with greater number of resonators show an increasing deviation from the flat box filter shape. The extinction (crosstalk) is maximum (minimum) for the central SB, -20 dB (-19 dB), and decreases down to -7.5 dB (-4 dB) for the other SBs. Figure 6.11(d) reports the simulated spectra for an apodized CROW, where the gaps have been linearly increased from the outer to the central racetracks. In this way, the flat filter shape is recovered. Gaps have been linearly increased from 183 to 210 nm moving from the outer to the central racetrack. In this case the extinction ratio for the outer SBs reaches a value of -18 dB.

The main characteristics of all proposed devices are reported in Table 6.4. The footprints are given without considering the electrical contacts. We have considered only the

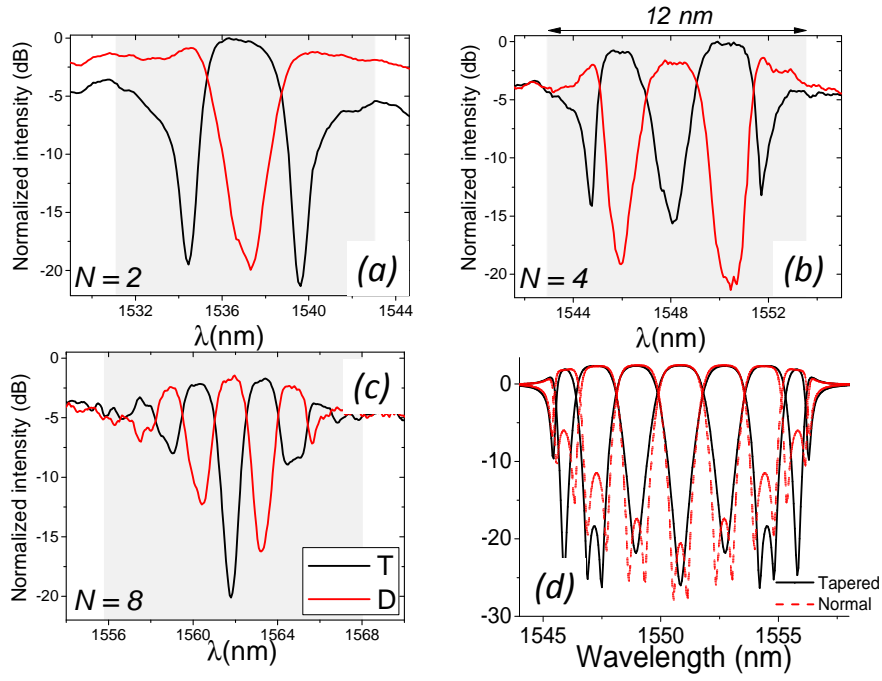


FIGURE 6.11: BIL transmission spectrum for the T and D ports measured on devices with different N : (a) 2, 4, 8 (a,b,c) resonators device. (d) Simulated spectra for a 8 resonators apodized device (black solid line) compared to a normal device (red dashed line). For clarity the T and D ports spectra are reported with the same color for the normal and the apodized devices. The grey region identifies the band width of the CROW. $\Delta\phi = \pi/2 (\sim 7.7mW)$ for all the spectra.

TABLE 6.4: Channel insertion losses, extinction ratio, band widths and footprint (FP) for the BIL device with N resonators

N	SBs	Loss (dB)	ER (dB)	FWHM (nm)	ChS (nm)	FSR (nm)	FP mm^2
2	1	-0.1	-23	3.8	4	14	0.0003
4	3	-0.3 to -1.8	-16	1	2	14	0.0032
8	7	-1 to -3.5	-20 to -7.5	0.5	1.4	14	0.0042

internals $N - 1$ SBs, because the two outermost SBs of the spectra are unusable without a gap apodization.

6.3.3 Influence of the fabrication defects

The fact of being able to fit, in a deterministic way, the experimental measure using random radii is undoubtedly a good sign (Fig. 6.8). In fact, this type of structure appears to show a good resistance to manufacturing defects. The main effect of the defects is to worsen the ER of the SB with respect to the nominal structure. Starting from the parameters of Table 6.2, we have studied the system a 4 resonator BIL resonators using

a normally distributed value of R with a sigma of 2, 4, 6 nm. Figure 6.12 shows the results of these simulations on the T port. For each value of σ , 6 curves were calculated (panels (a,b,c)). The values of the mean and standard deviation of the maximum ER inside the central SB (highlighted by the grey rectangle), are calculated for each σ and reported in figure 6.12(d).

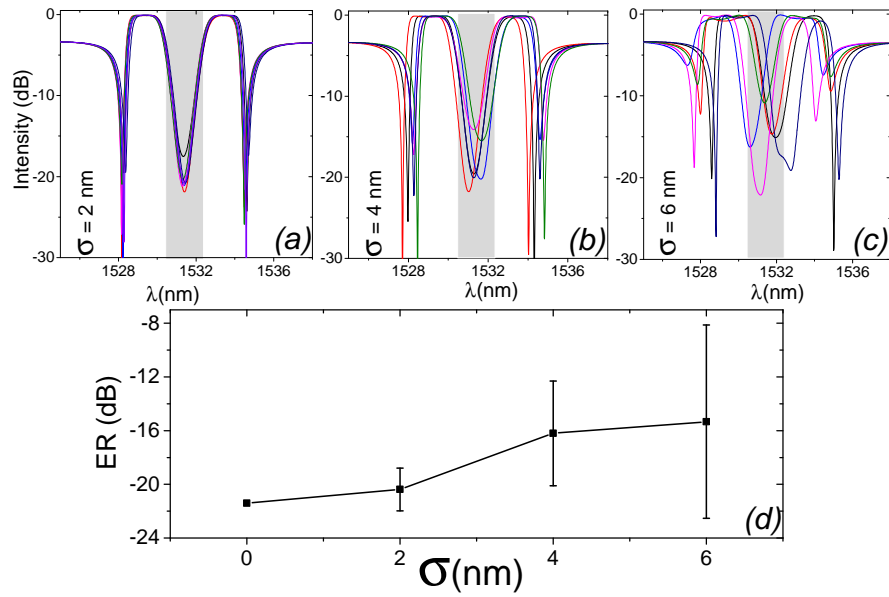


FIGURE 6.12: Transmission spectra for the T port of a 4 resonator BIL(normal state) calculated for several σ : (a) $2nm$, (b) $4nm$ and (c) $6nm$. (d) Maximum ER inside the grey rectangle as a function of σ .

The effect of $2nm$ of errors is practically irrelevant for the device performance, while from $4nm$ the situation worsens. It is interesting to note that, despite the local nature of the errors used, the whole band of the BIL coherently shifts to the red or to the blue the errors influence. We prove this, by aligning together the band edge (that towards the red) of the 6 simulations made with a σ of $4nm$.

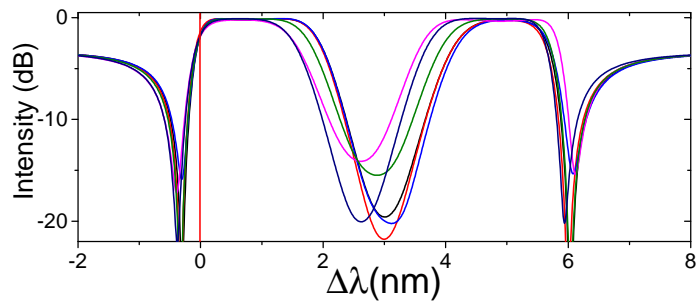


FIGURE 6.13: Transmission spectra for the T port of a 4 resonator BIL(normal state) calculated for $\sigma = 4nm$. The red line indicates where the band edges (high-energy) were aligned.

In figure 6.13 we see that, after the alignment to the red line, the total band width is constant. The values of the mean and standard deviations of the offset applied to the band edge is reported in table 6.5. To have a reference, we report also the offset necessary to align an ADF, calculated using the same parameters of the BIL case.

TABLE 6.5: Band edge offset and heating power required to compensate the errors. The errors σ is fixed to 4 nm .

Device	Band edge shift	Estimated trimming heating power
BIL	$0.3 \pm 0.3\text{ nm}$	$1.4 \pm 1.4\text{ mW}$
RTR	$1.3 \pm 0.9\text{ nm}$	$6 \pm 4\text{ mW}$

We believe that the robustness of this structure derived from two contributions:

- the averaging effect due to the $N > 1$.
- the fact that the SBs position is not only fixed by the resonator radii but mostly by the CC between the resonators that is less sensible to the defects.

In the perspective of thermal tuning, the overall effect of the defects suggests that it is not necessary to independently heat each RTR which composes the BIL but only the entire chain. Using the calculated efficiency of the omega heater (refere to section 5.10.2), we can estimate the energy consumption required by the post-process trimming procedure. The values, for a $\sigma = 4\text{ nm}$, are reported in the table 6.5.

6.4 Conclusions

The BIL may be considered comparable to a ring enhanced MZI device. But, there are some characteristics for which it differs from those found in the literature:

- The interleaving effect is applied only around the CROW photonic band. That is, only certain bands are interleaved. That's why it is called BIL.
- The splitter state. For a $\Delta\phi$ of $n\pi$ the device is no more sensitive to the input wavelength and behaves as a 3 dB splitter. This effect originates from a phenomenon similar to that used in an ADF to performs hitless switching [94].
- The robustness to fabrication errors. The position of the bands is mainly fixed by the CC between the resonators in the CROW. As a consequence, the system is less sensible to the fabrication errors. However, the extinction ratio worsens due to these errors.

The experimental results showed that the power required to a complete reconfiguration (normal-reverse) is about 14 mW . The ER of the switch reaches the value of -23 dB for the 2 resonator BIL. The devices with a greater N require an apodizing of the gaps in order to obtain an uniform ER for all the channels. Of course, the switch efficiency could be improved by a better engineering of the heater.

Our proposed designs are examples of more complex structures where both wavelength and phase differences can be used to implement complex networking protocols [208].

Chapter 7

Non linear effects in single and coupled microresonators

7.1 Introduction

The high index contrast provided by the SOI platform allows to have a tight light confinement in a sub-micrometer waveguide. Such a small confinement enhances the material non linearities as a consequence of a higher power density. Moreover, the silicon third-order nonlinearity exceeds that of silica by 400 times [120] and by a Raman gain coefficient 1000 times larger [121] in the telecom window . Therefore, a great effort has been used to study nonlinear effects in silicon as self-phase modulation (SPM) [123, 124, 125, 126], cross-phase modulation (XPM) [127, 128], stimulated Raman scattering (SRS) [78, 129], and four-wave mixing (FWM) [130, 131]. On top of those direct nonlinear effects, there come a number of secondary effects into play. The semiconductor property of silicon together with the imaginary part of the third-order nonlinearity give rise to several peculiar effects as two photon absorption (TPA) [120, 123], free-carrier dispersion (FCD) [4], and anisotropic and dispersive third-order nonlinearity [132]. The passive and active linear and nonlinear property of SOI based photonic devices allow many degrees of freedom to create integrated optical devices for practically any applications [133, 134, 135, 136]. Naturally, in a resonator these effects become more pronounced, due to the strong increase of the field at resonance. In magnitude, the thermal effects are actually dominant, but they are slow. Bistable behavior has been demonstrated in silicon microring resonators [43, 137]. Self-pulsing states will appear if, together with the thermal effects, free carrier effects are present. [44, 45, 138].

For this reason, microring resonators have gained a lot of importance in this field because they allow to reduce the amount of power required to activate a certain nonlinear process.

For a given incident power, the power inside the cavity P_{ins} is described by:

$$P_{ins} = EF P_{inc} = \frac{\lambda_m k^2 Q^2}{(1 - k^2)(P n_g \pi)^2} P_{inc} \quad (7.1)$$

A common RR add drop filter with radius of a couples of micrometers easily gives an EF of 10^2 . The dependency of the EF and of the Q factor on the coupling coefficient is reported in the figure 7.1.

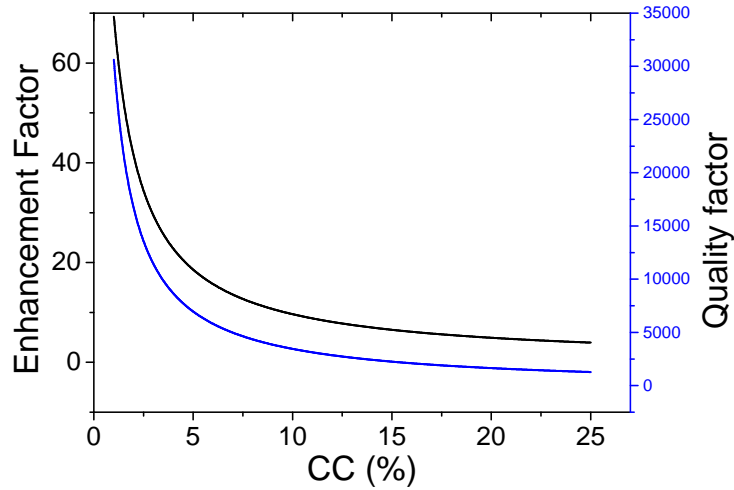


FIGURE 7.1: Enhancement factor and quality factor as a function of CC; black and blu curves respectively.

This chapter mainly focuses on the effects related to TPA since, in the telecom band and silicon based devices, it is a leading source of nonlinearity. For a sufficient high power density, two photons can be absorbed to generate free carriers that, in turn, give rise to FCD. The generated free carriers give rise to additional losses identified as FCA. The free carrier relaxation heats up the material activating the thermo optic effect (TOE). TOE effect is also very a important dispersive effect characterized by an high efficiency and, as drawback, a slow time response ($ns - \mu s$) compared to other nonlinearities.

We begin with an overview on the optical nonlinearities of a medium . The optical bistability and self-pulsing (SP) effects are then introduced and experimentally investigated in an ADF system. Afterwards, we moves the attention to the SCISSOR device. We are going to experimentally demonstrate that in non-linear regime a SCISSOR admits SP states and *chaotic states*. These states are allowed by the presence of errors-induced localized states.

7.2 Nonlinear optical medium: General theoretical introduction

A medium is optically linear when the relation between the electric field \mathbf{E} and the polarization per unit volume \mathbf{P} can be expressed as (in Fourier domain):

$$\mathbf{P}(\omega, \mathbf{k}) = \epsilon_0 \chi^{(1)}(\omega, \mathbf{k}) \cdot \mathbf{E}(\omega, \mathbf{k}) \quad (7.2)$$

where $\chi^{(1)}$ is the dielectric susceptibility first rank tensor, which depends on angular frequency ω and the spatial wavevector \mathbf{k} . The frequency dependence of $\chi^{(1)}$ is called *dispersion* and derives directly from the fact that the polarization response to the applied electric field is not instantaneous in the time domain.

Silicon is an isometric crystal system and then the $\chi^{(1)}$ can be treated as scalar quantity. In linear regime at telecom wavelength the $\chi^{(1)}$ is linked to the material refractive index as $\chi^{(1)} = n_{Si}^2 + 1$. The typical value of electric field of a bound electron in a solid material is about 10^9V/m . Since an electromagnetic wave commonly induces an electric field of one or two order of magnitude lower, we can expand the polarization as follows:

$$P_\alpha = \epsilon_0 \left(\sum_\beta \chi_{\alpha\beta}^{(1)} E_\beta + \sum_{\beta\gamma} \chi_{\alpha\beta\gamma}^{(2)} E_\beta E_\gamma + \sum_{\beta\gamma\delta} \chi_{\alpha\beta\gamma\delta}^{(3)} E_\beta E_\gamma E_\delta + \dots + \chi^{FC} \right) \quad (7.3)$$

where $\alpha = x, y, z$ and $\chi_{\alpha\beta\gamma}^{(2)}$, $\chi_{\alpha\beta\gamma\delta}^{(3)}$ are respectively the second and third order dielectric susceptibility tensors, while χ^{FC} is the free carrier susceptibility. For a matter of symmetry, the $\chi^{(2)}$ component is not present in silicon. Thus, the first non linear perturbation is the $\chi^{(3)}$. Since its real and imaginary part are $10^{-19} \frac{\text{m}^2}{\text{V}^2}$ and $10^{-5} \frac{\text{m}^2}{\text{V}^2}$, the non linear effect can be considered as small perturbation of the linear solution. Under this condition, by using an harmonic slow varying (space and time) electric field (single frequency) it is possible to derive:

$$n(|E(\mathbf{r}, t)|^2) \approx n_o + \frac{3\chi_{\hat{n}}^{(3)}}{8n_o} |E_0(\mathbf{r}, t)|^2 \quad (7.4)$$

where $n_o = \sqrt{1 + \chi^{(1)}}$ is the unperturbed refraction index. The spatial and temporal energy dependence of the refractive index leads to several non linear effect such as the *self focusing effects* and propagation of *solitons*. This is not always true as, for guided light, the mode confinement limits the spatial distribution of the field that can be considered flat. In this case, as already mentioned, the propagating guided mode can be described through an effective index. The value of $n_{eff}(|E|)^2$ can be derived integrating, over the

geometric dimension, the following equation

$$\nabla^2 E(\mathbf{r}, t) + \frac{n^2(|E(\mathbf{r}, t)|^2)}{c^2} E(\mathbf{r}, t) = 0 \quad (7.5)$$

where the third harmonic generation term is neglected (unfulfilled phase matching condition)[209]. All the effects, mentioned in the introduction, are obtained by means of an optical microresonator in which the mode effective index depends on the power inside the cavity. The effect generated by the real part of the $\chi^{(3)}$ is called *Kerr* non linearity and it is characterized by very fast time response (fast as the polarization speed of atomic electrons). While, the imaginary part is responsible of the non linear absorption called, two photons absorptions. The presence of nonlinear absorption in silicon at $1.55\mu m$ leads to the creation of free carriers, which is unexpected in the linear regime. Especially for large input signals, this free-carrier density can grow rapidly, leading to additional nonlinear effects such as free-carrier dispersion, free-carrier absorption and thermo-optic effect which are the topic of the next section.

7.2.1 TPA induced nonlinearities in silicon

Despite silicon is transparent in the third telecom window, for these wavelengths photons have an energy larger than half of the band gap. Therefore, TPA absorption is possible. Figure 7.2 shows a sketch that summarizes all the phenomena related to the TPA absorption. Through the TPA process, free carriers are excited which result in additional absorption, FCA, and an associated index change, FCD. After a certain time, that depends on the WG geometry, the carriers will recombine at the WG surface (inter-band relaxation). There is also an intra-band relaxation due to TPA and FCA effects that, together with the inter-band relaxation, will lead to a phonon creation and an heating of the mean. The heated waveguide is then subject to TOE with again a variation of refractive index. Then, the thermodynamic of the structure dictates the thermal relaxation time.

Below, all the previously described phenomena are singly described. The equations to describe the relative refractive index variation are reported with reference to the optical system discussed in this work. In the appendix A can be found a more in depth treatment.

- All optical TOE: In a different way from what was done in chapter 5, here the TOE is all optically induced. The unperturbed refractive index that appears in eq.7.4 is defined as :

$$n_0(\omega, \mathbf{k}) = \sqrt{\epsilon_r(\omega, \mathbf{k})} = \sqrt{(1 + \chi^{(1)}(\omega, \mathbf{k}))} \quad (7.6)$$

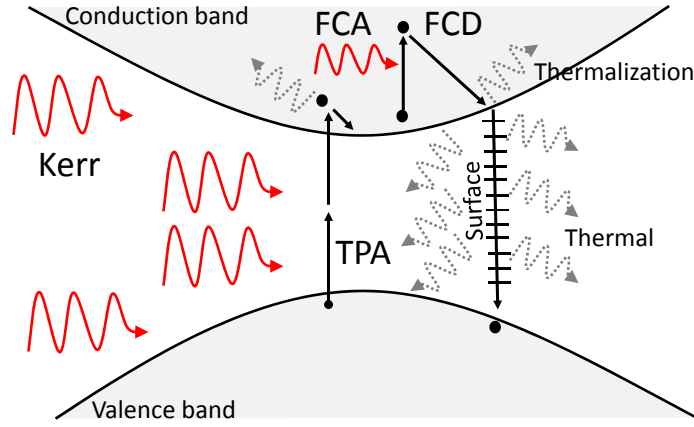


FIGURE 7.2: Representation of silicon's nonlinear phenomena.

The TOE effect arises from the interaction between the light and the electronic distribution around the nuclei. Such electronic distribution, changes with nuclei position, therefore with the phonon distribution. Temperature strongly affects phonon distribution, so we might expect that the polarization and, then, the refractive index will also depend on temperature. When we are close to room temperature T_0 , we can expand the refractive index as:

$$n_0(T, \omega) \approx n_0(T_0, \omega) + \left. \frac{dn_0}{dT} \right|_{T_0} (T - T_0) \quad (7.7)$$

where $n_0(T_0, \omega) \approx 3.5$ and $\frac{dn_0}{dT}$ is called the *thermo optic coefficient* and has a value of $1.86 \cdot 10^{-4} K^{-1}$ [144]. At steady state, when a differential temperature $\Delta T = T - T_0$ is achieved by material absorption of the electromagnetic field, we can relate ΔT to the intensity $|E|^2$ of the circulating field by means of the general relation (see appendix A):

$$\Delta T = \gamma_{lin}|E|^2 + \gamma_{TPA}|E|^4 + \gamma_{FCA}|E|^6 \quad (7.8)$$

where the three terms refers to different material absorption mechanisms: γ_{lin} to the usual linear absorption, γ_{TPA} to two photon absorption and γ_{FCA} to free carrier absorption. By substituting this relation in eq.7.7, we get:

$$n_0(|E|^2, \omega) = n_0(T_0, \omega) + \left. \frac{dn_0}{dT} \right|_{T_0} (\gamma_{lin}|E|^2 + \gamma_{TPA}|E|^4 + \gamma_{FCA}|E|^6) \quad (7.9)$$

that clearly shows that the thermo optic effect strongly depends on field amplitude. The positive sign of the thermo optic coefficient implies a red shift of the system spectral characteristic, since ($\gamma_{lin}, \gamma_{TPA}$ and γ_{FCA} are all > 0).

- Free carrier dispersion: As already shown, TPA is one of the main process that contributes to heat the material together with FCA. Through TPA a large number of electron-hole pairs can be generated, and the changes in free carrier distributions affect both the real and the imaginary part of the refractive index [144, 210]. In particular we have :

$$\Delta n^{FC} = \left. \frac{dn_{Si}}{dN} \right|_{N_0} \Delta N = -1.73 \cdot 10^{-21} \cdot \Delta N \quad (7.10)$$

$$\Delta \alpha^{FC} = \left. \frac{d\alpha}{dN} \right|_{\alpha_0} \Delta N = 1.45 \cdot 10^{-17} \cdot \Delta N \quad (7.11)$$

where Δn^{FC} is the change of the real part of the refractive index when a differential free carrier population ΔN ($[cm^{-3}]$) is generated with respect to the equilibrium value N_0 , $\Delta \alpha^{FC}$ ($[cm^{-1}]$) is the corresponding change of the absorption coefficient (defined as $\Delta \alpha^{FC} = 2\frac{\omega}{c}\Delta n_{FC}^I$, with Δn_{FC}^I the additional imaginary part acquired by the refractive index), also called the FCA coefficient. The negative sign of the free carrier dispersion coefficient $\frac{dn_{Si}}{dN}$ implies that the system spectral characteristic undergoes to a blue shift due to FCD. It can be demonstrated [41] that at steady state, when free carriers are generated by linear absorption, the relation between the intensity $|E|^2$ of the field and the differential population ΔN is linear, while when carriers are generated by TPA (main mechanism) the relation is quartic:

$$\Delta N = \eta_{lin}|E|^2 + \eta_{TPA}|E|^4 \quad (7.12)$$

where η_{lin} and η_{TPA} are coefficients that refers to the efficiency in generating free carriers through linear and TPA absorption respectively. Inserting eq. 7.12 in eq. 7.10 we obtain:

$$\Delta n^{FC} = \left. \frac{dn_{Si}}{dN} \right|_{N_0} (\eta_{lin}|E|^2 + \eta_{TPA}|E|^4) \quad (7.13)$$

$$\Delta \alpha^{FC} = \left. \frac{d\alpha^{FC}}{dN} \right|_{\alpha_0} (\eta_{lin}|E|^2 + \eta_{TPA}|E|^4) \quad (7.14)$$

The quantities Δn^{FC} and $\Delta \alpha^{FC}$ are related to the real and imaginary parts of χ^{FC} in eq. 7.3 by:

$$\chi^{FC} = 2n_0(\Delta n^{FC} + j\frac{c\Delta \alpha^{FC}}{2\omega}) \quad (7.15)$$

For a sub-micrometer WG the timescale of such phenomena are of the order of a nanosecond.

- **Kerr effect.** Kerr effect is due to non linear interactions of electromagnetic fields with valence electrons. Potential applications of this effect include self-phase modulation leading to all-optical switching and soliton propagation. In SOI based waveguides this effect can be exploited only if the characteristic time of the studied phenomenon is of the order of picoseconds. For a greater timescale the FCD and the TOE are the predominant effects. $\chi^{(3)}$ is rarely used in practice, one usually introduces the Kerr coefficient n_2 and the TPA coefficient β_{TPA} which are related to $\chi^{(3)}$ by [162]:

$$\frac{\omega}{c}n_2 + j\frac{\beta_{TPA}}{2} = \frac{3\omega}{4\epsilon_0 n_0^2 c^2} \chi_{1111}^{(3)} \quad (7.16)$$

It can be demonstrated [162] that all the components of the $\chi^{(3)}$ tensor can be expressed as a function of $\chi_{1111}^{(3)}$. The value of β_{TPA} for silicon is $0.79 \cdot 10^{-11} \frac{m}{W}$, while n_2 is equal to $0.45 \cdot 10^{-17} \frac{m^2}{W}$ at $\lambda = 1.54 \mu m$ [138].

7.3 Thermal bistability: theory and experiment

Let us focus to the microresonator scenario. The power dependence of the effective index, previously introduced, leads to a power dependent resonant frequency $\lambda_{res}(P) \propto n_{eff}(P)$. One of the first manifestations of this fact is the *optical bistability* (OB) [43]. When the input power becomes sufficiently high, the stationary behaviour of a SOI based device is dominated by the TOE nonlinearity. Thus in such devices the OB is TOE induced (this will be demonstrated in the next sections). A sketch of the OB phenomenon in an ADF is reported in figure 7.3. Before going into details, it is useful to think that TOE induces a resonance red shift. Therefore, a red detuned pump wavelength (λ_p) will attract the resonance to the pump (self lock) conversely, a blue detuned pump wavelength will push away the resonance (optical limiting). The former effect is related to a positive feedback between the pump induced resonance shift and the pump position, the latter to a negative feedback. We define the detuning $\Delta\lambda$ as $\Delta\lambda = \lambda_p - \lambda_0$ with λ_0 the wavelength of the cold cavity. The feedback and the detuning, for a TOE nonlinearity, are related as follows:

$$\Delta\lambda > 0 \rightarrow \text{positive feedback} \quad \Delta\lambda < 0 \rightarrow \text{negative feedback}$$

Taking as reference the figure 7.3, we can summarize OB in 3 main steps that composes the hysteresis loop:

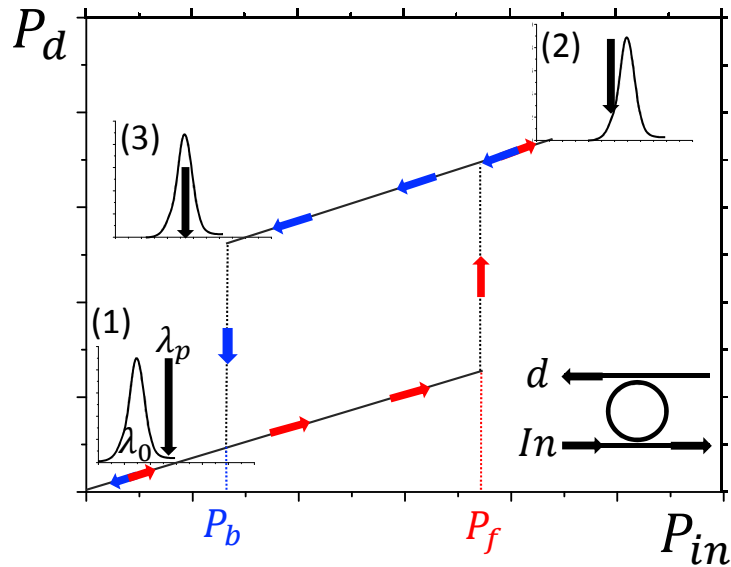


FIGURE 7.3: Hysteresis cycle for the D port of an ADF divided in the forward (red arrows) and backward direction (blue arrows). Inserts: Three sketches of the resonance and laser pump (black arrow) position during the cycle.

1. Cold cavity and positive $\Delta\lambda$: As the input power P_{in} starts to increase, the resonance shifts toward the pump as a consequence of the increased stored energy inside the cavity.
2. Cavity self-lock and negative detuning: at a certain power threshold P_f , there is enough stored energy to initiate the positive feedback mechanism. Thus the cavity locks on the laser pump and the drop signal increases. The equilibrium position is slightly blue shifted.
3. Hot cavity, negative detuning: as the input power starts to decrease, the negative feedback alters the return path (blue arrows) because the negative feedback tries to preserve the equilibrium point. But for a P_b input power, the detuning changes the sign again. The positive feedback restores the initial cavity position (1).

The stability of the hot state is proportional to the hysteresis width. For a very small width even a small perturbation is enough to relax the system. By means of a controlled perturbation, for example another laser, it is possible to choose the state of the system realizing then an all optical flip-flop [198].

But it is important to say that, the material properties have a crucial role on the stability of the position (2) and in some particular case the stability is lost. The system is no more suitable for a memory application if one of the 2 states are unstable. This will be the topic of the following sections.

7.3.1 Experimental verification: TOE induced optical bistability

In this section, the ADF nonlinear response is investigated. We focus on the stationary ADF response. In particular we are going to show the TOE induced OB in a RR.

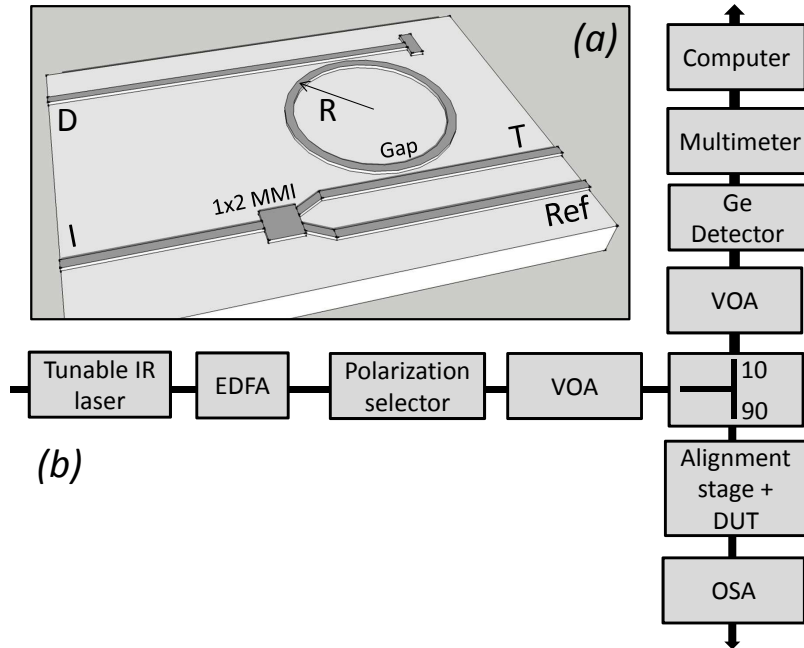


FIGURE 7.4: (a) Ring resonator based ADF. The 1×2 MMI provides the Ref channel. Device parameters: TE polarization, $R = 6.75\mu\text{m}$, $\text{gap} = 160\text{nm}$. Flowchart of the used setup (for additional details refers to appendix B.0.8).

The used setup is shown in appendix B.0.8. The flowchart in fig. 7.4 reports the components used for the OB verification. To measure at the same time the injection and transmitted power from the DUT, we modified the setup as follows: the output of EDFA goes to a *Variable Optical Attenuator* (VOA) which is fiber connected to a series of waveplates before going to a 10 – 90 beam splitter. The 10% branch goes to a *NEW FOCUS 2033* Germanium photodetector through another VOA to protect the device and avoid saturation. The 90% branch goes to the alignment stage. The output tapered fiber is connected to a OSA to register the output power. The power coupled inside the DUT is calculated considering insertion losses of 10dB .

In the inset of figure 7.5 it is shown the selected resonance with a center wavelength of $\lambda_0 = 1549.672\text{nm}$ and a Q factor of 10^4 . The λ_p is 1549.72nm corresponding to a positive detuning.

The input power is manually increased step by step by reducing the VOA attenuation, from $30\mu\text{W}$ to $2000\mu\text{W}$ while maintaining the wavelength fixed; once the forward path is completed we repeat the same procedure decreasing the power in order to close the cycle. The result is shown in fig.7.5 where the presence of hysteresis is clear. The difference

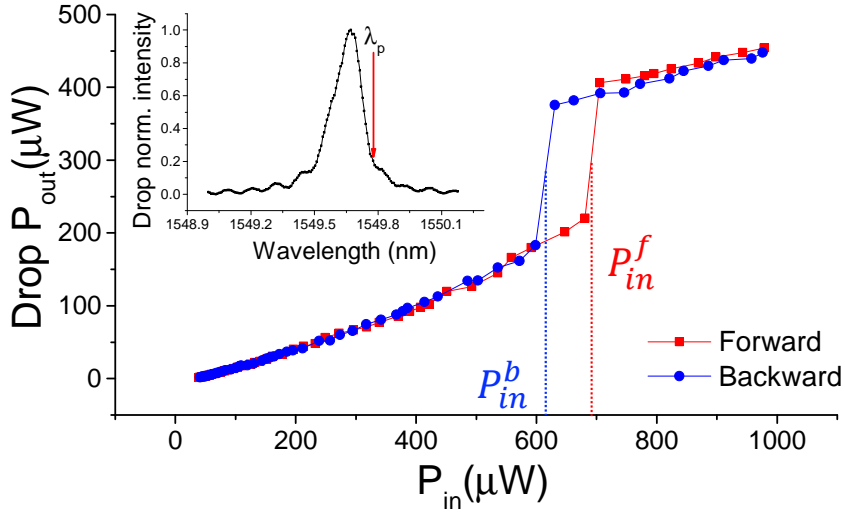


FIGURE 7.5: Drop power output P_{out} as a function of input power P_{in} : (Red) increasing power, (blu) decreasing power. The inset shows the transmission spectrum of the drop port. $P_{in}^{f,b}$ are the 2 threshold of bistability.

between the forward threshold power P_{in}^f and the backward one P_{in}^b is $(80 \pm 20)\mu W$. The power values refers to the one that is present in the waveguide, so coupling losses have been already included.

7.3.2 Nonlinear spectrum deformation

In this section, the spectral variations linked to nonlinear extra absorptions and the TOE coefficient are investigated. As previously introduced, silicon exhibit three main sources of absorption: the linear absorption and the two nonlinear absorptions, TPA and FCA. Some information about these effects can be extracted by looking at the ADF spectrum deformation for several input power.

The curves in figure 7.6 are obtained performing several transmission spectrum at different input power. The initial pump wavelength starts always with a negative $\Delta\lambda$ going towards the red.

The initial condition of the measure is the optical limiting case. As the pump wavelength approaches the resonance more power is coupled inside it and, as a consequence, it is being subjected to a red shift. The original position is restored when the pump power is no more sufficient to heat the cavity and to preserve the shift. The cavity relaxation coincides to an abrupt drop of the transmitted power. The insert in figure 7.6 reports the spectral position of the relaxation point as a function of the input power. The data has been fitted using a third order polynomial (red line). The origin of the 3 th polynomial

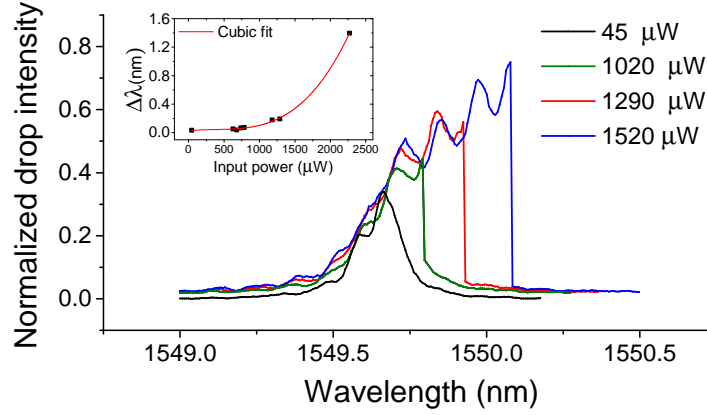


FIGURE 7.6: Normalized drop intensity as a function of wavelength for several input powers: (black) $45\mu W$, (green) $1.02mW$, (red) $1.29mW$ and $1.5mW$. The insert reports the detuning $\Delta\lambda$ as a function of the input power together with a polynomial cubic fit.

order shift is inherent in the nonlinear process, TPA and FCA, that induce the cavity heating. The relation between the absorbed power and the wavelength shift is:

$$\Delta\lambda = \frac{\lambda_0}{n_{Si}} \Delta n_{Si} = \frac{\lambda_0}{n_{Si}} \frac{dn_{Si}}{dT} \Delta T = \frac{\lambda_0}{n_{Si}} \frac{dn_{Si}}{dT} R_{th} P_{Abs} \quad (7.17)$$

where n_{Si} is the silicon refractive index at room temperature, $\frac{dn_{Si}}{dT}$ the thermo optic coefficient and R_{th} the thermal resistance of the cavity. The term P_{Abs} contains 3 main contributions (refer to the appendix A for more details)[211]:

$$\Delta\lambda = aP_{inc} + bP_{inc}^2 + cP_{inc}^3 \quad (7.18)$$

that correspond to the linear, TPA and FCA contribution respectively. That correspond to the linear, TPA and FCA contribution respectively. The relative importance of this terms can be extracted from the fitted coefficients reported in table 7.1:

Fit: $d + ax + bx^2 + cx^3$	Values
a	$(1 \pm 0.7) \cdot 10^{-4} \frac{nm}{\mu W}$
b	$(-2 \pm 0.8) \cdot 10^{-7} \frac{nm}{\mu W^2}$
c	$(1.9 \pm 0.2) \cdot 10^{-10} \frac{nm}{\mu W^3}$
d	$(2 \pm 1) \cdot 10^{-2} nm$

TABLE 7.1:

In the reported experiment, the nonlinear absorption is observed through the TOE effect, thus through a refractive index variation. In the next section, instead, the nonlinear absorption is directly observed by looking at the resonance broadening.

7.3.3 Non linear resonance broadening

We are going to show another experiment that confirms the presence of nonlinear absorption. This time the resonance quality factor variation, under an input power change, is observed. To track the Q variation, we add an ASE white source to the previously used setup (see Fig. 7.4). The laser+EDFA are then used to pump the $m+1$ -th resonance order (the one at $\sim 1550\text{ nm}$), while the m -th order spectrum is acquired with the OSA (the one at $\sim 1536\text{ nm}$). The results are reported in figure 7.7.

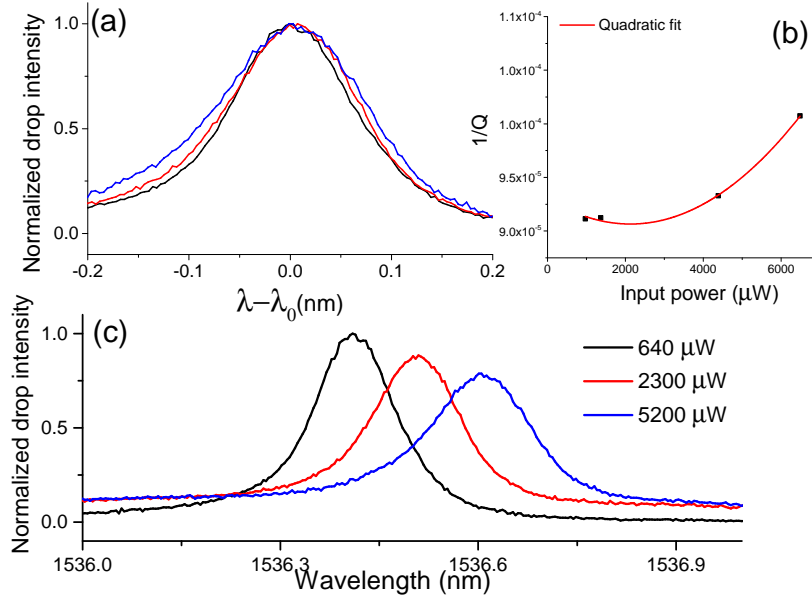


FIGURE 7.7: (a) Normalized D port transmission spectra as a function of the detuning, $\lambda - \lambda_0$. (b) Inverse of the quality factor as a function of the input power and relative quadratic fit (red). (c) Normalized D port transmission spectra: data normalized by the max of the black curve. (a,c) Three different input powers were used: (black) 0.64 mW , (red) 2.3 mW and (blue) 5.2 mW .

Panel (c) displays the T port spectra as were taken from OSA. As the input power increases, we notice a red shift of λ_0 due to TOE, a resonance broadening and a smaller ER caused by nonlinear absorption. To emphasize the resonance broadening, the spectra showed in panel (a) are plotted as a function of $\lambda - \lambda_0$, where λ_0 is the center of the resonances. The variation of the Q can be related to the already introduced quantity P_{abs} through the Q factor definition [45]:

$$Q = \frac{\omega U_{int}}{P_{abs}} \quad (7.19)$$

where U_{int} is the cavity energy. A similar method used to obtain eq. 7.18 can be used to deduce the energy dependence of P_{Abs} , $P_{abs} = a_1 U_{int} + a_2 U_{int}^2 + a_3 U_{int}^3$. Using again the fact that for a low loss resonator the internal energy is proportional to the incident

power P_{inc} , the quantity $\frac{1}{Q}$ can be expressed as:

$$\frac{1}{Q} = a + bP_{inc} + cP_{inc}^2 = \frac{1}{Q_{lin}} + \frac{1}{Q_{TPA}} + \frac{1}{Q_{FCA}} \quad (7.20)$$

where Q_{lin} , Q_{TPA} and Q_{FCA} refers, respectively, to linear, two photon absorption and free carrier absorption quality factors while a, b and c are constants that include all the pre-factors. These coefficients give an idea of the relative importance of the various processes to determine the total resonance Q factor. The expected quadratic dependence of $1/Q$ is shown in the panel (b) and the extracted coefficients are reported in table 7.2.

Polynomial fit: $a + bx + cx^2$	Values
a	$(9.30 \pm 0.06) \cdot 10^{-5}$
b	$(-2.2 \pm 0.5) \cdot 10^{-9} \mu W^{-1}$
c	$(5.3 \pm 0.6) \cdot 10^{-13} \mu W^{-2}$

TABLE 7.2: Fit coefficients

Obviously, the negative coefficient b leads to an absurd, i.e. a negative Q factor. This could be related to the high error present on that coefficient that suggests that more points have to be acquired to get the right coefficients.

7.4 A more in depth view of optical bistability

With the aim of clarifying the phenomena which will be treated in the following sections, here we introduce a simplified model of the system under study that explains both the OB and the SP (self-pulsing) phenomena [44, 138]. This section approaches the theoretical description of a non-linear cavity through the time dependent CMT. Firstly, an ADF with single nonlinearity is described and secondly, another nonlinearity is added.

7.4.1 Optical bistability with one nonlinearity

The system under study is shown below. The treatment is valid for whatever cavity shape, such as RR or RTR .

We define U_{int} as the internal field amplitude, E_{inc} as the incident field amplitude, τ_0 as the radiative losses decay time and k^2 as the coupling coefficient. The dynamic of the cavity around its resonant frequency ω_0 is described by a forced oscillator equation:

$$\frac{dU_{int}(t)}{dt} = \left(i\omega_0 - \frac{1}{\tau_t} \right) U_{int}(t) + i\sqrt{2/\tau_k} E_{inc}(t) \quad (7.21)$$

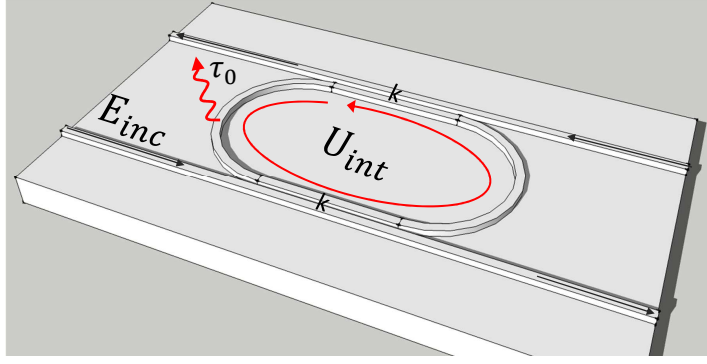


FIGURE 7.8: System under study: coupling coefficient k^2 , internal field amplitude U_{int} , radiative losses decay time τ_0 and incident field amplitude E_{inc} .

where $1/\tau_t = 1/\tau_0 + 2/\tau_k$ is the total decay time and τ_k is a decay time related to the coupling with the WG; k and τ_k are linked through $k^2 = \frac{2p^2}{\tau_k v_g}$. For a (quasi)monochromatic incident field, $E_{inc} = \tilde{E}(t)e^{i\omega_p t}$, and the ansatz, $U_{int} = \tilde{U}(t)e^{i\omega_p t}$, for the internal field amplitude we obtain:

$$\frac{d\tilde{U}(t)}{dt} = \left(i(\omega_0 - \omega_p) - \frac{1}{\tau_t} \right) \tilde{U}(t) + i\sqrt{2/\tau_k} \tilde{E}(t) \quad (7.22)$$

As we found in chapter 2, the last equation is characterized by a lorentzian stationary state. We now adds the first nonlinear term $Nl_1(U, t)$ to ω_0 , that induces a resonance red shift (in wavelength), in order to simulate the TOE effect.

$$\omega_0 = \omega_0(1 - B_1 Nl_1(\tilde{U})) \quad (7.23)$$

where B_1 is a factor that determines the magnitude of the nonlinearity. The effect of a nonlinearity is not instantaneous (only the Kerr can be modeled as instantaneous), but is characterized by a decay rate γ_1 .

$$\frac{dNl_1(\tilde{U})}{dt} = -\gamma_1 Nl_1(\tilde{U}) + G_1 |\tilde{U}|^2 \quad (7.24)$$

The constant γ_1 represents a decay rate linked to a thermal time constant of the system while $G_1 |U(t)|^2$ reminds a forcing factor. Nl_1 has a linear dependence on the energy $|U|^2$. In stationary condition, the equations 7.23 can be replaced in eq. 7.22 to obtain an implicit solution for the cavity energy $A = |\tilde{U}|^2$:

$$E = \left(i \left(\omega_0 \left(1 - B_1 \frac{G_1}{\gamma_1} A \right) - \omega_p \right)^2 - \frac{1}{\tau_t^2} \right) A \tau_k / 2 \quad (7.25)$$

where E is the incident energy in stationary regime. The figure 7.9(b) is a contour plot of E as a function of the internal energy A and pump wavelength.

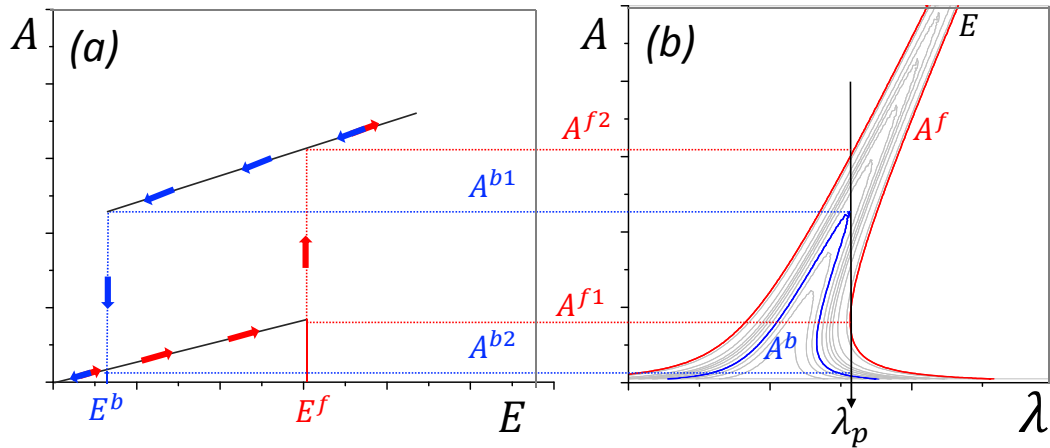


FIGURE 7.9: (a) Hysteresis cycle for the internal energy A as a function of input energy E : forward (red arrows) and backward (blue arrows) paths. (b) Incident energy (E) contour plot as a function of the internal energy (A) and of the pump wavelength. E^f : forward threshold energy related to the forward internal energies $A^{f1,2}$. E^b : backward threshold energy related to the backward internal energies $A^{b1,2}$.

A growing input power, deforms the Lorentzian shape towards the red as a consequence of the nonlinearity sign. The isometric curves of figure 7.9(b), in which the input power is constant, shows the allowed solutions for the cavity energy A . The OB phenomenon is hidden in the lumpy shape of the resonance (Fig. 7.9(a)). With reference to figure 7.9 we can describe the OB as follows:

- E is incremented with a constant λ_p (Fig. 7.9 red path) and the cavity energy responds with a linear growth (Fig. 7.9 (a)). The system admits continuous solutions up to $E = E^f$ point where, a further increase of E causes the internal energy to a jump from A^{f1} to A^{f2} (both energies belong to the same red isocurve). Here the $A(E)$ curve exhibits a sudden jump visible in the graph 7.9(a).
- Now, E is being decreased (7.9 blue path) and the cavity energy responds with a linear reduction (Fig. 7.9 (a)). The system admits continuous solutions up to $E = E^b$ point where a further decrease of E , induces the internal energy A to a jump from A^{b1} to A^{b2} (both energies belong to the same blue isocurve). Here the $A(E)$ curve exhibits a sudden drop visible in the graph 7.9(a). A further reduction of E is reflected in a linear reduction of A .

The same consideration could be made for the D port, since it is directly related to A through the coupling coefficient. Single nonlinearity thus, leads to OB. The response of the system, with an addition of a second nonlinearity will be investigated in the next session.

7.4.2 Optical bistability with two nonlinearities: self pulsing phenomena

We start from the equation 7.22 by adding a second nonlinear term similar to that of eq. 7.24.

$$\frac{d\tilde{U}(t)}{dt} = \left(i \left(\omega_0(1 - B_1 Nl_1(\tilde{U}) - B_2 Nl_2(\tilde{U})) - \omega_p \right) - \frac{1}{\tau_t} \right) \tilde{U}(t) + i\sqrt{2/\tau_k} E(t) \quad (7.26)$$

The parameters B_2 , γ_2 , G_2 are the already introduced coefficients related to the magnitude, decay rate and forcing term of Nl_2 respectively (see eq. 7.24).

In order to simulate a system near the real one, without the needs of taking into account all the numerous coefficients, the following conditions are imposed:

$$\frac{\gamma_2}{\gamma_1} \sim 10, \quad \gamma_2, \gamma_1 \ll \gamma_t \quad (7.27)$$

This means that the time scale of the nonlinearities is slow compared to that of cavity γ_t . The γ_2 is associated to the decay rate of free carriers while γ_1 to the thermal decay rate, as a consequence of the relation 7.27. Then, we fix the values of B_1 and B_2 by imposing the order of magnitude of $\Delta\omega/\omega$ to be about 10^{-4} (of the same order of $\frac{dn_{Si}}{dT}$) in the typical range of incident power.

$$-B_2/B_1 \sim 0.6 \quad B_1 \frac{G_1}{\gamma_1} A \sim 10^{-4} \quad (7.28)$$

The ratio between $-B_2/B_1$ means that, in this system, the relative importance of the the FCD and TOE is about 0.6 and, also, that the FCD has a negative sign (i.e. blue shift in wavelength). To study the system response as $P_{inc}(P_{int})$ we use the relation which will often be used to translate between the power picture and energy picture:

$$P_{inc} = p/v_g |E|^2, \quad P_{int} = p/v_g A \quad (7.29)$$

We can understand the system behaviour by looking at figure 7.10. Superimposed to the stationary solution plot (gray scale) (analog that to Fig. 7.9), there is a plot that indicates the system stability (red scale). The blue dashed line indicates the position of the cold cavity resonance (λ_0) while the red one the instability power threshold. The inserts report the time response of $|U(t)|^2$ for several initial conditions, obtained by numerical integration. The power is expressed in mW. The following comments can be made:

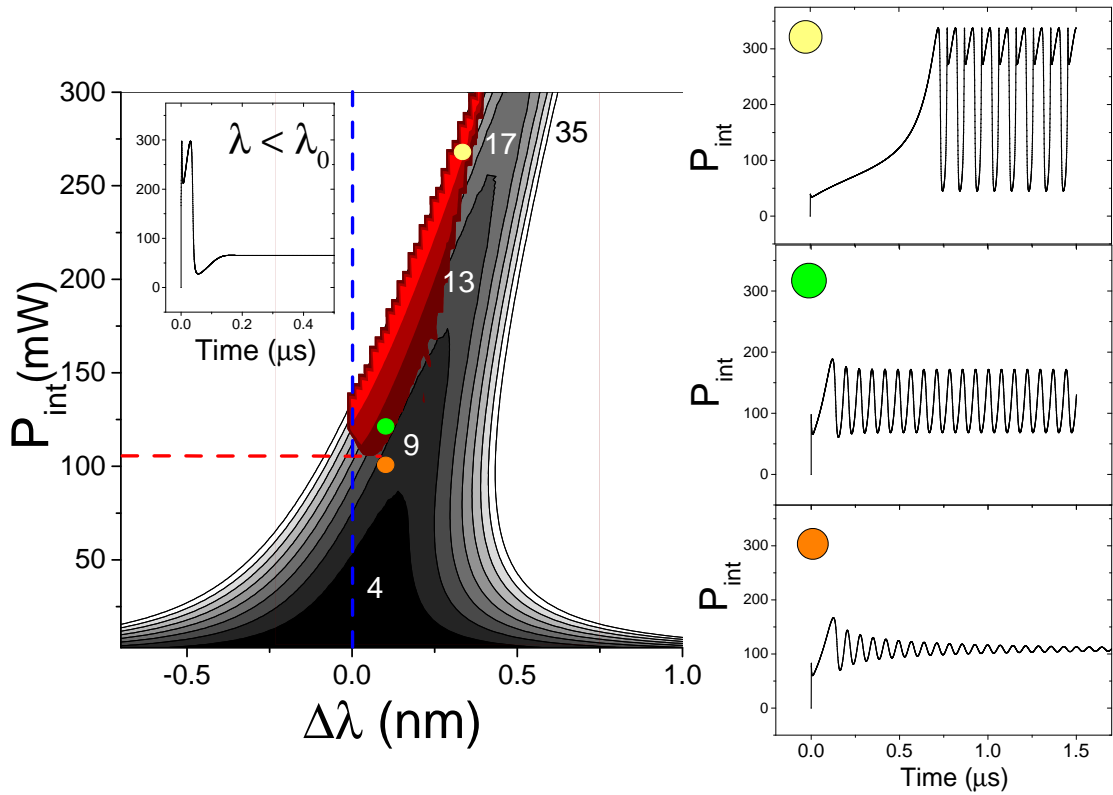


FIGURE 7.10: (Gray scale) Incident power contour plot as a function of the power inside the cavity and of the pump wavelength: the incident power of each contour is reported in white. (Red scale) Instability area of the system. Instability power threshold (red dashed line). Cold cavity resonance wavelength (blue dashed line). The insets show the time behaviour of the points indicated by the colored circles. Simulation parameters:
 $R = 6.75\mu\text{m}$, $k^2 = 5\%$, $n_g = 4.1$.

- The instability area is located only on the right of λ_0 (blue dashed line) which is in agreement with the greater instability sign.
- Only above about $P_{inc} = 9\text{ mW}$ (the power threshold), denoted by a red dashed line, the system becomes unstable.
- The threshold is wavelength dependents: the more you move away from λ_0 , the more the threshold increases .
- Just under the threshold the system is stable and, by looking at the time response (orange circle) behaves as a damped oscillator.
- The unstable behaviour takes place only after a bistable jump (Fig. 7.3(2)). This is because, the red area appears only above the upper branch of the iso-power curves.
- In the instability area, the system oscillates with a fixed period that depends on P_{inc} and λ (green and yellow circles). The order of magnitude, of about tens of

ns , is related to the time scale of the nonlinearities that generate the phenomenon. This is the so called *self-pulsing phenomenon*.

Despite the constant input power, the cavity temporal behaviour shows a self-pulsing characteristic. The oscillating nature of the system is a peculiarity of this condition where two nonlinearities, of opposite sign, modify the resonance position with different time constants. In equation 7.26 we have considered only the nonlinear dispersive effects that were described through an energy dependent resonant frequency. We know from section 7.2.1 that TPA adds also a non linear absorption that should be included in the γ_t term. The energy dependency of ω_0 , that was supposed to be linear, contains also a quadratic and a cubic term. A more realistic model will be discussed in the next section together with the experimental demonstration of the phenomenon.

7.5 Self pulsing in single microresonator: experiment and simulation results

The SP effect is well know in a SOI based microresonator system . It has been demonstrated in a RR and in a microdisk resonator (experiment [44, 45], theory [138]). It is, in any case, important to measure this system because it strongly depends on the geometry of the system, resonator size and waveguide section. Therefore it is necessary to verify if, the parameters that will be used in the simulation, are consistent with the experiment.

7.5.1 Experiment

A description of the experimental setup is found in the appendix B.0.8. Now we look for the device time response so, we uses a fast photodiode ($7GHz$ bandwidth), as detection unit, interfaced with an oscilloscope. In the following, we refer to the same structure used before: a RR with a radius of $6.75\mu m$, gap $160nm$, a waveguide width of $500nm$ in ADF configuration. The used polarization is TE and the considered resonance has $\lambda_0 = 1549.67 nm$.

We investigate the system as follows: we fix the power and we scans the system by moving the wavelength with steps of $0.01 nm$ until the stationary-SP transition is found. Once the SP regime is found, we fix the wavelength and we change the power. As anticipated in the previous section, the spectral region where the system oscillates is red shifted from the cold cavity resonance λ_0 . The width, $[\lambda_{Start} - \lambda_{Stop}]$, and the center of this region depends on the pump power. Three of these regions are reported in table 7.3.

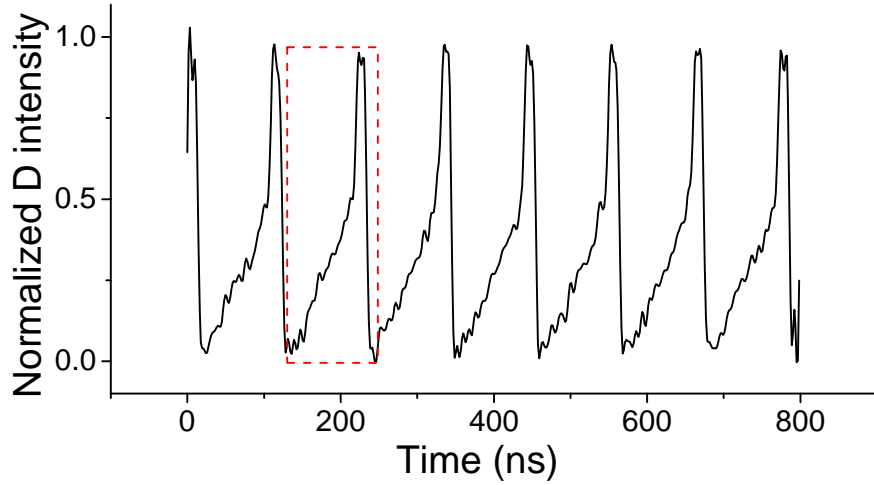


FIGURE 7.11: Measured SP regime: Normalized D port output as a function of time. $\lambda_p = 1550\text{ nm}$, $P_{inc} = 6\text{ mW}$. Red dashed rectangle: zoom area of the next figure.

Region	Pump power	λ_{Start}	λ_{Stop}
1	15.0mW	$(1550.16 \pm 0.01)\text{nm}$	$(1552.57 \pm 0.01)\text{nm}$
2	14.3mW	$(1550.14 \pm 0.01)\text{nm}$	$(1552.36 \pm 0.01)\text{nm}$
3	12.3mW	$(1550.11 \pm 0.01)\text{nm}$	$(1552.25 \pm 0.01)\text{nm}$

TABLE 7.3: SP regions for 3 inputs power: 12.3mW, 14.3mW and 15.0mW .

An example of SP effect can be seen in figure 7.11. The SP time scale is of the order of 40 – 100 ns which reminds the time scale of the thermal relaxation. The lineshape of the pulses depends on the presence of two bistability cycles induced by the FCD and the TOE effects. With reference to the figure 7.12, we interpret the phenomenon as follows:

1. FCD bistability: The negative resonance detuning ($\Delta\lambda = \lambda_p - \lambda_0$) lead to a FCD bistability. When the resonance crosses the pump, $\Delta\lambda = 0$, a great number of free carriers are generated and the D port transmission exhibits a fast (about 3ns) variation from low-high-low. Here the system is in a stable state ((1) dashed line).
2. TOE bistability: The equilibrium is broken by the heating of the RR due to absorption of the free carriers previously generated. Now the detuning is positive. Thus the system allows a TOE bistability. When the RR temperature reaches a sufficient level to counteract the FCD induced shift the system will change state. The signal grows up for about 15ns while the RR heats up. Then it suddenly drops to a low transmission state ((2) dashed line).
3. Thermal relaxation: The resonance is detuned with respect to the pump, therefore start it starts to cool down. Also the lowering of the free carriers contributes to the red shift of the resonance. After the thermal decay time of RR, of about 60 – 70ns, the system comes back to the initial conditions((3) dashed line).

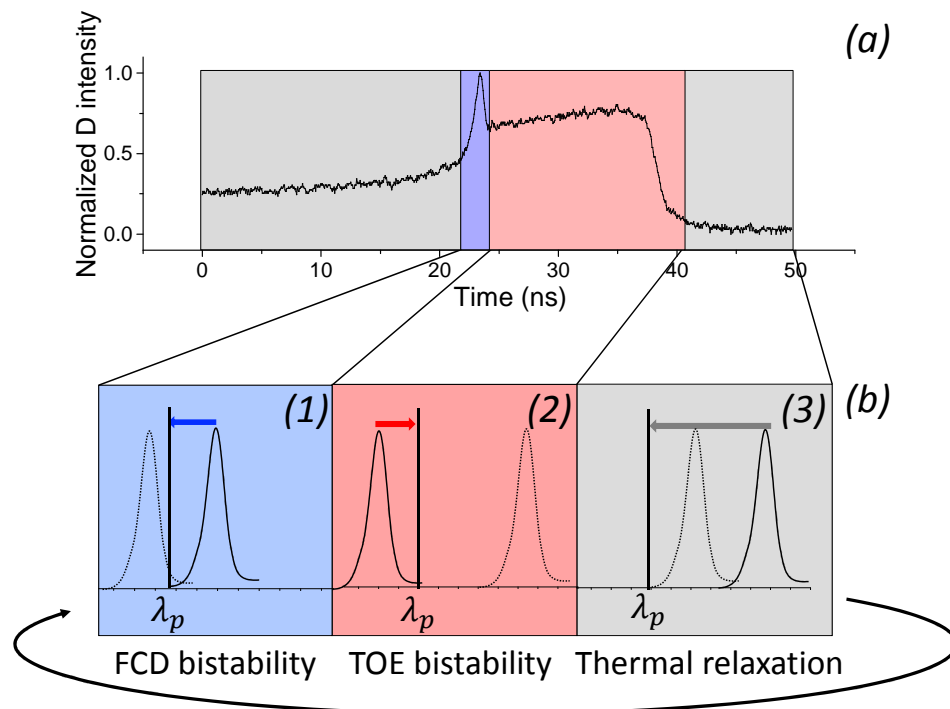


FIGURE 7.12: (a) A particular of a single pulse of figure 7.11 : normalized D intensity versus time. (b) Resonance shift around the pump wavelength λ_p for the 3 main physical processes involved: (1) FCD bistability, (2) TOE bistability and (3) Thermal relaxation. The solid(dashed) line represents the resonance position at $t(t + dt)$

The 3 steps are cyclically repeated with a power and wavelength dependent period as shown in figure 7.13.

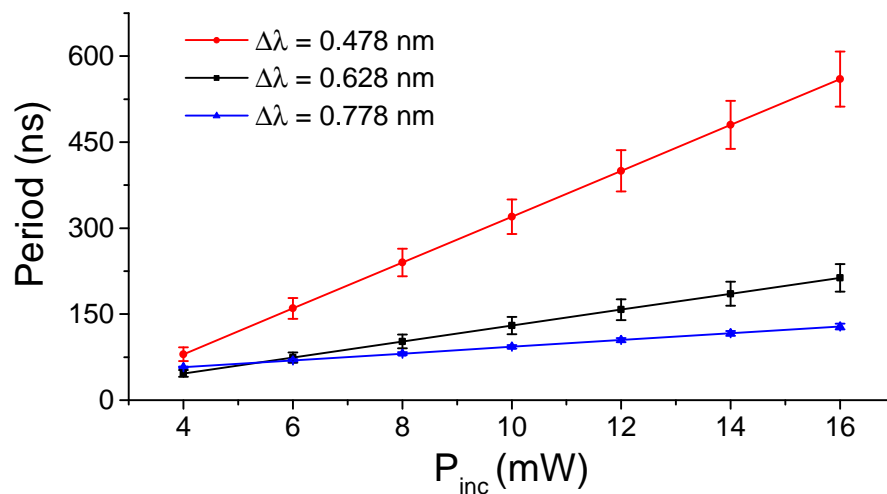


FIGURE 7.13: SP period versus pump power for 3 pump detunings, $0.478nm$, $0.628nm$, $0.778nm$.

It is observed that, the higher the input power, the longer the period, while, the larger the detuning, the smaller the period. The period is linearly depends on the power. In

particular, the period ranges from 60 – 70 ns (limited by the thermal decay rate) up to 600 ns. The incident power affects also the shape and the ER of the pulses (Fig. 7.14). A decrease of input power leads to a lineshape that becomes progressively similar to a sinusoid (small perturbation).

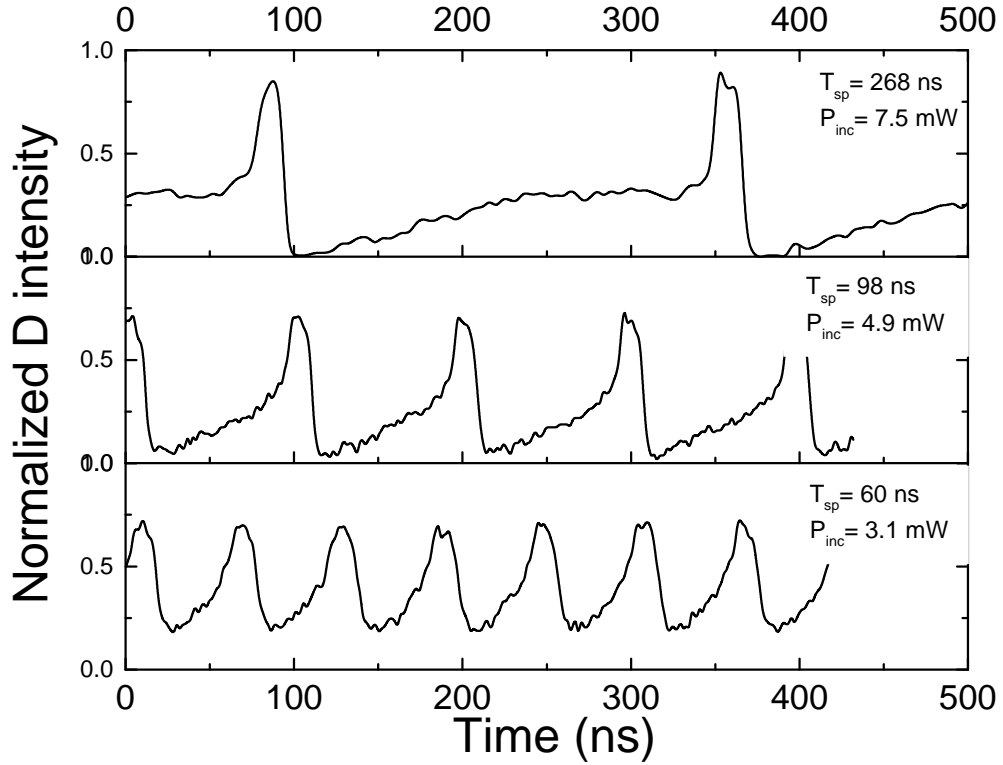


FIGURE 7.14: D port intensity, normalized to the maximum value of the upper curve, versus time for several input power: 3.1mW, 4.9mW and 7.5mW. Pump wavelength 1550nm .

The variation of ER can be understood by imagining the system as a low-pass filter with a cut-off frequency of $1/\tau_{th}$.

7.5.2 Simulations

A more realistic model is investigated in this section. As we did before (equations 7.24,7.26) we will use a set of coupled nonlinear differential equations to describe the cavity dynamic, the free carriers dynamic and the temperature dynamic. A simplified model by using pre-factors is here introduced, while a complete description of the equations is found in the appendix A. The used model is very similar to the one introduced in [45], but the following approximations were adopted: the differential temperature and free carrier population are considered constant in position and fully confined inside the RR volume, small losses per round trip which translate in a constant field amplitude inside the RR. The simulation parameters were in part deduced from the experiment,

in part taken from the literature. A collections of these parameters is found in the appendix A.

$$\begin{aligned} \frac{dU_{int}(t)}{dt} = & i\omega_0 [1 - F_{TOE}(A(t)^3) - F_{FCD}(A(t)^2) - F_{Kerr}(A(t))] U_{int}(t) \\ & - [\gamma_t + \gamma_{FCA}(A(t)^3) + \gamma_{TPA}(A(t)^2)] U_{int}(t) + i\sqrt{2/\tau_k} E_{inc}(t) \end{aligned} \quad (7.30)$$

Equation 7.30 takes into account the TOE, FCD and Kerr dispersion through the pre-factors $F_{TOE}(A(t)^3)$, $F_{FCD}(A(t)^2)$, $F_{Kerr}(A(t))$ with $A(t) = |U_{int}(t)|^2$. Also the non-linear losses are included through the factors $\gamma_{FCA}(A(t)^3)$ and $\gamma_{TPA}(A(t)^2)$. Figure 7.15 shows the refractive index relative variations (F pre-factors) (a) and the nonlinear decay rates, normalized to the total linear γ_t , for a common range of internal cavity powers.

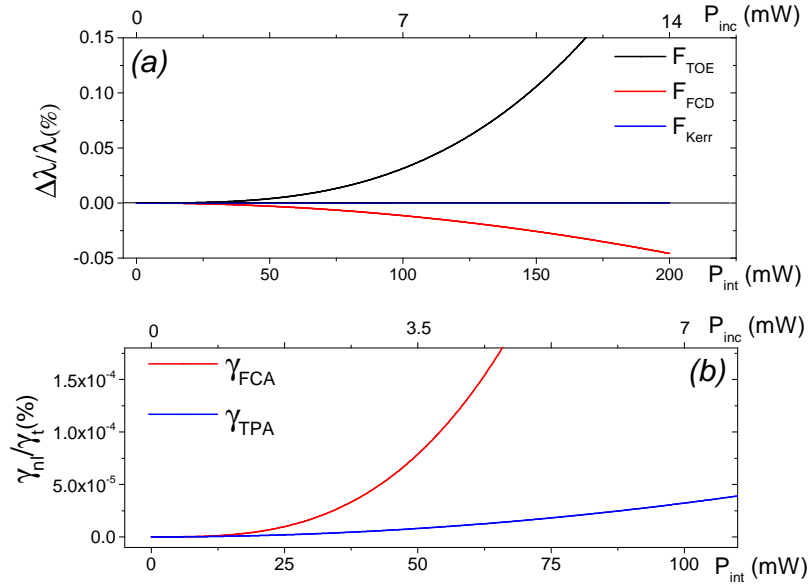


FIGURE 7.15: (a) Refractive index relative variations as a function of the internal cavity power P_{int} and input power P_{inc} for different sources, TOE (black), FCD (red), Kerr (blue). The insert shows a zoom on the low power range. (b) Nonlinear decay rate γ_{nl} , normalized to the cavity total decay rate, versus the internal cavity power for different sources, TPA (blue) and FCA (red). For the used parameters refer to the table in the appendix A .

It is observed that, the variation of the nonlinear refractive index, for an input power up to 8 mW , is about 0.01 to 0.1 %. At such power level, the dominant effect is the TOE since it scales with the third power of the internal energy. The Kerr effect is typically negligible unless at time scales of the order of $fs - ps$. For the power loss, figure 7.15(b), it comes out that the FCA losses are the dominant one.

The system stationary solution is reported in figure 7.16. Here the picture differs from the case of figure 7.10, since now we included also the quadratic and cubic nonlinear terms. Despite the three non-linear terms, one of which induces a blue shift, the stationary solution shows to a red shift. Thus, at this wavelength and power, the TPA (and consequently the FCA) dominates the scenario. This explains why OB is experimentally observed only for a positive detuning, as showed in section 7.5.

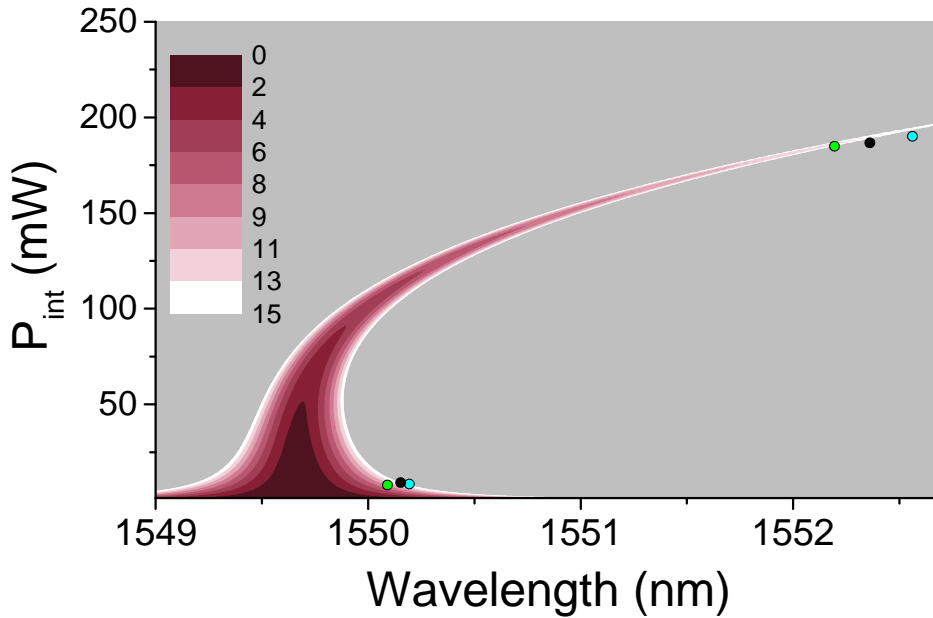


FIGURE 7.16: Contour plot for the stationary state of eq. 7.30 showing the internal power versus the pump wavelength. Contour levels: several input powers P_{inc} as indicated by the color bar in mW . Table 7.5.1 star-end point indicators: (1) cyan circle, (2) black circle, (3) green circle. For the used parameters refers to the table in the appendix A

In fact it was experimentally carried out the same operation reported in figure 7.6: the pump wavelength was moved from left to right while maintaining a constant input power. The internal power, proportional to port D through the factor k^2 , follows the upper hump and falls when the iso-curve ends. The small circles refer to the measured start-end point of table 7.3: (1) cyan, (2) black, (3) green. We note that the position of the start-end points, for the used input power 12 – 15 mW , lies inside the simulated stationary solution. This is a good indication to say that the chosen parameters are good.

The figure 7.17 shows the stationary solution with the instability area in blue. The SP regime starts only for positive λ detuning. The threshold input power is about 3 mW and increases with a detuning increase. The insets show the pulsing lineshape for two different parameter configurations which are indicated, on the contour plot, through the yellow and grey circles. The pulse shape is very close to that obtained in the previous

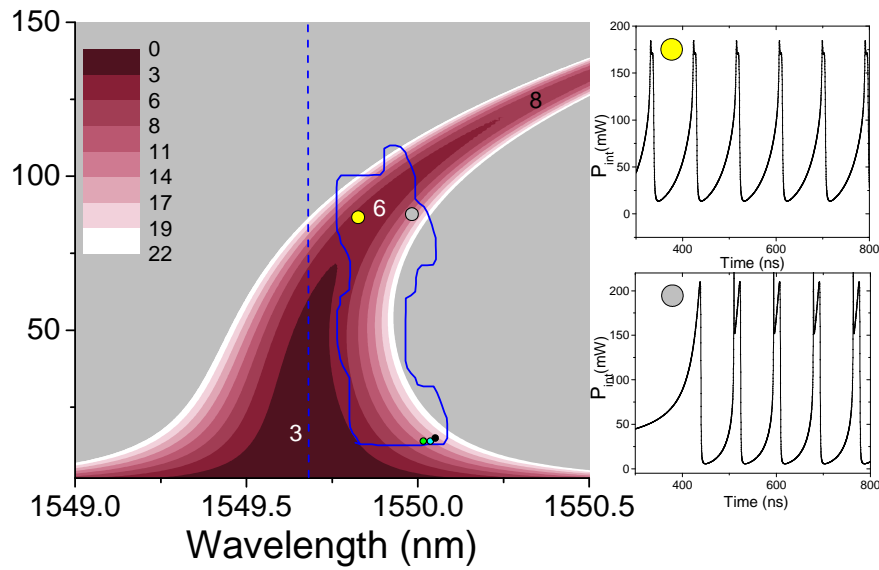


FIGURE 7.17: Contour plot for the stationary state of eq. 7.30 showing the internal power versus the pump wavelength. Contour levels: several input powers as indicated by the color bar in mW . Table 7.3 start point indicators: (1) cyan circle, (2) black circle, (3) green circle. Blue dashed line: Cold resonance wavelength. Blu area: SP region for input powers of up to $22 mW$. (Insets) System time response examples: the investigated points are identified by the grey and yellow circle. For the used parameters refer to the table in the appendix A.

sections. Their period is $87 ns$ and $100 ns$ for the grey and yellow respectively. An accurate model-experiment fit is reported in figure 7.18(a).

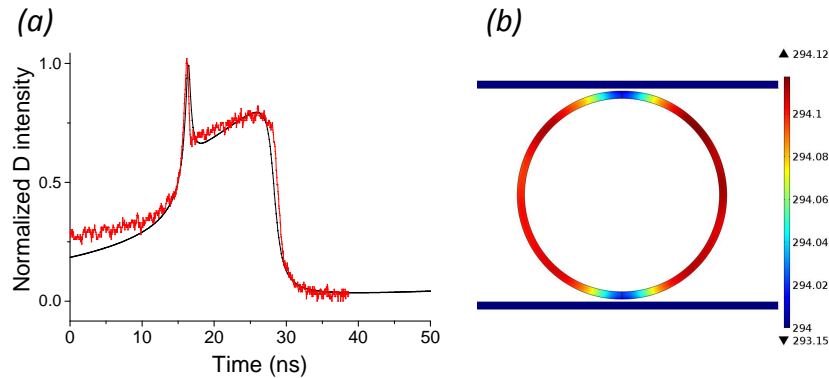


FIGURE 7.18: (a) black (red) curve: simulated (measured) normalized D port transmission versus time in ns . Pump wavelength $1550 nm$ (red, black) and input power $10 mW$ (red), $15 mW$ black. (b) Simulated thermal distribution on the RR after a cooling time of $100 ns$. Simulation parameters in table 7.4

The table 7.4 shows the values of the parameters used in the simulation compared with the experimental ones. Note that, the used τ_{FC} is very similar to that obtained from the system of the RTR pumped by the Ti:Sa laser (see section 5.11.2). This is comprehensible because of the similar WG surface of the two systems.

TABLE 7.4: Simulation parameters

λ_0	$\lambda_p^{exp.}$	$\lambda_p^{sim.}$	τ_{TOE}	τ_{FC}
1549.66 nm	1550.00 nm	1549.84 nm	83 ns	3.3 ns
$P_{inc}^{exp.}$	$P_{inc}^{sim.}$	CC	lossdB/90°	
5 mW	5 mW	5%	0.005	

The simulation fits well the experimental curve, but there are some small discrepancies. In particular, the thermal relaxation region ($0 - 10ns$) is the one which deviates more. The approximation of thermal uniformity along the ring, adopted to model the system, may be the source of the discrepancy. In fact, as we can see from figure 7.18(b), the presence of the WGs perturbs the temperature uniformity in the ring. The WGs act as heat pipes and help to the cool the ring. The simulated thermal decay constant for a $6.75 \mu m$ ring is $52 ns$.

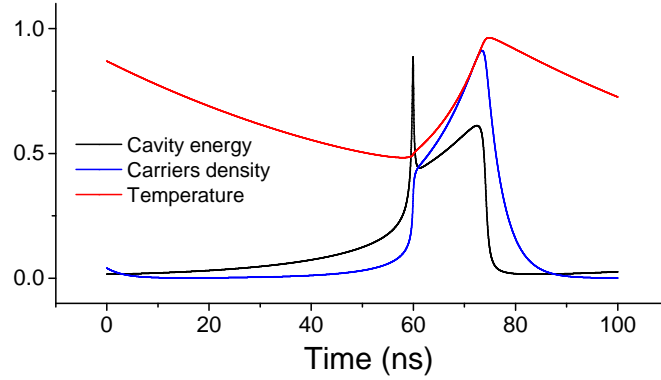


FIGURE 7.19: (black)Cavity energy, (red) differential temperature ΔT and (blu) carriers density ΔN normalized to their maximum as a function of time: $\Delta T_{max} = 15 K$, $\Delta N_{max} = 4.5 \times 10^{17} cm^{-3}$.

As a complement to figure 7.11, in figure 7.19 we show the differential temperature, defined as the RR temperature minus the environmental temperature, the free carrier density and the internal cavity energy dynamics.

7.6 Non linear effects in a SCISSOR device

Until now, only a single cavity non-linear system has been studied. We have seen that, if there are two competitive dispersive effects (FCD, TOE), the system admits self-pulsation states. The situation can change, even radically, in a sequence of coupled cavities. There are many theoretical articles describing systems of coupled cavities, with Kerr non-linearity, where *chaotic state* are predicted [46, 139, 141]. However, at least

to our knowledge, no such chaotic states, in systems of integrated coupled cavities, have been experimentally demonstrated. Furthermore, the theoretical treatment concerned only systems with a Kerr non-linearity. In silicon based systems this is far from the reality since the dominant effects are the FCD and the TOE generated by TPA.

In what follows, we are going to experimentally demonstrate the presence of SP states in a 8 RR SCISSOR. In some particular cases, some of these SP states show chaotic features.

7.6.1 Studied device: self-pulsation induced by localized states

The system under study is the same scissor studied in section 4.2.2. In this case, we are going to investigate the system with a large input power in order to give rise to non linear effects. The investigated spectral range is limited by our EDFA amplifier window between 1540 – 1570 nm .

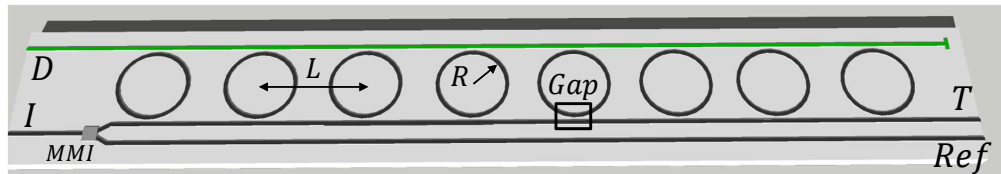


FIGURE 7.20: Sketch of the studied device. SCISSOR parameters are reported in table 7.5.

We report again the device parameters:

TABLE 7.5: Device parameters

CC	R	Spectral window	w	L	Polarization
15%	$6.75\mu m$	1540 – 1570 nm	$500nm$	$22\mu m$	TM

For a TM polarization the single RR has a CC of 15% instead of 5% as for the TE case. Simulations performed on an isolated RR, similar to the ones that composes the SCISSOR under study for TM polarization, do not show any SP effect for an input power up to 30 mW . Two are the reasons, a low EF and a broad the resonance lineshape. The Q factor and the EF for a single RR, with the parameters of table 7.5, are reported in the table 7.6 for two CC values. On the contrary, experiments show SP states in the SCISSOR transmission. We believe that this is due to the sequence of coupled cavities and to the fabrication errors which induce localized states. In fact, the cavity field of a localized state is far larger than that of an isolated cavity, as shown in figure 7.21.

TABLE 7.6: Q factor and EF for the single RR and two CC.

CC	Q factor	EF
15%	2000	6
5%	7000	19

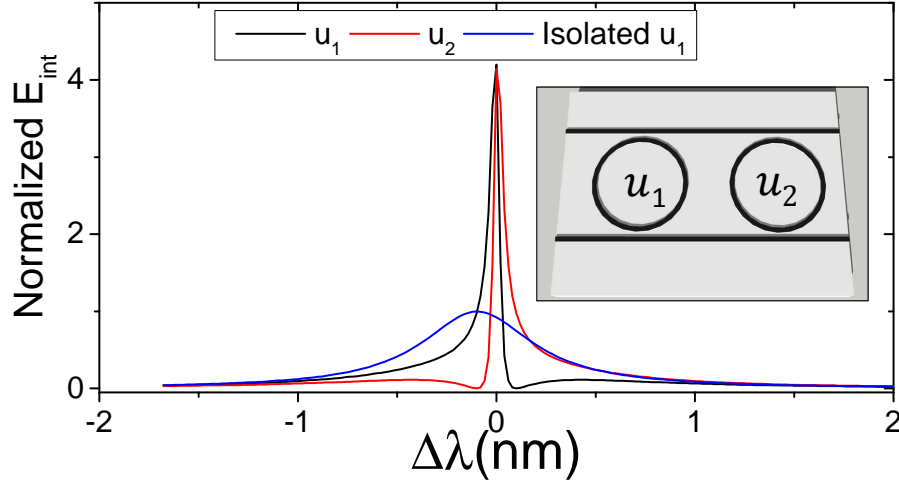


FIGURE 7.21: Normalized cavity field E_{int} as a function of $\Delta\lambda$: black and red lines refers to coupled cavities, blu line refers to an isolated cavity. The curves are normalized to the maximum of the isolated cavity field energy. The inset shows the considered system. Simulation parameters: $R = 6.75 \mu m$, $n_g = 3.4$, $\lambda_c = 1550 nm$, resonances detuning $0.7 nm$, losses $0.005 dB/cm$ and $CC = 15%$ (TM polarization).

Notice that, even in this case, the cavity fields show an asymmetric shape that can be related to Fano resonances [182].

7.6.2 Non linear regime: fixed power at different λ

The measures are performed using the setup described in the appendix B.0.8 with a little modification. During the wavelength scan at high CW power, it is necessary to reset the system initial conditions in order to avoid the spectral deformation, already seen in section 7.3.2: for each λ , we want to observe the system dynamic starting from the "zero" initial condition, which is close to that measured with the transmission spectrum. This was done by inserting an optical chopper in the EDFA line before entering in the sample. The chopper frequency is higher than that of the laser sweep rate and lower than the characteristic time of the expected SP oscillation (tens of nanosecond).

First, the low-power spectrum is measured in order to find the position of the RB and of the localized states. The result is reported in figure 7.22(a). As expected, we can clearly distinguish the BB and the RB. There are also some localized states, that are highlighted

by the colored rectangles in Fig. 7.22(a). The localized states are characterized by an high Q factor: the state in the 2-nd rectangle has a Q of about 38000.

Second, the time response of the SCISSOR is investigated. The CW pump power is fixed in the range 15 – 30 mW and the pump wavelength is scanned across the whole spectrum of figure 7.22(a). Here we consider as pump power the power in the WG which is the power measured at the WG input minus the insertion losses, which are estimated to be about 10 dB.

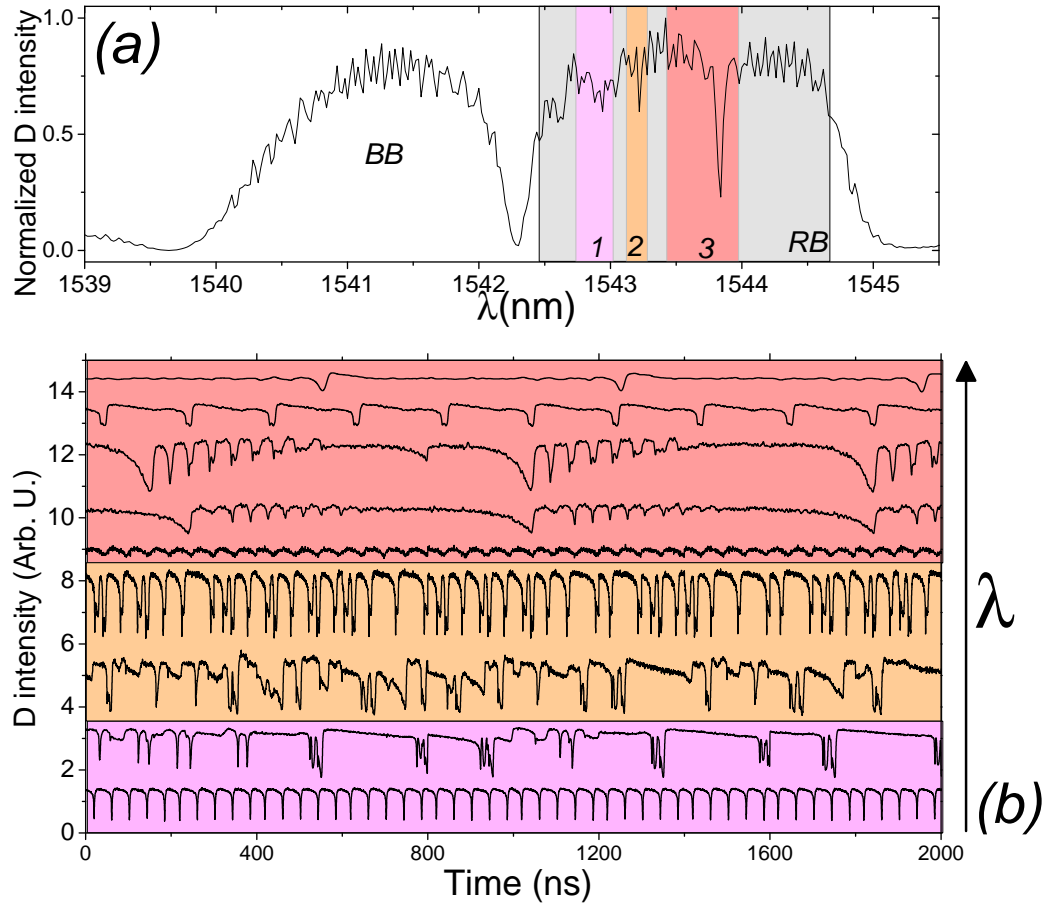


FIGURE 7.22: (a) SCISSOR D port transmission spectrum, linear regime. Rectangles 1,2,3: localized state regions. The grey rectangle indicates the RB. (b) Non linear regime: D port time response for several pumps wavelength.

The results are shown in figure 7.22(b). Obviously, a pump wavelength inside the BB do not generate any SP phenomenon: the pump power is distributed along all the resonators. Inside the RB the situation changes. The following observations can be made:

- The SP phenomena starts in proximity of the regions where the localized states appear.

- The outer regions, rectangles 1 and 3 of Fig. 7.22(b), show simple SP shapes that can be related to that of the single cavity shown in section 7.5. This is reasonable given that, the greater the distance from the RB center, the lower is the probability to find resonances. This is another evidence of the presence of the disorder that breaks the degeneracy between the resonances.
- On the contrary, in the middle region, rectangle 2, the SP shapes are very complicated. It is supposed that a great number of resonators are involved in the oscillations. This concept will be detailed in the next section.
- The SP periods are distributed from $40ns$ to $200ns$.

We are going to demonstrate the second observation. Figure 7.23 reports both the time behaviour of a RR (a) and of a SCISSOR (b) D port . The panel (c) shows the top-scattering of the SCISSOR, relative to the condition of the panel (b). The SCISSOR oscillations are related to the region 3 of figure 7.22 .The RR oscillations are measured from the same system of section 7.5. The top-scattering from the SCISSOR structure indicates that there is one pair of RR that are involved in the SP through a dynamic localized state.

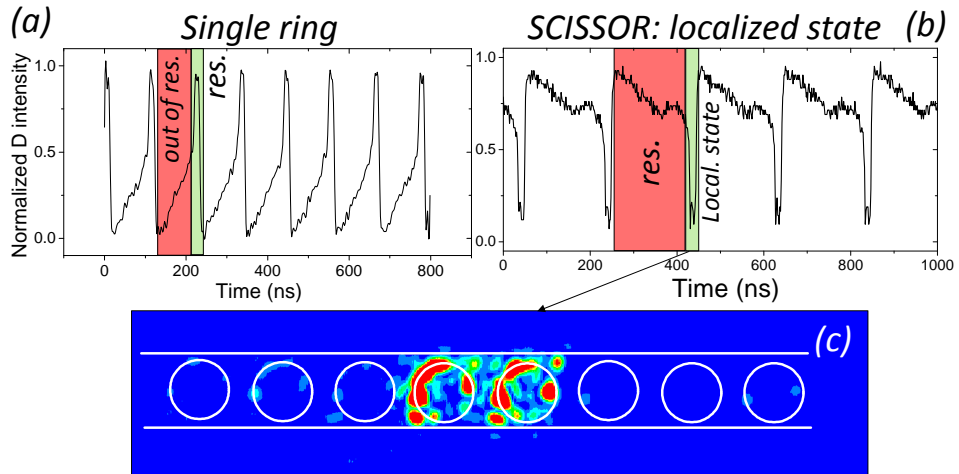


FIGURE 7.23: (a)ADF D port time response : pump power $P_{inc} \sim 6mW$ (for the other parameters refers to section 7.5). (b) SCISSOR D port time response: $\lambda_p = 1543.86 \pm 0.01nm$, $P_{inc} \sim 15mW$.(c)SCISSOR top scattering.

Also the SP shape is very regular (Fig. 7.23(b)) and recalls that of a single RR (Fig. 7.23(b)). The main differences are:

- RR SP regime: the RR oscillates between an out-of resonance condition to a resonance condition.

- the SCISSOR oscillates between a resonance condition to a localized state. In fact, the two waveforms are specular. A similar relation, between a RR and a localized state was found in the comparison between the CRITAD structure and the ADF structure for signal routing (see section 5.2.1).

7.6.3 Non linear regime: fixed λ at different powers

Here, we are going to focus on the region 2 of figure 7.22 where complex SP lineshapes were found. The pump wavelength is fixed at $\lambda_p = 1543.21 \pm 0.01nm$ and the power is varied from $14mW$ to $37mW$. The time response of the D port is reported in figure 7.24(a) while the top scattering in figure 7.24(b).

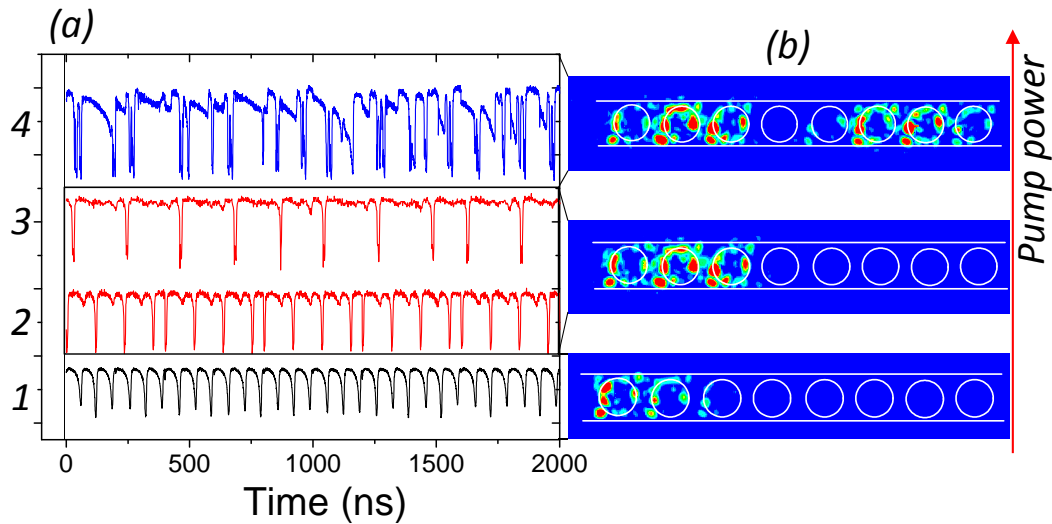


FIGURE 7.24: (a) SCISSOR D port intensity (Arb. U.) as a function of time for several pump powers: (1) $14mW$, (2) $20mW$, (3) $27mW$ and (4) $37mW$. (b) SCISSOR top scattering. $\lambda_p = 1543.21 \pm 0.01nm$.

The results can be summarized as:

- Fig. 7.24 case 1: For an input power of $14mW$ the system starts to oscillates. Only one pair of RR is involved and there is a well defined period of $T_{sp} = 42ns$ (black curve).
- Fig. 7.24 cases 2 and 3: For an input power of $20mW$ another cavity oscillates together with the previous pair and periodicity is lost. The system oscillates with more than one characteristic period (red curves).
- Fig. 7.24 case 4: For an input power of $37mW$ a total of 6 cavities oscillates. The system seems to show a chaotic behaviour (blue curve).

At a larger pump, the light is scattered from 6 cavities (Fig. 7.24(b)). This means that the pump induces defects in the SCISSOR giving rise to dynamic localized states.

Figure 7.25 shows the D port transmission when a power scan is performed. We simply chopped an input signal of peak power equals to 30 mW . As theoretically demonstrated in section 7.4.2, the oscillations start after a bistable transition at the threshold power of $\sim 14\text{ mW}$ (black line). As the power decreases after the peak power, the oscillations continue below the first threshold down to a new threshold of 7 mW . For even lower power, there is a second bistable jump (red line) and the cycle closes.

The measurement was carried out simply by exploiting the non-instantaneous rising edge of the chopper. The input power was about $\sim 30\text{ mW}$.

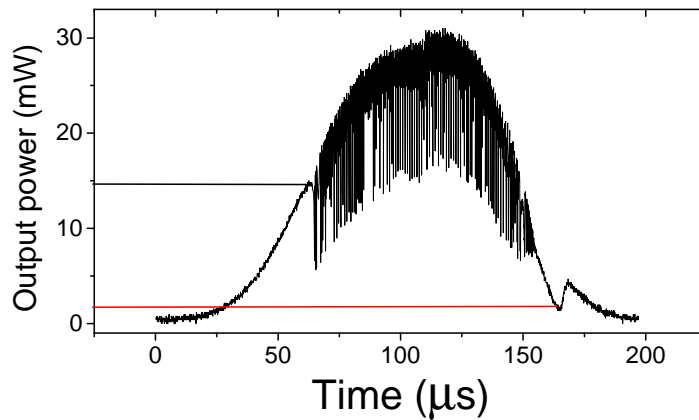


FIGURE 7.25: SCISSOR D port output power as a function of time.

7.6.4 Non linear regime: characteristics time distribution and auto-correlation

In order to understand the time response of the system, we calculate the characteristic time distribution of the temporal separation between two pulses ΔT_{sp} and the auto-correlation function of the time sequences 2 and 4 of figure 7.24. The ΔT_{sp} is calculated by performing an automatic squaring of the signal as shown in figure 7.26.

A pulse is then created, each time a negative edge crosses the threshold value Th_{sq} (blue line) which is set to a values equal to $0.6 - 0.8$ times the signal mean. A Smith trigger, with an hysteresis time of 2 ns , was used to avoid the trigger of the noise. Then ΔT_{sp} is defined as the temporal separation between two negative edges of consecutive pulses (Fig. 7.26 black arrow).

Figure 7.27 shows the histogram of the ΔT_{sp} distribution and the auto-correlation function of the signal of the sequences 2 and 4 of figure 7.24.

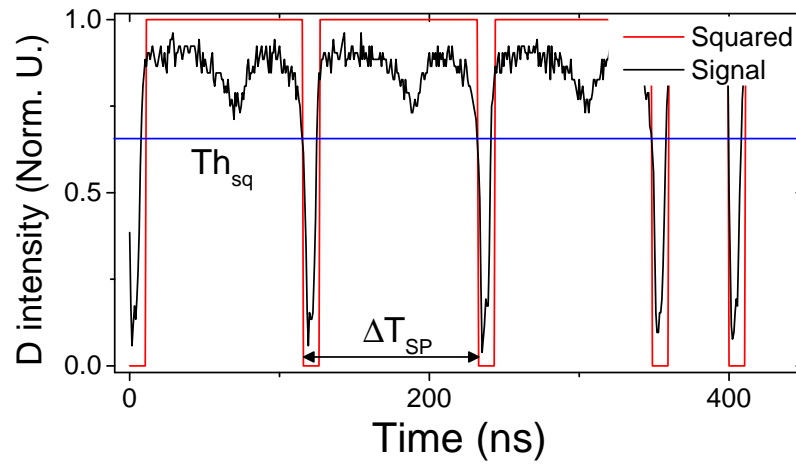


FIGURE 7.26: (Black line) Normalized (from 0 to 1) D port intensity as a function of time. (Red line) Squared signal.

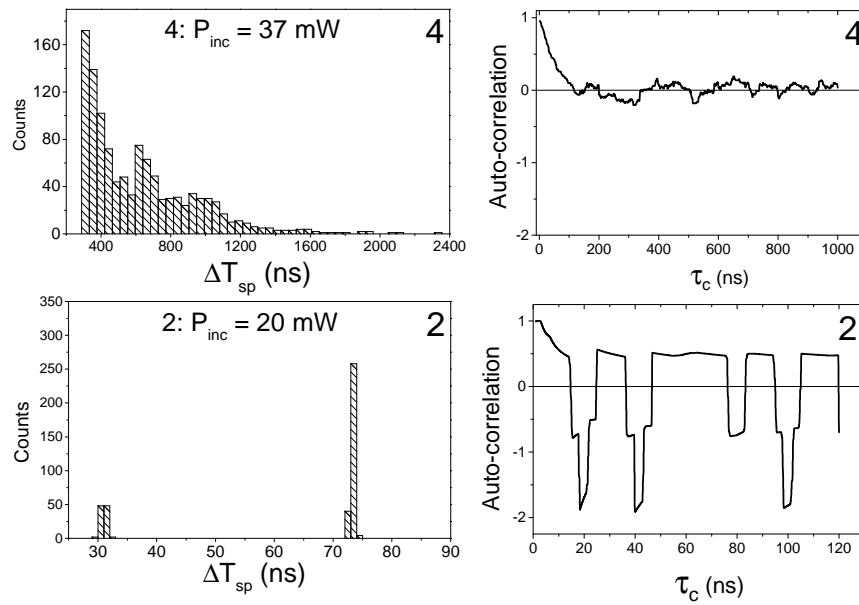


FIGURE 7.27: (Top panel) Histogram of ΔT_{sp} and auto-correlation function for two different input powers: (4) 37 mW and (2) 20 mW . $\lambda_p = 1543.21 \pm 0.01\text{ nm}$.

We can notice that:

- Case 2, $P_{inc} = 20\text{ mW}$: the histogram of ΔT_{sp} shows that there are two characteristic frequencies at about 31 ns and 73 ns . The system never loses correlation.
- Case 4, $P_{inc} = 37\text{ mW}$: the histogram of ΔT_{sp} shows that there is a broad distribution of frequencies that spans from about 100 ns to beyond 600 ns . The system loses correlation after about 80 ns .

It is noted that, the time scale of the system is set by the cavity thermal relaxation, that is of about 80 ns . The broad characteristic time interval distribution and the fast decay of the correlation function are good indicators that the system might show chaos.

7.6.5 A possible approach to prove the presence of chaos

To prove the presence of chaos one has to calculate the Lyapunov coefficients of the system [212]. The system can be described by a set of coupled non linear equations similar to those used for the single RR in section 7.5.2. Note that, a system of 8 cavities means 24 coupled non-linear equations and 32 degrees of freedom. The presence of fabrication errors makes difficult to determine the exact geometrical parameters of the cavities, so it is almost impossible fit theory and experiment in the time domain. Thus, we simulate an 8 ring SCISSOR structure by these equations to see whether chaotic states are admitted as solutions.

The SCISSOR radii were random values similar to the nominal values while the other parameters were the nominal ones. We changed the radii distribution to get a time sequence, for the D port transmission, similar to the experimental one.

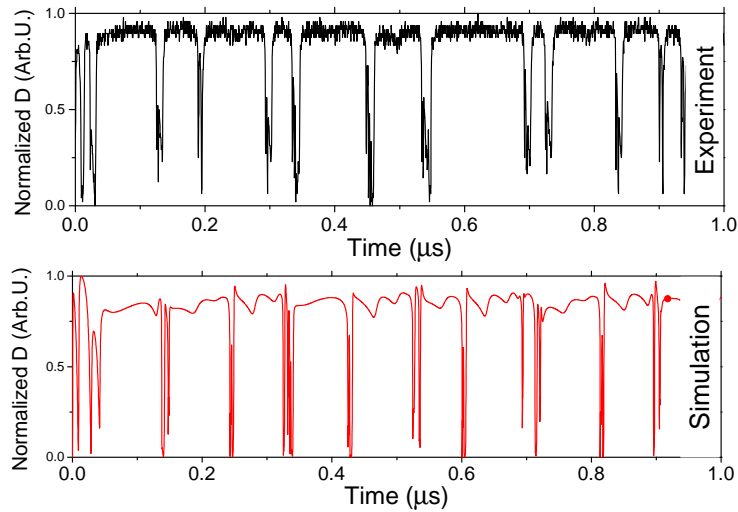


FIGURE 7.28: Comparison between simulation (red line) and experiment (black line) at 34 mW of input power and 1544.38 nm of input wavelength.

Then, the system Lyapunov exponents (LLEs) are calculated. Only the three largest exponents are given. In the first case, LLEs converges at $(0 - 10.0 - 11.1)\mu\text{s}$, while in the second case at $(15.7 - 4.16 - 0)\mu\text{s}$. It is enough that, one of the LLEs is larger than 0 to have a chaotic system while a SP state require an exponent equal to zero. In figure 7.29(a) we see that, for an input power of 15 mW , the system exhibit SP but there is no sign of chaos while, for 45 mW one of the LLEs remains greater than zero. From this configuration we can expect chaotic features, as reported in the inset of figure

7.29(b). Also the phase space is largely filled by the system trajectory. The axis of the phase-space graphs report the values of the cavity temperature, the cavity energy and the free carriers density of the third cavity.

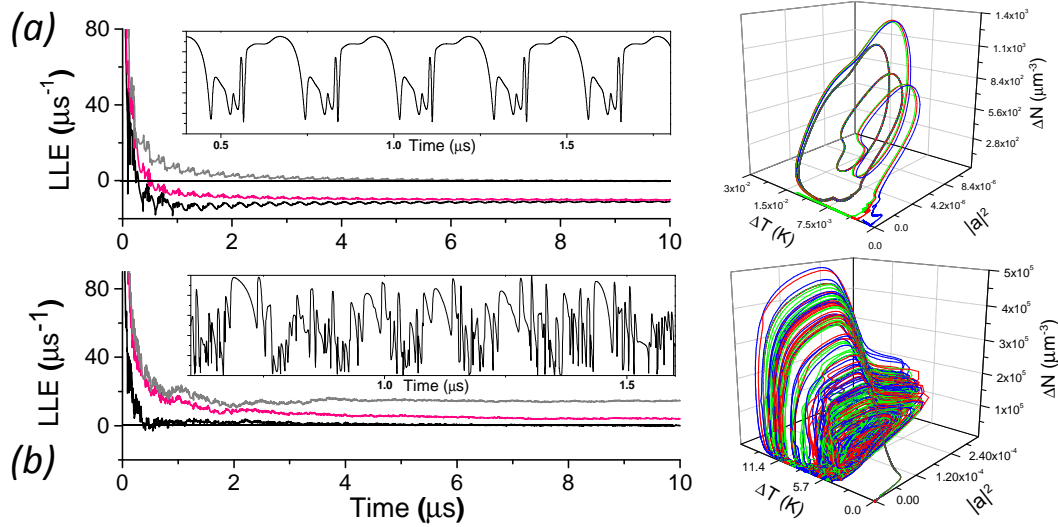


FIGURE 7.29: System stability analysis at two input power. (a) Convergence of the three largest Lyapunov exponents as a function of time at 15 mW (top) and 45 mW (bottom) of input power. Insets show the output waveforms. (b) Phase space trajectories of the third cavity in the SCISSOR at 15 mW (top) and 45 mW (bottom). Curves at different colors (blue, green, red) refer to slightly different initial conditions.

The code, starting from that for a single cavity, has been extended to more than one cavity in a similar way to what done in appendix C. We have found that, for an input power similar to the experimental one, the system allows chaotic states that are revealed by the analysis of the Lyapunov exponents. So, we can say that the experimental sequences, assumed as chaotic, are actually chaotic.

Another interesting observation concerns the deterministic nature of the sequences. It is observed that, a reset of the initial conditions does not bring the system on the same temporal evolution. This is probably due to the environmental fluctuations and to the overall stability of the instruments such as, the pump laser wavelength, and the EDFA amplification level. These small perturbations, in a system with a so narrow spectral characteristics, are enough to significantly change every time the initial conditions of the system. This is a very important feature in view of cryptographic applications.

7.7 Conclusions

In the first part of this section, the presence of optical bistability and SP phenomena in a single RR system under a CW input is verified. These features are triggered by the silicon non linear effects, enhanced by the cavity. The validity of the model developed

to describe such system (the model is in depth described in Appendix A) is verified and some of the unknown parameters are extracted from the experiment. The second part was focused on the investigations of the presence of non-linear phenomena in a SCISSOR system. The presence of localized states, demonstrated in chapter 4, radically changes the system time dynamics. In fact, localized states allow to get a large field enhancement which in turn sustain SP phenomena. Furthermore, the presence of a strong coupling between the cavities allows the system to enter into disordered dynamic states. Supported by the simulations, we claim that these states are chaotic states.

The chaotic dynamic suggests that the system could be used to generate random bit-streams. The maximum bitrate is limited by the correlation time to about 12 MBit/s . For an input power of $\sim 30\text{ mW}$, this is about 80 ns . However, the device performances can be improved by modifying the device geometry adopting a different pumping scheme. A shrinking of the ring size leads to a faster response, because of the reduction of the RR thermal capacity. A further increase of the bitrate can be achieved by combining, within the same chip, the chaotic output of several SCISSORs, to obtain a new random signal which posses also a lower de-correlation time. A reduction of the ring size should also decrease the pump power needed to activate the chaotic regime, because the internal energy density becomes higher. To further reduce the input intensity, an alternative design could be used. This consists in increasing the input pump until the chaotic dynamic begins, and then decrease the pump level by exploiting the fact that the threshold power required to exit from the oscillating regime is now lower (Fig. 7.25). However, these enhancements are not enough to reach the bitrate levels of up to 140 Gbps which are achieved in active gain materials with feedback [213]. Nevertheless, the small footprint, the lack of bulky external complex instruments required to generate high CW inputs and the low cost of the fabrication process make this device of considerable interest for future applications in on-chip cryptography. Performing an engineering of the parameters of the system, the device could also find application in an all-optical waveforms generator, by noting all the different shapes that can be generated (Fig. 7.22).

Conclusions

My PhD work was focused on the study of integrated optical components for the creation of devices to be used in optical networks-on-chip. In particular, I have developed and tested novel components for routing signals. Thanks to the possibilities offered by the european project WADIMOS to process different SOI wafers with the deep UV lithography (193 nm), we achieved this purpose. In fact, we developed several novel optical devices that provide solid performance and robustness to the lithography errors, a real plague for integrated photonics in silicon. The developed designs have renewed the attention the coupled resonator configurations, in particular in SCISSOR device [196, 214, 215, 216, 217], and in the study of the effects of fabrication errors on final device [215, 218, 219, 220].

In fact, the whole thesis was practically focused on phenomena that were caused by process errors in SCISSOR structures: the *localized states* and the *coupled-resonators-induced-transparency* resonances. For the first time, we studied in depth these phenomena in a SCISSOR device [33]. I had to deal with both the theoretical and the experimental investigation of this problems. Several physical models, to simulate both the stationary and the time-dependent response of coupled resonators, were developed. Also several experimental setups were created to test the accuracy of the theoretical models and the performances of the realized devices [221]. On the basis of these knowledge, the CRITAD structure has been developed and demonstrated. It is a device based on the CRIT effect, robust to defects, for UWDM and routing applications with hitless features [34, 36, 222]. Also an in-line, non-invasive test structure able to quantify the errors by lithography processes was theoretically demonstrated. Reconfigurable devices based on the interference of signals, suitable for bands routing (coarse WDM), have been developed [208, 223]. They are able to exploit both the phase and the wavelength of the signals as routing protocols.

I also investigated the presence of nonlinear effects in these structures mainly related to the two-photons-absorption effect of silicon. After the verification of the presence of self-pulsations in a single resonator device, I focused the attention on the SCISSOR

structure. I discovered, for the first time to my knowledge, that the localized states induced by defects, together with the material non-linearity, are able to establish chaotic dynamics. The demonstration that from these chaotic oscillations is possible to extract bit sequences with low correlation, paves the way to a new approach for the management of all-optical on-chip cryptography.

This thesis work shows that the use of coupled resonators structures leads to several advantages:

- Easy management of DWDM channels.
- Efficient channel switching with hitless features.
- Robustness to fabrication errors: less waste of energy for the post-trim process.
- Network topology flexibility: different ways to perform switching and different routing protocols, phase and wavelength.

This leads to the following perspectives:

- New way to approach the signal routing.
- Together with the upcoming new lithographic technologies, the possibility to have a trim-less device.
- Small and efficient all-optical-chip chaos generator or complex waveforms generator.

List of publications

Mancinelli M., R. Guider, P. Bettotti, M. Masi, M. Rao Vanacharla, and L. Pavesi. " *Coupled-resonator-induced-transparency concept for wavelength routing applications.*" Optics Express 19, no. 13 (2011): 12227-12240.

Mancinelli Mattia, Romain Guider, Marco Masi, Paolo Bettotti, Manga Rao Vanacharla, Jean-Marc Fedeli, and Lorenzo Pavesi. " *Optical characterization of a SCISSOR device.*" Optics Express 19, no. 14 (2011): 13664-13674.

Mancinelli M., P. Bettotti, J. M. Fedeli, and L. Pavesi. " *Reconfigurable optical routers based on Coupled Resonator Induced Transparency resonances.*" Optics express 20, no. 21 (2012): 23856-23864.

Mancinelli Mattia, Romain Guider, Paolo Bettotti, Marco Masi, Manga Rao Vanacharla, Jean-Marc Fedeli, Dries Van Thourhout, and Lorenzo Pavesi. " *Optical characterization of silicon-on-insulatorbased single and coupled racetrack resonators.*" Journal of Nanophotonics 5, no. 1 (2011): 051705-051705.

Mancinelli Mattia, Paolo Bettotti, Jean Marc Fedeli, and Lorenzo Pavesi. " *Interferometric switching in coupled resonator optical waveguides-based reconfigurable optical device.*" Optics Letters 38, no. 2 (2013): 217-219.

Masi Marco, Mattia Mancinelli, Paolo Bettotti, and Lorenzo Pavesi. " *Light Combining for Interferometric Switching.*" International Journal of Optics 2012 (2012).

Bettotti P., M. Mancinelli, R. Guider, M. Masi, M. Rao Vanacharla, and L. Pavesi. " *Robust design of an optical router based on a tapered side-coupled integrated spaced sequence of optical resonators.*" Optics letters 36, no. 8 (2011): 1473-1475.

Masi Marco, Mattia Mancinelli, Alberto Battarelli, Romain Guider, Manga Rao Vanacharla, Paolo Bettotti, J. Fedeli, and Lorenzo Pavesi. " *A silicon photonic interferometric router device based on SCISSOR concept.*" Lightwave Technology, Journal of 29, no. 18 (2011): 2747-2753.

Appendix A

Time domain analysis of the cavity dynamics

The goal of this section is to derive an expression for the time evolution of the energy stored inside a ring cavity in the presence of optical nonlinearities induced by TOE and FCD, in order to investigate the dynamics of the self induced oscillations discussed in section 7.5.1. We start from a general approach based on ordinary perturbation theory applied to Maxwell equations that allows to obtain an explicit expression for the changes in the complex resonance frequency of a resonating system when a small perturbation of the refractive index is applied. Results will be inserted in the equation that describes the time evolution of the energy to obtain, together with the ones that govern the temperature and the free carrier dynamics, a set of three coupled non linear differential equations that will be numerically integrated.

Note: The model was developed together with Mr. Massimo Borghi.

A.1 Resonance frequency shift induced by small refractive index perturbations

We start from Maxwell equations in absence of charges and conduction currents:

$$\nabla \cdot \mathbf{D} = 0; \quad \nabla \cdot \mathbf{B} = 0; \quad (\text{A.1})$$

$$\nabla \times \mathbf{E} = -\frac{\partial \mathbf{B}}{\partial t}; \quad \nabla \times \mathbf{H} = \frac{\partial \mathbf{D}}{\partial t}; \quad (\text{A.2})$$

and the linear material relations:

$$\mathbf{D} = \epsilon_0 \epsilon_r \mathbf{E} \quad (\text{A.3})$$

$$\mathbf{B} = \mu\mathbf{H} \quad (\text{A.4})$$

By applying the curl operator on both sides of eq.A.2 and assuming a time dependence of the electric field $e^{j\omega t}$ we obtain:

$$\nabla \times \nabla \times \mathbf{E}(\mathbf{r}) = \left(\frac{\omega}{c}\right)^2 \epsilon_r(\omega, \mathbf{r})\mathbf{E} \quad (\text{A.5})$$

which has the form of a generalized eigenvalue problem. Eq.A.5 can be solved for the silicon microring obtaining a set of bounded modes $|\mathbf{E}_i^0\rangle = \mathbf{E}_i^0(\mathbf{r}_T)e^{j(\omega_i^0 t - \beta_i^0 z)}$ (we adopt the Dirac formalism to represent eigenvectors and scalar products, i.e $\langle \mathbf{E}_i^0 | \mathbf{E}_j^0 \rangle = \int (\mathbf{E}_i^0)^* \cdot (\mathbf{E}_j^0) d\mathbf{r}$, and choose \mathbf{r}_T as the transverse direction with respect to z , taken along the ring circumference) corresponding to discrete eigenvalues ω_i^0 and a continuum of radiation modes. If ϵ_r is real, eq.A.5 is a complete hermitian generalized eigenvalue problem, the eigenvectors form then a complete set and satisfy the orthogonality relation $\langle \mathbf{E}_i^0 | \epsilon_r(\mathbf{r}) | \mathbf{E}_j^0 \rangle = \delta_{ij}$. When a small perturbation $\Delta\epsilon_r(\mathbf{r})$ is applied to the dielectric constant, the new resonance frequencies and modal fields profiles can be found by applying the same time independent perturbation theory developed for quantum mechanical systems [?], with $(\frac{\omega}{c})^2$ playing the role of energy and \mathbf{E} of the wavefunction, obtaining for the change in the resonance frequency $\Delta\omega_i^0$:

$$\Delta\omega_i^0 = -\omega_i^0 \frac{\langle \mathbf{E}_i^0 | \Delta\epsilon_r(\mathbf{r}) | \mathbf{E}_i^0 \rangle}{\langle \mathbf{E}_i^0 | \epsilon_r(\mathbf{r}) | \mathbf{E}_i^0 \rangle} \quad (\text{A.6})$$

A.1.0.1 Resonance frequency shift induced by thermo optic effect

Thermo optic induced perturbation of the refractive index can be expressed as:

$$\Delta n_{TOE}(\mathbf{r}) = \frac{dn}{dT} \Delta T(\mathbf{r}) \quad (\text{A.7})$$

where $\frac{dn}{dT}$ is the thermo optic coefficient at room temperature and ΔT the differential temperature. Knowing that the refractive index change Δn can be related to the dielectric constant variation through the relation $\Delta\epsilon = 2n_0\Delta n$ (with n_0 the unperturbed index), we can insert eq.A.7 in eq.A.6 to obtain for the resonance shift:

$$\Delta\omega_{TOE}^0 = -\omega_0 \frac{dn}{dT} \frac{\int |\mathbf{E}^0(\mathbf{r})|^2 n(\mathbf{r}) \Delta T(\mathbf{r}) d\mathbf{r}}{\int |\mathbf{E}^0(\mathbf{r})|^2 n_0^2(\mathbf{r}) d\mathbf{r}} \quad (\text{A.8})$$

When the raise in temperature is achieved by material absorption of the field, as in the case of all optical TOE, the differential temperature ΔT is appreciable only in the

microring volume V , so eq.A.8 can be rewritten as:

$$\Delta\omega_{TOE}^0 = -\frac{\omega_0}{n_{Si}} \frac{dn}{dT} \overline{\Delta T} \quad (\text{A.9})$$

where:

$$\overline{\Delta T} = \frac{\int_V |\mathbf{E}^0(\mathbf{r})|^2 n_0^2(\mathbf{r}) \Delta T(\mathbf{r}) d\mathbf{r}}{\int |\mathbf{E}^0(\mathbf{r})|^2 n_0^2(\mathbf{r}) d\mathbf{r}} \quad (\text{A.10})$$

A.1.0.2 Resonance frequency shift induced by free carrier dispersion

The presence of a free carrier population ΔN alters both the real and the imaginary part of the refractive index through the already encountered relations (section 7.2.1):

$$\Delta n_{FC}^R = \frac{dn_{Si}}{dN} \Delta N \quad (\text{A.11})$$

$$\Delta n_{FC}^I = \frac{d\alpha^{FC}}{dN} \frac{c\Delta N}{2\omega_0} \quad (\text{A.12})$$

By inserting eq.A.11 and eq.A.12 into eq.A.6, and considering again the differential population ΔN appreciable only in the microring volume (good approximation when ΔN is achieved by TPA and the free carrier diffusion lengths are small, as in the case of a microring), we obtain for the FCD complex frequency shift:

$$\Delta\omega_{FC}^0 = -\frac{\omega_0}{n_{Si}} \frac{dn_{Si}}{dN} \overline{\Delta N} + j \frac{d\alpha^{FC}}{dN} \frac{c}{2n_{Si}} \overline{\Delta N} \quad (\text{A.13})$$

where:

$$\overline{\Delta N} = \frac{\int_V |\mathbf{E}^0(\mathbf{r})|^2 n_0^2(\mathbf{r}) \Delta N(\mathbf{r}) d\mathbf{r}}{\int |\mathbf{E}^0(\mathbf{r})|^2 n_0^2(\mathbf{r}) d\mathbf{r}} \quad (\text{A.14})$$

A.1.0.3 Resonance frequency shift induced by Kerr effect

The perturbation of the refractive index induced by the Kerr effect can be directly derived by the equations:

$$\Delta n_{Kerr}(|\mathbf{E}(\mathbf{r}, t)|^2) \approx \frac{3\chi_{\hat{n}}^{(3)}}{8n_o} |\mathbf{E}(\mathbf{r}, t)|^2$$

$$\frac{\omega}{c} n_2 + j \frac{\beta_{TPA}}{2} = \frac{3\omega}{4\epsilon_0 n_0^2 c^2} \chi_{1111}^{(3)}$$

By combining these two equations we find, for the real and the imaginary part of the perturbed index:

$$\Delta n_{Kerr}^R = \frac{1}{2} c \epsilon_0 n_0 n_2 |\mathbf{E}(\mathbf{r}, t)|^2 \quad (\text{A.15})$$

$$\Delta n_{Kerr}^I = \frac{c^2 \beta_{TPA} \epsilon_0 n_0 |\mathbf{E}(\mathbf{r}, t)|^2}{4\omega_0} \quad (\text{A.16})$$

Inserting eq.A.15-A.16 in eq.A.6 and multiplying and dividing by $p \int n(\mathbf{r}_T) |\mathbf{E}^0(\mathbf{r}_T)|^2 d\mathbf{r}_T$ (p is the microring length) yields:

$$\Delta \omega_{Kerr}^0 = \left(\frac{1}{2} c \omega_0 \epsilon_0 n_0 n_2 + j \frac{c^2 \beta_{TPA} \epsilon_0 n_0}{4} \right) \cdot \left(\frac{(\int_V n_0(\mathbf{r}) |\mathbf{E}(\mathbf{r}, t)|^2 |\mathbf{E}^0(\mathbf{r})|^2 d\mathbf{r}) (\int |\mathbf{E}^0(\mathbf{r}_T)|^2 n_0^2(\mathbf{r}_T) d\mathbf{r}_T)}{p (\int |\mathbf{E}^0(\mathbf{r}_T)|^2 n_0^2(\mathbf{r}_T) d\mathbf{r}_T)^2} \right) \quad (\text{A.17})$$

In a low loss ring resonator where the linear losses per round trip $e^{-\alpha p} \approx 1$, the actual field $\mathbf{E}(\mathbf{r}, t)$ can be expressed with good approximation as $\mathbf{E}(\mathbf{r}, t) = A(\omega) \mathbf{E}^0(\mathbf{r}_T, t) e^{i(\omega t - \beta z)}$, where $A(\omega)$ is a constant amplitude and β is the real propagation constant. Eq.A.17 can then be casted in the form:

$$\Delta \omega_{Kerr}^0 = -\omega_0 \frac{cn_2 U_{int}}{n_{Si}^2 V_{eff}} + j \frac{\beta_{TPA} c^2}{2n_{Si}^2 V_{eff}} U_{int} \quad (\text{A.18})$$

where V_{eff} is the mode effective volume and U_{int} is the cavity internal energy, defined respectively as:

$$V_{eff} = p \frac{(\int |\mathbf{E}^0(\mathbf{r}_T)|^2 n_0^2(\mathbf{r}_T) d\mathbf{r}_T)^2}{\int_V |\mathbf{E}^0(\mathbf{r}_T)|^4 n_0^4(\mathbf{r}_T) d\mathbf{r}_T} \quad (\text{A.19})$$

$$U_{int} = \frac{1}{2} \epsilon_0 p \int |A|^2 |\mathbf{E}^0(\mathbf{r}_T)|^2 n_0^2(\mathbf{r}_T) d\mathbf{r}_T \quad (\text{A.20})$$

A.1.1 Cavity energy dynamics

The transfer matrix formalism developed in section 2.9.1 allows us to derive an explicit expression for the complex field amplitude E_{int} inside the ring, with reference to fig.A.1 we obtain:

$$E_{int}(\omega) = \frac{j\kappa_a E_{inc}(\omega)}{1 - e^{-\alpha p} e^{-j\beta(\omega)p} \sqrt{1 - \kappa_a^2} \sqrt{1 - \kappa_b^2}} \quad (\text{A.21})$$

with κ_a , κ_b the coupling coefficients for regions a and b , E_{inc} the incident field amplitude, p the resonator length, $\beta(\omega)$ the propagation constant and α the linear absorption coefficient. When $(\omega - \omega_0) \ll \omega_0$, we can expand $\beta(\omega)$ around a resonance frequency ω_0 as $\beta(\omega) \approx \beta(\omega_0) + (\omega - \omega_0) \frac{v_g}{p}$, where v_g is the group velocity, defined as $v_g = \frac{c}{n_g}$ (n_g is the group index); inserting this expression into eq.A.21 leads to:

$$E_{int}(\omega) \left[\frac{1 - e^{-\alpha p} \sqrt{1 - \kappa_a^2} \sqrt{1 - \kappa_b^2} \frac{v_g}{p}}{e^{-\alpha p} \sqrt{1 - \kappa_a^2} \sqrt{1 - \kappa_b^2} \frac{v_g}{p}} + j(\omega - \omega_0) \right] = \frac{j\kappa_a}{e^{-\alpha p} \sqrt{1 - \kappa_a^2} \sqrt{1 - \kappa_b^2} \frac{v_g}{p}} E_{inc}(\omega) \quad (\text{A.22})$$

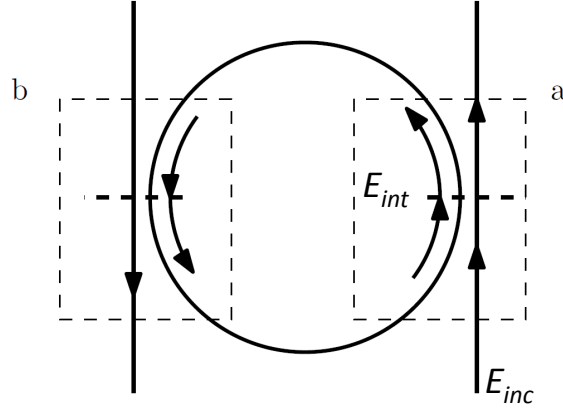


FIGURE A.1: Schematic of the ADP configuration with represented the driving field complex amplitude E_{inc} , the field inside the resonator E_{int} and the two coupling regions a and b .

For low losses and weak coupling (i.e $\alpha p \ll 1$, $\kappa_{a,b} \ll 1$) we can write $e^{-\alpha p} \approx 1 - \alpha p$ and $\sqrt{1 - \kappa_{a,b}^2} \approx 1 - \frac{\kappa_{a,b}^2}{2}$, inserting these approximations in eq.A.22 and keeping only the leading terms we get:

$$E_{int}(\omega) \left[\left(\frac{\kappa_a^2}{2} + \frac{\kappa_b^2}{2} + \alpha p \right) \frac{v_g}{p} + j(\omega - \omega_0) \right] = \frac{j\kappa_a v_g}{p} E_{inc}(\omega) \quad (\text{A.23})$$

We can now normalize the complex field amplitudes E_{int} and E_{inc} in such a way that their squared modulus represent respectively the power circulating inside the ring and the incident power; this can be accomplished by multiplying both sides of eq.A.23 by a common normalization factor σ , that we don't need to know for our purposes (this is true only if the input waveguide and the ring waveguide have approximately the same geometry, which is often the case of SOI integrated resonators), we call the new amplitudes $E'_{int} = \sigma E_{int}$ and $E'_{inc} = \sigma E_{inc}$. By Fourier anti-transforming eq.A.23 we came back to the time domain:

$$\frac{dE'_{int}(t)}{dt} = \left[j\omega_0 - \left(\frac{1}{\tau_a} + \frac{1}{\tau_b} + \frac{1}{\tau_o} \right) \right] E'_{int}(t) + j \frac{\kappa_a v_g}{p} E'_{inc}(t) \quad (\text{A.24})$$

where we set $\frac{\kappa_{a,b}^2 v_g}{2p} = \frac{1}{\tau_{a,b}}$ and $\alpha v_g = \frac{1}{\tau_o}$.

The energy density per unit length $\rho_E(z)$ is related in low loss waveguides to the power by the well know relation [224]:

$$\rho_E(z) = \frac{P_{int}}{v_g} = \frac{|E'_{int}|^2}{v_g} \quad (\text{A.25})$$

that is a direct consequence of energy conservation. By integrating eq.A.25 along the ring perimeter we obtain for the total cavity energy:

$$U_{int} = \int_{Ring} \frac{|E'_{int}|^2}{v_g} dz = \frac{p}{v_g} |E'_{int}|^2 \quad (\text{A.26})$$

By multiplying both sides of eq.A.24 by $\sqrt{\frac{p}{v_g}}$ and setting $U'_{int} = \sqrt{\frac{p}{v_g}} E'_{int}$ gives:

$$\frac{dU'_{int}(t)}{dt} = \left[j\omega_0 - \left(\frac{1}{\tau_a} + \frac{1}{\tau_b} + \frac{1}{\tau_o} \right) \right] U'_{int}(t) + j\sqrt{\frac{2}{\tau_a}} E'_{inc}(t) \quad (\text{A.27})$$

By definition, $|U'_{int}|^2 = U_{int}$, so eq.A.27 governs the time evolution of the energy amplitude in the microring. The time domain analysis highlights the analogy existing between optical and mechanical oscillators: when no driving force is applied, the cavity behaves like a mass-spring system with natural frequency ω_0 and damping rate $\gamma_{TOT} = \left(\frac{1}{\tau_a} + \frac{1}{\tau_b} + \frac{1}{\tau_o} \right)$, which express losses into the two loading waveguides and due to linear absorption, when a driving force $E'_{inc}(t)$ is present the cavity oscillates at the same frequency ω_p of the force, exhibiting a resonance when $\omega_p = \omega_0$.

Eq.A.27 has been derived for a linear cavity, we can now include the resonance shifts induced by TOE and FCD non linearities by making the substitution: $\omega_0 \rightarrow \omega_0 + \Delta\omega_{TOE}^0 + \Delta\omega_{FC}^0 + \Delta\omega_{Kerr}^0 = \omega_0 + \Delta\omega_{NL}(|U'_{int}(t)|^2, \Delta T(t), \Delta N(t))$:

$$\frac{dU'_{int}(t)}{dt} = \left[j(\omega_0 + \Delta\omega_{NL}^R(t)) - \left(\frac{1}{\tau_a} + \frac{1}{\tau_b} + \frac{1}{\tau_o} + \Delta\omega_{NL}^I(t) \right) \right] U'_{int}(t) + j\sqrt{\frac{2}{\tau_a}} E'_{inc}(t) \quad (\text{A.28})$$

Eq.A.28 alone can not be directly integrated since ΔT and ΔN appears in the nonlinear frequency shift $\Delta\omega_{NL}$, we must provide other two equations governing temperature and free carrier dynamics in order to have a full description of the energy evolution in the non linear cavity.

A.1.2 Temperature dynamics

Power absorbed inside the cavity changes it's temperature according to the Fourier law:

$$\frac{d\Delta T(t)}{dt} = -\gamma_{TH}\Delta T(t) + \frac{P_{abs}}{M_{ring}C_p} \quad (\text{A.29})$$

where γ_{TH} is a phenomenological loss rate that includes the heat loss by conduction in the surrounding medium, M_{ring} is the microring mass, C_p the silicon specific heat at constant pressure and P_{abs} the total absorbed power. We neglect the spatial dependence of ΔT due to the higher silicon conductivity with respect to the external oxide, that ensures a quite flat temperature distribution inside the ring. Absorbed power comes

from three distinct contributions: linear, two photon and free carrier absorption, all these mechanism releases energy to the lattice by carrier thermalization at rates that are so high compared to the temperature dynamics that can be considered as instantaneous. We can derive an explicit expression for the absorbed power by evaluating the energy decay rate of the cavity from eq.A.28:

$$\begin{aligned}
 P_{abs} &= 2 \left(\frac{1}{\tau_o} + \Delta\omega_{FC}^I + \Delta\omega_{Kerr}^I \right) |U'_{int}|^2 = \\
 &= \left(\frac{d\alpha^{FC}}{dN} \frac{c\overline{\Delta N}}{n_{Si}} \right) |U'_{int}|^2 + \left(\frac{c^2\beta_{TPA}}{n_{Si}^2 V_{eff}} \right) |U'_{int}|^4 + \frac{2}{\tau_o} |U'_{int}|^2
 \end{aligned} \tag{A.30}$$

A.1.3 Free carrier dynamics

The standard equation describing free carrier dynamics in the ring is the continuity equation that can be found in various textbooks:

$$\frac{d\Delta N}{dt} = -\gamma_{FC}\Delta N + G \tag{A.31}$$

where γ_{FC} is a phenomenological loss rate that includes carrier recombination and diffusion outside the ring and G the total generation rate per unit volume. At Telecom wavelengths the main mechanism that generates free carriers is two photon absorption, so G acquires the following expression:

$$G = \frac{P_{abs}^{TPA}}{2\hbar\omega_p V} = \frac{c^2\beta_{TPA}|U'_{int}|^4}{2\hbar\omega_p V V_{eff} n_{Si}^2} \tag{A.32}$$

where P_{abs}^{TPA} is the TPA absorbed power, V the ring volume and ω_p the frequency of the radiation. Eq.A.32 comes from the fact that it's required an energy of $2\hbar\omega_p$ to generate an electron hole pair.

In eq.A.31 the spatial dependence of the free carrier concentration has been neglected, this is a good approximation when the absorbed power does not fluctuate appreciably over the ring and the carrier diffusion lengths are comparable with the waveguide width.

A.1.4 Final set of coupled equations

When the spatial dependence of temperature and free carriers is neglected (the conditions of this approximation have been discussed above), when can write the quantities $\overline{\Delta T}$ and $\overline{\Delta N}$ that appears in eq.A.10 and eq.A.14 as $\overline{\Delta T} = \Gamma\Delta T$ and $\overline{\Delta N} = \Gamma\Delta N$, where Γ

is the modal confinement factor, defined as:

$$\Gamma = \frac{\int_V |\mathbf{E}^0(\mathbf{r})|^2 n_0^2(\mathbf{r}) d\mathbf{r}}{\int |\mathbf{E}^0(\mathbf{r})|^2 n_0^2(\mathbf{r}) d\mathbf{r}} \quad (\text{A.33})$$

The last step before proceeding into the integration of eqs.A.28, A.29 and A.31 is to give an expression for the driving field $E'_{int}(t)$, which in this work has the form of a monochromatic radiation at frequency ω_p : $E'_{int}(t) = \tilde{E}'_{int} e^{i\omega_p t}$. With the ansatz solution for the energy amplitude $U'_{int}(t) = \tilde{U}'_{int}(t) e^{i\omega_p t}$ the final set of three coupled non linear differential equations that fully describes the cavity dynamics are:

$$\begin{aligned} \frac{d\tilde{U}'_{int}(t)}{dt} = -j \left[\omega_p - \omega_0 \left(1 - \frac{dn}{dT} \frac{\Gamma}{n_{Si}} \Delta T(t) - \frac{dn_{Si}}{dN} \frac{\Gamma}{n_{Si}} \Delta N(t) - \omega_0 \frac{cn_2 \tilde{U}'_{int}}{n_{Si}^2 V_{eff}} \right) \right] \tilde{U}'_{int} - \\ + \left(\frac{1}{\tau_{tot}} + \frac{d\alpha^{FC}}{dN} \frac{c\Gamma}{2n_{Si}} \Delta N(t) + \frac{c^2 \beta_{TPA}}{2n_{Si}^2 V_{eff}} |\tilde{U}'_{int}(t)|^2 \right) \tilde{U}'_{int}(t) + j \sqrt{\frac{2}{\tau_a}} \tilde{E}'_{int} \end{aligned} \quad (\text{A.34})$$

$$\frac{d\Delta N(t)}{dt} = -\gamma_{FC} \Delta N(t) + \frac{c^2 \beta_{TPA}}{2\hbar\omega_p V V_{eff} n_{Si}^2} |\tilde{U}'_{int}(t)|^4 \quad (\text{A.35})$$

$$\begin{aligned} \frac{d\Delta T(t)}{dt} = -\gamma_{TH} \Delta T(t) + \frac{1}{M_{ring} C_p} \left(\frac{2}{\tau_o} + \frac{d\alpha^{FC}}{dN} \frac{c\Gamma}{n_{Si}} \Delta N(t) + \right. \\ \left. + \frac{c^2 \beta_{TPA}}{n_{Si}^2 V_{eff}} |\tilde{U}'_{int}(t)|^2 \right) |\tilde{U}'_{int}(t)|^2 \end{aligned} \quad (\text{A.36})$$

When the whole set admits steady states solutions, i.e when $\frac{d\tilde{U}'_{int}}{dt} = \frac{d\Delta N}{dt} = \frac{d\Delta T}{dt} = 0$, we can get the values of ΔT and ΔN at steady state by solving the now algebraic equations A.35 and A.36, recovering eqs.7.8 and eq.7.12 with an explicit expression for γ_{lin} , γ_{TPA} , γ_{FCA} and η_{TPA} :

$$\gamma_{lin} = \frac{2\sigma^2 p}{M_{Ring} C_p \tau_o \gamma_{TH} v_g} \quad (\text{A.37})$$

$$\gamma_{TPA} = \frac{c^2 \beta_{TPA} \sigma^4 p^2}{M_{Ring} C_p \gamma_{TH} n_{Si}^2 V_{eff} v_g^2} \quad (\text{A.38})$$

$$\gamma_{FCD} = \frac{c^3 \Gamma \beta_{TPA} \sigma^6 p^3}{2M_{Ring} C_p \gamma_{TH} \gamma_{FC} n_{Si}^3 V V_{eff} \hbar \omega_p v_g^3} \frac{d\alpha^{FC}}{dN} \quad (\text{A.39})$$

$$\eta_{TPA} = \frac{c^2 \beta_{TPA} \sigma^4 p^2}{2\hbar \omega_p V V_{eff} n_{Si}^2 \gamma_{FC} v_g^2} \quad (\text{A.40})$$

Parameter	Value	Source	Unit
$\frac{1}{\tau_{tot}}$	51	Measured	GHz
$\frac{1}{\tau_0}$	0.33	Measured	GHz
$\frac{dn_{Si}}{dT}$	$1.86 \cdot 10^{-4}$	[45]	K^{-1}
$\frac{dn_{Si}}{dN}$	$-4.2 \cdot 10^{-27}$	Fit	m^3
$\frac{d\alpha^{FC}}{dN}$	$1.45 \cdot 10^{-15}$	[45]	m^2
β_{TPA}	$0.79 \cdot 10^{-11}$	[211]	$\frac{m}{W}$
n_2	$0.45 \cdot 10^{-17}$	[211]	$\frac{m^2}{W}$
Γ	0.9	[120]	-
n_{Si}	3.485	[45]	-
V	4.347	Calculated	μm^3
V_{eff}	5.331	Calculated and [120]	μm^3
M_{Ring}	$1.013 \cdot 10^{-11}$	Calculated	g
C_p	0.7	[45]	$\frac{J}{gK}$
γ_{TH}	12	Fit and COMSOL	μs^{-1}
γ_{FC}	300	Fit from section 5.11.2	μs^{-1}

TABLE A.1: Parameters used in the numerical integration of eqs A.34 used in section 7.5.2.

Appendix B

Experimental Set-Up

This appendix introduces all the experimental setup used in this work. Four configurations will be mainly used:

1. *Transmission spectrum setup*: this is the basic setup with which transmission spectrum measures are performed. All other setups share the same configuration of this with some modifications.
2. *Optical pump setup*: this allows to measure the variation of the spectrum and time response of the device under test (DUT) as a function of an external optical pump.
3. *Electrical setup*: it is used where there are samples with metal heater wires for thermal tuning. It allows to measure the variation of the spectrum and time response of the DUT as a function of the power dissipated into the heater.
4. *Non-linear setup*: It is used for testing the self-induced optical non linearities of the DUT through an high power erbium doped fiber amplifier (EDFA)

The whole optical circuit of the setup is made with optical fibers, while the integrated optical chip is located in the DUT. The setup is interfaced to the chip via two tapered fibers in butt coupling configuration.

B.0.5 Transmission spectrum setup

DUT transmission spectrum are performed through the setup shown in figure [B.1](#). Two versions of this setup are used:

- Laser source: The signal source is a *TUNICS BT* laser which can provide an optical power up to $5mW$ in the $1500 - 1600nm$ range with $1pm$ of maximum resolution.

The laser output is fiber pig-tailed with an APC connector. The output fiber is feeded into several waveplates that allow to select the proper polarization. The incoming signal is coupled into the DUT via the alignment stage, that is described below. The transmitted signal is then sent to a *NEW FOCUS 2033* Germanium photodetector (IR detector), directly connected to an *Oriel* multimeter which is interfaced with a computer software that controls also the wavelength scan steps of the laser source.

- Amplified Spontaneous Emission (ASE) source. In this case the same set-up is used but the laser is replaced with an amplified spontaneous emission source that cover the third telecom window and the transmission light is detected by means of an optical spectrum analyzer (OSA)

The alignment stage based on a butt coupling configuration with tapered fibers (a description of the butt coupling technique is found in section 2.7.0.1). All the WGs in the DUT are terminated with adiabatic tapers with a final width of $2\ \mu\text{m}$.

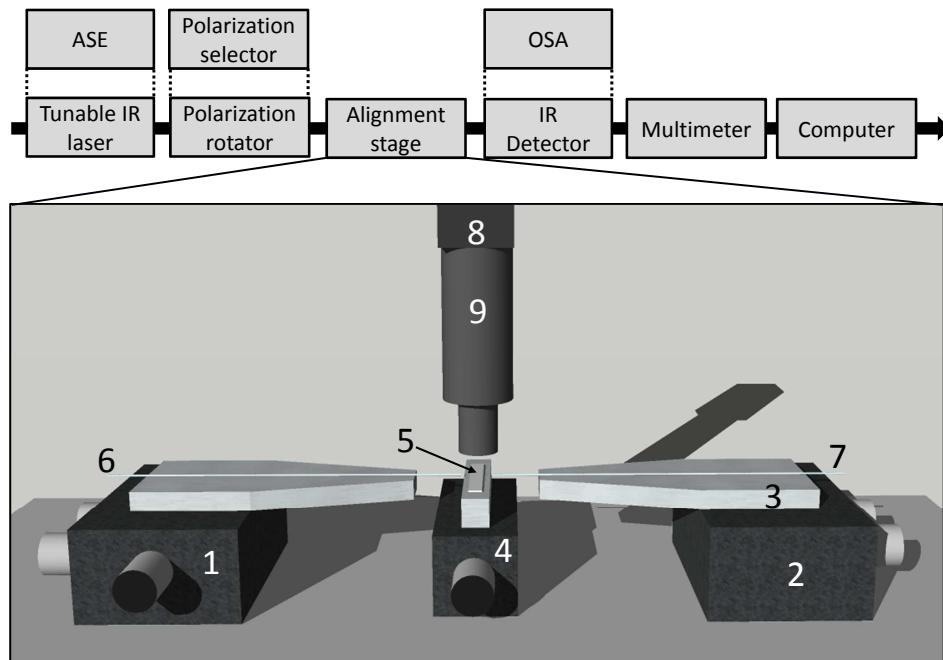


FIGURE B.1: Flowchart of the transmission setup and sketch of the alignment stage. The numbers represent the following objects: Input(1)/output(2) nanometer piezoelectric XYZ positioning system, (3) output fiber v-groove, (4) DUT mechanical translation stage, (5) DUT, Input(6)/output(7) tapered fibers, (8) Spiricon 320m IR InGaAs camera and (9) objective with 12x zoom and focus ring.

The input and output fiber(6,7) tips are tapered down to $2\ \mu\text{m}$ to form lenses that allow to minimize the coupling losses with the DUT(5). Fibers are aligned to the DUT WGs by means of nanometer piezoelectric/mechanical XYZ positioning systems (1,2). The

estimated insertion losses are about $10dB$ for each facet. The surface of the DUT is inspected through an IR camera (8) and a zoom objective (9). The imaging system is also useful to make a 2D map of the scattered light out of the DUT surface during the measuring process.

B.0.6 Optical pump setup

The setup discussed below is used to measure the variation of the spectrum and time response of the DUT when the external pump laser intensity is varied. Two kind of pump lasers are being used (Fig. B.2(1)):

- CW Nd:YAG green laser: 1.5 W of maximum power, wavelength of $532nm$ and free air output.
- Pulsed $Ti : Al_2O_3$ laser: 4 mW of mean power, repetition rate of 1 KHz, central wavelength of $800nm$, $10ps$ pulse width and free air output .

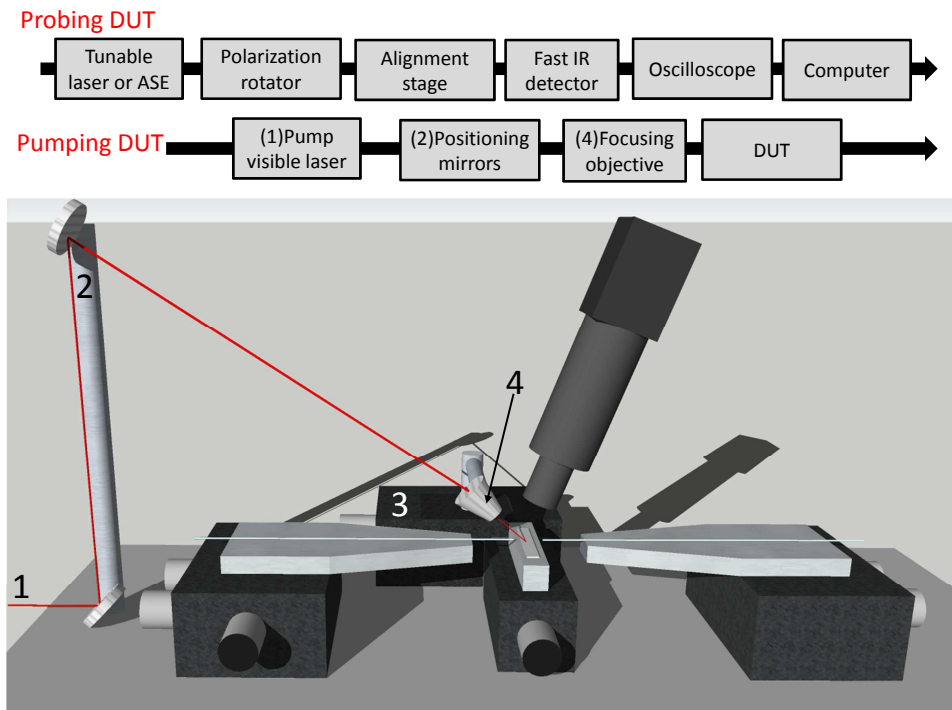


FIGURE B.2: Flowchart of the optical pump setup divided into probe and pump section. Sketch of the system used to focus the laser pump upon the DUT. The numbers represent the following objects:(1) Pump laser beam, (2) beam up mirrors, (3) XYZ stage form beam positioning and (4) corrected infinity objective.

The probing stage is similar to the one employed in the transmission setup but with a time resolved detection stage. A *Picometrix* Fast APD with time constant of $130ps$ and a $6GHz$ Tecktronic oscilloscope are used for this purpose. The pump section is build up

as follows: the pump laser beam (1) is pulled up by two mirrors (2) and focused onto the DUT by means of a corrected infinity objective (4). The observed spot size is about $10\mu\text{m}$ in diameter. The XYZ mechanical positioning stage (3) helps to move the spot above the surface. The aim of this setup is induce a refractive index perturbation in the area covered by the pump laser spot. Visible light impinging the DUT will generate free carrier absorption (FCA) since the photons energy is well above the band gap of silicon. This is the means through which the local refractive index is modified.

B.0.7 Electrical setup

The *electrical setup* is used to measure the variation of the transmission spectrum when the dissipated power into the metal heater is varied (see section 3.3.1). In this case the active refractive index tuning is carried out by metal heaters integrated into the chip. The physics involved phenomenon is the thermo-optical effect.

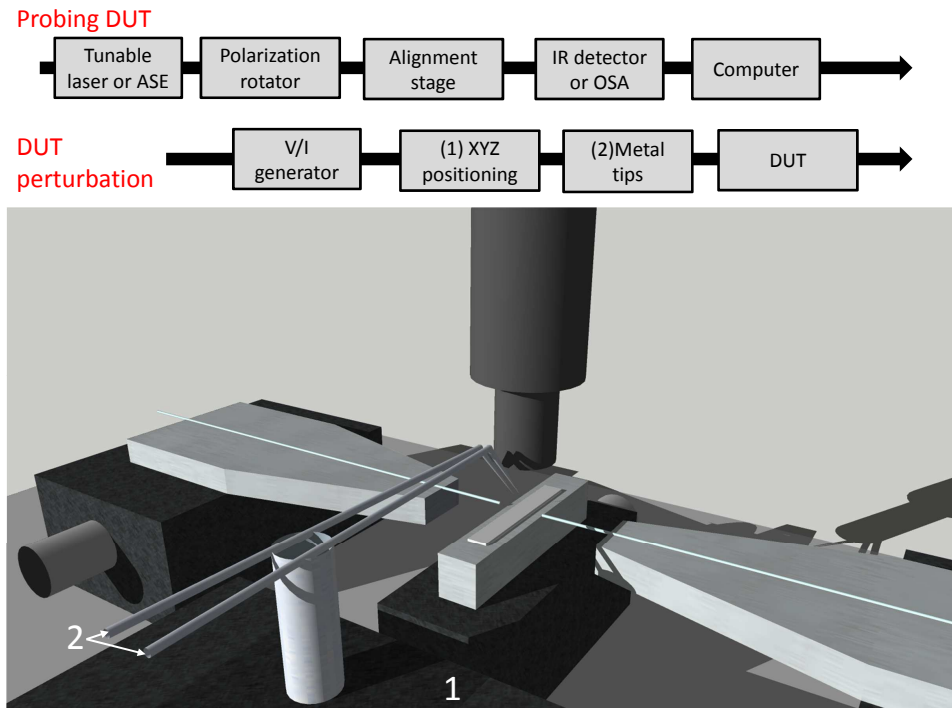


FIGURE B.3: Flowchart of the electrical setup. Sketch of the system used to inject current inside the metal strips. The numbers represent the following objects:(1) XYZ mechanical positioning stage, (2) metal tips.

The setup is reported in figure B.3. The probing stage is similar to the one employed in the transmission setup. A Keithley tension/current source is connected to the metal tips (2). The metal tips are then aligned (1) and placed in contact on the metal pads linked to the heater. The generator dissipated power will be linearly proportional to the refractive index variation.

B.0.8 Non-linear setup

The *Non-linear setup* is used to measure both the variation of the transmission spectrum and the output time response as a function of the optical power inside the DUT. This is a modified version of the *transmission setup* where, in order to reach enough power inside the DUT to activate non linear phenomena, an EDFA amplifies the source laser power to the desired level. The laser source is the tunable laser (*Tunics BT*) and the EDFA is a *IPG Photonics Fiber Amplifier*. The CW output power ranges from 500 mW to 5 W and it is directly coupled to a SMF . The output of the EDFA goes to a series of waveplates which are fiber connected to a *Variable Optical Attenuator* (VOA) before going to a 10 – 90 beam splitter. The 10% branch, used as power reference, goes to a *NEW FOCUS 2033* Germanium photodetector and the 90% branch goes to the alignment stage together with the ASE signal added through an in fiber combiner.

The OSA and to the *Picometrix* Fast APD are used to register the output power spectrum and the time response of the alignment stage output respectively. With this experimental setup, knowing the insertion and coupling losses of the various parts, we can simultaneously measure the input and output power of the sample, which are registered through a computer software. Thus, we can have a power reference for normalizing or scaling the data. This is important for characterize a power dependent phenomenon.

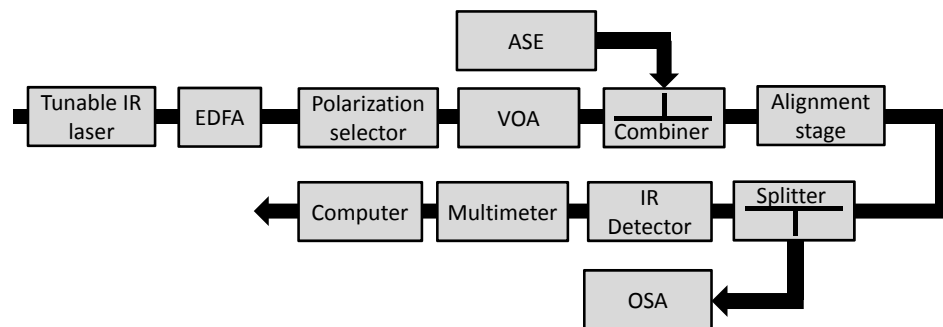


FIGURE B.4: Flowchart of the Non-linear setup.

Appendix C

A simplified model to describe the Ti:Sa external pump effect in a CRITAD

The goal of this appendix is to derive a phenomenological model to describe the time evolution of a CRITAD channel under the perturbation of an external pump laser. The model is based on the temporal CMT [181, 186] applied on a system of two coupled cavities. This model is used to explain the experimental results of section 5.11.2.

The system under study is shown in figure C.1 . $u_{(1,2)}(t)$ are the time dependent field amplitude inside the cavities and $\omega_{(1,2)}$ are their resonant frequencies. ϕ is the phase relation that exists between the cavities that are coupled through the bus WGs.

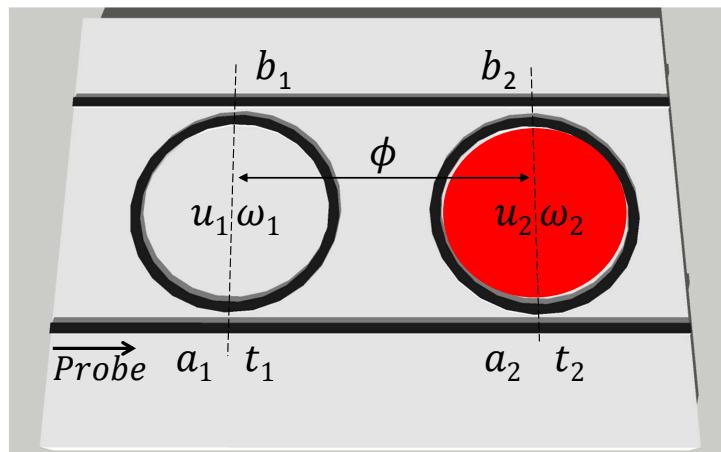


FIGURE C.1: System under study. The red circle indicates the pumped cavity.

The cavity decay rate associated to the bus WG is k_t and the intrinsic cavity decay rate is $2/\tau_0$. We are in the approximation of: $\omega - \omega_{1,2} \ll \omega$ where ω is the probe frequency and $k_t \ll 1$. Under these considerations, we write the equations to describe the time evolution of this system considering the input field a_1 (probe).

$$\frac{du_1(t)}{dt} = \left(i(\omega_1 - \omega) - \frac{1}{\tau_t} \right) u_1(t) + ia_1 k_t + ik_t b_1 \quad (\text{C.1})$$

$$\frac{du_2(t)}{dt} = \left(i \left(\omega_2 \left(1 + \frac{\Delta n}{n} f(t) \right) - \omega \right) - \frac{1}{\tau_t} \right) u_2(t) + ia_2 k_t + ib_2 k_t \quad (\text{C.2})$$

The term $\frac{\Delta n}{n}$ takes into account of the free carrier coefficient dispersion and of the number of generated carriers by the Ti:Sa pump. This equation is a sum of two exponentials with different time constants that represents how fast the carrier are generated and then recombines. τ_t is the total decay time of the cavity defined as $1/\tau_t = 1/\tau_0 + 2/\tau_k$. $f(t)$ is the function that approximates the free carrier generation and recombination defined as the sum of two exponential:

$$f(t) = \left(e^{\frac{t-t_0}{\tau_G}} + e^{-\frac{t-t_0}{\tau_R}} \right)^{-1} \quad (\text{C.3})$$

where t_0 is the time at which the perturbation starts, τ_G is the generation time constant of the free carriers and τ_R is the recombination time constant of the free carriers.

The fields between the cavities are linked through the following equations:

$$t_{1,2} = a_{1,2} + ik_t u_{1,2}(t) \quad a_2 = e^{-i\phi} t_1 \quad b_2 = ik_t u_2(t) \quad b_1 = e^{-i\phi} b_2$$

we imposes the ChC as $\phi = \pi$, obtaining:

$$\frac{du_1(t)}{dt} = \left(i(\omega_1 - \omega) - \frac{1}{\tau_t} \right) u_1(t) + ia_1 k_t + k_t^2 u_2(t) \quad (\text{C.4})$$

$$\frac{du_2(t)}{dt} = \left(i \left(\omega_2 \left(1 + \frac{\Delta n}{n} f(t) \right) - \omega \right) - \frac{1}{\tau_t} \right) u_2(t) - k_t a_1(t) + k_t^2 u_1(t) \quad (\text{C.5})$$

The behaviour of the T port is described by the equation below:

$$t_2 = -a_1 + ik_t (u_2(t) - u_1(t)) \rightarrow |t_2|^2 \equiv T$$

The used parameters are linked to the ones of the TMM through the following relations:

$$k_t^2 = k \frac{v_g}{p} \quad \tau_0 = \frac{1}{\alpha v_g}$$

where $k^2 = CC$, v_g is the group velocity, p the cavity perimeter and α the loss factor. Under these substitutions, the input power is equivalent to $|a_1|^2$.

Acknowledgements

I am grateful to Prof. Lorenzo Pavesi, my supervisor and head of the Nanoscience Lab of the University of Trento, for his scientific support, for the patience, and openness that has shown in carrying me along the path of research

I thank Paolo for the valuable advices and for helping me in throughout the research activity, from the paperwork to the lab. I thank him for all the good time we spent together in the beautiful mountains of Trentino through the magnesite dust.

I thank Romain for having initiated me to the laboratory life.

I thank Massimo for have been my "theoretic right arm" and for the patience in dealing with a true experimental stubborn.

I thank Fernando for his help in the lab and for the tobacco plantations in the lab that made me feel like in the green.

I thank Fabrizio for the time spent together which includes, talking about interesting scientific speeches, leave the feathers of some cliff and spend whole nights to hit the wall with the head trying to write something meaningful in this thesis.

I thank Tenga to making me warm up the wrist during the lunch break.

I thank Eveline for the fantastic macros shot together.

I also thank Federica, Niko and the whole group of Nanoscience for the time spent together.

I and the Nanoscience Lab of the physics department of the university of Trento acknowledge the support of the EU through the FP7 ICT-(216405) project Wavelength Division Multiplexed Photonic Layer on CMOS.

Bibliography

- [1] E. A. J. Marcatilli. Bends in optical dielectric waveguides. *Bell Syst. Tech. J.*, 48:21032132, 1969.
- [2] RA Soref and JP Lorenzo. Single-crystal silicon: a new material for 1.3 and 1.6 μm integrated-optical components. *Electronics Letters*, 21(21):953–954, 1985.
- [3] Richard Soref and J Lorenzo. All-silicon active and passive guided-wave components for $\lambda= 1.3$ and 1.6 μm . *Quantum Electronics, IEEE Journal of*, 22(6):873–879, 1986.
- [4] RICHARDA Soref and BRIANR Bennett. Electrooptical effects in silicon. *Quantum Electronics, IEEE Journal of*, 23(1):123–129, 1987.
- [5] Michal Lipson. Overcoming the limitations of microelectronics using si nanophotonics: solving the coupling, modulation and switching challenges. *Nanotechnology*, 15(10):S622, 2004.
- [6] Richard Soref. The past, present, and future of silicon photonics. *Selected Topics in Quantum Electronics, IEEE Journal of*, 12(6):1678–1687, 2006.
- [7] Richard A Soref. Silicon-based optoelectronics. *Proceedings of the IEEE*, 81(12):1687–1706, 1993.
- [8] F. Xia, L. Sekaric, and Y. Vlasov. Ultracompact optical buffers on a silicon chip. *Nature Photonics*, 1(1):65–71, 2006.
- [9] Shijun Xiao, Maroof H Khan, Hao Shen, and Minghao Qi. A highly compact third-order silicon microring add-drop filter with a very large free spectral range, a flat passband and a low delay dispersion. 2007.
- [10] Qianfan Xu, Bradley Schmidt, Sameer Pradhan, and Michal Lipson. Micrometre-scale silicon electro-optic modulator. *Nature*, 435(7040):325–327, 2005.
- [11] Qianfan Xu, Sunil Sandhu, Michelle L Povinelli, Jagat Shakya, Shanhui Fan, and Michal Lipson. Experimental realization of an on-chip all-optical analogue to

- electromagnetically induced transparency. *Physical review letters*, 96(12):123901, 2006.
- [12] Haisheng Rong, Shengbo Xu, Ying-Hao Kuo, Vanessa Sih, Oded Cohen, Omri Raday, and Mario Paniccia. Low-threshold continuous-wave raman silicon laser. *Nature Photonics*, 1(4):232–237, 2007.
- [13] Steven J Koester, Clint L Schow, Laurent Schares, Gabriel Dehlinger, Jeremy D Schaub, Fuad E Doany, and Richard A John. Ge-on-soi-detector/si-cmos-amplifier receivers for high-performance optical-communication applications. *Journal of Lightwave Technology*, 25(1):46–57, 2007.
- [14] Jifeng Liu, Jurgen Michel, Wojciech Giziewicz, Dong Pan, Kazumi Wada, Douglas D Cannon, Samerkhah Jongthammanurak, David T Danielson, Lionel C Kimerling, Jian Chen, et al. High-performance, tensile-strained ge_{1-x}si_x photodetectors on a si platform. *Applied Physics Letters*, 87(10):103501–103501, 2005.
- [15] Luca Benini and Giovanni De Micheli. Networks on chips: A new soc paradigm. *Computer*, 35(1):70–78, 2002.
- [16] Yurii Vlasov. Silicon photonics for next generation computing systems. In *European Conference on Optical Communications*, 2008.
- [17] RG Beausoleil, J Ahn, N Binkert, A Davis, D Fattal, M Fiorentino, NP Jouppi, M McLaren, CM Santori, RS Schreiber, et al. A nanophotonic interconnect for high-performance many-core computation. In *High Performance Interconnects, 2008. HOTI'08. 16th IEEE Symposium on*, pages 182–189. IEEE, 2008.
- [18] David AB Miller. Optical interconnects to silicon. *Selected Topics in Quantum Electronics, IEEE Journal of*, 6(6):1312–1317, 2000.
- [19] Mikhail Haurylau, Guoqing Chen, Hui Chen, Jidong Zhang, Nicholas A Nelson, David H Albonesi, Eby G Friedman, and Philippe M Fauchet. On-chip optical interconnect roadmap: Challenges and critical directions. *Selected Topics in Quantum Electronics, IEEE Journal of*, 12(6):1699–1705, 2006.
- [20] P. Dumon, G. Roelkens, W. Bogaerts, D. Van Thourhout, J. Wouters, S. Beckx, P. Jaenen, and R. Baets. Basic photonic wire components in silicon-on-insulator. In *Group IV Photonics, 2005. 2nd IEEE International Conference on*, pages 189–191. IEEE, 2005.
- [21] Andrew W Poon, Xianshu Luo, Fang Xu, and Hui Chen. Cascaded microresonator-based matrix switch for silicon on-chip optical interconnection. *Proceedings of the IEEE*, 97(7):1216–1238, 2009.

- [22] S. Feng, T. Lei, H. Chen, H. Cai, X. Luo, and A.W. Poon. Silicon photonics: from a microresonator perspective. *Laser & Photonics Reviews*, 6(2):145–177, 2011.
- [23] Byeong Gi Lee and Woojune Kim. *Integrated Broadband Networks: Tcp/Ip, Atm, Sdh/Sonet, and Wdm/Optics*. Artech House Publishers, 2002.
- [24] Wim Bogaerts, Pieter Dumon, D Van Thourhout, Dirk Taillaert, Patrick Jaenen, Johan Wouters, Stephan Beckx, Vincent Wiaux, and Roel G Baets. Compact wavelength-selective functions in silicon-on-insulator photonic wires. *Selected Topics in Quantum Electronics, IEEE Journal of*, 12(6):1394–1401, 2006.
- [25] Qianfan Xu, Brad Schmidt, Jagat Shakya, and Michal Lipson. Cascaded silicon micro-ring modulators for wdm optical interconnection. *Optics Express*, 14(20):9431–9435, 2006.
- [26] J Capmany, P Muñoz, JD Domenech, and MA Muriel. Apodized coupled resonator waveguides. *Optics express*, 15(16):10196–10206, 2007.
- [27] Sang-Yeon Cho and Richard Soref. Apodized scissors for filtering and switching. *Optics Express*, 16(23):19078–19090, 2008.
- [28] John E Heebner, Robert W Boyd, and Q-Han Park. Scissor solitons and other novel propagation effects in microresonator-modified waveguides. *JOSA B*, 19(4):722–731, 2002.
- [29] John E Heebner, Philip Chak, Suresh Pereira, John E Sipe, and Robert W Boyd. Distributed and localized feedback in microresonator sequences for linear and non-linear optics. *JOSA B*, 21(10):1818–1832, 2004.
- [30] Amnon Yariv, Yong Xu, Reginald K Lee, and Axel Scherer. Coupled-resonator optical waveguide: a proposal and analysis. *Optics Letters*, 24(11):711–713, 1999.
- [31]
- [32] <http://www.mapperlithography.com/>.
- [33] Mattia Mancinelli, Romain Guider, Marco Masi, Paolo Bettotti, Manga Rao Vanacharla, Jean-Marc Fedeli, and Lorenzo Pavesi. Optical characterization of a scissor device. *Optics Express*, 19(14):13664–13674, 2011.
- [34] M Mancinelli, R Guider, P Bettotti, M Masi, M Rao Vanacharla, and L Pavesi. Coupled-resonator-induced-transparency concept for wavelength routing applications. *Optics Express*, 19(13):12227–12240, 2011.

- [35] Hugo LR Lira, Sasikanth Manipatruni, and Michal Lipson. Broadband hitless silicon electro-optic switch for on-chip optical networks. *Optics Express*, 17(25):22271–22280, 2009.
- [36] M Mancinelli, P Bettotti, JM Fedeli, and L Pavesi. Reconfigurable optical routers based on coupled resonator induced transparency resonances. *Optics Express*, 20(21):23856–23864, 2012.
- [37] Marco Masi, Mattia Mancinelli, Alberto Battarelli, Romain Guider, Manga Rao Vanacharla, Paolo Bettotti, J Fedeli, and Lorenzo Pavesi. A silicon photonic interferometric router device based on scissor concept. *Lightwave Technology, Journal of*, 29(18):2747–2753, 2011.
- [38] Mattia Mancinelli, Paolo Bettotti, Jean Marc Fedeli, and Lorenzo Pavesi. Interferometric switching in coupled resonator optical waveguides-based reconfigurable optical device. *Optics Letters*, 38(2):217–219, 2013.
- [39] William MJ Green, Michael J Rooks, Lidija Sekaric, Yurii A Vlasov, et al. Ultra-compact, low rf power, 10 gb/s silicon mach-zehnder modulator. *Opt. Express*, 15(25):17106–17113, 2007.
- [40] Junfeng Song, Q Fang, SH Tao, MB Yu, GQ Lo, and DL Kwong. Passive ring-assisted mach-zehnder interleaver on silicon-on-insulator. *Optics Express*, 16(12):8359–8365, 2008.
- [41] Q Lin, Oskar J Painter, and Govind P Agrawal. Nonlinear optical phenomena in silicon waveguides: modeling and applications. *Optics Express*, 15(25):16604–16644, 2007.
- [42] Pieter Dumon, Gino Priem, Luis Romeu Nunes, Wim Bogaerts, Dries Van Thourhout, Peter Bienstman, Tak Keung Liang, Masahiro Tsuchiya, Patrick Jaenen, Stephan Beckx, et al. Linear and nonlinear nanophotonic devices based on silicon-on-insulator wire waveguides. *JAPANESE JOURNAL OF APPLIED PHYSICS PART 1-REGULAR PAPERS BRIEF COMMUNICATIONS & REVIEW PAPERS*, 45(8B):6589–6602, 2006.
- [43] Vilson R Almeida and Michal Lipson. Optical bistability on a silicon chip. *Optics letters*, 29(20):2387–2389, 2004.
- [44] Gino Priem, Pieter Dumon, Wim Bogaerts, Dries Van Thourhout, Geert Morthier, and Roel Baets. Optical bistability and pulsating behaviour in silicon-on-insulator ring resonator structures. *Optics express*, 13(23):9623–9628, 2005.

- [45] Thomas J Johnson, Matthew Borselli, and Oskar Painter. Self-induced optical modulation of the transmission through a high-q silicon microdisk resonator. *Optics express*, 14(2):817–831, 2006.
- [46] Anna Sterkhova, Jaroslav Luksch, and J Petracek. Simulation of self-pulsing and chaos in coupled microring resonators. In *Transparent Optical Networks (ICTON), 2010 12th International Conference on*, pages 1–4. IEEE, 2010.
- [47] <http://www.leti.fr/en>.
- [48] <http://www2.imec.be/>.
- [49] Comsol Multiphysics. Comsol. Inc., Burlington, MA, www.comsol.com, 1994.
- [50] Andrew W Poon, Xianshu Luo, Fang Xu, and Hui Chen. Cascaded microresonator-based matrix switch for silicon on-chip optical interconnection. *Proceedings of the IEEE*, 97(7):1216–1238, 2009.
- [51] Wim Bogaerts, Peter De Heyn, Thomas Van Vaerenbergh, Katrien De Vos, Shankar Kumar Selvaraja, Tom Claes, Pieter Dumon, Peter Bienstman, Dries Van Thourhout, and Roel Baets. Silicon microring resonators. *Laser & Photonics Reviews*, 6(1):47–73, 2011.
- [52] Michael Hochberg, Nicholas C Harris, Ran Ding, Yi Zhang, Ari Novack, Zhe Xuan, and Tom Baehr-Jones. Silicon photonics: The next fabless semiconductor industry. *Solid-State Circuits Magazine, IEEE*, 5(1):48–58, 2013.
- [53] Xu Wang, Wei Shi, Han Yun, Samantha Grist, Nicolas AF Jaeger, and Lukas Chrostowski. Narrow-band waveguide bragg gratings on soi wafers with cmos-compatible fabrication process. *Optics Express*, 20(14):15547–15558, 2012.
- [54] X Fu and D Dai. Ultra-small si-nanowire-based 400 ghz-spacing 15 x 15 arrayed-waveguide grating router with microbends. *Electronics letters*, 47(4):266–268, 2011.
- [55] Pieter Dumon, Wim Bogaerts, Vincent Wiaux, Johan Wouters, Stephan Beckx, Joris Van Campenhout, Dirk Taillaert, Bert Luyssaert, Peter Bienstman, Dries Van Thourhout, et al. Low-loss soi photonic wires and ring resonators fabricated with deep uv lithography. *Photonics Technology Letters, IEEE*, 16(5):1328–1330, 2004.
- [56] Qianfan Xu, Bradley Schmidt, Sameer Pradhan, and Michal Lipson. Micrometre-scale silicon electro-optic modulator. *Nature*, 435(7040):325–327, 2005.

- [57] Kevin K Lee, Desmond R Lim, Hsin-Chiao Luan, Anuradha Agarwal, James Foresi, and Lionel C Kimerling. Effect of size and roughness on light transmission in a si/sio₂ waveguide: Experiments and model. *Applied Physics Letters*, 77:1617, 2000.
- [58] Kevin K Lee, Desmond R Lim, Lionel C Kimerling, Jangho Shin, and Franco Cerrina. Fabrication of ultralow-loss si/sio₂ waveguides by roughness reduction. *Optics letters*, 26(23):1888–1890, 2001.
- [59] F Grillot, L Vivien, S Laval, D Pascal, and E Cassan. Size influence on the propagation loss induced by sidewall roughness in ultrasmall soi waveguides. *Photonics Technology Letters, IEEE*, 16(7):1661–1663, 2004.
- [60] U Fischer, T Zinke, J-R Kropp, F Arndt, and K Petermann. 0.1 db/cm waveguide losses in single-mode soi rib waveguides. *Photonics Technology Letters, IEEE*, 8(5):647–648, 1996.
- [61] Po Dong, Wei Qian, Shirong Liao, Hong Liang, Cheng-Chih Kung, Ning-Ning Feng, Roshanak Shafiiha, Joan Fong, Dazeng Feng, Ashok V Krishnamoorthy, et al. Low loss shallow-ridge silicon waveguides. *Optics express*, 18(14):14474–14479, 2010.
- [62] www.epixfab.com.
- [63] Guoliang Li, Jin Yao, Hiren Thacker, Attila Mekis, Xuezhe Zheng, Ivan Shubin, Ying Luo, Jin-hyoung Lee, Kannan Raj, John E Cunningham, et al. Ultralow-loss, high-density soi optical waveguide routing for macrochip interconnects. *Optics Express*, 20(11):12035–12039, 2012.
- [64] Daoxin Dai, Zhi Wang, Jared F Bauters, M-C Tien, Martijn JR Heck, Daniel J Blumenthal, and John E Bowers. Low-loss si₃n₄ arrayed-waveguide grating (de) multiplexer using nano-core optical waveguides. *Optics express*, 19(15):14130–14136, 2011.
- [65] Dana Vantrease, Robert Schreiber, Matteo Monchiero, Moray McLaren, Norman P Jouppi, Marco Fiorentino, Al Davis, Nathan Binkert, Raymond G Beausoleil, and Jung Ho Ahn. Corona: System implications of emerging nanophotonic technology. *ACM SIGARCH Computer Architecture News*, 36(3):153–164, 2008.
- [66] Wim Bogaerts, Pieter Dumon, Dries Van Thourhout, and Roel Baets. Low-loss, low-cross-talk crossings for silicon-on-insulator nanophotonic waveguides. *Optics Letters*, 32(19):2801–2803, 2007.

- [67] Ashok V Krishnamoorthy, Ron Ho, Xuezhe Zheng, Herb Schwetman, Jon Lexau, Pranay Koka, GuoLiang Li, Ivan Shubin, and John E Cunningham. Computer systems based on silicon photonic interconnects. *Proceedings of the IEEE*, 97(7):1337–1361, 2009.
- [68] Jin Yao, Xuezhe Zheng, Guoliang Li, Ivan Shubin, Hiren Thacker, Ying Luo, Kannan Raj, John E Cunningham, and Ashok V Krishnamoorthy. Grating-coupler based low-loss optical interlayer coupling. In *Group IV Photonics (GFP), 2011 8th IEEE International Conference on*, pages 383–385. IEEE, 2011.
- [69] Michael J Wale and Colin Edge. Self-aligned flip-chip assembly of protonic devices with electrical and optical connections. *Components, Hybrids, and Manufacturing Technology, IEEE Transactions on*, 13(4):780–786, 1990.
- [70] Wim Bogaerts, Shankar Kumar Selvaraja, Pieter Dumon, Joost Brouckaert, Katrien De Vos, Dries Van Thourhout, and Roel Baets. Silicon-on-insulator spectral filters fabricated with cmos technology. *Selected Topics in Quantum Electronics, IEEE Journal of*, 16(1):33–44, 2010.
- [71] David Kwong, Yang Zhang, Amir Hosseini, YaZhao Liu, and Ray T Chen. Demonstration of rib waveguide based 1x12 multimode interference optical beam splitter on silicon-on-insulator. In *Photonics Society Summer Topical Meeting Series, 2010 IEEE*, pages 221–222. IEEE, 2010.
- [72] Alexander W Fang, Hyundai Park, Oded Cohen, Richard Jones, Mario J Paniccia, and John E Bowers. Electrically pumped hybrid alginas-silicon evanescent laser. *Optics Express*, 14(20):9203–9210, 2006.
- [73] Huiyun Liu, Ting Wang, Qi Jiang, Richard Hogg, Frank Tutu, Francesca Pozzi, and Alwyn Seeds. Long-wavelength inas/gaas quantum-dot laser diode monolithically grown on ge substrate. *Nature Photonics*, 5(7):416–419, 2011.
- [74] Rodolfo E Camacho-Aguilera, Yan Cai, Neil Patel, Jonathan T Bessette, Marco Romagnoli, Lionel C Kimerling, and Jurgen Michel. An electrically pumped germanium laser. *Optics express*, 20(10):11316–11320, 2012.
- [75] Q. Xu, D. Fattal, and R.G. Beausoleil. Silicon microring resonators with 1.5- μm radius. *Optics express*, 16(6):4309–4315, 2008.
- [76] Andrew W Poon, Xianshu Luo, Linjie Zhou, Chao Li, Jonathan Y Lee, Fang Xu, Hui Chen, and Nick K Hon. Microresonator-based devices on a silicon chip: novel shaped cavities and resonance coherent interference. *Practical applications of microresonators in optics and photonics*, 2009.

- [77] Andrea Melloni, Francesco Morichetti, Carlo Ferrari, and Mario Martinelli. Continuously tunable 1 byte delay in coupled-resonator optical waveguides. *Optics letters*, 33(20):2389–2391, 2008.
- [78] Yoshitomo Okawachi, Mark A Foster, Jay E Sharping, Alexander L Gaeta, Qianfan Xu, Michal Lipson, et al. All-optical slow-light on a photonic chip. *Opt. Express*, 14(6):2317–2322, 2006.
- [79] Lei Jin, Mingyu Li, and Jian-Jun He. Highly-sensitive silicon-on-insulator sensor based on two cascaded micro-ring resonators with vernier effect. *Optics Communications*, 284(1):156–159, 2011.
- [80] Robi Boeck, Nicolas A Jaeger, Nicolas Rouger, and Lukas Chrostowski. Series-coupled silicon racetrack resonators and the vernier effect: theory and measurement. *Optics express*, 18(24):25151–25157, 2010.
- [81] Qing Li, Mohammad Soltani, Amir H Atabaki, Siva Yegnanarayanan, and Ali Adibi. Quantitative modeling of coupling-induced resonance frequency shift in microring resonators. *Optics express*, 17(26):23474–23487, 2009.
- [82] Sang-Yeon Cho and Richard Soref. Apodized scissors for filtering and switching. *Optics Express*, 16(23):19078–19090, 2008.
- [83] John E Heebner, Robert W Boyd, and Q-Han Park. Scissor solitons and other novel propagation effects in microresonator-modified waveguides. *JOSA B*, 19(4):722–731, 2002.
- [84] Qianfan Xu, Jagat Shakya, Michal Lipson, et al. Direct measurement of tunable optical delays on chip analogue to electromagnetically induced transparency. *Opt. Express*, 14(14):6463–6468, 2006.
- [85] Qianfan Xu, Po Dong, and Michal Lipson. Breaking the delay-bandwidth limit in a photonic structure. *Nature Physics*, 3(6):406–410, 2007.
- [86] Yonghui Tian, Lei Zhang, Qianfan Xu, and Lin Yang. Xor/xnor directed logic circuit based on coupled-resonator-induced transparency. *Laser & Photonics Reviews*, 7(1):109–113, 2013.
- [87] Ning-Ning Feng, Po Dong, Dazeng Feng, Wei Qian, Hong Liang, Daniel C Lee, Jonathan B Luff, Anjali Agarwal, Tom Banwell, Ron Menendez, et al. Thermally-efficient reconfigurable narrowband rf-photonic filter. *Optics express*, 18(24):24648–24653, 2010.

- [88] John E Cunningham, Ivan Shubin, Xuezhe Zheng, Thierry Pinguet, Attila Mekis, Ying Luo, Hiren Thacker, Guoliang Li, Jin Yao, Kannan Raj, et al. Highly-efficient thermally-tuned resonant optical filters. *Optics express*, 18(18):19055–19063, 2010.
- [89] Antonio Canciamilla, Francesco Morichetti, Stefano Grillanda, Philippe Velha, Marc Sorel, Vivek Singh, Anu Agarwal, Lionel C Kimerling, and Andrea Melloni. Photo-induced trimming of chalcogenide-assisted silicon waveguides. *Optics Express*, 20(14):15807–15817, 2012.
- [90] Jonathan Schrauwen, Dries Van Thourhout, and Roel Baets. Trimming of silicon ring resonator by electron beam induced compaction and strain. *Optics Express*, 16(6):3738–3743, 2008.
- [91] Nicolás Sherwood-Droz, Howard Wang, Long Chen, Benjamin G Lee, Aleksandr Biberman, Keren Bergman, Michal Lipson, et al. Optical 4x4 hitless silicon router for optical networks-on-chip (noc). *Opt. Express*, 16(20):15915–15922, 2008.
- [92] Linjie Zhou and Andrew W Poon. Fano resonance-based electrically reconfigurable add-drop filters in silicon microring resonator-coupled mach-zehnder interferometers. *Optics letters*, 32(7):781–783, 2007.
- [93] Linjie Zhou and Andrew W Poon. Electrically reconfigurable silicon microring resonator-based filter with waveguide-coupled feedback. *Optics express*, 15(15):9194–9204, 2007.
- [94] Milos A Popovic, Tymon Barwicz, Fuwan Gan, Marcus S Dahlem, Charles W Holzwarth, Peter T Rakich, Henry I Smith, Erich P Ippen, and Franz X Kärtner. Transparent wavelength switching of resonant filters. In *Conference on Lasers and Electro-Optics*. Optical Society of America, 2007.
- [95] Douglas M Gill, Sanjay S Patel, Mahmoud Rasras, Kun-Yü Tu, Alice E White, Young-Kai Chen, Andrew Pomerene, Daniel Carothers, Robert L Kamocsai, Craig M Hill, et al. Cmos-compatible si-ring-assisted mach-zehnder interferometer with internal bandwidth equalization. *Selected Topics in Quantum Electronics, IEEE Journal of*, 16(1):45–52, 2010.
- [96] Matthew Terrel, Michel JF Dignonnet, and Shanhui Fan. Ring-coupled mach-zehnder interferometer optimized for sensing. *Applied optics*, 48(26):4874–4879, 2009.
- [97] Lian-Wee Luo, Salah Ibrahim, Arthur Nitkowski, Zhi Ding, Carl B Poitras, SJ Ben Yoo, and Michal Lipson. High bandwidth on-chip silicon photonic interleaver. *Optics Express*, 18(22):23079–23087, 2010.

- [98] DJ Thomson, FY Gardes, Y Hu, G Mashanovich, M Fournier, P Grosse, JM Fedeli, and GT Reed. High contrast 40gb/s optical modulation in silicon. *Optics Express*, 19(12):11507–11516, 2011.
- [99] Ansheng Liu, Richard Jones, Ling Liao, Dean Samara-Rubio, Doron Rubin, Oded Cohen, Remus Nicolaescu, and Mario Paniccia. A high-speed silicon optical modulator based on a metal–oxide–semiconductor capacitor. *Nature*, 427(6975):615–618, 2004.
- [100] CZ Zhao, GZ Li, EK Liu, Y Gao, and XD Liu. Silicon on insulator mach–zehnder waveguide interferometers operating at 1.3 μm . *Applied physics letters*, 67(17):2448–2449, 1995.
- [101] Po Dong, Long Chen, and Young-kai Chen. High-speed low-voltage single-drive push-pull silicon mach-zehnder modulators. *Optics Express*, 20(6):6163–6169, 2012.
- [102] David J Thomson, Frederic Y Gardes, J-M Fedeli, Sanja Zlatanovic, Youfang Hu, Bill Ping Piu Kuo, Evgeny Myslivets, Nikola Alic, Stojan Radic, Goran Z Mashanovich, et al. 50-gb/s silicon optical modulator. *Photonics Technology Letters, IEEE*, 24(4):234–236, 2012.
- [103] Tom Baehr-Jones, Ran Ding, Yang Liu, Ali Ayazi, Thierry Pinguet, Nicholas C Harris, Matt Streshinsky, Poshen Lee, Yi Zhang, Andy Eu-Jin Lim, et al. Ultralow drive voltage silicon traveling-wave modulator. *Optics Express*, 20(11):12014–12020, 2012.
- [104] Yingtao Hu, Xi Xiao, Hao Xu, Xianyao Li, Kang Xiong, Zhiyong Li, Tao Chu, Yude Yu, and Jinzhong Yu. High-speed silicon modulator based on cascaded microring resonators. *Optics Express*, 20(14):15079–15085, 2012.
- [105] Guoliang Li, Xuezhe Zheng, Jin Yao, Hiren Thacker, Ivan Shubin, Ying Luo, Kannan Raj, John E Cunningham, and Ashok V Krishnamoorthy. 25gb/s 1v-driving cmos ring modulator with integrated thermal tuning. *Optics express*, 19(21):20435–20443, 2011.
- [106] Wesley D Sacher, William MJ Green, Solomon Assefa, Tymon Barwicz, Huapu Pan, Steven M Shank, Yurii A Vlasov, and Joyce KS Poon. Breaking the cavity linewidth limit of resonant optical modulators. *arXiv preprint arXiv:1206.5337*, 2012.
- [107] Jian Wang and Sungjoo Lee. Ge-photodetectors for si-based optoelectronic integration. *Sensors*, 11(1):696–718, 2011.

- [108] Hyundai Park, Alexander W Fang, Richard Jones, Oded Cohen, Omri Raday, Matthew N Sysak, Mario J Paniccia, and John E Bowers. A hybrid alginasilicon evanescent waveguide photodetector. *Optics Express*, 15(10):6044–6052, 2007.
- [109] Laurent Vivien, Andreas Polzer, Delphine Marris-Morini, Johann Osmond, Jean Michel Hartmann, Paul Crozat, Eric Cassan, Christophe Kopp, Horst Zimmermann, and Jean Marc Fédéli. Zero-bias 40gbit/s germanium waveguide photodetector on silicon. *Optics express*, 20(2):1096–1101, 2012.
- [110] Shirong Liao, Ning-Ning Feng, Dazeng Feng, Po Dong, Roshanak Shafiiha, Cheng-Chih Kung, Hong Liang, Wei Qian, Yong Liu, Joan Fong, et al. 36 ghz submicron silicon waveguide germanium photodetector. *Optics Express*, 19(11):10967–10972, 2011.
- [111] Long Chen and Michal Lipson. Ultra-low capacitance and high speed germanium photodetectors on silicon. *Opt. Express*, 17(10):7901–7906, 2009.
- [112] Solomon Assefa, Fengnian Xia, and Yurii A Vlasov. Reinventing germanium avalanche photodetector for nanophotonic on-chip optical interconnects. *Nature*, 464(7285):80–84, 2010.
- [113] Dirk Taillaert, Wim Bogaerts, Peter Bienstman, Thomas F Krauss, Peter Van Daele, Ingrid Moerman, Steven Verstuyft, Kurt De Mesel, and Roel Baets. An out-of-plane grating coupler for efficient butt-coupling between compact planar waveguides and single-mode fibers. *Quantum Electronics, IEEE Journal of*, 38(7):949–955, 2002.
- [114] Dirk Taillaert, Harold Chong, Peter I Borel, Lars H Frandsen, RM De La Rue, and Roel Baets. A compact two-dimensional grating coupler used as a polarization splitter. *Photonics Technology Letters, IEEE*, 15(9):1249–1251, 2003.
- [115] Günther Roelkens, Dries Van Thourhout, and Roel Baets. High efficiency grating coupler between silicon-on-insulator waveguides and perfectly vertical optical fibers. *Optics letters*, 32(11):1495–1497, 2007.
- [116] Dirk Taillaert, Peter Bienstman, and Roel Baets. Compact efficient broadband grating coupler for silicon-on-insulator waveguides. *Optics letters*, 29(23):2749–2751, 2004.
- [117] Günther Roelkens, Dries Van Thourhout, and Roel Baets. High efficiency silicon-on-insulator grating coupler based on a poly-silicon overlay. *Optics Express*, 14(24):11622–11630, 2006.

- [118] Bin Wang, Jianhua Jiang, and Gregory P Nordin. Embedded slanted grating for vertical coupling between fibers and silicon-on-insulator planar waveguides. *Photonics Technology Letters, IEEE*, 17(9):1884–1886, 2005.
- [119] Xia Chen, Ke Xu, Zhenzhou Cheng, Christy KY Fung, and Hon K Tsang. Wide-band subwavelength gratings for coupling between silicon-on-insulator waveguides and optical fibers. *Optics Letters*, 37(17):3483–3485, 2012.
- [120] M Dinu, F Quochi, and H Garcia. Third-order nonlinearities in silicon at telecom wavelengths. *Applied Physics Letters*, 82(18):2954–2956, 2003.
- [121] Ricardo Claps, Dimitri Dimitropoulos, Varun Raghunathan, and Bahrain Jalali. Observation of stimulated raman amplification in silicon waveguides. In *Lasers and Electro-Optics Society, 2003. LEOS 2003. The 16th Annual Meeting of the IEEE*, volume 1, pages 134–135. IEEE, 2003.
- [122] Richard A Soref, Stephen J Emelett, and Walter R Buchwald. Silicon waveguided components for the long-wave infrared region. *Journal of Optics A: Pure and Applied Optics*, 8(10):840, 2006.
- [123] Hon Ki Tsang, CS Wong, TK Liang, IE Day, SW Roberts, A Harpin, J Drake, and M Asghari. Optical dispersion, two-photon absorption and self-phase modulation in silicon waveguides at $1.5\ \mu\text{m}$. *Applied physics letters*, 80(3):416–418, 2002.
- [124] Eric Dulkeith, Yurii A Vlasov, Xiaogang Chen, Nicolae C Panoiu, Richard M Osgood Jr, et al. Self-phase-modulation in submicron silicon-on-insulator photonic wires. *Optics express*, 14(12):5524–5534, 2006.
- [125] Lianghong Yin, Qiang Lin, and Govind P Agrawal. Soliton fission and supercontinuum generation in silicon waveguides. *Optics letters*, 32(4):391–393, 2007.
- [126] Reza Salem, Mark A Foster, Amy C Turner, David F Geraghty, Michal Lipson, and Alexander L Gaeta. All-optical regeneration on a silicon chip. *Opt. Express*, 15(12):7802–7809, 2007.
- [127] R Dekker, A Driessen, T Wahlbrink, C Moormann, J Niehusmann, and M Först. Ultrafast kerr-induced all-optical wavelength conversion in silicon waveguides using $1.55\ \mu\text{m}$ femtosecond pulses. 2006.
- [128] Alain Haché and Martin Bourgeois. Ultrafast all-optical switching in a silicon-based photonic crystal. *Applied Physics Letters*, 77(25):4089–4091, 2000.

- [129] Haisheng Rong, Richard Jones, Ansheng Liu, Oded Cohen, Dani Hak, Alexander Fang, and Mario Paniccia. A continuous-wave raman silicon laser. *Nature*, 433(7027):725–728, 2005.
- [130] Qiang Lin, Jidong Zhang, Philippe M Fauchet, Govind P Agrawal, et al. Ultra-broadband parametric generation and wavelength conversion in silicon waveguides. *Opt. Express*, 14(11):4786–4799, 2006.
- [131] Mark A Foster, Amy C Turner, Jay E Sharping, Bradley S Schmidt, Michal Lipson, and Alexander L Gaeta. Broad-band optical parametric gain on a silicon photonic chip. *Nature*, 441(7096):960–963, 2006.
- [132] Q Lin, J Zhang, G Piredda, RW Boyd, PM Fauchet, and GP Agrawal. Dispersion of silicon nonlinearities in the near infrared region. *Applied physics letters*, 91(2):021111–021111, 2007.
- [133] Takasumi Tanabe, Masaya Notomi, Satoshi Mitsugi, Akihiko Shinya, and Eiichi Kuramochi. All-optical switches on a silicon chip realized using photonic crystal nanocavities. *Applied Physics Letters*, 87(15):151112–151112, 2005.
- [134] Stefan F Preble, Qianfan Xu, Bradley S Schmidt, and Michal Lipson. Ultrafast all-optical modulation on a silicon chip. *Optics letters*, 30(21):2891–2893, 2005.
- [135] Kazuhiro Ikeda and Yeshaiahu Fainman. Nonlinear fabry-perot resonator with a silicon photonic crystal waveguide. *Optics letters*, 31(23):3486–3488, 2006.
- [136] En-Kuang Tien, Nuh S Yuksek, Feng Qian, and Ozdal Boyraz. Pulse compression and modelocking by using tpa in silicon waveguides. In *Lasers and Electro-Optics, 2007. CLEO 2007. Conference on*, pages 1–2. IEEE, 2007.
- [137] Qianfan Xu and Michal Lipson. Carrier-induced optical bistability in silicon ring resonators. *Optics letters*, 31(3):341–343, 2006.
- [138] Shaowu Chen, Libin Zhang, Yonghao Fei, and Tongtong Cao. Bistability and self-pulsation phenomena in silicon microring resonators based on nonlinear optical effects. *Optics Express*, 20(7):7454–7468, 2012.
- [139] Bjorn Maes, Martin Fiers, and Peter Bienstman. Self-pulsing and chaos in short chains of coupled nonlinear microcavities. *PHYSICAL REVIEW A Phys Rev A*, 80:033805, 2009.
- [140] Thomas Van Vaerenbergh, Martin Fiers, Pauline Mechet, Thijs Spuesens, Rajesh Kumar, Geert Mortier, Kristof Vandoorne, Bendix Schneider, Benjamin Schrauwen, Joni Dambre, et al. Self-pulsation and excitability mechanism in

- silicon-on-insulator microrings. In *Asia Communications and Photonics Conference*. Optical Society of America, 2012.
- [141] Thomas Van Vaerenbergh, Martin Fiers, Pauline Mechet, Thijs Spuesens, Rajesh Kumar, Geert Morthier, Benjamin Schrauwen, Joni Dambre, and Peter Bienstman. Cascadable excitability in microrings. *Optics Express*, 20(18):20292–20308, 2012.
- [142] Jiří Petráček, Anna Sterkhova, et al. Numerical scheme for simulation of self-pulsing and chaos in coupled microring resonators. *Microwave and Optical Technology Letters*, 53(10):2238–2242, 2011.
- [143] Marco Masi, Régis Orobtcouk, Guofang Fan, J-M Fedeli, and Lorenzo Pavesi. Towards a realistic modelling of ultra-compact racetrack resonators. *Lightwave Technology, Journal of*, 28(22):3233–3242, 2010.
- [144] G.T. Reed and A.P. Knights. *Silicon photonics*. Wiley Online Library, 2008.
- [145] Y.A. Vlasov, S.J. McNab, et al. Losses in single-mode silicon-on-insulator strip waveguides and bends. *Opt. Express*, 12(8):1622–1631, 2004.
- [146] P. Dumon, W. Bogaerts, V. Wiaux, J. Wouters, S. Beckx, J. Van Campenhout, D. Taillaert, B. Luyssaert, P. Bienstman, D. Van Thourhout, et al. Low-loss silicon photonic wires and ring resonators fabricated with deep uv lithography. *Photonics Technology Letters, IEEE*, 16(5):1328–1330, 2004.
- [147] F. Morichetti, A. Canciamilla, C. Ferrari, M. Torregiani, A. Melloni, and M. Martinelli. Roughness induced backscattering in optical silicon waveguides. *Physical review letters*, 104(3):33902, 2010.
- [148] Daniel Knight Sparacin. *Process and design techniques for low loss integrated silicon photonics*. PhD thesis, Massachusetts Institute of Technology, 2006.
- [149] R.G. Hunsperger and J.R. Meyer-Arendt. Integrated optics: Theory and technology. *Applied Optics*, 31:298, 1992.
- [150] Marco Masi. *Modeling of sequences of Silicon micro-Resonators for On-Chip Optical Routing and Switching*. PhD thesis.
- [151] D. Marcuse. Theory of dielectric optical waveguides. *New York, Academic Press, Inc., 1974*. 267 p., 1, 1974.
- [152] M.A. Popović, C. Manolatou, and M.R. Watts. Coupling-induced resonance frequency shifts in coupled dielectric multi-cavity filters. *Opt. Express*, 14(3):1208–1222, 2006.

- [153] M.V. Williamson and A.R. Neureuther. Enhanced quantitative analysis of resist image contrast upon line- edge roughness(ler). In *Proceedings of SPIE*, volume 5039, pages 423–432, 2003.
- [154] H. Fukuda. Analysis of line edge roughness using probability process model for chemically amplified resists. In *Microprocesses and Nanotechnology Conference, 2002. Digest of Papers. Microprocesses and Nanotechnology 2002. 2002 International*, pages 76–77. IEEE, 2002.
- [155] R. Stoffer, K.R. Hiremath, and M. Hammer. Comparison of coupled mode theory and fdtd simulations of coupling between bent and straight optical waveguides. In *AIP Conference Proceedings: Microresonators as building blocks for VLSI photonics (2004)*, volume 709, pages 366–377. Springer, 2004.
- [156] FP Payne and JPR Lacey. A theoretical analysis of scattering loss from planar optical waveguides. *Optical and Quantum Electronics*, 26(10):977–986, 1994.
- [157] F. Grillot, L. Vivien, S. Laval, D. Pascal, and E. Cassan. Size influence on the propagation loss induced by sidewall roughness in ultrasmall soi waveguides. *Photonics Technology Letters, IEEE*, 16(7):1661–1663, 2004.
- [158] Minhao Pu, Liu Liu, Haiyan Ou, Kresten Yvind, and Jørn M Hvam. Ultra-low-loss inverted taper coupler for silicon-on-insulator ridge waveguide. *Optics Communications*, 283(19):3678–3682, 2010.
- [159] Frederik Van Laere, Tom Claes, Jonathan Schrauwen, Stijn Scheerlinck, Wim Bogaerts, Dirk Taillaert, Liam O’Faolain, Dries Van Thourhout, and Roel Baets. Compact focusing grating couplers for silicon-on-insulator integrated circuits. *Photonics Technology Letters, IEEE*, 19(23):1919–1921, 2007.
- [160] Daniel K Sparacin, Steven J Spector, and Lionel C Kimerling. Silicon waveguide sidewall smoothing by wet chemical oxidation. *Journal of lightwave technology*, 23(8):2455, 2005.
- [161] Richard Jones, Jonathan Doylend, Paniz Ebrahimi, Simon Ayotte, Omri Raday, and Oded Cohen. Silicon photonic tunable optical dispersion compensator. *Opt. Express*, 15(24):15836, 2007.
- [162] Matthew Borselli, Thomas J Johnson, and Oskar Painter. Beyond the rayleigh scattering limit in high-q silicon microdisks: theory and experiment. *Optics Express*, 13(5):1515–1530, 2005.
- [163] H.A. Haus. *Waves and fields in optoelectronics*, volume 1. Prentice-Hall New Jersey, 1984.

- [164] G. Lenz, BJ Eggleton, C.K. Madsen, and RE Slusher. Optical delay lines based on optical filters. *Quantum Electronics, IEEE Journal of*, 37(4):525–532, 2001.
- [165] A. Melloni, A. Canciamilla, C. Ferrari, F. Morichetti, L. O’Faolain, TF Krauss, R. De La Rue, A. Samarelli, and M. Sorel. Tunable delay lines in silicon photonics: coupled resonators and photonic crystals, a comparison. *Photonics Journal, IEEE*, 2(2):181–194, 2010.
- [166] E. Dulkeith, F. Xia, L. Schares, W.M.J. Green, and Y.A. Vlasov. Group index and group velocity dispersion in silicon-on-insulator photonic wires. *Optics express*, 14(9):3853–3863, 2006.
- [167] Brent E Little, Juha-Pekka Laine, and Sai T Chu. Surface-roughness-induced contradirectional coupling in ring and disk resonators. *Optics letters*, 22(1):4–6, 1997.
- [168] A. Allan, D. Edenfeld, W.H. Joyner Jr, A.B. Kahng, M. Rodgers, and Y. Zorian. 2001 technology roadmap for semiconductors. *Computer*, 35(1):42–53, 2002.
- [169] L.J. Guo. Recent progress in nanoimprint technology and its applications. *Journal of Physics D: Applied Physics*, 37(11):R123, 2004.
- [170] M. Born and E. Wolf. *Principles of optics: electromagnetic theory of propagation, interference and diffraction of light*. Cambridge university press, 1999.
- [171] B.W. Smith, H. Kang, A. Bourov, F. Cropanese, and Y. Fan. Water immersion optical lithography for 45-nm node. In *Microlithography 2003*, pages 679–689. International Society for Optics and Photonics, 2003.
- [172] C. Mack. *Fundamental principles of optical lithography: the science of microfabrication*. Wiley, 2011.
- [173] <http://www.soitec.com/en/index.php>.
- [174] Hsi-Chun Liu and Amnon Yariv. Synthesis of high-order bandpass filters based on coupled-resonator optical waveguides (crows). *Optics express*, 19(18):17653–17668, 2011.
- [175] Yong Xu, Yi Li, Reginald K Lee, and Amnon Yariv. Scattering-theory analysis of waveguide-resonator coupling. *Physical Review E*, 62(5):7389, 2000.
- [176] Makoto Tomita, Kouki Totsuka, Ryosuke Hanamura, and Takahiro Matsumoto. Tunable fano interference effect in coupled-microsphere resonator-induced transparency. *JOSA B*, 26(4):813–818, 2009.

- [177] Robert W Boyd and Daniel J Gauthier. Photonics: transparency on an optical chip. *Nature*, 441(7094):701–702, 2006.
- [178] Xiaodong Yang, Mingbin Yu, Dim-Lee Kwong, and Chee Wei Wong. All-optical analog to electromagnetically induced transparency in multiple coupled photonic crystal cavities. *Physical review letters*, 102(17):173902, 2009.
- [179] Ugo Fano. Effects of configuration interaction on intensities and phase shifts. *Physical Review*, 124(6):1866, 1961.
- [180] M Galli, SL Portalupi, M Belotti, LC Andreani, L OFaolain, and TF Krauss. Light scattering and fano resonances in high- Q photonic crystal nanocavities. *Applied Physics Letters*, 94(7):071101–071101, 2009.
- [181] Shanhui Fan, Wonjoo Suh, and JD Joannopoulos. Temporal coupled-mode theory for the fano resonance in optical resonators. *JOSA A*, 20(3):569–572, 2003.
- [182] Andrey E Miroschnichenko, Sergej Flach, and Yuri S Kivshar. Fano resonances in nanoscale structures. *Reviews of Modern Physics*, 82(3):2257, 2010.
- [183] J.D. Plummer, M.D. Deal, P.B. Griffin, et al. *Silicon VLSI technology: fundamentals, practice and modeling*, volume 4. Prentice Hall Upper Saddle River, NJ, 2000.
- [184] Mattia Mancinelli, Romain Guider, Marco Masi, Paolo Bettotti, Manga Rao Vanacharla, Jean-Marc Fedeli, and Lorenzo Pavesi. Optical characterization of a scissor device. *Optics Express*, 19(14):13664–13674, 2011.
- [185] David D Smith, Hongrok Chang, Kirk A Fuller, AT Rosenberger, and Robert W Boyd. Coupled-resonator-induced transparency. *Physical Review A*, 69(6):063804, 2004.
- [186] Brent E Little, Sai T Chu, Hermann A Haus, J Foresi, and J-P Laine. Microring resonator channel dropping filters. *Lightwave Technology, Journal of*, 15(6):998–1005, 1997.
- [187] Yun-Feng Xiao, Xu-Bo Zou, Wei Jiang, You-Ling Chen, and Guang-Can Guo. Analog to multiple electromagnetically induced transparency in all-optical drop-filter systems. *Physical Review A*, 75(6):063833, 2007.
- [188] Michal Lipson. Guiding, modulating, and emitting light on silicon-challenges and opportunities. *Journal of Lightwave Technology*, 23(12):4222, 2005.
- [189] Yurii Vlasov, William MJ Green, and Fengnian Xia. High-throughput silicon nanophotonic wavelength-insensitive switch for on-chip optical networks. *Nature Photonics*, 2(4):242–246, 2008.

- [190] Xuezhe Zheng, Frankie Y Liu, Jon Lexau, Dinesh Patil, Guoliang Li, Ying Luo, Hiren D Thacker, Ivan Shubin, Jin Yao, Kannan Raj, et al. Ultralow power 80 gb/s arrayed cmos silicon photonic transceivers for wdm optical links. *Lightwave Technology, Journal of*, 30(4):641–650, 2012.
- [191] Zhen Sheng, Liu Liu, Sailing He, Dries Van Thourhout, and Roel Baets. Silicon-on-insulator microring resonator for ultra dense wdm applications. In *Group IV Photonics, 2009. GFP'09. 6th IEEE International Conference on*, pages 122–124. IEEE, 2009.
- [192] Charles A. Brackett. Dense wavelength division multiplexing networks: Principles and applications. *Selected Areas in Communications, IEEE Journal on*, 8(6):948–964, 1990.
- [193] Qianfan Xu, Sasikanth Manipatruni, Brad Schmidt, Jagat Shakya, and Michal Lipson. 12.5 gbit/s carrier-injection-based silicon micro-ring silicon modulators. *Opt. Express*, 15(2):430–436, 2007.
- [194] Vilson R Almeida, Carlos A Barrios, Roberto R Panepucci, Michal Lipson, Mark A Foster, Dimitre G Ouzounov, and Alexander L Gaeta. All-optical switching on a silicon chip. *Optics Letters*, 29(24):2867–2869, 2004.
- [195] Milos A Popovic, Tymon Barwicz, Fuwan Gan, Marcus S Dahlem, Charles W Holzwarth, Peter T Rakich, Henry I Smith, Erich P Ippen, and Franz X Kärtner. Transparent wavelength switching of resonant filters. In *Conference on Lasers and Electro-Optics*. Optical Society of America, 2007.
- [196] Klaas Maerten. Induced transparency in high order coupled resonators.
- [197] RL Espinola, MC Tsai, James T Yardley, and RM Osgood Jr. Fast and low-power thermo-optic switch on thin silicon-on-insulator. *Photonics Technology Letters, IEEE*, 15(10):1366–1368, 2003.
- [198] Vilson R Almeida, Carlos A Barrios, Roberto R Panepucci, and Michal Lipson. All-optical control of light on a silicon chip. *Nature*, 431(7012):1081–1084, 2004.
- [199] Zhipeng Wang, Shih-Jung Chang, Chi-Yu Ni, and Yung Jui Chen. A high-performance ultracompact optical interleaver based on double-ring assisted mach-zehnder interferometer. *Photonics Technology Letters, IEEE*, 19(14):1072–1074, 2007.
- [200] Ying Lu, Jianquan Yao, Xifu Li, and Peng Wang. Tunable asymmetrical fano resonance and bistability in a microcavity-resonator-coupled mach-zehnder interferometer. *Optics letters*, 30(22):3069–3071, 2005.

- [201] Fan Wang, Xiang Wang, Haifeng Zhou, Qiang Zhou, Yinlei Hao, Xiaoqing Jiang, Minghua Wang, and Jianyi Yang. Fano-resonance-based mach-zehnder optical switch employing dual-bus coupled ring resonator as two-beam interferometer. *Optics Express*, 17(9):7708–7716, 2009.
- [202] Minming Geng, Lianxi Jia, Lei Zhang, Lin Yang, Ping Chen, Tong Wang, and Yuliang Liu. Four-channel reconfigurable optical add-drop multiplexer based on photonic wire waveguide. *Optics Express*, 17(7):5502–5516, 2009.
- [203] Adam Densmore, Siegfried Janz, Rubin Ma, Jens H Schmid, Dan-Xia Xu, André Delâge, Jean Lapointe, Martin Vachon, and Pavel Cheben. Compact and low power thermo-optic switch using folded silicon waveguides. *Optics Express*, 17(13):10457–10465, 2009.
- [204] Landobasa Y Mario, S Darmawan, and Mee K Chin. Asymmetric fano resonance and bistability for high extinction ratio, large modulation depth, and low power switching. *Optics Express*, 14(26):12770–12781, 2006.
- [205] Sang-Yeon Cho and Richard Soref. Interferometric microring-resonant 2 x 2 optical switches. *Optics Express*, 16(17):13304–13314, 2008.
- [206] Marco Masi, Mattia Mancinelli, Paolo Bettotti, and Lorenzo Pavesi. Light combining for interferometric switching. *International Journal of Optics*, 2012, 2012.
- [207] Xianshu Luo, Junfeng Song, Shaoqi Feng, Andrew W Poon, Tsung-Yang Liow, Mingbin Yu, Guo-Qiang Lo, and Dim-Lee Kwong. Silicon high-order coupled-microring-based electro-optical switches for on-chip optical interconnects. *Photonics Technology Letters, IEEE*, 24(10):821–823, 2012.
- [208] M. Masi, M. Mancinelli, A. Battarelli, R. Guider, M.R. Vanacharla, P. Bettotti, J. Fedeli, and L. Pavesi. A silicon photonic interferometric router device based on scissor concept. *Lightwave Technology, Journal of*, 29(18):2747–2753, 2011.
- [209] DL Mills. *Non linear optics: basic concepts*.
- [210] B Ellis TS Moss, GJ Burrell. *Semiconductor optoelectronics*.
- [211] Christina Manolatou and Michal Lipson. All-optical silicon modulators based on carrier injection by two-photon absorption. *Journal of lightwave technology*, 24(3):1433, 2006.
- [212] Aleksandr Mikhailovich Lyapunov. The general problem of the stability of motion. *International Journal of Control*, 55(3):531–534, 1992.

- [213] Ido Kanter, Yaara Aviad, Igor Reidler, Elad Cohen, and Michael Rosenbluh. An optical ultrafast random bit generator. *Nature Photonics*, 4(1):58–61, 2009.
- [214] Linjie Zhou, Jingya Xie, Liangjun Lu, Xinwan Li, Jianping Chen, et al. Tunable two-stage self-coupled optical waveguide (scow) resonators. In *Optical Fiber Communication Conference*. Optical Society of America, 2013.
- [215] Anna Baldycheva, Vladimir A Tolmachev, Kevin Berwick, and Tatiana S Perova. Multi-channel si-liquid crystal filter with fine tuning capability of individual channels for compensation of fabrication tolerances. *Nanoscale research letters*, 7(1):387, 2012.
- [216] Yonghui Tian, Lei Zhang, Qianfan Xu, and Lin Yang. Xor/xnor directed logic circuit based on coupled-resonator-induced transparency. *Laser & Photonics Reviews*, 7(1):109–113, 2013.
- [217] Thomas YL Ang and Nam Quoc Ngo. Tunable flat-band slow light via contra-propagating cavity modes in twin coupled microresonators. *JOSA B*, 29(5):924–933, 2012.
- [218] Landobasa YM Tobing, Liliana Tjahjana, and Dao Hua Zhang. Characteristics of defect modes in side-coupled and mutually coupled microresonator arrays. *JOSA B*, 29(4):738–747, 2012.
- [219] N Caselli, F Intonti, C Bianchi, F Riboli, S Vignolini, L Balet, LH Li, M Francardi, A Gerardino, A Fiore, et al. Post-fabrication control of evanescent tunnelling in photonic crystal molecules. *Applied Physics Letters*, 101:211108, 2012.
- [220] Samee ur Rehman, Matthijs Langelaar, and Fred Van Keulen. Robust optimization of 2x2 multimode interference couplers with fabrication uncertainties. In *SPIE OPTO*, pages 862713–862713. International Society for Optics and Photonics, 2013.
- [221] M. Mancinelli, R. Guider, P. Bettotti, M. Masi, M.R. Vanacharla, J.M. Fedeli, D. Van Thourhout, and L. Pavesi. Optical characterization of silicon-on-insulator-based single and coupled racetrack resonators. *Journal of Nanophotonics*, 5(1):051705–051705, 2011.
- [222] P Bettotti, M Mancinelli, R Guider, M Masi, M Rao Vanacharla, and L Pavesi. Robust design of an optical router based on a tapered side-coupled integrated spaced sequence of optical resonators. *Optics letters*, 36(8):1473–1475, 2011.
- [223] M. Mancinelli, P. Bettotti, J.M. Fedeli, and L. Pavesi. Interferometric switching in coupled resonator optical waveguides-based reconfigurable optical device. *Optics Letters*, 38(2):217–219, 2013.

- [224] Andy Wolski. Theory of electromagnetic fields part iii: Travellingwaves.